Elliptical galaxies: fundamental relations, environmental effects and peculiar motions

Rafael Guzmán Llorente

ELLIPTICAL GALAXIES: FUNDAMENTAL RELATIONS, ENVIRONMENTAL EFFECTS AND PECULIAR MOTIONS

by

Rafael Guzmán Llorente

December 1993

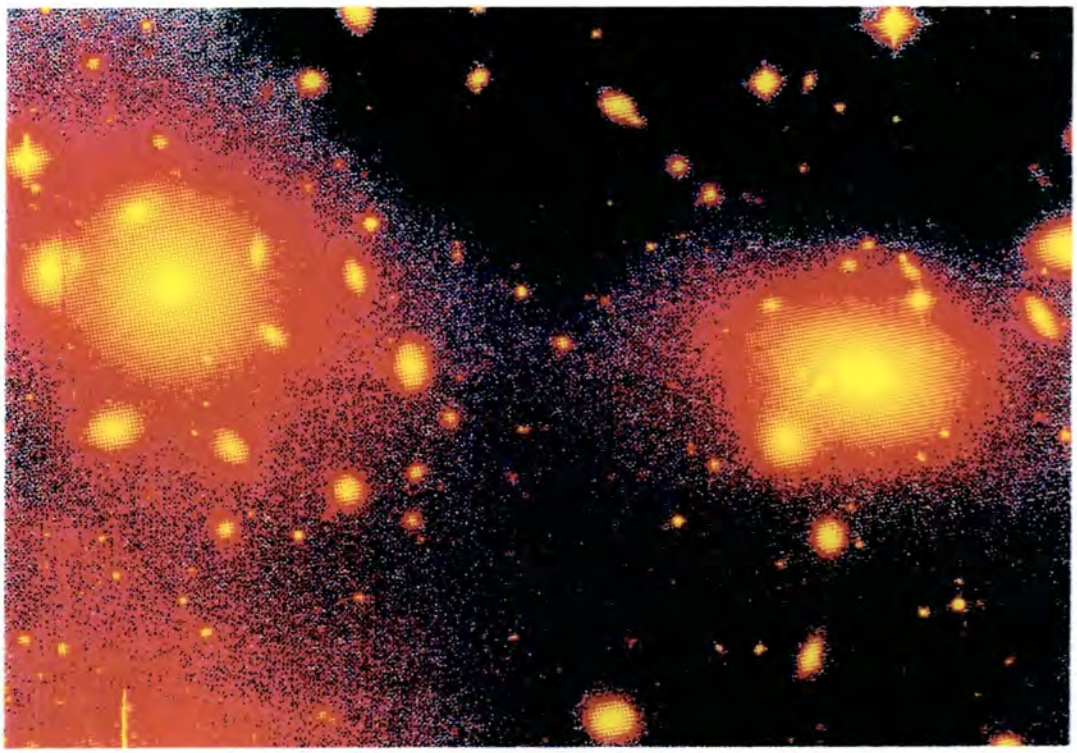

An account of research undertaken at the Department of Physics, submitted to the University of Durham in accordance with the regulations for admission to the degree of Doctor of Philosophy.

ABSTRACT

This thesis investigates the reliability of the $D-\sigma$ and $D-Mg_2$ distance indicators for elliptical galaxies. In particular, we test whether these empirical correlations are affected by differences in the stellar populations of elliptical galaxies associated with their environment. Our final goal is to assess the reality of the large peculiar velocities measured in the local universe as derived using these relations.

Our galaxy sample includes ellipticals located in high and low galaxian density regions. The cluster sample is mainly based on new observations of ellipticals in Coma, Abell 2199 and Abell 2634, while the field sample is selected from the literature. For each galaxy we list measurements of the effective radius, effective surface brightness, photometric diameter, velocity dispersion and magnesium index.

We first develop a phenomenological framework of galaxy properties that describes all empirical correlations for spheroidal systems, including both giant and dwarf ellipticals. Despite the wide variety of observed correlations, we show that only three provide independent information on the overall structure and metal abundance of these systems. These three 'fundamental relations' can be expressed in terms of physical variables assuming that both the galaxy mass-to-light ratio (M/L) and the ratio between the effective radii of the dark and luminous matter distributions (R/R_e) depend on the mass of the galaxy. The structure of elliptical galaxies is then determined by both the virial theorem *and* an intrinsic mass-radius relation. The metallicity of their stellar populations in turn is a function of the galaxy velocity dispersion alone. We compare this framework with a theoretical scenario of galaxy formation that combines the hierarchical clustering and the galactic wind models. This picture provides a consistent explanation of the fundamental relations of all elliptical galaxies assuming $R/R_e \sim$ constant for dwarf ellipticals while, for giant ellipticals, we find that R/R_e must be a decreasing function of galaxy mass. Our framework strongly suggests that this dependence of R/R_e on galaxy mass is the only difference between the two galaxy families.

We then study the effect of the environment on the $D-\sigma$ and $D-Mg_2$ distance indicators by comparing ellipticals that reside in the core of the Coma cluster with those in the cluster halo. By studying the variations within one cluster, we avoid the difficulty of decoupling effects induced by distance errors from those due to real environmental differences. We find that ellipticals located in the outer, low-density areas of the Coma cluster have D diameters that are, on average at a given σ or Mg_2, 10% or 30% larger than their counterparts in the cluster core. Using galaxy evolution models we demonstrate that this effect is consistent with the presence of an intermediate age stellar component in some halo ellipticals. We use the framework of galaxy properties in combination with galaxy evolution models to design a new age-independent distance indicator for ellipticals. This relation allows distances to be estimated with an uncertainty of $\sim$20% and is independent of age/environmental effects. We also offer a simple explanation of the trends observed in the $D-\sigma$ versus $D-Mg_2$ residuals plot.

Finally, we use our new distance indicator to readdress previous measurements of peculiar velocities in both the cluster and field environments. For Abell 2199 and Abell 2634 ellipticals, we show that the new distance estimates are in good agreement with those derived using the $D-\sigma$ and $D-Mg_2$ relations. Both clusters are found to have peculiar velocities which are not significantly different from zero. However, when the new distance indicator is applied to field ellipticals we find that the age/environmental effect translates into a spurious positive component of the local peculiar velocity field as derived from $D-\sigma$ and $D-Mg_2$. This effect may provide a simple explanation of the large positive peculiar motions observed towards the Great Attractor.

PREFACE

The work described in this thesis was undertaken between 1989 and 1993 whilst the author was a research student under the supervision of Dr. J. Lucey, in the Department of Physics at the University of Durham. This work has not been submitted for any other degree, diploma or other qualification at any other University.

Part of the work presented in this thesis was undertaken in collaboration with Dr. J. Lucey and the following research staff: Mr. J. Steel (University of Durham) (Chapter 2), Dr. R.G. Bower (Royal Observatory of Edinburgh) (Chapter 3), Dr. D. Carter and Prof. R.J. Terlevich (Royal Greenwich Observatory) (Chapter 4). However, the majority of this research is the author's own work.

Certain results described here have appeared in the following papers:

Lucey J.R., Guzmán R., Carter D. & Terlevich R.J., 1991. *Mon. Not. R. astron. Soc.*, **253**, 584.

Guzmán R., Lucey J.R., Carter D. & Terlevich R.J., 1992. *Mon. Not. R. astron. Soc.*, **257**, 187.

Guzmán R. & Lucey J.R., 1993. *Mon. Not. R. astron. Soc.*, **263**, L47.

Guzmán R., Lucey J.R. & Bower R.G., 1993. *Mon. Not. R. astron. Soc.*, **265**, 731.

A mis padres, María y Juan.

CONTENTS

1 INTRODUCTION

1.1 PERSPECTIVE

The discovery of large-scale inhomogeneities in the spatial distribution of galaxies is one of the major results achieved within extragalactic astronomy during the last decade. Three-dimensional maps with the true positions of thousands of galaxies in space were constructed by measuring galaxy redshifts in addition to the two-dimensional projection of galaxy positions in the night sky (e.g. Huchra *et al.* 1983). The observed redshifts of the lines in the galaxy spectra are commonly interpreted as Doppler shifts caused by the motions of galaxies in an expanding universe. In a pure Hubble flow, the derived recession velocities are then proportional to the galaxy distances. The results of these galaxy redshift surveys revealed the existence of large, nearly empty regions with surprisingly thin filaments of galaxies wrapped around them. The half-century-old dogma that the distribution is smooth on large scales, interrupted only by occasional concentrations of galaxies into clusters, began to give way to persuasive evidence of a complex and highly structured distribution of galaxies in space.

The origin of this large-scale structure in the universe is a fundamental problem of theoretical cosmology. A widely accepted picture is that such structure might be the

imprint of early-universe physics, i.e. the result of small primordial density fluctuations that would have grown in cosmic time as gravitation drew more matter into overdense regions at the expense of underdense regions. Among the different cosmological theories, the inflationary model universe (Guth 1981) has proved remarkably successful in explaining the cause of the cosmological expansion, the uniformity of the microwave background radiation and, more importantly for the present discussion, the mechanism that can increase the size of adiabatic fluctuations enough to seed large-scale structure. The inflation model even predicts a precise spectrum of the primordial fluctuations which serves as a starting place for models of growth based on gravitational instability. With this input spectrum and the simple physics of gravity, numerical N-body simulations have been successful at producing structures resembling those found in the universe at small scales (Frenk *et al.* 1985). However, for structure on the largest scales, superclusters and voids, these simulations produced model universes that were rather too smooth.

The failure of theoretical models to describe the observed structure on the largest scales may simply reflect the fact that the N-body simulations actually predict the distribution of matter, not galaxies. It is well known that there is considerably more matter between galaxies in clusters than can be attributed to that in the galaxies themselves. The remarkable success of the Big Bang nucleosynthesis indicates that this unseen extra matter, probably 10–100 times as much as we see in the galaxies, is almost certainly nonbaryonic. Most N-body simulations have been based on the model of cold dark matter (CDM) –so named because it postulates massive particles which move slowly compared with the speed of light– in a universe with critical density –as predicted by inflation–. Conventionally, it has been assumed that the galaxies trace this invisible mass distribution. Indeed, it would be more desirable to map the distribution of dark matter directly and then compare to the predictions of the N-body simulations. As a result, comparison of

the galaxy and dark matter distributions would test whether galaxies are accurate tracers of the mass, which in turn might be revealing itself of the process of galaxy formation.

Fortunately, nature has provided a way to map the mass distribution directly. Although the major component of galaxy motions is due to the expansion of the universe, a nearby overdensity of matter will pull galaxies, imparting additional velocities. Thus galaxies will stream towards overdense regions and away from underdense regions. A map of these 'peculiar velocities', i.e. the motions of galaxies relative to the Hubble flow, will reveal where the dark matter is and how great are the swells and troughs of its density. The inferred velocities from redshift measurements are thus a combination of the expansion of the universe and any gravitationally induced motions. The peculiar velocities are simply determined by subtracting the contribution of the cosmic expansion. This step requires a knowledge of the distance to the galaxy, because velocities in a pure Hubble flow are a linear function of distance.

Methods used at present to estimate distances to galaxies are mainly based on empirical correlations between global galaxy parameters. Tully and Fisher (1977) showed that for spiral galaxies the total luminosity is well correlated with galaxy rotation speed. In this case, the rotation speed measurement, which is independent of the galaxy distance, is used to predict a distance-dependent quantity, the luminosity. The Tully-Fisher relation allows galaxy distances to be estimated with a typical uncertainty of $\sim$20%. In a pioneering study, Aaronson *et al.* (1982) used this relation to measure the distances to a sample of spirals in the Local Supercluster and subtracted the inferred cosmic expansion component from the observed recession velocities to produce the first map of peculiar velocities. This study confirmed that the higher local density of galaxies did indeed outline a region of higher mass density and that the effect of gravity over a denser region could be actually seen.

In the last few years, considerable observational work has been undertaken to map the large-scale distribution of matter in the local universe by measuring the peculiar motions of galaxies. The most surprising and controversial results were derived using a new family of distance indicator relations for elliptical galaxies. This thesis investigates the nature of such empirical relations and the reality of the inferred peculiar motions of elliptical galaxies.

1.2 BACKGROUND

The use of elliptical galaxies in peculiar velocity analyses developed from studies aimed at determining their physical properties (see review by Jacoby *et al.* 1992). Normal ellipticals can be considered, in a first approximation, as simple one-spheroidal-component systems, with a homogeneous population of old stars whose random motions provide the shape of the galaxy. In addition to the simplicity of their physical properties, there are two important characteristics that make elliptical galaxies attractive for peculiar motions studies: a) they are luminous galaxies so that their global properties can be measured accurately at large distances; and b) they are strongly clustered so that many objects can contribute to the determination of the distance to an aggregate of galaxies, increasing thus the precision of the distance estimates.

The discovery of the correlation between luminosity and central velocity dispersion by Faber and Jackson (1976) marks the beginning of the potential use of elliptical galaxies as 'standard candles'. Following that discovery, automatic, quantitative techniques based on Fourier or cross-correlation methods for measuring velocity dispersions came into frequent use (Sargeant *et al.* 1977; Tonry & Davis 1981; Davies 1981). The use of these new techniques led to a growth of work on the properties and distances of elliptical galaxies,

notably the suggestion by Terlevich *et al.* (1981) of a second parameter at work in the Faber-Jackson relation and the use of that relation by Tonry and Davis to measure the infall of the Local Group towards the Virgo cluster. The uncertainty in the distance to a single galaxy in Tonry and Davis' use of the Faber-Jackson relation was ~30%.

Further work investigating the nature of the second parameter in the Faber-Jackson relation led to the development of the $D-\sigma$ relation (Dressler *et al.* 1987). This correlation between a characteristic diameter of the galaxy and its central velocity dispersion can be understood in terms of the physics of galaxy equilibrium (Faber *et al.* 1987; Djorgovski & Davies 1987) and implies a certain dependence of the mass-to-light ratio on galaxy mass. The $D-\sigma$ relation allows distances to be estimated with an uncertainty of ~20%, comparable to the Tully-Fisher relation for spirals. An alternative form of this relation, in which σ is substituted by the Mg_2 line strength index, has often been used to corroborate the results derived using $D-\sigma$ (Dressler *et al.* 1987; Dressler, Faber & Burstein 1991).

The largest uniform body of $D-\sigma$ data is summarized in Faber *et al.* (1989) and includes photometric and spectroscopic measurements for ~400 ellipticals listed in Burstein *et al.* (1987) and Davies *et al.* (1987). These data formed the basis for the first and currently most extensive application of the method. Using the $D-\sigma$ relation, these authors measured the pattern of peculiar motions of elliptical galaxies over the whole sky out to recession velocities of 8000 km s^{-1}. The result was surprising. They found a large-scale coherence to this pattern from which they inferred that galaxies in a large volume, nearly five times the size of the Local Supercluster, partake in a large-scale flow towards $l = 307°$, $b = 9°$ (Lynden-Bell *et al.* 1988). These authors postulated that this flow arises from the gravitational attraction of an overdense region, whose centre lay at a distance corresponding to a recession velocity of ~4500 km s^{-1}, which they termed the 'Great Attractor'.

The Great Attractor model offers a serious challenge for the CDM theory. N-body simulations by Bertschinger and Juskiewicz (1988) showed that such a massive and extended concentration is extremely improbable, especially in the commonly assumed case where galaxies are supposed to cluster more strongly than the dark matter. Comparisons have also been made with redshift surveys based on samples selected using infrared fluxes (such as those from the IRAS satellite). The IRAS reconstruction of the peculiar velocity field relies on an iterative method that enables one to measure galaxy accelerations in an all-sky redshift sample on the assumption that mass traces light over large scales. The peculiar motions deduced from this analysis are also in clear disagreement with the Great Attractor model (Rowan-Robinson *et al.* 1990).

More important, however, were new measurements of peculiar motions which showed inconsistent results from Tully-Fisher and $D - \sigma$ analyses of spiral and elliptical galaxies located in the same cluster (Aaronson *et al.* 1986; Lucey *et al.* 1991). This suggests that the distance indicator relations used to map the peculiar motions of galaxies may be sensitive to subtle differences in the physical properties of galaxies or in the data measurements themselves.

Indeed, new studies have revealed that the previous description of the properties of elliptical galaxies was oversimplified. It is now accepted that bright ellipticals tend to be supported by velocity anisotropy while the faint ones are flattened by rotation (Davies *et al.* 1983). In fact, there are indications, from isophote shapes, of embedded stellar disks in many rotationally supported ellipticals (Bender 1992). Also, it has been suggested that some elliptical galaxies have a spread in ages of the constituent stars, with an intermediate age population, $\sim$5 Gyr younger than the bulk of the stars, providing a significant fraction of the integrated galaxy light (Pickles 1985; Rose 1985). All these intrinsic variations in galaxy properties may bias the use of elliptical galaxies as 'standard candles'.

Because of the serious implications of the large-scale streaming motions for cosmology, it is of the greatest importance to understand the nature of the distance indicators used and any systematic effects or sources of errors. The constraints on galaxy mass-to-light ratio implied by the $D-\sigma$ relation led several authors to suggest that the environments of ellipticals might act to modify M/L and thus cause the zero-point of the $D-\sigma$ relation to vary between the field and cluster environments (Kaiser 1988; Silk 1989). The casual connection between galaxy properties and environment remains debatable, with *"nature versus nurture"* the centre of much ongoing discussion. However, field ellipticals do show systematic differences in some global correlations as compared to their cluster counterparts (Larson, Tinsley & Caldwell 1980). This has been recently confirmed by de Carvalho & Djorgovski 1992. Limits to the accuracy of distance indicator relations, such as $D-\sigma$ and $D-Mg_2$, due to environment-dependent effects should be better understood before secure measurements of large-scale peculiar velocities can be made.

1.3 THESIS

The primary aim of this thesis is to test the reliability of the $D-\sigma$ and $D-Mg_2$ distance indicators. In particular, we investigate whether these empirical relations are affected by differences in the stellar populations of elliptical galaxies associated with their environment. Our final goal is to assess the reality of the large peculiar velocities measured in the local universe as derived using these relations.

Recent studies have shown that ellipticals located in low-density environments tend to have a stronger intermediate age stellar component (Bower *et al.* 1990). Previous work on the environmental dependence of the distance indicators for ellipticals do suggest that, as a result of this younger stellar component, the distances to some field ellipticals may

be systematically underestimated compared to their measured redshifts (Burstein, Faber & Dressler 1990; de Carvalho & Djorgovski 1992). However, any difference between the galaxy redshift and its estimated distance can be interpreted as a real detection of its peculiar velocity (which affects the redshift), or as the result of an intrinsic variation in the galaxy properties (which may modify the distance estimate). This coupling between galaxy characteristics and peculiar motions has so far prevented any consensus on the importance of environmental effects in the distance indicator relations.

Our approach to this problem is to compare the $D-\sigma$ and $D-Mg_2$ relations for elliptical galaxies that reside in the core with those in the halo of an individual cluster. If an environmental effect exists, there will be a systematic difference between the cluster distances derived from the core and halo samples. This simple and powerful test avoids the difficulty of decoupling effects induced by peculiar motions from intrinsic environmental differences.

The thesis naturally divides into three parts. We start with a general analysis of the empirical correlations between the global parameters of elliptical galaxies. This analysis focuses on the physical nature of the distance indicators within a new framework of galaxy properties. We then study the age/environmental dependence of the $D-\sigma$ and $D-Mg_2$ relations and design a new age-independent distance indicator for ellipticals. Finally, we use this relation to readdress the measurement of peculiar motions for different samples of cluster and field ellipticals. Below, we briefly summarize the Chapter structure of this thesis.

In Chapter 2 we present the different galaxy samples used in this study. These include elliptical galaxies located in both the cluster and field environments. The cluster sample is based on new observations of ellipticals in Coma, Abell 2199 and Abell 2634,

although it includes a few Coma galaxies observed by Dressler (1984). A detailed description of our selection criterion, observational set-up and data reduction technique is presented. The field sample consists of isolated galaxies as listed in Faber *et al.* (1989). For each galaxy we list measurements of the effective radius, effective surface brightness, photometric diameter, velocity dispersion and Mg_2 line strength index. The systematic and experimental errors of all these measurements are carefully assessed.

In Chapter 3 we develop a new framework of galaxy properties that describes all empirical correlations for spheroidal systems, including both giant and dwarf ellipticals. Despite the wide variety of observed correlations, we show that only three provide independent information on the overall structure and metal abundance of these systems. These three fundamental relations can be expressed in terms of physical variables assuming that both the galaxy mass-to-light ratio (M/L) and the ratio between the effective radii of the dark and luminous matter distributions (R/R_e) depend on the mass of the galaxy. The structure of elliptical galaxies is then determined by both the virial theorem *and* an intrinsic mass-radius relation. The metallicity of their stellar populations in turn is a function of the galaxy velocity dispersion alone. We compare this framework with a theoretical scenario of galaxy formation that combines the hierarchical clustering and the galactic wind models. This picture provides a consistent explanation of the fundamental relations of all elliptical galaxies assuming $R/R_e \sim$ constant for dwarf ellipticals while, for giant ellipticals, we find that R/R_e must be a decreasing function of galaxy mass. Our framework strongly suggests that this dependence of R/R_e on galaxy mass is the only difference between the two galaxy families.

In Chapter 4 we study the effect of the environment on the $D-\sigma$ and $D-Mg_2$ distance indicators. We find that ellipticals located in the outer, low-density areas of the Coma cluster have, on average at a given σ or Mg_2, larger D diameters than those located in the cluster core. Using galaxy evolution models we demonstrate that this effect

is consistent with the presence of an intermediate age stellar component in some ellipticals located in the outer part of Coma. The environment-dependent effect translates into a spurious positive peculiar velocity for Coma as derived from the distance estimates to halo ellipticals. We use our framework of galaxy properties in combination with galaxy evolution models to design a new age-independent distance indicator for ellipticals. This relation allows distances to be estimated with an uncertainty of $\sim$20% and is independent of environmental effects. Using our framework we also offer a simple explanation of the trends observed in the $D - \sigma$ versus $D - Mg_2$ residuals plot.

In Chapter 5 we use our new distance indicator to readdress previous measurements of large peculiar velocities in both the cluster and field environments. For Abell 2199 and Abell 2634 ellipticals, we show that the new distance estimates are in good agreement with those derived using the $D - \sigma$ and $D - Mg_2$ relations. Both clusters are found to have peculiar velocities which are not significantly different from zero. However, when the new distance indicator is applied to field ellipticals we find that the age/environmental effect translates into a spurious positive component of the local peculiar velocity field derived from $D - \sigma$ and $D - Mg_2$. This effect may provide a simple explanation of the large positive peculiar motions observed towards the Great Attractor.

Finally, Chapter 6 summarizes the results presented in this thesis and outlines a future research programme to further investigate some of these new ideas.

2 OBSERVATIONS AND DATA REDUCTION

2.1 INTRODUCTION

This thesis is concerned with the study of environmental differences in the structural and stellar population properties of elliptical galaxies, and its effect on the distance indicator relations used to map the local peculiar velocity field. The global structure of elliptical galaxies is best described by the three-dimensional parameter space defined by the effective radius (R_e), effective surface brightness (SB_e) and central velocity dispersion (σ) (Djorgovski & Davies 1987; Bender, Burstein & Faber 1992). The characteristics of their stellar populations can be parameterized by the Mg_2 line strength index, which is sensitive to both the age and metallicity of the galaxy stellar content (Gorgas *et al.* 1991). These four global parameters provide an adequate description of the galaxy properties we wish to investigate. The results presented in this thesis are mainly based on new measurements of these parameters for elliptical galaxies located in different environments. For convenience, the photometric diameter D (Dressler *et al.* 1987), widely used in peculiar motion studies, is also included in our analysis.

In Section 2.2 we present the sample of Coma ellipticals used to perform the comparison between core and halo galaxies. In Section 2.3 we present the sample of

cluster ellipticals located in Abell 2199 and Abell 2634. The characteristics of the field galaxy sample are described in Section 2.4.

2.2 THE COMA SAMPLE

2.2.1 Selection of objects.

The Coma cluster, because of its richness, is an ideal laboratory to study the properties of a large sample of elliptical galaxies at a common distance. In order to perform our study on the environmental effects we need first to ensure that the selected Coma sample includes ellipticals that are located in different environments. The & White (1986) have shown that the galaxian surface density profile in Coma decreases by over a factor of 150 at a distance of $\sim$ 4 h^{-1} Mpc ($\sim$ 3.3°) from the cluster centre. Although the present environment of galaxies located in the inner and outer areas of the cluster is obviously different, the interpretation of possible variations in galaxy properties induced by the environment depends on the internal structure of the Coma cluster. For example, if the orbits of all galaxies were similar and there was sufficient time to produce a well-mixed system, then no variation in galaxy properties between ellipticals located in the inner and outer areas of the cluster would be expected. The extent of the well-mixed region defines the border between cluster areas characterized by different environmental conditions. Our galaxy sample must thus include ellipticals that are located outside this well-mixed region of the Coma cluster.

To a first approximation a rich cluster, like Coma, can be considered as a virialised core that is embedded in a collapsing halo which merges into the surrounding Hubble flow.

The transition between the separate regions is smooth and parallels the change in density. A convenient scale is given by the zero-velocity radius, i.e. the radius which corresponds to that shell of material that has been decelerated from the Hubble flow and is currently at rest with respect to the cluster centre (see Gunn & Gott 1972). From timing arguments of infalling shells, the zero-velocity radius is given by

$$R_{V=0} = \left(\frac{8GMt^2}{\pi^2}\right)^{1/3}$$

where M is the cluster mass and t is the age of the universe (Gunn & Gott 1972, Kent & Gunn 1982). Expressed in degrees, the zero-velocity radius is independent of the Hubble constant and only depends weakly on q_0. Kent & Gunn (1982) estimated Coma's mass to be $1.5 \times 10^{15}\ h^{-1}\ M_\odot$, and hence derived a zero-velocity radius of $6.1\ h^{-1}$ Mpc. Other studies of Coma (The & White 1986, Merritt 1987) have derived similar masses. These estimates are based on the assumption that galaxies trace the mass distribution. Without this assumption cluster masses a factor of two smaller or larger are derived (The & White 1986, Merritt 1987). Thus the zero-velocity radius for Coma probably lies in the range 4.8 to $7.7\ h^{-1}$ Mpc i.e. a projected angular distance of 3.8° to 6.1°.

Applying a similar timing argument we can estimate the radius outside which the Coma cluster is unlikely to be well-mixed. Consider a galaxy that is pulled into the cluster core and simply travels unimpeded out the other side. While such a journey through the cluster core is improbable as interactions are likely to randomize the galaxy's velocity, this approach provides a useful upper limit to how far a galaxy could, in principle, travel in the available time. If we take the age of the universe as the available time, the mixing radius that can be reached is

$$R_{\rm mix} = \left(\frac{1}{9}\right)^{1/3} R_{V=0} = 0.48 R_{V=0}$$

i.e. about half that of the zero-velocity radius. Thus galaxies that lie outside 1.8° to 2.9° have yet to visit the cluster core. As projection effects will reduce this radius further, these values can be considered as relatively firm upper limits.

By contrast the galaxies that lie in Coma's core are unlikely to travel out to large radii. By adopting the mass density profile of The & White (1986) for their galaxies-trace-mass model, we can estimate the maximum radii that can be reached by the galaxies that currently lie in the inner regions of Coma. We adopt 2700 km s^{-1} as a likely extreme value for a core galaxy's velocity in a radial direction. If a galaxy possesses such a radial velocity at a typical radius of 0.15 h^{-1} Mpc it has only sufficient kinetic energy to climb out to a radius of 0.9 h^{-1} Mpc, i.e. a projected angular distance of 0.7°. Hence galaxies that currently reside in the cluster core are likely to continue to do so. These rough estimates are in good agreement with previous work on the dynamics of the Coma cluster that considered this well-mixed core to include all Coma galaxies within $\sim$ 1° of the cluster centre (Simon White, private communication).

The above arguments indicate that the galaxian environmental conditions are very likely to change at a distance $r \sim 1°$ from the centre of the Coma cluster. While the ellipticals that lie in Coma's core ($r < 1°$) will have experienced strong dynamical interactions, those that lie in the outer halo ($r > 1°$) will be relatively unaffected.

Previous work on Coma ellipticals (Dressler 1987, Davies *et al.* 1987 and Burstein *et al.* 1987) have mainly concentrated on galaxies that lie near the cluster centre. Our observations were targeted mostly on ellipticals that lie in the outer part of the cluster. Our sample was selected from the galaxy lists of Dressler (1980) and Kent & Gunn (1982). Dressler (1980) gives positions and morphological types for 247 galaxies in a central 1.5° × 1.5° area of the cluster. The high plate scale and low contrast of the photographic plates used in this study ensured a reliable set of morphological classifications. Kent & Gunn

list positions, redshifts and morphological types for galaxies over a wider area gathered from a variety of sources. In general there is good agreement between the morphological classifications listed in the two studies, although there is disagreement over the classification of some early-type galaxies. In the central area about 20% of the galaxies typed by Dressler as ellipticals are listed by Kent & Gunn as S0s. About 25% of the galaxies listed by Kent & Gunn as ellipticals are classified by Dressler as S0s. In our analysis, because of the probable higher reliability of Dressler's types, we have adopted these where available in preference to those listed in Kent & Gunn.

For the central region ($r < 0.7°$) we have cross-referenced Dressler's list with the photometry of Godwin, Metcalfe & Peach (1983) to provide a magnitude-limited sample of 41 ellipticals brighter than 16.6 mag (B-band) and with velocity dispersions greater than 100 km s^{-1}, which is the usually adopted limit of the most widely used distance indicator relation (i.e. $D - \sigma$). Four of our sample of 41 ellipticals were later excluded from the analysis: one (D#55) was found to be background; one (D#107) has a velocity dispersion less than 100 km s^{-1}; two (NGC 4898A/B) form a very close pair which limits the accuracy of the photometric measurements. For 24 of the remaining 37 galaxies, high quality velocity dispersion measurements by Dressler are listed in Davies *et al.*. To enable a complete magnitude limited sample to be studied, we have made observations of the remaining 13 ellipticals. In order to provide an overlap, 12 galaxies (including NGC 4908 typed as S0/E by Dressler) in common with Dressler's work were also observed.

We have made observations of 33 Coma ellipticals that lie outside 0.7°. These were selected mainly from Kent & Gunn, although six ellipticals typed by Dressler are included in this sample. We selected all the ellipticals listed in Kent & Gunn brighter than 16.0 mag in the radius range 0.7° to 5° that are considered bound to the cluster (see Figure 2.1). Five galaxies were later excluded from the analysis: three (159-57, 159-58, NGC 4715) had very noticeable disks on our CCD frames and were rejected; two (159-42,

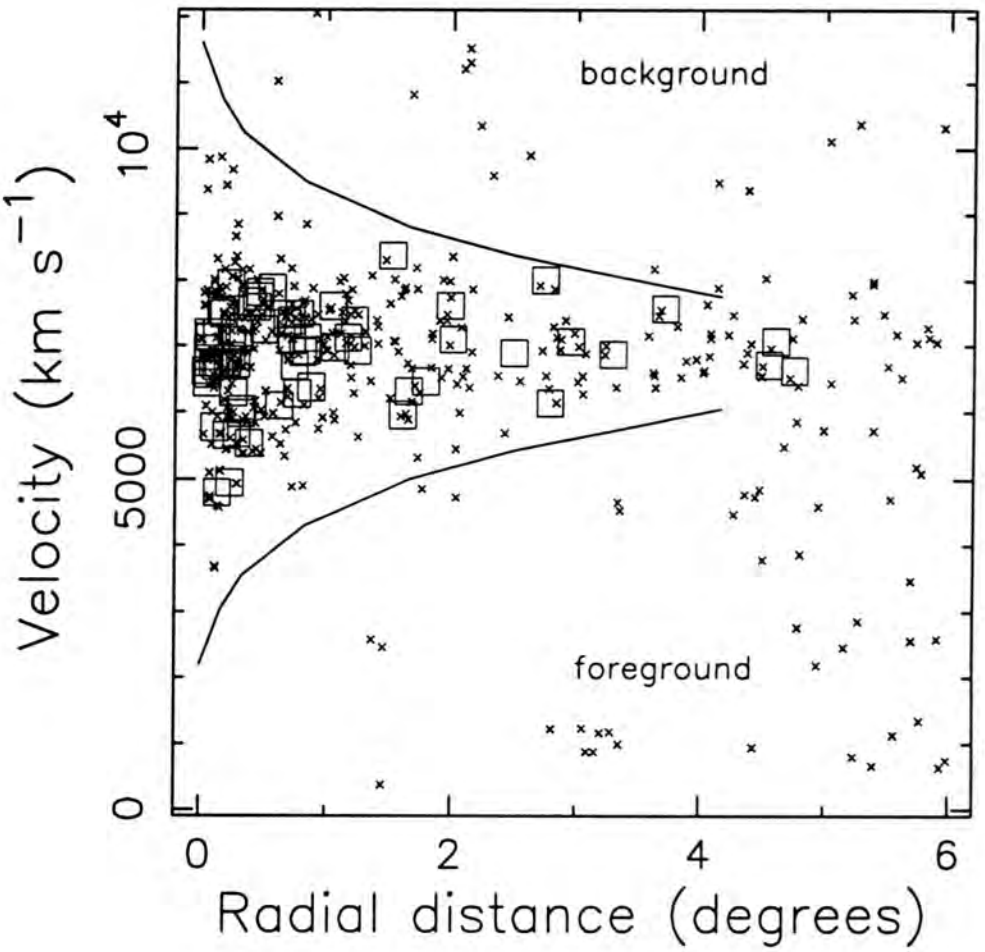

Figure 2.1. Distribution of recession velocities in the Coma cluster region as a function of the projected distance from the cluster centre (Kent & Gunn 1982). Solid lines separate cluster members from foreground and background galaxies. Open squares represent the elliptical galaxies included in our sample.

Table 2.1 Coma sample of elliptical galaxies.

Name	D#	α (1950)	δ	type$_D$	type$_{KG}$	m
NGC 4840	46	12 55 07.5	27 52 48	E/S0	E	14.86
160-49A	210	12 55 23.6	28 27 01	Ep	S0	15.97
	238	12 55 29.0	28 46 10	E		16.47
NGC 4850	137	12 55 56.8	28 14 16	E/S0	S0	15.39
RB 241	161	12 56 05.3	28 17 04	E	E	15.19
IC 3947	72	12 56 27.0	28 03 16	E	S0	15.94
RB 257	136	12 56 30.3	28 14 03	E	S0	16.57
NGC 4860	194	12 56 39.1	28 23 36	E	E	14.69
IC 3957	70	12 56 42.4	28 02 14	E	E	15.88
IC 3959	69	12 56 43.2	28 03 13	E	E	15.27
NGC 4864	159	12 56 48.1	28 14 47	E	E	14.70
NGC 4867	133	12 56 50.3	28 14 25	E	E	15.44
NGC 4869	105	12 56 58.5	28 10 49	E	E	14.97
RB 18	156	12 57 01.7	28 16 04	E/S0	S0	16.45
NGC 4872	130	12 57 09.3	28 12 57	E/S0	S0	14.79
NGC 4874	129	12 57 11.0	28 13 42	D	E	12.78
RB 43	125	12 57 17.5	28 11 37	E	E	16.47
RB 45	153	12 57 18.9	28 15 51	E	E	16.14
NGC 4876	124	12 57 19.6	28 10 53	E	E	15.51
RB 155	193	12 57 30.4	28 23 51	E	S0	16.43
NGC 4881	217	12 57 33.1	28 30 57	E	E	14.73
NGC 4886	151	12 57 39.6	28 15 24	E	E	14.83
IC 4011	150	12 57 41.6	28 16 23	E	E	16.08
IC 4012	174	12 57 43.3	28 20 51	E	E	15.93

Table 2.1 Cont.

Name	D#	α (1950)	δ	type$_D$	type$_{KG}$	m
NGC 4889	148	12 57 43.4	28 14 45	D	E	12.62
RB 167	207	12 57 44.4	28 26 22	E	E	16.07
IC 4021	172	12 57 50.1	28 18 38	E	E	16.01
	27	12 58 02.0	27 47 04	E	E	16.45
NGC 4906	118	12 58 15.0	28 11 34	E	E	15.44
IC 4045	168	12 58 24.1	28 21 36	E	E	15.17
IC 4051	143	12 58 29.9	28 16 36	E	E	14.47
160-92	81	12 58 44.6	28 05 18	E	E/S0	16.10
	204	12 58 58.3	28 27 53	E		15.99
NGC 4923	78	12 59 07.2	28 06 57	E	E	14.78
160-100	96	12 59 25.7	28 09 43	E	E	15.77
NGC 4926	49	12 59 29.1	27 53 34	E	E	14.16
NGC 4927	141	12 59 33.1	28 16 28	Ep	E	14.95
159-41		12 36 48.4	26 57 19		E	15.5
159-43		12 36 51.0	28 02 51		E	15.3
159-46		12 36 59.9	27 22 28		E	15.2
159-63		12 41 25.2	27 08 11		E	15.7
NGC 4673		12 43 07.6	27 20 08		E	13.7
NGC 4692		12 45 28.3	27 29 39		E	14.0
159-83		12 47 15.7	27 09 37		E	14.9
159-89		12 48 27.5	28 06 54		E	14.8
IC 832		12 51 32.8	26 42 46		E	15.0
NGC 4789		12 51 53.0	27 20 19		E	13.3
NGC 4807		12 53 03.5	27 47 31		E	14.64

Table 2.1 Cont.

Name	D#	α (1950)	δ	type$_D$	type$_{KG}$	m
IC 3900		12 53 15.6	27 31 15		E/S0	14.95
NGC 4816		12 53 46.8	28 00 58		E	14.08
160-22		12 53 53.0	26 37 40		E	15.2
160-23		12 53 54.4	28 01 16		E	15.66
160-27		12 54 01.3	28 06 03		E	15.57
	140	12 54 04.5	28 12 37	E		15.68
NGC 4824	35	12 54 08.7	27 48 33	E		15.96
NGC 4827		12 54 17.9	27 26 55		E	14.18
160-37	24	12 54 44.1	27 44 11	E	S0	15.46
NGC 4839	31	12 54 59.0	27 46 04	E/S0	E	13.51
NGC 4841A	240	12 55 07.0	28 44 48	E	E	13.88
IC 843		12 59 09.6	29 23 58		E	14.74
IC 4133		13 01 26.6	28 15 23		E	15.51
NGC 4952		13 02 34.8	29 23 23		E	13.6
NGC 4957		13 02 48.2	27 50 14		E	14.2
NGC 4971		13 04 31.3	28 48 45		E	15.0
NGC 5004		13 08 39.3	29 53 59		E	14.3
160-159		13 09 44.4	27 35 35		E	15.0

Notes: D# is the galaxy number given by Dressler (1980); type$_D$ and type$_{KG}$ are the morphological types as listed by Dressler (1980) and Kent and Gunn (1982); m is the integrated magnitude of the galaxy. Those values with one decimal figure are the Zwicky magnitudes as listed in Kent and Gunn (1982). Values with two decimal figures correspond to the $b_{26.5}$ magnitudes of Godwin, Metcalfe and Peach (1983).

160-33) had velocity dispersions less than 100 km s^{-1}. We also include the galaxy NGC 4841A studied by Dressler (1984). This outermost sample is not magnitude limited and contains few faint ellipticals.

The final Coma sample consists of 66 elliptical galaxies and is listed in Table 2.1.

2.2.2 Photometry

Short exposure (i.e. 100 to 180 seconds) V-band images were obtained for 51 galaxies in our Coma sample in June 1990 with a P8603 CCD at the prime focus of the 2.5m Isaac Newton Telescope (INT) at La Palma. The remaining galaxies of this sample had already been observed with the same telescope with an RCA CCD (Bower, Lucey & Ellis 1991). The images covered an area of $3.5' \times 5.2'$ at a scale of $0.54''$ $pixel^{-1}$. A summary of these observations is given in Table 2.2. The reduction of the CCD images was carried out using the software developed by Dr. John Lucey on the Starlink computer network. As the standard techniques are described in detail elsewhere (e.g. the RGO CCD User's Guide, Wall *et al.* 1989), we confine ourselves to a brief outline of the procedure adopted.

Each CCD image was bias-subtracted, to allow for the dc-bias voltage of the amplifier, and flatfielded, to allow for the spatial variation in the detector efficiency. The dark current was found to be negligible. The master bias frame was obtained by median filtering the bias frames taken at the beginning and end of the night. Similarly, the master flatfield was created from the individual flatfield frames obtained during twilight.

The images were calibrated for instrumental zero-point, atmospheric extinction and colour correction by observations of Landolt (1983) stars in a wide range of airmasses and colours. The magnitudes of both stars and galaxies were obtained by applying the relation:

Table 2.2 Log of photometric observations for Coma galaxies.

Date	June 16, 1990
Site	La Palma
Telescope	INT
CCD	GEC P8063
Readout Noise	$8e^-$
Pixel scale	0.54″
Photometric Band	V
Exposure time	100–180 seconds

$$\text{magnitude} = \text{zero-point} - \text{extinction} \times \text{airmass} - \text{colour-term} \times \text{colour}$$
$$-2.5 \log \{(\text{total flux in aperture} - \text{sky flux}) / \text{exposure time}\}$$

The zero-point, extinction and colour terms can be determined by minimizing the residuals of the measurements of standard stars. The measured extinction and colour terms were typically 0.12 mag airmass^{-1} and 0.03×(B-V) mag, respectively. For galaxy images, the sky flux was determined from interactively selected regions devoid of contaminating stars. The uncertainty in the sky background is less than 1%. The FWHM of the point spread function (PSF) of each CCD image was determined from stellar profiles and ranged from 0.9″ to 2.2″. Aperture photometry was measured for each galaxy and is listed in Table 2.3 along with the FWHM of the PSF. The aperture range is limited by seeing at the small sizes and sky-subtraction uncertainties at the large sizes. Cosmic ray events that were within these photometric apertures were interactively identified and removed by interpolation. From comparison between repeat observations and with measurements for 10 galaxies in common with previous observations with the same telescope (Bower, Lucey & Ellis 1991) we estimate that the zero-point uncertainty of our photometry is less than ±0.02 mag (see Figure 2.2).

Effective radii (R_e), effective surface brightnesses (SB_e) and photometric diameters (D) were derived from the aperture photometry and are listed in Table 2.6. The effective radius is defined as the radius of the circular aperture that encloses half of the total luminosity of the galaxy. The surface brightness within this aperture, corrected for seeing effects, galactic extinction and cosmological effects, is SB_e. The photometric diameter D is the diameter of a circular aperture within which the average surface brightness is 19.80 V-mag arcsec^{-2}. For an elliptical with a normal B-V colour of 0.95, the D diameter will be closely equivalent to the B-band diameter used by Dressler *et al.* (1987). For a few ellipticals of this sample, we used the aperture photometry listed in Bower, Lucey & Ellis (1991) to derive these parameters.

Table 2.3 V-band aperture photometry.

Name	D#	PSF	4″	6″	8″	10″	13″	16″	20″	25″	32″	40″	50″
159-42		1.1	16.48	15.96	15.70	15.56	15.41	15.30	15.19	15.10	15.03	14.98	14.93
159-42		1.1	16.47	15.96	15.70	15.55	15.40	15.29	15.18	15.10	15.02	14.97	14.92
159-41		1.2	15.76	15.48	15.31	15.19	15.05	14.94	14.83	14.73	14.66	14.63	14.59
159-43		1.1	15.52	15.18	14.98	14.84	14.69	14.58	14.48	14.38	14.30	14.23	14.18
159-46		1.0	15.66	15.32	15.12	14.98	14.83	14.70	14.56	14.45	14.34	14.25	14.17
159-57		1.0	16.89	16.46	16.14	15.87	15.55	15.33	15.10	14.91	14.78	14.70	14.65
159-58		1.0	16.42	15.99	15.72	15.52	15.28	15.12	14.96	14.81	14.68	14.59	14.53
159-63		0.9	16.13	15.80	15.58	15.42	15.24	15.10	14.96	14.84	14.74	14.65	14.57
N4673		0.9	14.68	14.30	14.08	13.92	13.75	13.63	13.51	13.40	13.30	13.22	13.16
N4692		0.9	15.36	14.90	14.60	14.38	14.15	13.97	13.79	13.62	13.45	13.33	13.22
159-83		1.0	15.75	15.27	14.96	14.76	14.55	14.41	14.28	14.16	14.03	13.93	13.84
N4715		1.0	15.63	15.29	15.09	14.92	14.73	14.60	14.45	14.30	14.13	13.96	13.78
159-89		0.9	15.88	15.48	15.21	15.02	14.82	14.69	14.55	14.43	14.30	14.19	14.11
I832		0.9	15.84	15.42	15.16	14.98	14.78	14.63	14.48	14.36	14.23	14.14	14.06
N4789		1.0	15.04	14.59	14.30	14.10	13.88	13.72	13.54	13.39	13.22	13.07	12.94
N4807		1.0	15.21	14.85	14.64	14.49	14.32	14.20	14.07	13.96	13.85	13.77	13.70
I3900		1.1	15.39	15.03	14.82	14.68	14.52	14.41	14.31	14.22	14.13	14.06	14.00
N4816		1.1	15.49	15.12	14.88	14.70	14.50	14.34	14.16	13.98	13.79	13.62	13.45
N4816		1.1	15.51	15.13	14.88	14.70	14.50	14.34	14.16	13.98	13.79	13.62	13.45
160-22		1.1	15.44	15.09	14.90	14.77	14.62	14.50	14.38	14.27	14.16	14.09	14.04
160-23		1.1	15.95	15.61	15.36	15.21	15.06	14.97	14.89	14.82	14.77	14.72	14.68
160-23		1.1	15.98	15.59	15.36	15.21	15.06	14.97	14.89	14.82	14.76	14.72	14.66
160-27		1.2	16.07	15.71	15.50	15.34	15.16	15.04	14.93	14.84	14.76	14.69	14.63

Table 2.3 Cont.

Name	D#	PSF	4″	6″	8″	10″	13″	16″	20″	25″	32″	40″	50″
	140	1.1	16.11	15.81	15.62	15.49	15.34	15.23	15.12	15.00	14.88	14.78	14.70
N4824	34	1.2	16.15	15.84	15.65	15.51	15.36	15.24	15.14	15.06	14.98	14.93	14.88
N4827		1.1	15.27	14.89	14.64	14.45	14.26	14.12	13.97	13.83	13.69	13.57	13.46
160-37	24	1.3	15.72	15.34	15.13	15.00	14.86	14.76	14.66	14.59	14.52	14.48	14.44
N4840	46	1.3	15.45	15.06	14.82	14.67	14.49	14.36	14.24	14.14	14.05	13.98	13.92
160-49A	210	1.4	16.15	15.77	15.56	15.42	15.29	15.20	15.12	15.05	15.00	14.97	14.94
	238	1.5	16.47	16.13	15.93	15.80	15.68	15.60	15.54	15.49	15.45	15.41	15.39
	238	1.8	16.52	16.13	15.94	15.80	15.67	15.59	15.53	15.48	15.44	15.41	
N4850	137	1.3	15.90	15.47	15.21	15.04	14.87	14.76	14.68	14.59	14.50	14.43	14.36
RB241	161	2.2	16.07	15.57	15.27	15.08	14.88	14.75	14.61	14.49	14.37	14.28	14.20
N4854	58	2.1	16.39	15.89	15.59	15.39	15.17	15.00	14.82	14.67	14.51	14.38	14.27
	72	2.2	16.34	15.83	15.58	15.41	15.25	15.15	15.07	15.01	14.95		
N4860	194	1.3	15.47	15.05	14.77	14.59	14.42	14.28	14.15	14.04	13.92	13.83	13.76
N4860	194	1.8	15.56	15.06	14.79	14.60	14.40	14.27	14.14	14.02	13.90	13.82	
	156	1.7	17.18	16.78	16.54	16.40	16.27	16.18	16.11	16.06			
N4881	217	1.9	15.82	15.33	15.04	14.84	14.63	14.48	14.33	14.19	14.06	13.95	13.84
N4881	217	1.2	15.67	15.25	15.01	14.83	14.63	14.48	14.34	14.20	14.06	13.95	13.85
N4881	217	1.2	15.70	15.27	15.03	14.83	14.64	14.49	14.34	14.20	14.07	13.95	13.85
TT41	27	1.6	16.84	16.40	16.15	15.97	15.81	15.70	15.61	15.54	15.49	15.45	
N4908	167	1.7	15.69	15.27	14.99	14.81	14.62	14.49	14.36	14.25	14.14	14.06	13.98
I4051	143	1.1	16.05	15.52	15.19	14.97	14.71	14.52	14.34	14.17	14.00	13.87	13.76
I4051	143	1.2	16.06	15.53	15.21	14.98	14.73	14.54	14.35	14.18	14.01	13.88	13.76
160-92	81	1.8	16.75	16.34	16.10	15.94	15.77	15.64	15.52	15.41	15.30	15.20	15.12

Table 2.3 Cont.

Name	D#	PSF	4″	6″	8″	10″	13″	16″	20″	25″	32″	40″	50″
	204	2.0	16.68	16.21	15.97	15.81	15.65	15.54	15.43	15.32	15.20	15.12	15.05
N4923	78	1.4	15.59	15.17	14.92	14.75	14.58	14.46	14.33	14.21	14.09	14.00	13.91
I843		1.7	15.73	15.22	14.92	14.71	14.50	14.35	14.20	14.07	13.96	13.87	13.79
160-100	96	1.3	16.05	15.74	15.57	15.44	15.30	15.20	15.10	15.01	14.92	14.84	14.77
N4926	49	1.2	15.23	14.79	14.54	14.36	14.17	14.03	13.88	13.75	13.60	13.48	13.38
N4927	141	1.3	15.86	15.38	15.07	14.86	14.64	14.49	14.33	14.20	14.07	13.96	13.87
N4929	166	1.2	16.06	15.62	15.37	15.19	14.99	14.84	14.69	14.55	14.41	14.30	14.20
I4133		1.3	15.87	15.52	15.32	15.20	15.05	14.94	14.83	14.74	14.65	14.58	14.52
N4952		1.3	15.08	14.63	14.36	14.18	13.98	13.84	13.69	13.55	13.41	13.30	13.20
N4957		1.2	15.56	15.08	14.79	14.59	14.36	14.20	14.03	13.88	13.72	13.59	13.48
N4957		1.5	15.57	15.09	14.81	14.59	14.36	14.19	14.03	13.87	13.71	13.59	13.47
N4971		1.2	15.75	15.36	15.12	14.97	14.82	14.70	14.57	14.45	14.31	14.21	14.13
N5004		1.6	15.29	14.79	14.52	14.32	14.12	13.97	13.81	13.68	13.54	13.43	13.34
N5004		1.1	15.19	14.76	14.50	14.32	14.12	13.97	13.82	13.68	13.54	13.44	13.34
160-159		1.1	15.78	15.39	15.15	14.98	14.80	14.66	14.54	14.43	14.33	14.26	

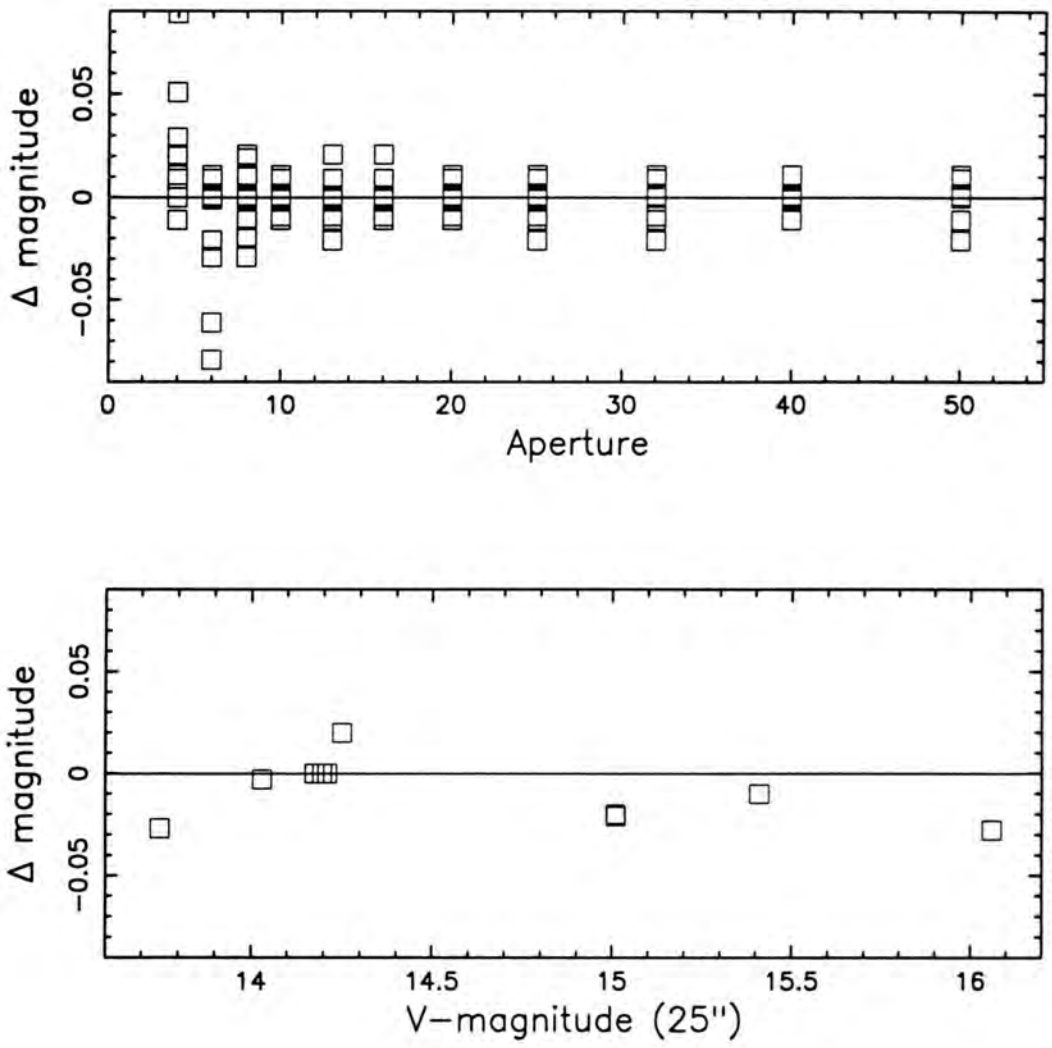

Figure 2.2. Top panel: Internal comparison of our aperture photometry for 10 Coma ellipticals with repeat observations. Bottom panel: Comparison of our photometry with that of Bower, Lucey & Ellis (1991) for 10 galaxies in common between the two studies. Measurements within 25″ aperture are compared.

The method to measure these photometric parameters is summarised in Figure 2.3. In the top panel we show a contour plot of the CCD image of NGC 4881 (down to 24 mag arcsec^{-2} in intervals of 0.5 mag). The scale represents the size of our largest aperture (60"). The bottom panels show the standard $r^{1/4}$ luminosity growth curve fit to the observed aperture versus magnitude over the 6″ to 50″ range and the residuals from this fit. The 4″ and 60″ apertures are not used due to the uncertainties introduced by the seeing correction (solid line in first aperture) and sky subtraction (error bars in last aperture). The horizontal and vertical dashed lines represent the values of the total magnitude and effective diameter derived for this galaxy using the $r^{1/4}$ growth curve. The D values were derived by interpolation using the range of apertures in the region outlined by the two curved dashed lines.

In the derivation of these parameters the following corrections were applied:

(a) seeing: a set of seeing corrections were determined by broadening a model galaxy image with an adopted PSF. Aperture photometry was performed on the broadened and unbroadened model galaxy images and the magnitude offset taken as the correction. For the PSF we adopted the Hankel transform of the combined modulation transfer function of the telescope and atmosphere, (see e.g. Roddier 1981). A set of coherence diameters were chosen to cover the PSF FWHM range of the observations. Unlike the often adopted gaussian function, this representation provides an excellent fit to the observed PSF. For the model galaxy image we adopted an $r^{1/4}$ profile. The derived corrections only weakly depend on the profile's effective radius and hence, for simplicity, we adopted for all galaxies the corrections for an effective radius of 5″, which is a representative value for the Coma ellipticals. The set of corrections are tabulated in Bower, Lucey & Ellis (1991). We note that the seeing correction has a very minor effect on the derived

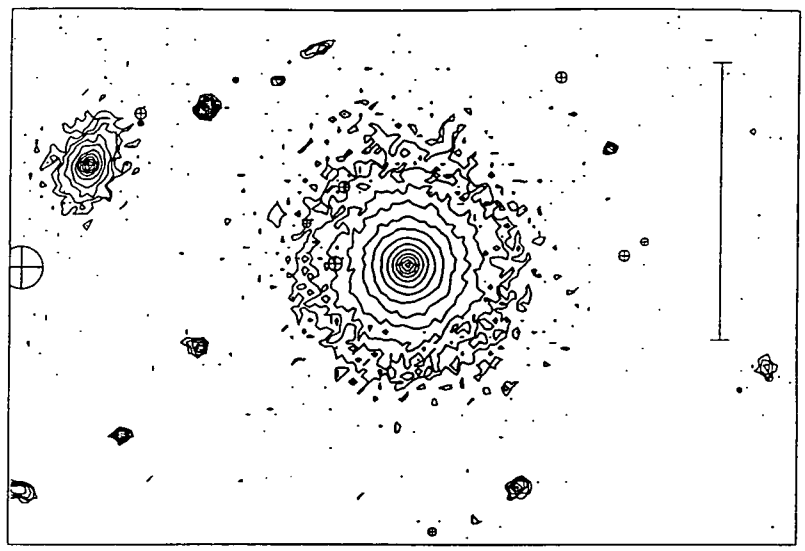

Galaxy: N4881 coma_outer.vfot see_005.cor

No of data points 30 aperture limits : 5.0 55.0

Corr app RQ: V_T= 13.35 A_e= 20.84 1.319 Avedel= 0.015 SB_e^c= 20.44

GalCZ = 6730 A_V = 0.038 Tot. corr −0.179

Global: D_{1980Q} = 13.65 1.135 21.00 D_{2060Q} = 26.11 1.417 22.31

Local : D_{1980Q} = 13.55 1.132 21.05 D_{2060Q} = 25.95 1.414 22.26

Local : D_{1980P} = 13.51 1.131 21.03 D_{2060P} = 25.89 1.413 22.26

P(1.1) = 0.895 P(1.5) = 1.458

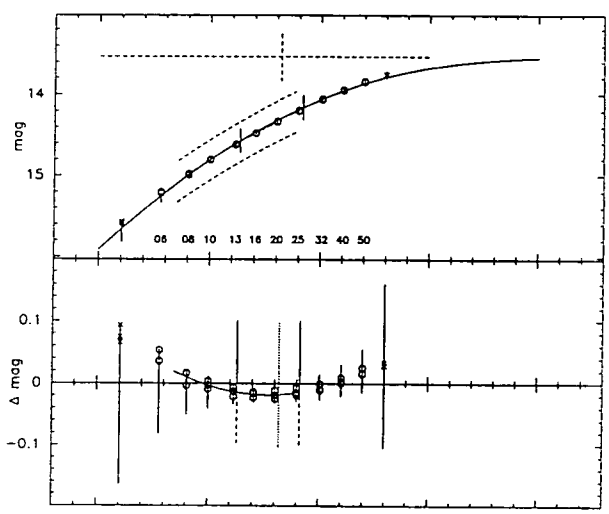

Figure 2.3. Example of our data reduction technique: Measurement of the photometric parameters for NGC 4881. The scale shown in the galaxy contour plot represents the size of our largest aperture (60").

D diameters, i.e. the correction for a 10″ D diameter in 1.5″ FWHM seeing being equivalent to a change of only 0.01 dex ;

(b) galactic extinction (values from Burstein & Heiles 1984) ; and

(c) k-corrections (from Oke & Sandage 1968).

The D photometric diameters and effective surface brightnesses also include the $(1+z)^4$ cosmological correction.

The values of R_e and SB_e listed in Table 2.6 are those derived from global fits to the aperture photometry. There is the usual strong coupling of the two $r^{1/4}$-profile parameters, i.e. if R_e is overestimated then a fainter SB_e is derived and viceversa. Because of this strong coupling the errors in $\log R_e$ and SB_e are correlated (Hamabe & Kormendy 1987):

$$\Delta \log R_e \sim 0.3\ \Delta SB_e \tag{2.1}$$

Comparison of values derived from independent Lucey, Bower & Ellis (1991) data indicates that the listed R_e and SB_e measurements have uncertainties of 0.028 dex and 0.14 mag respectively (see Figure 2.4). However, due to the correlation between these errors, the typical uncertainty in $\{\log R_e - 0.3\ SB_e\}$ is only ~0.011 dex (Figure 2.4). The D values are significantly more accurate than the individual measurements of R_e and SB_e. Comparison of values derived from the Lucey, Bower & Ellis' (1991) data indicated that the uncertainty of our D values is 0.005 dex (Figure 2.4).

The three photometric parameters are intrinsically related. If all elliptical galaxies followed the same growth curve, then the ratio D/R_e would be a function only of SB_e, the vertical normalization of the growth curve (Dressler *et al.* 1987). When the D diameter was introduced, Dressler *et al.* (1987) showed that this relation is well described by:

$$\log D = \log R_e - 0.32\ SB_e + constant \tag{2.2}$$

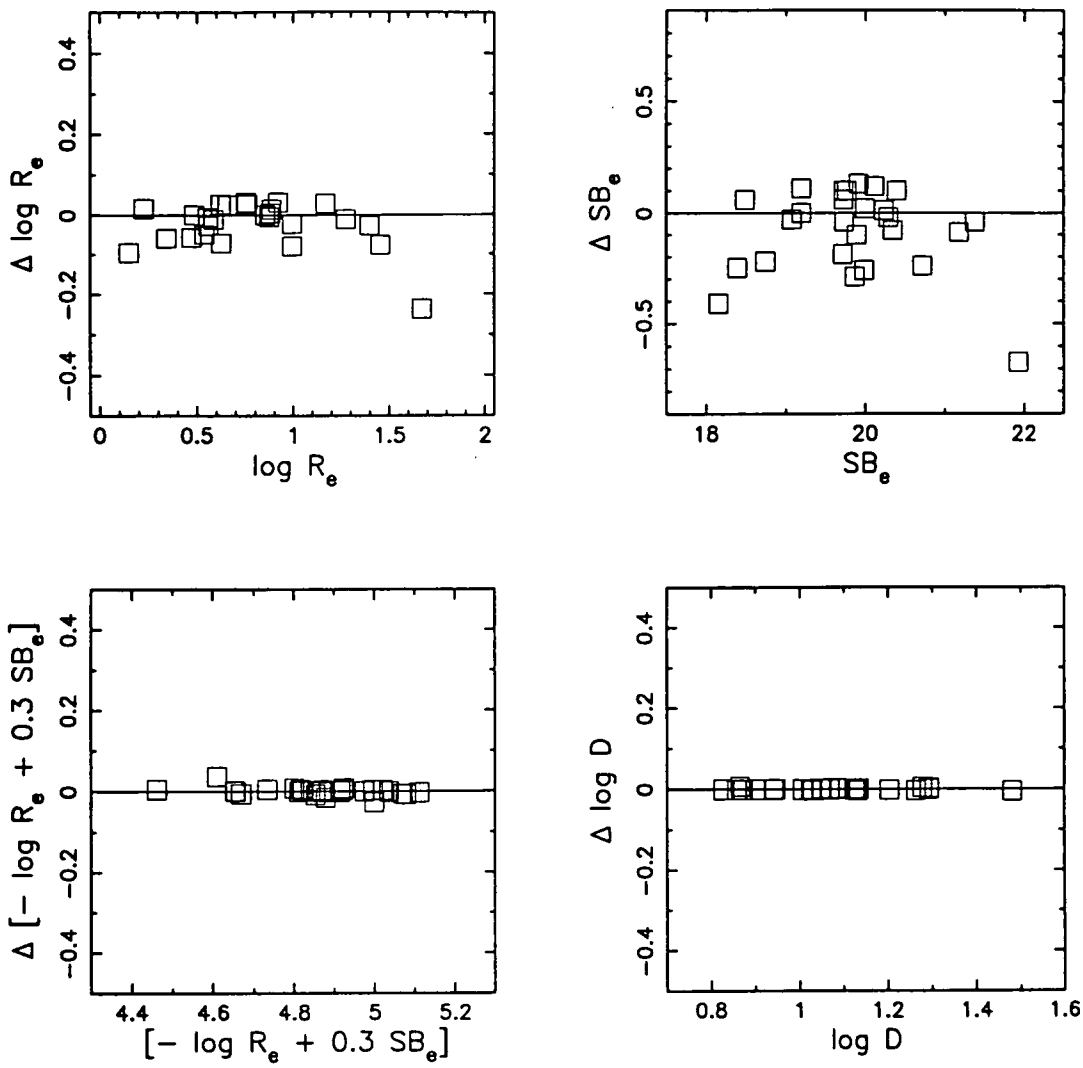

Figure 2.4. Comparison between the different photometric parameters derived in Lucey, Bower & Ellis (1991) and in this study.

For our V-band photometric parameters we derive:

$$\log D = \log R_e - 0.286\ SB_e + constant \tag{2.3}$$

These linear expressions are, however, simple approximations that can be applied only over a restricted range in surface brightnesses. For galaxies with $r^{1/4}$-profiles it is possible to determine the exact form of the equation that relates R_e, SB_e and D (Phillips 1988; Jorgensen, Franx & Kjaergaard 1993). As it can be clearly seen in Figure 2.5, the equation [2.3] is only valid for ellipticals with $19.0 \leq SB_e < 21.0$ mag.

2.2.3 Spectroscopy

Spectroscopic observations were made in May 1990 using the Intermediate Dispersion Spectrograph on the INT in good seeing, i.e. ~1″. The 632 grooves mm^{-1} grating blazed at 5460Å was used on the 235 camera to produce a dispersion of 1.46Å $pixel^{-1}$ on a GEC P8603 CCD. The spectra covered about 800Å centred on Mg*b*, i.e. 4800Å to 5600Å . Observations were made with a 2″ slit which gave a FWHM resolution of 220 km s^{-1}. Data were recorded over a slit length of 3′. Along the slit a factor-of-three on-chip binning was used to give a scale of 1.94″ $pixel^{-1}$. Exposures of 600 to 1800 seconds gave signal-to-noise ratios of between 10 and 25 per Å in the extracted spectra. A summary of these observations is presented in Table 2.4.

CuAr arc lamp calibration exposures were taken only every other frame because the instrument proved to be very stable. A large number of the galaxies were observed more than once to improve reliability. Several galaxies with previous measurements were also observed in order to assess systematic errors. High signal-to-noise (>50) observations of 18 stars were also made for use as templates in the data reduction. These were giants of spectral types G8 to K5 and included three super metal-rich K giants (HR 7352, HR

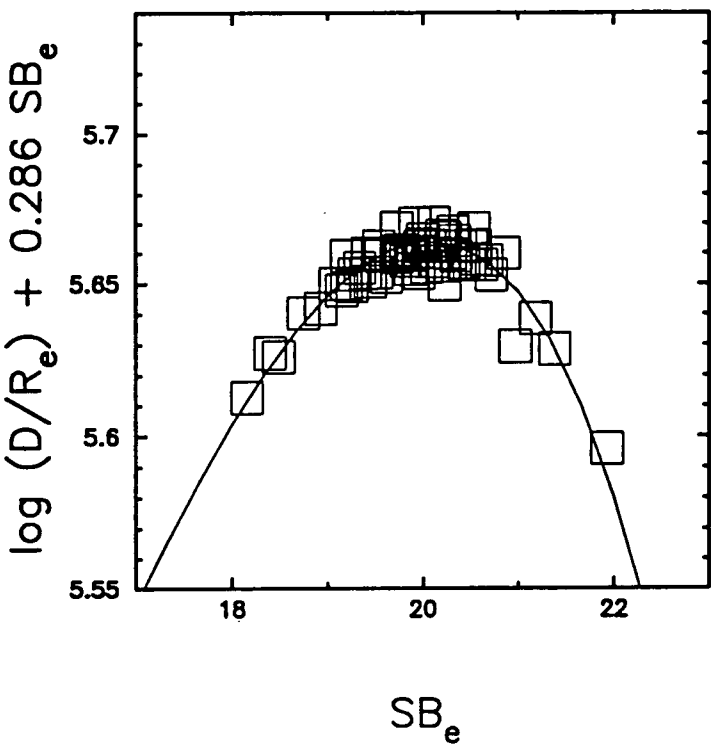

Figure 2.5. The difference between $\log D$ and the linear combination $\log R_e - 0.286\ SB_e$ as a function of surface brightness for our sample of Coma ellipticals (open squares). The solid line represents the theoretical relation derived from the $r^{1/4}$-profile.

Table 2.4 Log of spectroscopic observations for Coma galaxies.

Date	May 14-23, 1990
Site	La Palma
Telescope	INT
Spectrograph	IDS-235
CCD	GEC P8063
Readout Noise	8 e^-
Dispersion	1.46 Å $pixel^{-1}$
Resolution (FWHM)	220 km s^{-1}
Wavelength range	4800Å –5600Å
Exposure time	600–1800 seconds

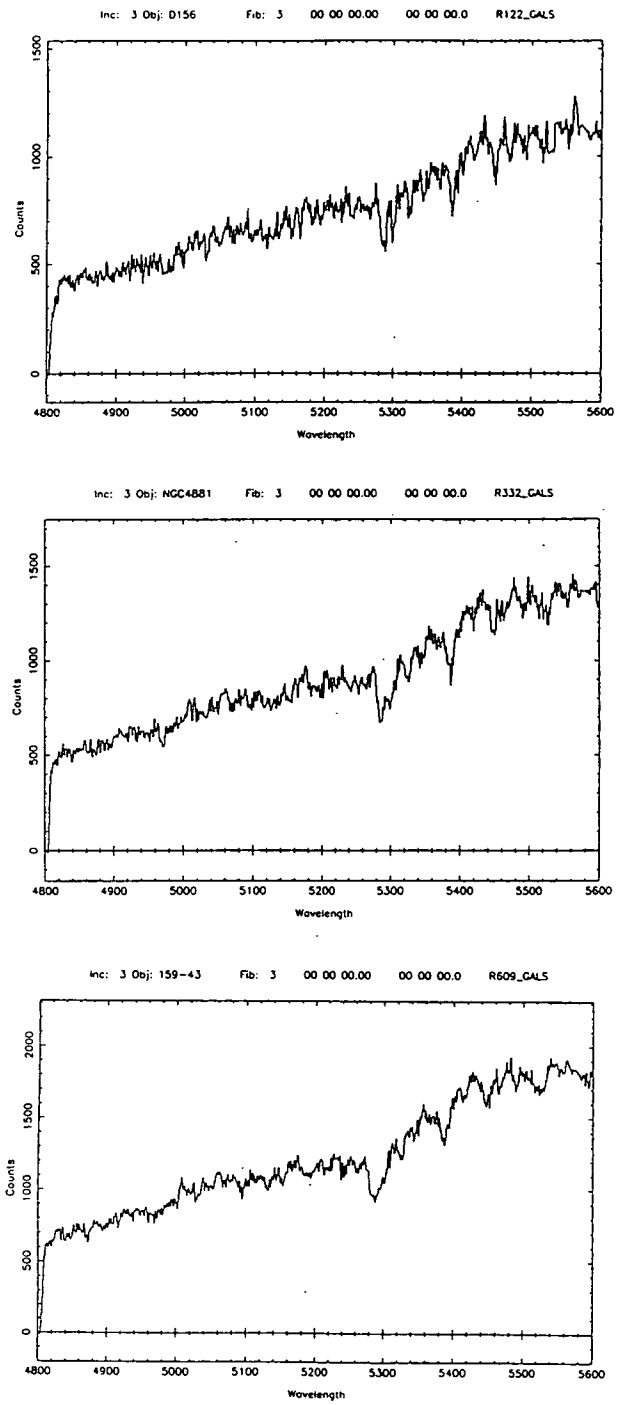

Figure 2.6. Spectra of the elliptical galaxies D156, NGC 4881 and 159-43. The velocity dispersions of these objects are 107, 204 and 267 km s^{-1}, respectively. Their Mg_2 line indices are 0.223, 0.288 and 0.330 mag, respectively.

7576 and HR 8413) from Faber *et al.* (1985). Observations of three flux standards were also made.

These spectra were reduced with FIGARO using the standard procedure briefly described here. The images were: a) debiased using the overscan strips to estimate the bias value to be subtracted from each frame; b) flatfielded using a master flatfield obtained by averaging the Tungsten flats from each night, after checking that there was no significant variation amongst different nights; c) corrected for uneven illumination with a slit function made from twilight sky flats; and d) wavelength calibrated using the CuAr arc frames (the rms residual from the fits used in this calibration were, typically, $\sim$5 km s^{-1}). After calibration, the spectra were background subtracted. The underlying sky contribution was determined by using the median of sky spectra observed well-away from the galaxy position on the slit. Because the objects filled only small parts of the slit, the sky subtraction was straightforward. The central three pixel (5.8″) region was extracted and co-added to form each galaxy spectrum. Finally, cosmic ray events were interactively removed from the 1-D spectra. A representative sample of these spectra is shown in Figure 2.6.

2.2.3.1 Measurements of the velocity dispersion

Redshifts and velocity dispersions (σ) were derived using the well-known Fourier quotient method (Sargent *et al.* 1977) as implemented in the DUSDERS software package (Inglis 1985) with subsequent modifications and improvements made by Dr. John Lucey. Results were derived independently for all 18 templates. Templates of spectral types G8 to K3 gave very consistent velocity dispersions, the typically rms scatter being about 3% for an individual galaxy spectrum. The super metal-rich giants gave velocity dispersions that were close to the average. In contrast, the K4 and K5 giants gave velocity dispersions that were about 5% greater than the average. This trend in the σ measurements with

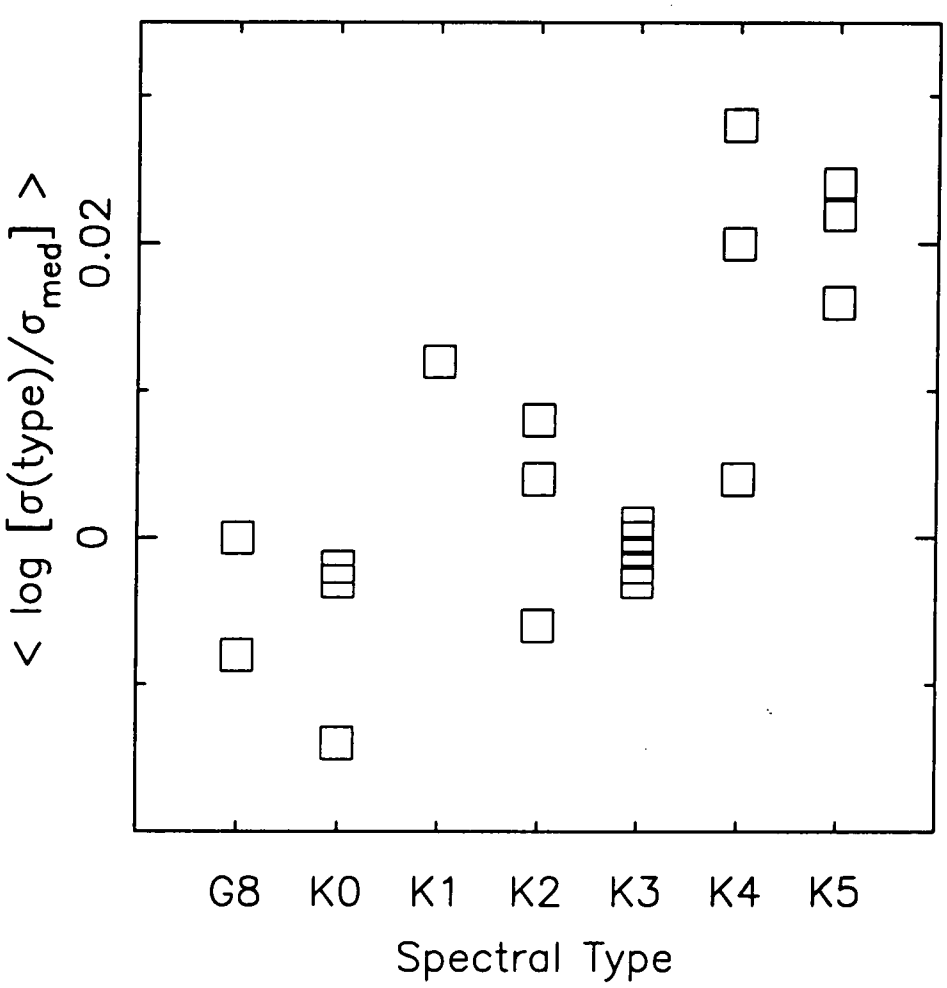

Figure 2.7. The ratio between the velocity dispersions derived for each template and the median value, averaged for all galaxy spectra, as a function of the spectral type of the template.

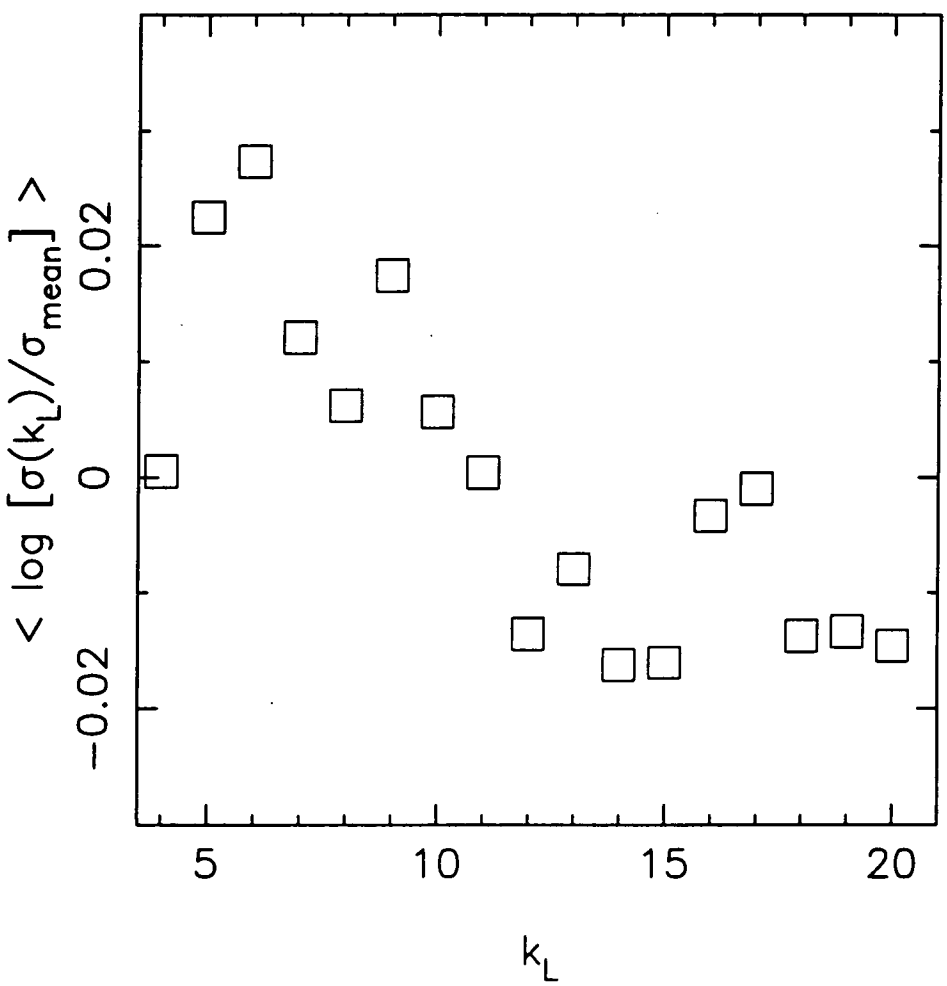

Figure 2.8. The dependence of the velocity dispersions derived in the Fourier quotient method on the low wavenumber cutoff adopted to filter the spectra. These velocity dispersions have been normalized to the mean values for all filters and averaged for a sub-sample of 10 Coma ellipticals. The spectral type of the template used here is K1.

the spectral type of the template is shown in Figure 2.7. The σ values derived using this Fourier technique were also found to be slightly dependent on the low wavenumber cutoff (k_L) adopted in the filtering procedure. This is in the sense that the velocity dispersions tend to decrease systematically with increasing k_L (see Figure 2.8). In practice, we chose $3 < k_L < 9$ and adopted the average value of the derived velocity dispersions from each individual value of k_L. These relatively low values of k_L were preferred since larger k_L filters tend to leave the spectra featureless.

In Table 2.5 we list our derived redshifts, velocity dispersions and error estimates. The σ listed is the median of that derived from the 18 templates and is equivalent to a value derived from a K0 giant. Errors in the measured velocity dispersions were derived by bootstrap re-sampling the spectra. Comparison of measurements and their errors for galaxies observed more than once confirmed this to be a reliable technique for error estimation (Figure 2.9). While the average uncertainty of our individual σ measurements is 0.033 dex, i.e. ~8%, because of repeat measurements our final σ's have an average error of 0.025 dex, i.e. ~6%.

Included in our sample are several ellipticals which have previously published velocity dispersion measurements. Comparison of our values with those listed in Davies *et al.* is shown in Figure 2.9. The Davies *et al.*'s study includes the measurements made at Lick which have an uncertainty of ~11% and those made by Alan Dressler at Las Campanas with the high dispersion configuration, i.e. those measurements denoted as LCO-HI, which have an uncertainty of ~6%. For 14 galaxies in common with Lick measurements the mean offset (INT–LICK) is 0.002 ± 0.014 dex with an rms scatter of 0.051 dex. Most of this scatter can be attributed to Lick measurement errors. For 12 galaxies in common with Dressler's work the mean offset (INT–DRESSLER) is 0.015 ± 0.015 dex with an rms scatter of 0.052 dex (this comparison includes one S0 galaxy reported in Dressler 1987). Most of this relatively large scatter is caused by the large difference in the derived values

Table 2.5 Spectroscopic Measurements

Name	D#	cz	σ	ϵ_σ	Mg_2	ϵ_{Mg2}
159-41		6623	196	10	0.316	0.012
159-43		6710	268	14	0.329	0.009
"		6694	252	16	0.332	0.010
159-46		7068	171	10	0.261	0.009
159-63		7566	154	12	0.258	0.012
NGC 4673		6868	237	17	0.266	0.010
"		6840	227	12	0.260	0.007
NGC 4692		7996	239	12	0.311	0.010
159-83		6887	210	17	0.267	0.010
159-89		7606	176	10	0.265	0.012
IC 832		7094	217	18	0.258	0.013
NGC 4789		8371	294	19	0.296	0.017
"		8367	267	10	0.296	0.007
NGC 4807		6973	212	13	0.277	0.010
IC 3900		7115	280	15	0.312	0.009
NGC 4816		6922	198	13	0.312	0.015
"		6941	228	15	0.304	0.009
160-22		6457	269	15	0.308	0.010
160-23		6903	184	10	0.302	0.011
160-27		6275	178	13	0.274	0.011
	140	6689	177	17	0.289	0.012
NGC 4824	35	7117	174	15	0.261	0.013
"		7125	159	12	0.279	0.013

Table 2.5 Cont.

Name	D#	cz	σ	ϵ_σ	Mg_2	ϵ_{Mg2}
NGC 4827		7599	279	15	0.325	0.009
160-37	24	7480	237	16	0.293	0.011
NGC 4839	31	7378	298	26	0.309	0.013
NGC 4840	46	6097	250	16	0.311	0.011
160-49A	210	7245	179	11	0.262	0.011
GMP 4229	238	7339	121	17	0.230	0.015
"		7338	106	11	0.226	0.016
NGC 4850	137	6039	182	15	0.269	0.012
"		6049	177	20	0.252	0.012
RB 241	161	7185	199	16	0.290	0.016
"		7191	178	13	0.296	0.012
IC 3947	72	5677	155	13	0.276	0.013
"		5677	140	14	0.262	0.014
RB 257	136	5702	122	11	0.266	0.015
"		5711	152	12	0.259	0.015
NGC 4860	194	7948	239	14	0.309	0.010
"		7990	289	18	0.366	0.014
"		7960	274	18	0.353	0.011
IC 3959	69	7077	193	19	0.285	0.014
"		7092	197	18	0.305	0.013
RB 18	156	6731	102	10	0.222	0.014
"		6717	115	11	0.224	0.015
NGC 4874	129	7200	279	20	0.311	0.013

Table 2.5 Cont.

Name	D#	cz	σ	ϵ_σ	Mg_2	ϵ_{Mg2}
NGC 4876	124	6739	191	11	0.234	0.011
"		6743	201	16	0.237	0.012
RB 43	125	6946	189	14	0.279	0.014
"		6951	176	19	0.252	0.014
NGC 4881	217	6716	205	12	0.303	0.011
"		6743	216	12	0.285	0.011
NGC 4886	151	6434	205	24	0.251	0.019
"		6421	133	12	0.229	0.018
NGC 4889	148	6567	393	35	0.323	0.013
"		6538	452	23	0.331	0.008
"		6505	429	25	0.334	0.009
"		6451	398	14	0.349	0.008
TT41	27	7815	107	10	0.233	0.016
"		7835	105	13	0.271	0.016
160-92	81	5979	172	25	0.251	0.018
"		5972	151	18	0.263	0.018
	204	7667	135	12	0.260	0.014
NGC 4923	78	5535	211	14	0.292	0.013
"		5516	207	12	0.299	0.011
IC 843		7377	229	24	0.287	0.016
"		7397	267	16	0.297	0.009
160-100	96	7587	195	14	0.281	0.012
"		7621	190	12	0.273	0.012

Table 2.5 Cont.

Name	D#	cz	σ	ϵ_σ	Mg_2	ϵ_{Mg2}
NGC 4926	49	7881	278	16	0.317	0.013
"		7867	259	13	0.314	0.009
NGC 4927	141	7747	292	15	0.346	0.010
IC 4133		6369	159	18	0.283	0.013
"		6386	198	29	0.279	0.016
NGC 4952		5957	239	20	0.282	0.015
"		5939	289	12	0.290	0.008
NGC 4957		6922	268	25	0.277	0.014
"		6921	229	12	0.290	0.017
NGC 4971		6307	184	17	0.278	0.014
"		6277	185	18	0.287	0.014
NGC 5004		7065	255	15	0.280	0.010
"		7056	234	15	0.284	0.009
160-159		6136	237	16	0.272	0.012

Notes: cz is the heliocentric velocity. σ is the velocity dispersion. ϵ_σ is the estimated error in the velocity dispersion. All values are listed in km s^{-1}. Mg_2 is the line strength index. ϵ_{Mg2} is the estimated error in this index. Both values are in mag.

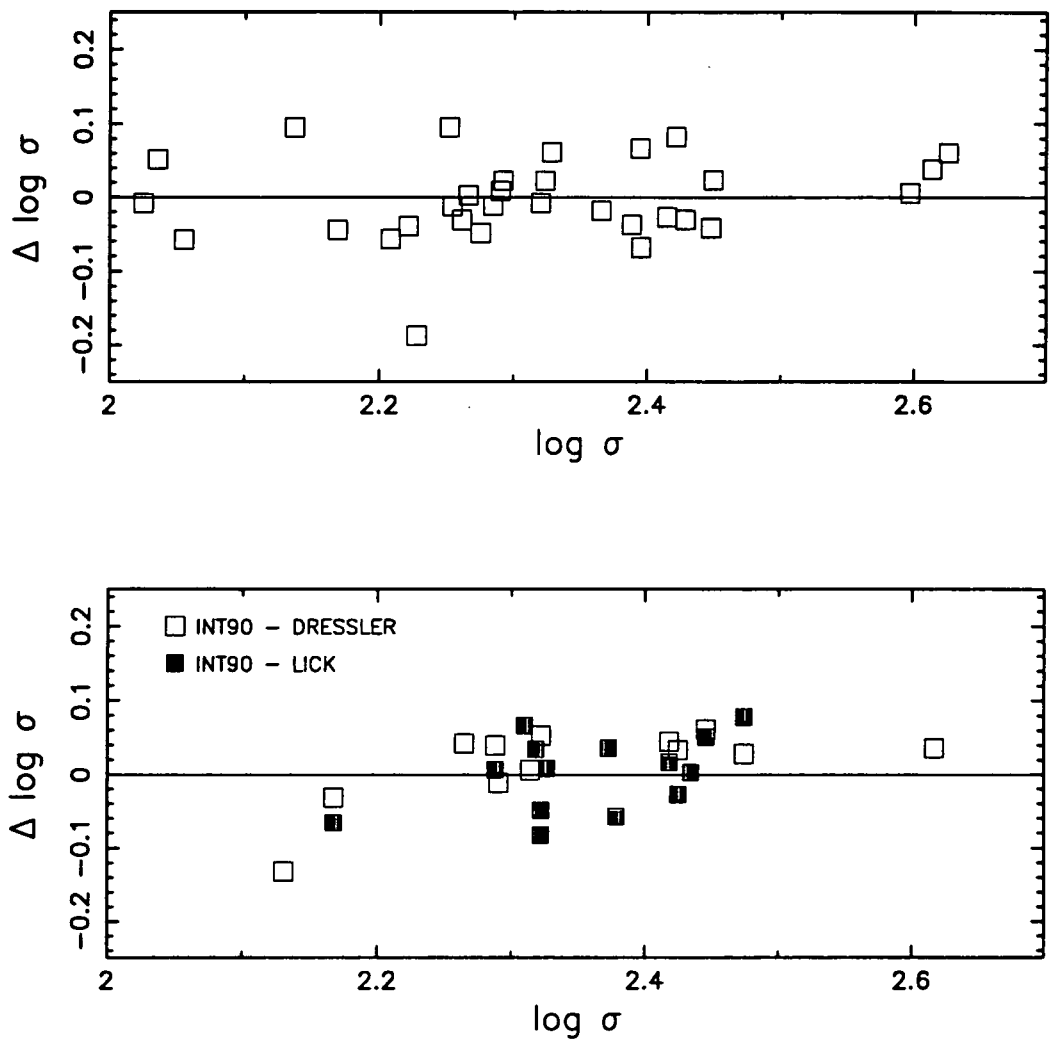

Figure 2.9. Top panel: Internal comparison of the derived velocity dispersions from repeat observations. Bottom panel: Comparison of our velocity dispersion measurements with values previously published in the literature.

for the elliptical D#136. Both our measurement and Dressler's for this galaxy are based on two observations. Whereas Dressler found an average value of 182 ± 9 km s^{-1} for this galaxy, we measured an average value of 136 ± 8 km s^{-1}. The removal of this galaxy from the comparison increases the mean offset to 0.028 ± 0.009 dex (i.e. our values are 6.7% greater than those of Dressler) and decreases the rms scatter to 0.028 dex. While again this scatter is adequately explained by the measurement errors the offset of 6.7% is surprisingly large. However the Lick data shows a similar (although not significant) offset from Dressler's Coma data. The 12 Coma galaxies that are in common between these two studies have a mean offset (LICK–DRESSLER) of 0.026 ± 0.015 dex. Davies *et al.* from a more extensive comparison of these two studies find an offset of 0.016 ± 0.008 dex. Moreover Dressler's velocity dispersions of Coma ellipticals were based on combining separate measurements from the Mg*b* and *G*-band spectral regions. He noted that his Mg*b*-region determinations of σ were systematically 10% higher than those from the *G*-band region (Dressler 1984). The listed measurements are the average of these two determinations. Alan Dressler kindly provided his individual velocity dispersion values derived from the Mgb region. For the 11 ellipticals in common (D#136 is excluded), the offset (INT-DRESSLER(Mg*b*)) is 0.016 ± 0.008 dex and the rms scatter is 0.025 dex. Hence about half of the observed difference can be attributed to this systematic effect. The remaining offset is at a level that is often found and can be ascribed to factors such as: a) the different aperture size used for the two studies. Dressler's measurements were made with a 4″×4″ aperture as compared to the 2″×5.8″ used in our study; and, b) software differences.

2.2.3.2 Measurements of the Mg_2 line strength index.

The Mg_2 index measures the depression, expressed in magnitudes, of the spectral intensity due to the combined effect of the broad MgH feature and the Mgb triplet (Burstein *et al.*

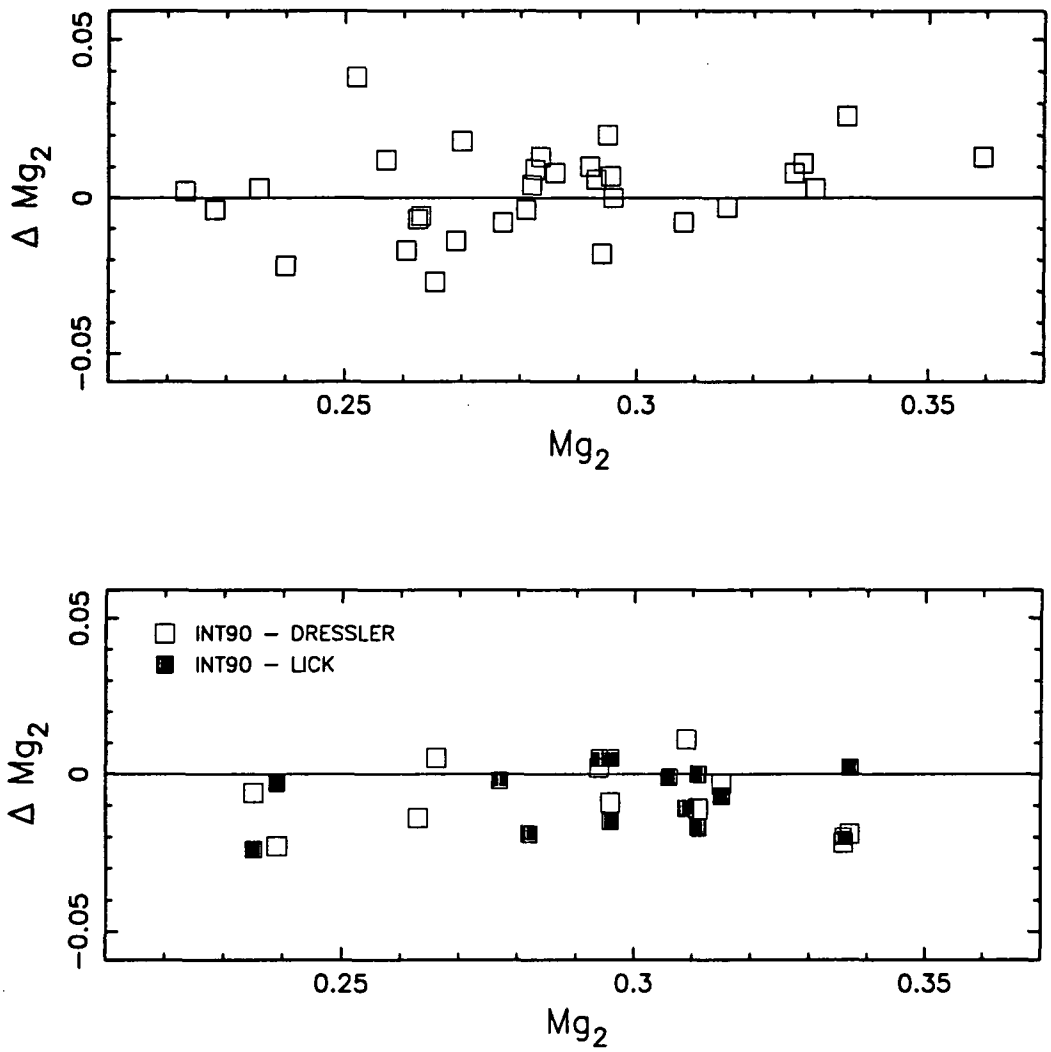

Figure 2.10. Top panel: Internal comparison of the derived Mg_2 indices from repeat observations. Bottom panel: Comparison of our Mg_2 measurements with values previously published in the literature.

1984). This index has been widely used as a metallicity indicator and varies from about 0.10 mag for metal-poor to 0.40 mag for super metal-rich giant stars. Before measuring Mg_2 we flux calibrated the galaxy spectra using an average spectral response function derived from the observations of three flux standard stars. Since the variation in Mg_2 due to velocity dispersion broadening amounts to only ± 0.003 mag, no further correction has been applied (Gorgas, Esftathiou & Aragón Salamanca 1990). Our Mg_2 measurements and the associated errors are given in Table 2.5. The quoted errors were estimated from the photon and readout noise. Comparison of repeat measurements confirmed the reliability of this technique for error estimation (Figure 2.10).

The average uncertainty of our individual Mg_2 measurements is 0.013 mag. Because of repeat measurements our final Mg_2 values have an average error of 0.010 mag. Mg_2 values for some galaxies in our sample have been previously measured at Lick (Davies *et al.* 1987) and by Dressler (1984). A comparison of our Mg_2 values with these studies is shown in Figure 2.10. For 14 galaxies in common between our study and the Lick work the mean offset (INT–LICK) is -0.009 ± 0.003 mag with an rms scatter of only 0.010 mag. For 11 galaxies in common between our study and Dressler's, we find a mean offset (INT–DRESSLER) of -0.010 ± 0.003 mag with an rms scatter of 0.010 mag. The observed offsets are at the level that are often found (see Davies *et al.* 1987) and can be attributed to different fluxing techniques. There are 13 Coma galaxies in common between the Lick work and Dressler's. The mean offset (LICK–DRESSLER) for these 13 galaxies is -0.002 ± 0.005 mag with an rms scatter of 0.018 mag. Thus, apart from relatively small offsets, the Mg_2 measurements of the three studies are in very good agreement.

2.2.4 The Coma data set.

In Table 2.6 we list the photometric and spectroscopic parameters for our Coma sample of

elliptical galaxies which are used in the subsequent analysis. This sample includes 26 ellipticals with spectroscopic data measured by Dressler (as listed in Davies *et al.* 1987). For those galaxies in common between the two studies we have adopted the weighted average velocity dispersions and Mg_2 indices after offsets of +0.028 dex and −0.010 mag, respectively, were applied to all Dressler's measurements (see Sections 2.2.3.1 and 2.2.3.2).

2.3 THE ABELL 2199 AND ABELL 2634 SAMPLES

2.3.1 Selection of objects.

The redshifts of Abell 2199 and Abell 2634 are ~25% greater than the Coma cluster. These two clusters were chosen to test whether their large, negative peculiar motions are induced by systematic differences in galaxy properties due to the cluster environment (Lucey *et al.* 1991). Our data set is based on new spectroscopic and photometric observations of early-type galaxies located in the dense, central areas of Abell 2199 and Abell 2634. The initial sample consisted of 80 early-type galaxies in both clusters selected from published lists (i.e. Rood & Sastry 1972; Strom & Strom 1978; Dressler 1980; Butcher & Oemler 1985; Dixon, Godwin & Peach 1989), and includes 36 galaxies in common with those studied by Lucey *et al.* (1991).

All galaxies were classified in different morphological types using our own CCD images. This classification is in good agreement with the morphological types listed in previous studies (Dressler 1980; Butcher & Oemler 1985), although there is some disagreement over some early-type galaxies. In our analysis, because of the higher reliability of the CCD images, we have adopted this classification in preference to the types previously

Table 2.6 Coma data set.

Name	D#	r (°)	log$D$ (arcsec)	logR_e (arcsec)	SB_e (mag arcs^{-2})	logσ (km s^{-1})	Mg_2 (mag)
RB45	153	0.04	0.859	0.538	19.72	2.158	0.275
NGC4886	151	0.05	1.030	0.872	20.29	2.197	0.246
RB43	125	0.06	0.866	0.227	18.49	2.257	0.259
NGC4889	148	0.06	1.481	1.453	20.72	2.613	0.342
NGC4874	129	0.06	1.294	1.669	21.93	2.429	0.312
NGC4876	124	0.06	1.026	0.752	19.92	2.282	0.233
IC4011	150	0.06	0.873	0.626	19.99	2.051	0.267
NGC4872	130	0.07	1.051	0.472	18.75	2.353	0.286
RB18	156	0.10	0.678	0.513	20.23	2.029	0.223
IC4021	172	0.11	0.945	0.485	19.20	2.227	0.286
NGC4869	105	0.12	1.136	0.919	20.12	2.315	0.316
IC4012	174	0.13	1.007	0.341	18.40	2.280	0.281
NGC4867	133	0.13	1.050	0.556	19.08	2.373	0.296
NGC4864	159	0.14	1.125	0.879	20.00	2.302	0.276
RB155	193	0.16	0.827	0.558	19.90	2.107	0.251
NGC4906	118	0.18	1.029	0.851	20.24	2.251	0.292
RB257	136	0.21	0.868	0.148	18.16	2.217	0.265
RB167	207	0.21	0.901	0.586	19.74	2.195	0.252
IC4051	143	0.23	1.088	1.273	21.38	2.392	0.314
NGC4860	194	0.24	1.204	0.885	19.73	2.410	0.342
IC4045	168	0.24	1.128	0.659	19.20	2.351	0.292
IC3959	69	0.24	1.068	0.760	19.77	2.309	0.296

Table 2.6 Cont.

Name	D#	r (°)	log$D$ (arcsec)	logR_e (arcsec)	SB_e (mag arcs^{-2})	logσ (km s^{-1})	Mg_2 (mag)
IC3957	70	0.26	0.942	0.623	19.73	2.203	0.272
NGC4881	217	0.28	1.131	0.993	20.44	2.310	0.288
IC3947	72	0.29	0.966	0.591	19.54	2.170	0.270
RB241	161	0.30	1.070	0.881	20.19	2.270	0.294
160-92	81	0.32	0.806	0.808	20.85	2.199	0.257
NGC4850	137	0.33	1.065	0.738	19.73	2.255	0.260
NGC4923	78	0.39	1.136	0.866	19.89	2.318	0.296
	204	0.40	0.860	0.765	20.54	2.130	0.260
160-100	96	0.44	0.956	0.652	19.78	2.283	0.277
NGC4927	141	0.46	1.134	1.048	20.55	2.465	0.346
TT41	27	0.47	0.792	0.677	20.43	2.025	0.252
160-49A	210	0.50	0.964	0.539	19.34	2.253	0.262
NGC4926	49	0.56	1.264	0.991	19.87	2.422	0.312
NGC4840	46	0.63	1.160	0.794	19.56	2.398	0.311
	238	0.69	0.869	0.429	19.28	2.041	0.228
NGC4839	31	0.72	1.279	1.397	21.18	2.474	0.299
NGC4841A	240	0.72	1.294	1.165	20.40	2.408	0.311
	140	0.74	0.934	0.786	20.34	2.248	0.289
160-27		0.77	0.970	0.766	20.13	2.250	0.274
160-37	24	0.78	1.070	0.598	19.15	2.375	0.293
160-23		0.81	1.011	0.604	19.42	2.265	0.302
NGC4816		0.84	1.168	1.235	20.97	2.322	0.306

Table 2.6 Cont.

Name	D#	r (°)	log$D$ (arcsec)	logR_e (arcsec)	SB_e (mag arcs^{-2})	logσ (km s^{-1})	Mg_2 (mag)
NGC4824	35	0.85	0.930	0.678	19.97	2.215	0.270
IC4133		0.88	1.020	0.703	19.73	2.228	0.281
NGC4827		1.05	1.236	1.011	20.04	2.446	0.325
NGC4807		1.07	1.209	0.837	19.52	2.326	0.277
IC3900		1.17	1.152	0.710	19.26	2.447	0.312
IC843		1.22	1.170	0.980	20.20	2.407	0.295
NGC4957		1.25	1.212	1.152	20.62	2.373	0.282
NGC4789		1.52	1.365	1.191	20.22	2.435	0.296
NGC4952		1.61	1.307	1.017	19.82	2.439	0.288
NGC4971		1.66	1.071	0.867	20.12	2.265	0.283
160-22		1.79	1.128	0.786	19.62	2.430	0.308
159-89		1.99	1.075	0.977	20.51	2.246	0.265
IC832		2.01	1.080	0.983	20.49	2.336	0.258
159-83		2.50	1.152	0.995	20.32	2.322	0.267
NGC4692		2.75	1.293	1.214	20.56	2.378	0.311
160-159		2.79	1.072	0.851	20.08	2.375	0.272
NGC5004		2.96	1.275	1.019	19.95	2.387	0.282
NGC4673		3.30	1.356	0.827	18.93	2.362	0.262
159-63		3.72	0.951	0.904	20.67	2.188	0.258
159-43		4.55	1.118	0.712	19.40	2.417	0.330
159-46		4.60	1.085	0.839	19.96	2.233	0.261
159-41		4.75	1.024	0.635	19.45	2.292	0.316

published. In total we observed 26 ellipticals, 14 S0 galaxies and 1 early spiral in Abell 2199. The Abell 2634 sample in turn included 20 ellipticals, 18 S0 and 1 Sa galaxies. In this thesis we discuss only the results derived for elliptical galaxies. The S0 galaxy sample will be used as part of an on-going project to study the global properties of S0 galaxies whose results will be reported elsewhere.

Six of our sample of 46 ellipticals were later excluded from our analysis: three (BO#13 in Abell 2199, NGC 7745 and BO#3 in Abell 2634) were found to be background objects, and three (BO#34, BO#70 and RB28 in Abell 2199) have velocity dispersions less than 100 km s^{-1}. The final cluster sample listed in Table 2.7 includes 22 ellipticals in Abell 2199 and 18 ellipticals in Abell 2634. All galaxies, except N1 and NGC 7735, are located within 45′ from the centre of each cluster.

2.3.2 Photometry.

V-band images were obtained with the GEC CCD on the 1.2m Jacobus Kapteyn Telescope (JKT) at La Palma in June 1991. Each frame covered an area of 2.9′×1.9′ at a scale of 0.30″ pixel^{-1}. The exposure time was, typically, 300 seconds. The average seeing was ∼1.2″. A summary of these observations is given in Table 2.8. The reduction and calibration of these CCD images, as well as the derivation of the photometric parameters R_e, SB_e and D, followed the same standard procedure described in Section 2.2.2. A few galaxies, notably NGC 6166 in Abell 2199 and NGC 7720 in Abell 2634, have close companions. Aperture photometry for these galaxies was derived by measuring photometry from the relatively unaffected half of the galaxy and doubling the observed half. The aperture photometry for most galaxies in our sample is listed in Table 2.9. For a few galaxies in Abell 2634 we used the aperture photometry obtained by Lucey *et al.* (1991) to derive their photometric parameters. From repeat observations of the same galaxies in different

Table 2.8 The sample of Abell 2199 and Abell 2634 cluster ellipticals.

Abell 2199

F#	BO#	Other Id.	α (1950)	δ	type
F164	BO1	N6166	16 26 55.7	39 39 39	cD
	BO2	N6158	16 25 57.6	39 29 21	E
	BO5	Z34A	16 26 12.0	39 21 53	E
F121	BO15	S26	16 26 40.3	39 40 46	E
	BO20	S18	16 26 12.4	39 23 19	E
F105	BO38	S43	16 27 17.1	39 47 33	E
F103	BO45	S44	16 27 14.6	39 49 01	E
F148	BO61	S33	16 27 01.4	39 37 27	E
F113	BO73		16 27 03.1	39 43 07	E
F144	BO74	S30	16 26 53.1	39 38 34	E
F141	BO84	FCOM	16 26 51.0	39 39 29	E
F146	BO95	S34	16 27 02.7	39 38 12	E
F163		NCOM	16 26 52.9	39 39 45	E
	BO8	RB38	16 25 20.4	39 37 59	E
	BO26	RB130	16 28 02.7	39 55 19	E
	BO35	RB43	16 25 34.0	39 14 56	E
	BO48	RB40	16 25 27.4	39 24 39	E
	BO54	RB78	16 26 37.5	40 04 03	E
		N1	16 22 33.6	39 19 30	E/S0
		RB8	16 23 58.7	39 42 45	E/S0
		RB72	16 26 35.7	38 55 15	E
		RB162	16 29 35.8	39 15 24	E

Table 2.8 Cont.

Abell 2634

F#	BO#	Other Id.	α (1950)	δ	type
F1221	BO1	N7720	23 35 58.9	26 45 15	cD
F110	BO4	D68	23 36 32.1	26 49 32	E
F139	BO11	D57	23 35 58.8	26 42 06	E
F102	BO15	D107	23 35 52.4	26 52 52	E
F134	BO18	D55	23 36 08.4	26 44 03	E
F1482	BO20	D38	23 35 47.4	26 36 41	E
F121	BO82	D80	23 35 48.2	26 45 30	E
F105			23 36 15.9	26 53 43	E
F1222		D76	23 35 59.1	26 45 29	E
F124		D75	23 36 02.9	26 45 29	E
	BO2	N7728	23 37 30.2	26 51 24	E
	BO3c	BU32	23 38 19.8	26 33 11	E/S0
	BO5	D119	23 36 20.1	26 59 27	E
	BO9	D127	23 37 18.7	27 05 57	E/S0
	BO13		23 35 58.3	26 32 29	E
	BO16		23 36 42.8	27 16 18	E
	BO32	D93	23 37 32.5	26 53 24	E
		N7735	23 41 00.0	26 05 38	E

Notes: F# is the galaxy number listed in Lucey et al. (1991); BO# is the galaxy number given by Butcher & Oemler (1985); RB# and D# are the galaxy numbers given by Rood & Sastry (1972) and Dressler (1980), respectively; the listed morphological types are taken from our own classification.

Table 2.8 Log of photometric observations for Abell 2199 and Abell 2634 galaxies.

Date	June 5-12, 1991
Site	La Palma
Telescope	JKT
CCD	GEC
Readout Noise	$8e^-$
Pixel scale	0.30″
Photometric Band	V
Exposure time	300 seconds

Table 2.9 V-band aperture photometry.

Abell 2199

Name	PSF	4″	6″	8″	10″	13″	16″	20″	25″	32″	40″	50″	63″
F103	1.2	16.33	16.05	15.86	15.74	15.62	15.54	15.47	15.42	15.39	15.37	15.37	15.35
F105	1.4	16.60	16.18	15.95	15.81	15.66	15.57	15.50	15.44	15.39	15.35	15.34	
F113	1.4	16.82	16.50	16.34	16.24	16.14	16.08	16.03	15.98	15.94	15.90	15.86	15.78
F121	1.4	16.46	15.97	15.69	15.50	15.30	15.16	15.02	14.89	14.77	14.68	14.61	14.56
F141	1.7	17.07	16.69	16.48	16.36	16.25	16.19	16.15	16.14				
F141	0.8	16.93	16.62	16.44	16.33	16.23	16.17	16.13	16.12				
F144	1.3	16.05	15.77	15.61									
F144	0.8	15.98	15.74	15.61	15.52	15.45	15.41	15.37					
F146	1.3	16.72	16.40	16.22	16.11	16.00	15.94	15.89	15.87	15.85	15.85	15.82	
F146	1.2	16.82	16.45	16.24	16.11	16.00	15.94	15.89	15.86	15.85			
F146	0.9	16.67	16.38	16.21	16.10	16.00	15.94						
F148	1.7	16.27	15.94	15.76	15.64	15.52	15.45	15.40	15.37	15.35	15.34	15.34	
F148	1.2	16.31	15.96	15.77	15.64	15.52	15.45	15.40	15.37	15.35	15.33	15.33	15.32
F148	0.9	16.17	15.91	15.74	15.62	15.51	15.45	15.40	15.37	15.36	15.35	15.35	15.35
F163	1.7	17.45	17.17	17.06	17.01	16.98	16.96						
F163	0.8	17.30	17.11	17.04	17.01								
F164	1.7	16.50	15.78	15.26	14.93	14.55	14.28	14.01	13.76	13.51	13.30	13.11	12.94
F164	0.8	16.44	15.71	15.24	14.90	14.54	14.27	14.00	13.75	13.50	13.30	13.11	12.93
BO2	1.1	15.72	15.30	15.04	14.86	14.66	14.52	14.37	14.24	14.11	14.00	13.89	13.80
BO2	1.2	15.75	15.32	15.04	14.86	14.66	14.51	14.37	14.23	14.10	13.98	13.88	13.78
BO5	1.6	16.04	15.59	15.32	15.14	14.94	14.80	14.66	14.52	14.38			
BO8	1.3	16.18	15.72	15.44	15.24	15.02	14.87	14.72	14.59	14.47	14.38	14.29	14.23

Table 2.9 Cont.

Name	PSF	4″	6″	8″	10″	13″	16″	20″	25″	32″	40″	50″	63″
BO20	1.1	16.09	15.74	15.54	15.40	15.26	15.16	15.07	14.99	14.93	14.87	14.83	14.80
BO20	1.1	16.08	15.75	15.54	15.39	15.25	15.15	15.06	14.98	14.91	14.86	14.80	14.75
BO26	1.5	16.14	15.80	15.60	15.46	15.33	15.25	15.17	15.10	15.05	15.01	14.98	14.95
BO35	1.6	16.31	15.96	15.79	15.69	15.59	15.53	15.46	15.41	15.34	15.28	15.24	15.21
BO48	2.3	16.64	16.24	16.01	15.87	15.75	15.66	15.58	15.51	15.45	15.39		
BO54	1.4	16.59	16.26	16.05	15.89	15.74	15.65	15.59	15.55	15.54	15.54	15.56	
RB8	1.5	15.75	15.32	15.08	14.91	14.74	14.61	14.50	14.38	14.27	14.17	14.09	14.01
RB72	1.6	15.91	15.48	15.21	15.04	14.87	14.75	14.64	14.52	14.41	14.33	14.25	14.19
RB162	1.5	16.04	15.62	15.38	15.21	15.04	14.91	14.80	14.70	14.61	14.54	14.48	14.44
N1	1.5	16.09	15.67	15.39	15.22	15.03	14.91	14.78	14.66	14.53	14.42	14.32	14.24

Table 2.9 Cont.

Abell 2634

Name	PSF	4″	6″	8″	10″	13″	16″	20″	25″	32″	40″	50″	63″
F110	1.8	16.80	16.37	16.11	15.96	15.79	15.69	15.60	15.53	15.46	15.42		
F121	2.1	16.93	16.54	16.32	16.19	16.06	15.98	15.90	15.86				
F121	1.0	16.67	16.40	16.25	16.15	16.04	15.97	15.90	15.84	15.79	15.76	15.72	15.69
F1221	1.0	15.62	15.12	14.78	14.57	14.33	14.16	13.98	13.81	13.63	13.47	13.30	13.14
F1222	1.0	16.22	15.86	15.66	15.54	15.42	15.35	15.30	15.27	15.25	15.26	15.29	
F124	1.0	16.72	16.39	16.18	16.06	15.95	15.89	15.84	15.80				
D93	2.0	16.79	16.36	16.13	15.98	15.83	15.72	15.63	15.55	15.46	15.40	15.33	15.27
D93	1.0	16.62	16.30	16.10	15.97	15.83	15.72	15.63	15.55	15.47	15.42	15.37	15.33
D93	1.9	16.78	16.38	16.14	15.98	15.83	15.72	15.62	15.53	15.45	15.38	15.31	15.26
D95	1.7	15.70	15.11	14.76	14.52	14.26	14.07	13.89	13.73	13.57	13.44	13.34	13.25
D119	1.7	15.80	15.33	15.05	14.85	14.65	14.51	14.37	14.26	14.14	14.05	13.97	13.89
D119	1.0	15.67	15.27	15.02	14.84	14.65	14.51	14.38	14.27	14.16	14.08	14.02	13.96
D127	1.6	16.27	15.83	15.56	15.38	15.18	15.05	14.93	14.80	14.67	14.55	14.45	14.36
BO3	1.6	16.32	15.77	15.42	15.18	14.92	14.73	14.54	14.37	14.20	14.09		
BO3	1.5	16.22	15.71	15.39	15.16	14.91	14.72	14.54	14.37	14.20	14.09	13.99	
BO3c	1.6	16.68	16.23	15.99	15.81	15.62	15.50	15.39	15.28	15.17	15.10	15.03	
BO3c	1.5	16.53	16.17	15.96	15.79	15.62	15.51	15.40	15.32	15.21			
BO13	1.2	15.95	15.58	15.36	15.21	15.06	14.96	14.86	14.77	14.67	14.59	14.53	14.47
BO16	2.2	16.42	15.97	15.69	15.49	15.27	15.13	15.01	14.92	14.87	14.84	14.83	
BO16	1.7	16.29	15.89	15.64	15.45	15.25	15.11	14.99	14.90	14.83	14.78	14.75	
NGC7735	1.2	15.79	15.30	15.00	14.79	14.55	14.38	14.20	14.03	13.86			

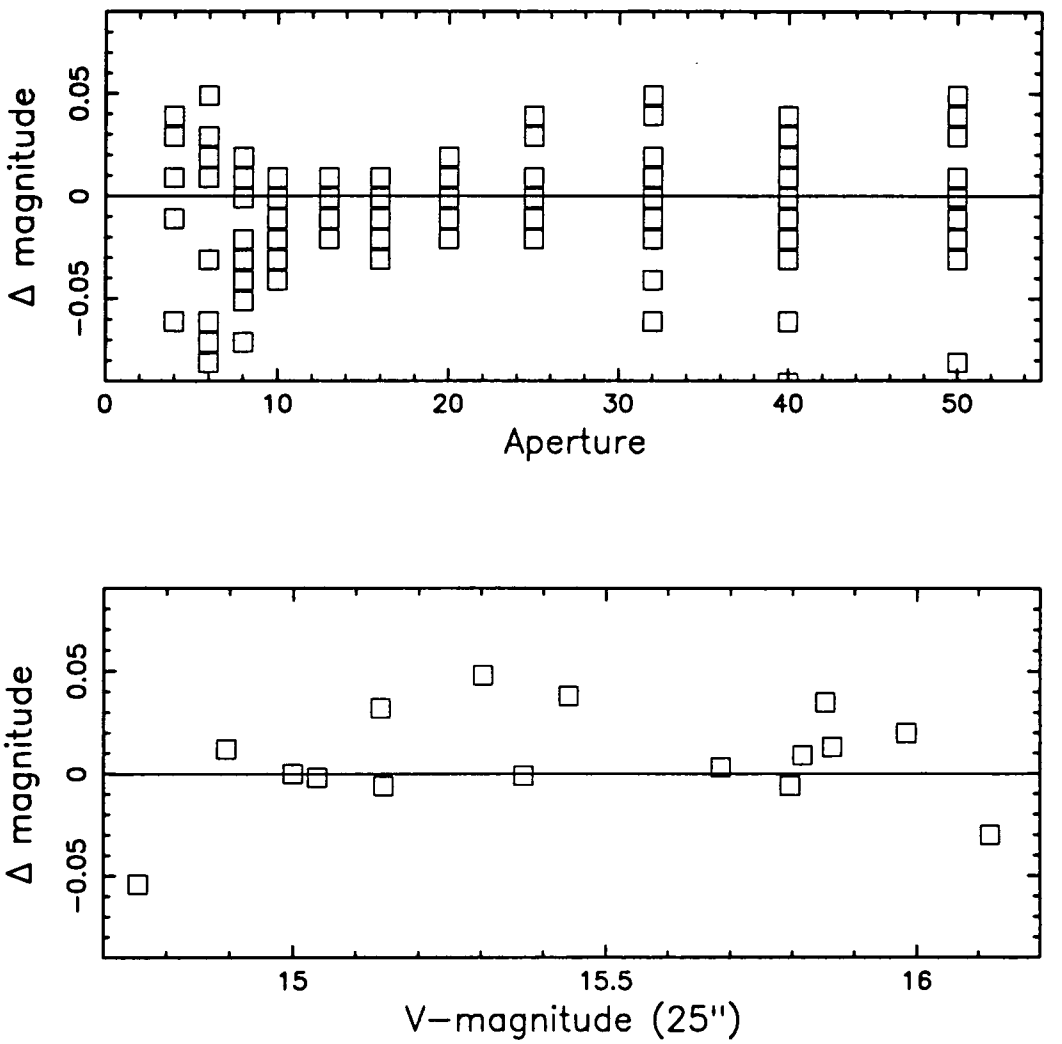

Figure 2.11. Top panel: Internal comparison of our aperture photometry for 20 cluster ellipticals with repeat observations. Bottom panel: Comparison of our photometry with that of Lucey *et al.* (1991) for 17 galaxies in common between the two studies. Measurements within 25″ aperture are compared.

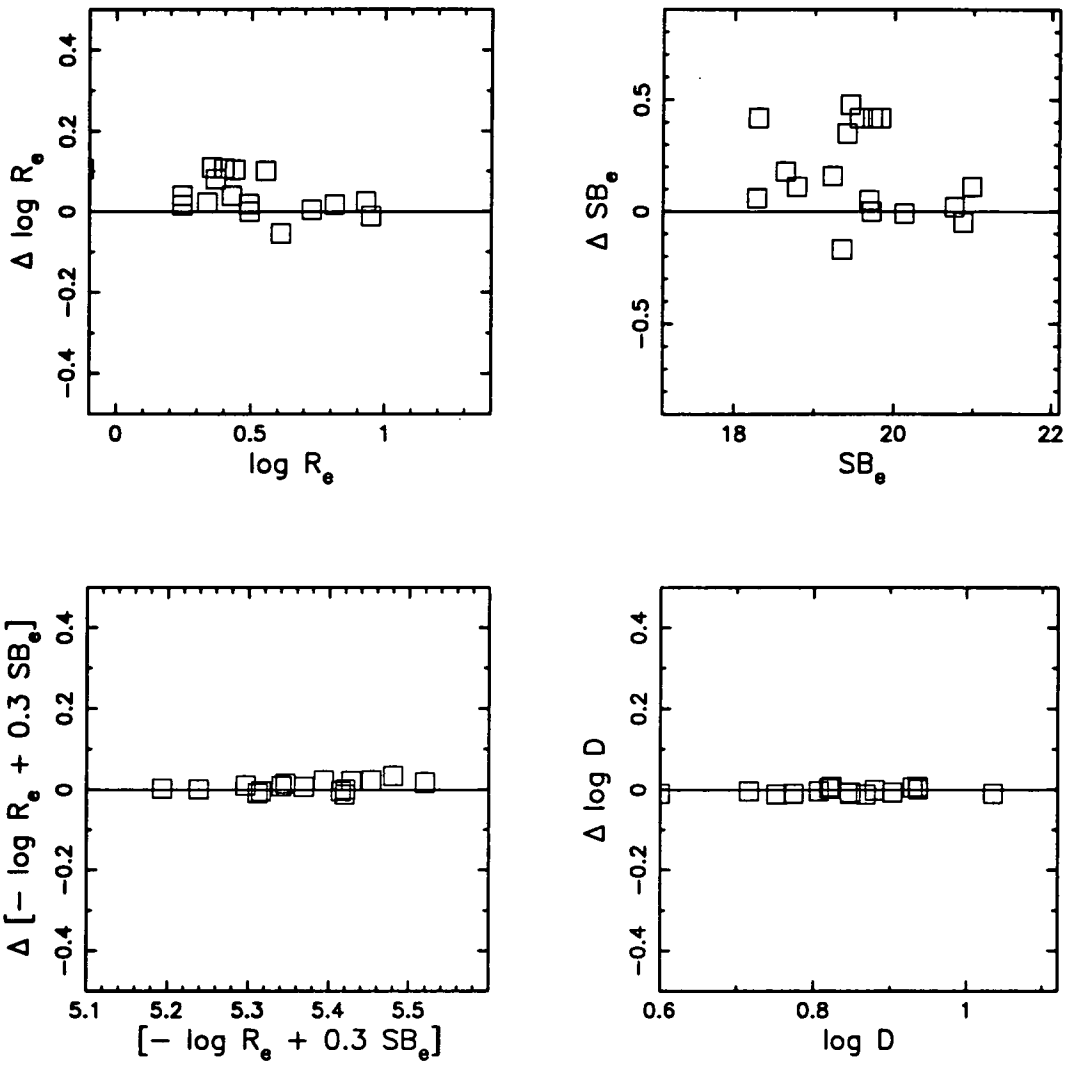

Figure 2.12. Comparison between the different photometric parameters obtained using Lucey *et al.* (1991) aperture photometry and those derived in this study.

nights and comparison with previous unpublished values (Lucey, private communication) we estimate that the zero-point uncertainty is ±0.02 mag (Figure 2.11). Comparison with values derived from independent Lucey *et al.* (1991) data indicates that the measured R_e, SB_e and D parameters have uncertainties of 0.035 dex, 0.14 mag and 0.005 dex, respectively (Figure 2.12). Note, however, that the error in $\{\log R_e - 0.3\ SB_e\}$ is only 0.009 dex (see discussion in Section 2.2.2).

2.3.3 Spectroscopy.

Spectroscopic observations for 20 early-type galaxies in Abell 2199 and Abell 2634 were initially made in May 1990 during the same run in which the Coma galaxy spectra reported in Section 2.2.3 were obtained. The aim of these early observations was to provide a good overlap with subsequent observations in order to reliably assess systematics. The bulk of spectroscopic observations were made in July 1992 using the Intermediate Dispersion Spectrograph on the INT in good seeing, i.e. $\sim 1''$. We used the 900 grooves mm^{-1} grating blazed at 5300Å on the 235 camera to produce a dispersion of 1.04Å $pixel^{-1}$ on a EEV CCD. The spectra were centered on the Magnesium triplet and covered the range 4560Å to 5790Å. We used a $3''$ slit which gave a FWHM resolution of 200 km s^{-1}. Data were recorded over a slit length of $3'$. Along the slit the scale is $0.65''$ $pixel^{-1}$. Typical exposure times ranged from 1000 to 1800 seconds. These exposures were expected to provide a similar signal-to-noise ratio to our Coma galaxy spectra. However, two factors contributed to reduce the quality of the new spectra. Firstly, the extinction due to dust in the atmosphere was exceptionally high during this run (i.e. k_V = 0.2–0.6 mag). Secondly, problems with the cryostat that kept the CCD at low temperatures caused a slight overheating of the detector during some observations. This in turn translated into a larger contribution of

the background noise in some of the recorded spectra. To achieve the required signal-to-noise ratio (i.e. S/N $\geq$ 10 per Å) we coadded all repeat observations for these spectra. A summary of these observations is presented in Table 2.10.

The observing strategy, data reduction procedure and measurement of spectroscopic parameters follow exactly the same technique described in Section 2.2.3. There are only three minor differences that we comment here in more detail:

(i) The 15 stars observed to be used as templates were giants of spectral types G9 to K2. This restricted range in spectral stellar types was suggested by our previous results for the Coma sample, in the sense that later type stars yield systematically larger values of σ (Figure 2.7). As expected, the variation between individual σ measurements for each of these templates is less than $\sim$3%.

(ii) In the final step of the data reduction procedure, the five pixel region centred on the galaxy along the slit was extracted and coadded to form the galaxy spectrum. These spectra cover thus the central 3.3″ $\times$ 3″ region of the galaxy (compared to the central 5.8″ $\times$ 2″ area mapped in our previous observations). Although the existence of σ-gradients may affect the values of central velocity dispersions measured over different areas of the galaxy, we estimate that, in our case, this effect is negligible (i.e. $\sim$ 0.005 dex).

(iii) These spectra were found to yield σ measurements that showed, on average, larger variations with the lower cutoff wavenumber (k_L) than the effect previously observed for Coma galaxies (Figure 2.8). We noted, however, that this dependence on k_L could be significantly reduced by measuring σ over a smaller wavelength range of the spectrum (i.e. 4800Å to 5700Å, which includes all the main spectral features of interest).

Table 2.10 Log of spectroscopic observations for Abell 2199 and Abell 2634 galaxies.

Date	July 25-31, 1992
Site	La Palma
Telescope	INT
Spectrograph	IDS-235
CCD	EEV
Readout Noise	6 e^-
Dispersion	1.04 Å $pixel^{-1}$
Resolution (FWHM)	200 km s^{-1}
Wavelength range	4560Å –5790Å
Exposure time	1000–1800 seconds

Table 2.11 Spectroscopic Measurements

Abell 2199

Name	cz	σ^{INT92}	ϵ_σ	Mg_2^{INT92}	ϵ_{Mg2}	σ^{INT90}	ϵ_σ	Mg_2^{INT90}	ϵ_{Mg2}
F103	9379	197	20	0.276	0.023	164	19	0.301	0.016
"	9378	180	10	0.272	0.010				
F105	8416	144	10	0.278	0.016				
"	8398	161	11	0.265	0.011				
F113	8027	175	11	0.256	0.011				
F121	8750	157	14	0.257	0.015	192	17	0.303	0.018
F141	9708	157	8	0.236	0.013				
F144	8538	216	14	0.243	0.011	261	24	0.267	0.013
"	8524	221	14	0.250	0.010				
F146	8292	152	10	0.241	0.013	159	8	0.308	0.011
F148	8248	277	17	0.285	0.014				
"	8269	238	17	0.281	0.014				
F163	8915	120	12	0.238	0.016				
F164	9322	288	18	0.258	0.010	335	31	0.293	0.014
BO2	8945	239	13	0.250	0.012	213	13	0.278	0.011
BO5	8754	222	21	0.238	0.009	226	16	0.291	0.012
BO20	9646	189	9	0.282	0.012				
BO26	9134	205	14	0.252	0.013				
"	9094	192	13	0.243	0.013				

Table 2.11 Cont.

Abell 2199

Name	cz	σ^{INT92}	ϵ_σ	Mg_2^{INT92}	ϵ_{Mg2}	σ^{INT90}	ϵ_σ	Mg_2^{INT90}	ϵ_{Mg2}
BO35	8713	182	19	0.289	0.014				
BO48	7832	159	11	0.221	0.018				
BO54	9505	147	10	0.253	0.013				
RB8	9021	241	20	0.269	0.010				
RB72	9326	190	11	0.276	0.011				
RB162	8867	230	12	0.260	0.013				
N1	9033	188	10	0.285	0.012				

Abell 2634

Name	cz	σ^{INT92}	ϵ_σ	Mg_2^{INT92}	ϵ_{Mg2}	σ^{INT90}	ϵ_σ	Mg_2^{INT90}	ϵ_{Mg2}
F102	9122	156	14	0.230	0.015	192	17	0.281	0.013
F110	9976	204	14	0.265	0.012				
F121	9551	178	9	0.250	0.009	193	14	0.300	0.011
F1221	9102	348	11	0.314	0.007				
F1222	8131	162	9	0.265	0.009				
F124	10003	187	13	0.255	0.014	191	17	0.309	0.013
F134	9280	221	10	0.277	0.009	232	14	0.309	0.009
F139	9531	215	14	0.315	0.010	237	16	0.303	0.010
"	9509	203	16	0.279	0.014				
F1482	9306	238	14	0.246	0.010	214	31	0.299	0.024

Table 2.11 Cont.

Abell 2634

Name	cz	σ^{INT92}	ϵ_σ	Mg_2^{INT92}	ϵ_{Mg2}	σ^{INT90}	ϵ_σ	Mg_2^{INT90}	ϵ_{Mg2}
BO32	9003	167	10	0.236	0.012				
BO2	9448	303	23	0.304	0.013				
"	9413	316	20	0.303	0.013				
"	9388	325	25	0.302	0.014				
BO5	9312	270	15	0.279	0.009				
"	9291	275	13	0.292	0.009				
BO9	10119	236	15	0.242	0.011				
"	9922	178	19	0.279	0.014				
F105	9795	149	9	0.247	0.011				
BO3c	8753	162	12	0.238	0.016				
BO13	9501	155	10	0.219	0.012				
BO16	9272	190	12	0.286	0.014				
"	9406	246	14	0.302	0.012				
NGC 7735	9578	285	18	0.266	0.010				

Notes: cz is the heliocentric velocity. σ is the velocity dispersion. ϵ_σ is the estimated error in the velocity dispersion. All values are listed in km s^{-1}. Mg_2 is the line strength index. ϵ_{Mg2} is the estimated error in this index. Both values are in mag. Measurements obtained in both observing runs (INT90 and INT92) are listed.

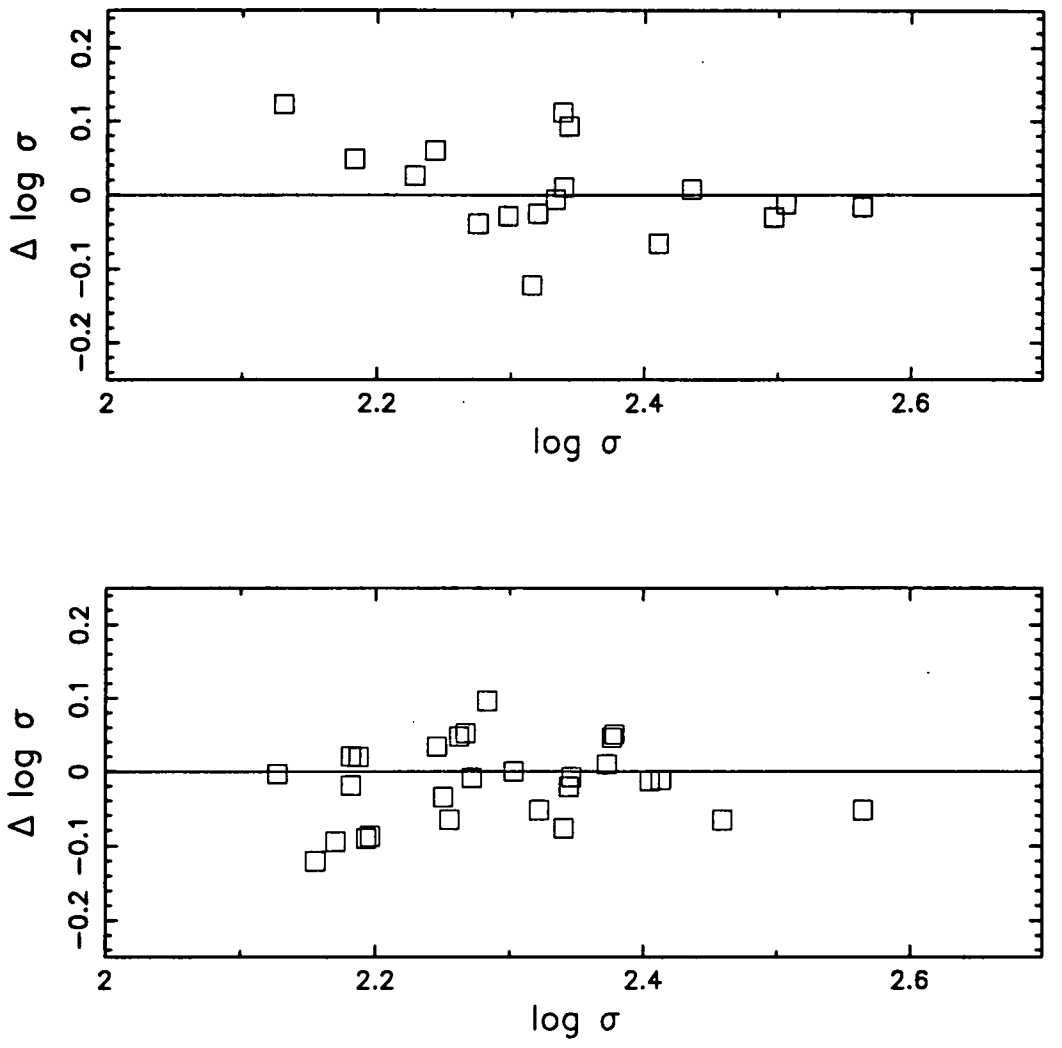

Figure 2.13. Top panel: Internal comparison of the derived velocity dispersions from repeat observations. Bottom panel: Comparison between the INT92 and INT90 velocity dispersion measurements.

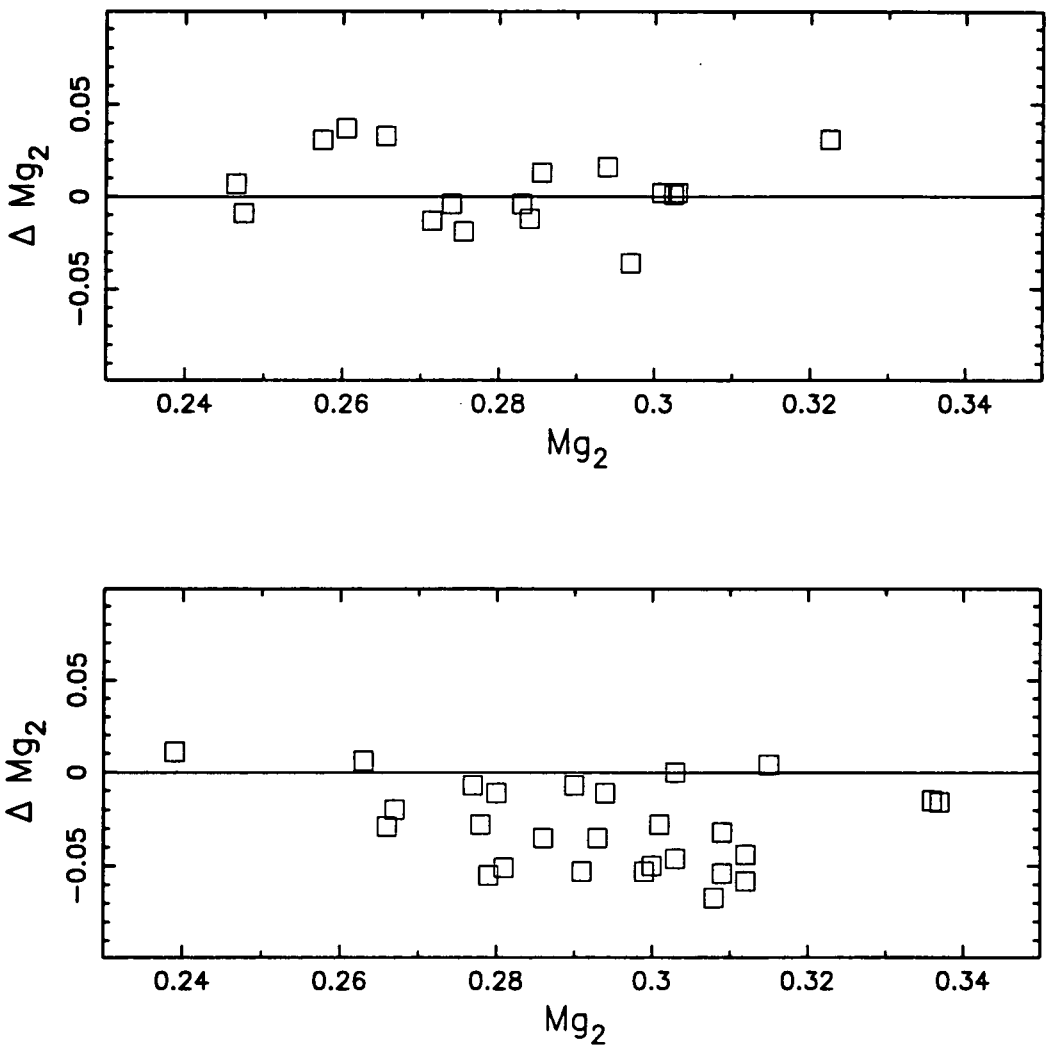

Figure 2.14. Top panel: Internal comparison of the derived Mg_2 indices from repeat observations. Bottom panel: Comparison between the INT92 and INT90 Mg_2 indices.

The raw measurements of velocity dispersion and Mg_2 index, as well as our error estimates, are listed for each galaxy in Table 2.11. The average uncertainties in our σ and Mg_2 values are 0.037 dex (i.e. $\sim$9%) and 0.015 mag, respectively. These estimates are in good agreement with the internal comparison of measurements for galaxies observed more than once (Figures 2.13 and 2.14).

In Figures 2.13 and 2.14 we also show the comparison between these σ and Mg_2 values with those measured in May, 1990. Including 7 Coma ellipticals, there are 27 galaxies in common to both observing runs (referred to below as INT90 and INT92, respectively). The mean offsets between both data sets are:

$$\log\sigma^{INT92} - \log\sigma^{INT90} = -0.016 \pm 0.010 \text{ dex} \qquad (\text{rms} = 0.054 \text{ dex})$$

$$Mg_2^{INT92} - Mg_2^{INT90} = -0.029 \pm 0.004 \text{ mag} \qquad (\text{rms} = 0.022 \text{ mag})$$

The offsets and the rms scatter reflect the average quality of these spectra, as compared to the high quality data for Coma galaxies. In both cases, however, these values are at a level that is often found in the literature (see Davies *et al.* 1987). Hence, despite the slightly larger uncertainty intrinsic to these measurements, there is good agreement between the INT90 and INT92 data sets.

2.3.4 The Abell 2199 and Abell 2634 data sets.

The photometric and spectroscopic parameters for our sample of cluster ellipticals in Abell 2199 and Abell 2634 are listed in Table 2.12. For those galaxies in common between the INT90 and INT92 observing runs we have adopted the weighted average velocity dispersions and Mg_2 indices after offsets of +0.016 dex and +0.029 mag, respectively, were applied to all INT92 measurements. This data set is in the same system than the Coma data set presented in Section 2.2.4.

Table 2.12 Abell 2199 and Abell 2634 data sets.

Abell 2199

Name	r (′)	log$D$ (arcsec)	logR_e (arcsec)	SB_e (mag arcs^{-2})	logσ (km s^{-1})	Mg_2 (mag)
F164	0.00	1.191	1.974	22.93	2.500	0.290
F163	0.53	0.600	-0.079	18.30	2.095	0.267
F141	0.91	0.716	0.399	19.73	2.212	0.265
F144	1.19	0.937	0.245	18.28	2.387	0.272
F146	1.99	0.774	0.370	19.41	2.200	0.289
F148	2.46	0.903	0.337	18.78	2.428	0.290
F121	3.15	0.929	0.948	20.88	2.248	0.295
F113	3.74	0.752	0.355	19.45	2.259	0.285
F105	8.91	0.848	0.555	19.83	2.198	0.298
F103	10.05	0.880	0.428	19.23	2.247	0.302
BO2	15.21	1.123	0.990	20.37	2.361	0.279
BO20	18.34	0.969	0.624	19.64	2.292	0.311
BO8	18.41	1.013	1.004	20.79	2.162	0.268
BO5	19.66	1.042	0.915	20.39	2.358	0.279
BO26	20.28	0.953	0.513	19.28	2.313	0.277
BO48	22.68	0.850	0.473	19.52	2.217	0.250
BO54	24.65	0.830	0.505	19.70	2.183	0.282
BO35	29.31	0.900	0.389	19.01	2.276	0.318
RB8	34.18	1.106	0.819	19.83	2.398	0.298
RB162	39.29	1.019	0.776	20.00	2.378	0.289
RB72	44.57	1.070	0.819	19.98	2.295	0.305
N1	54.42	1.020	0.899	20.43	2.290	0.314

Table 2.12 Cont.

Abell 2634

Name	r	$\log D$	$\log R_e$	SB_e	$\log\sigma$	Mg_2
	(′)	(arcsec)	(arcsec)	(mag arcs^{-2})	(km s^{-1})	(mag)
F1221	0.00	1.266	1.270	20.81	2.558	0.343
F1222	0.23	0.955	0.401	18.87	2.226	0.294
F124	0.92	0.823	0.495	19.72	2.284	0.297
F121	2.39	0.807	0.440	19.56	2.276	0.290
F134	2.44	1.020	0.765	19.95	2.363	0.308
F139	3.14	1.024	0.895	20.39	2.356	0.318
F102	7.76	0.996	0.764	20.04	2.246	0.270
F110	8.57	0.850	0.639	20.12	2.326	0.294
F1482	8.99	0.969	0.755	20.10	2.361	0.287
F105	9.27	0.783	0.545	20.02	2.189	0.276
BO13	12.78	1.051	0.705	19.63	2.206	0.248
BO5	14.96	1.163	0.911	19.98	2.452	0.315
BO2	21.28	1.298	1.250	20.68	2.513	0.332
BO32	22.41	0.842	0.643	20.16	2.239	0.265
BO9	27.28	1.013	0.907	20.46	2.344	0.285
BO16	32.54	0.985	0.773	20.10	2.346	0.315
BO3c	33.72	0.882	0.806	20.58	2.226	0.267
NGC7735	78.19	1.201	1.168	20.70	2.471	0.295

2.4 THE FIELD SAMPLE

The field galaxy sample includes all 78 elliptical galaxies with no group assignment and good quality photometric data (i.e. class 1 or 2) listed in Faber *et al.* (1989). This study provides a homogeneous data set to readdress previous claims that a systematic difference in the stellar populations of field ellipticals may translate into a spurious component of the local peculiar velocity field (de Carvalho & Djorgovski 1992). Six of these field ellipticals show evidence of recent star formation (Schweizer *et al.* 1990). For convenience, we include in our analysis 28 ellipticals located mainly in loose groups, which also have younger stellar populations (Schweizer *et al.* 1990). Following Gregg (1992) this combined sample of 34 ellipticals will be used to investigate the effect of residual formation on the different distance indicators for elliptical galaxies.

Redshifts, B-band photometric diameters, velocity dispersions and Mg_2 indices for all these ellipticals are taken from Faber *et al.* (1989). In order to apply directly the results derived from our analysis of the Coma, Abell 2199 and Abell 2634 cluster samples to this sample, we have also determined V-band photometric parameters for these galaxies. Only one galaxy, NGC 1060, appears to have no published V-band data. R_e, SB_e and D parameters for the remainder were measured from published V-band aperture photometry (Burstein *et al.* 1987; Longo & de Vaucouleurs 1983; 1985) following the general procedure described in Section 2.2.2.

The global parameters for the field galaxy sample are listed in Table 2.13a. Galaxies with recent star formation are marked with the symbol '*'. The data set for ellipticals located in loose groups is listed in Table 2.13b. From comparison with Faber *et al.* (1989) B-band parameters we estimate that the uncertainty in our V-band R_e, SB_e and D measurements are 0.051 dex, 0.191 mag and 0.012 dex, respectively (see Figure 2.14). The

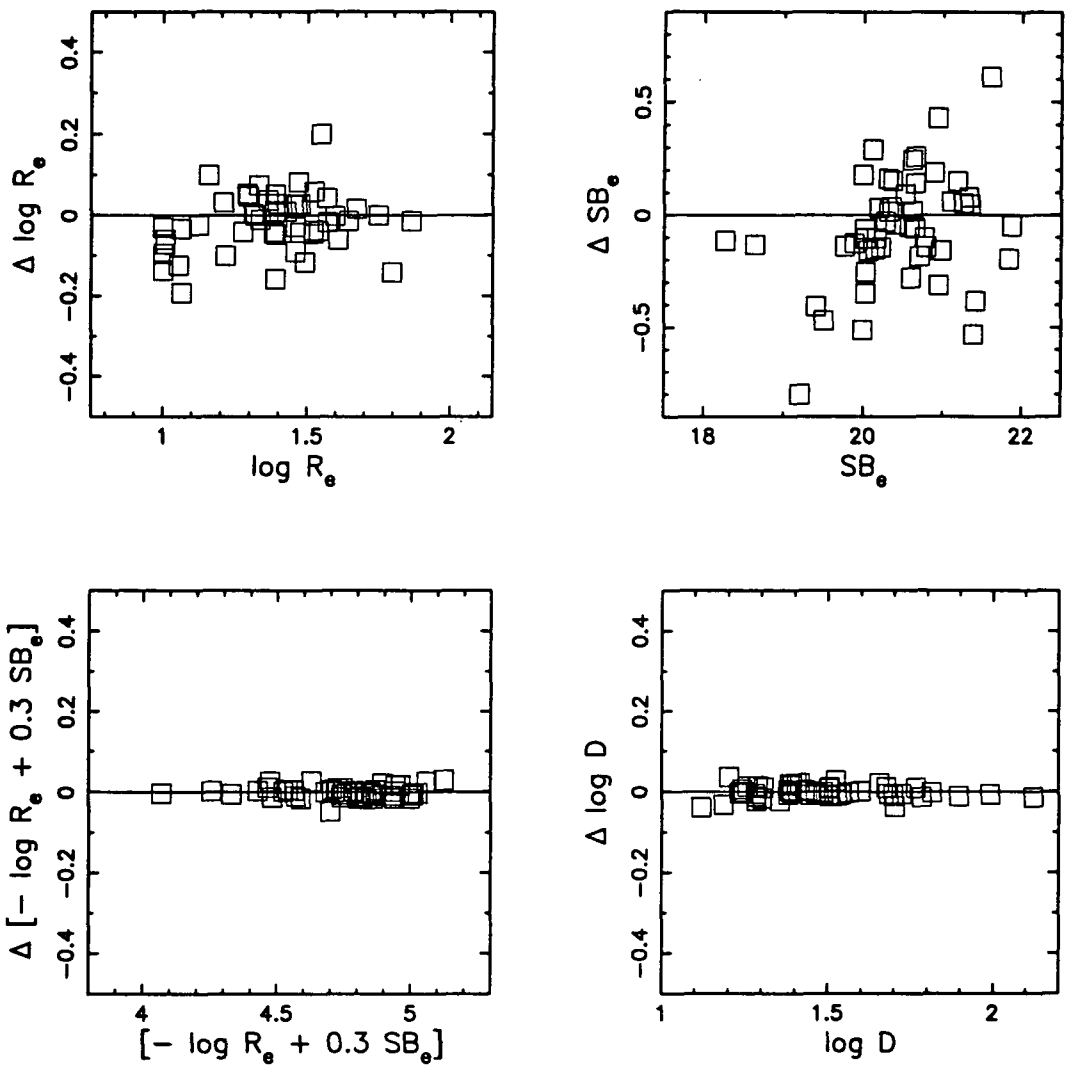

Figure 2.15. Comparison between the different B-band (Faber *et al.* 1989) and V-band (this study) photometric parameters. All B-band surface brightnesses have been corrected for cosmological and colour terms, i.e. $SB_e^B - 2.5\log(1+z)^4 - (B-V)$, assuming $(B-V) = 0.95$.

Table 2.13a The field galaxy data set.

Name	v_{CMB} (km s^{-1})	logD^B (0.1′)	logD^V (arcsec)	logR_e (arcsec)	SB_e (mag arcs^{-2})	logσ (km s^{-1})	Mg_2 (mag)
E409-G012	7693.	0.46	1.244	1.007	20.03	2.280	0.236
NGC 179	5737.	0.46	1.238	1.002	20.03	2.381	0.280
IC 1625	6524.	0.47	1.260	1.608	21.84	2.409	0.312
NGC 641	6206.	0.62	1.395	1.386	20.79	2.399	0.272
NGC 720	1461.	1.02	1.785	1.596	20.20	2.392	0.330
NGC 822	5221.	0.46	1.235	0.998	20.03	2.190	0.251
NGC 821	1454.	0.86	1.658	1.643	20.77	2.298	0.304
NGC 1060	4124.	0.74				2.517	0.325
NGC 1403	4086.	0.54	1.302	1.064	20.02	2.213	0.279
NGC 1521	4742.	0.71	1.488	1.427	20.62	2.349	0.271
NGC 1595	4148.	0.53	1.286	1.123	20.28	2.067	0.226
NGC 1573	4059.	0.72	1.509	1.475	20.71	2.435	0.336
NGC 1726	4570.	0.76	1.529	1.388	20.36	2.326	0.308
E552-G052	4779.	0.44	1.186	1.210	20.90	2.244	0.269
E553-G002	4276.	0.52	1.308	1.453	21.26	2.388	0.311
NGC 1930	2164.	0.61	1.381	1.332	20.66	2.289	0.263
NGC 2293	3687.	0.89	1.678	1.526	20.32	2.414	0.307
NGC 2305	2432.	0.79	1.566	1.384	20.22	2.334	0.304
NGC 2325	3892.	0.82	1.600	1.797	21.42	2.128	0.294
NGC 2314	1214.	0.72	1.525	1.066	19.21	2.463	0.327
E208-G021	4902.	0.91	1.683	1.471	20.12	2.228	0.321
NGC 2513	4881.	0.68	1.450	1.570	21.19	2.401	0.318

Table 2.13a Cont.

Name	v_{CMB} (km s^{-1})	logD^B (0.1′)	logD^V (arcsec)	logR_e (arcsec)	SB_e (mag arcs^{-2})	logσ (km s^{-1})	Mg_2 (mag)
NGC 2563	4869.	0.60	1.383	1.476	21.11	2.416	0.330
NGC 2749	4468.	0.62	1.418	1.458	20.95	2.353	0.317
NGC 2810	3643.	0.60	1.394	1.318	20.58	2.309	0.310
U 4956	5477.	0.39	1.204	1.391	21.39	2.270	0.315
NGC 2887	3050.	0.93	1.699	1.390	19.77	2.445	0.260
NGC 2872	3545.	0.72	1.505	1.277	20.06	2.439	0.322
NGC 2974*	2272.	0.95	1.723	1.521	20.15	2.346	0.300
NGC 3070	5730.	0.65	1.433	1.054	19.51	2.335	0.273
NGC 3090	6411.	0.51	1.283	1.548	21.61	2.408	0.334
NGC 3115	1062.	1.36	2.124	1.521	18.64	2.425	0.309
NGC 3158	7075.	0.66	1.439	1.390	20.66	2.488	0.336
E567-G051	4051.	0.47	1.248	1.001	19.99	2.149	0.266
NGC 3375	2738.	0.52	1.286	1.217	20.60	2.156	0.239
NGC 3411	4789.	0.61	1.408	1.459	20.98	2.487	0.334
E318-G021	5136.	0.60	1.356	1.292	20.62	2.188	0.260
IC 2623	4121.	0.38	1.120	1.158	20.94	2.152	0.266
NGC 3557	3342.	1.04	1.816	1.538	19.89	2.465	0.307
NGC 3562	6828.	0.61	1.388	1.336	20.65	2.451	0.299
NGC 3818*	1874.	0.73	1.502	1.365	20.37	2.314	0.315
NGC 3872	3564.	0.77	1.541	1.296	20.00	2.385	0.318
NGC 4073	6333.	0.59	1.386	1.747	21.87	2.442	0.321
NGC 4168*	2658.	0.74	1.506	1.673	21.33	2.259	0.260

Table 2.13a Cont.

Name	v_{CMB} (km s^{-1})	logD^B (0.1′)	logD^V (arcsec)	logR_e (arcsec)	SB_e (mag arcs^{-2})	logσ (km s^{-1})	Mg_2 (mag)
NGC 4261*	2560.	0.98	1.767	1.570	20.17	2.468	0.330
NGC 4697*	1567.	1.22	1.992	1.863	20.40	2.218	0.297
NGC 4742	1676.	0.96	1.702	1.008	18.27	1.970	0.177
NGC 4786	4996.	0.71	1.487	1.397	20.53	2.471	0.305
NGC 4830	3661.	0.69	1.465	1.313	20.32	2.256	0.258
E575-G043	7257.	0.50	1.292	1.466	21.35	2.378	0.337
NGC 4976	1643.	1.13	1.897	1.492	19.41	2.231	0.280
NGC 5198*	2695.	0.65	1.427	1.411	20.77	2.297	0.310
E221-G026	1649.	1.06	1.828	1.432	19.45	2.175	0.222
NGC 5582	1528.	0.65	1.382	1.574	21.40	2.182	0.296
IC 4421	3891.	0.65	1.423	1.254	20.26	2.347	0.286
NGC 5629	4718.	0.58	1.350	1.427	21.06	2.394	0.300
NGC 5812	2307.	0.91	1.650	1.554	20.51	2.310	0.324
NGC 6020	4521.	0.48	1.307	1.174	20.39	2.296	0.306
NGC 6127/8	4642.	0.64	1.415	1.348	20.60	2.355	0.316
NGC 6411	3661.	0.65	1.430	1.412	20.76	2.192	0.270
NGC 6482	3906.	1.03	1.761	1.043	18.17	2.458	0.320
NGC 6702	4613.	0.58	1.370	1.432	21.01	2.259	0.272
NGC 6703	2272.	0.88	1.652	1.432	20.09	2.233	0.280
NGC 6721	4385.	0.69	1.459	1.374	20.55	2.394	0.318
NGC 6849	5912.	0.53	1.343	1.489	21.27	2.273	0.259
E462-G015	5620.	0.75	1.515	1.388	20.41	2.467	0.292

Table 2.13a Cont.

Name	v_{CMB} (km s^{-1})	logD^B (0.1′)	logD^V (arcsec)	logR_e (arcsec)	SB_e (mag arcs^{-2})	logσ (km s^{-1})	Mg_2 (mag)
NGC 7002	7358.	0.47	1.246	1.541	21.69	2.395	0.288
E286-G059	8982.	0.39	1.173	1.133	20.69	2.410	0.276
NGC 7192	2787.	0.80	1.571	1.583	20.86	2.266	0.250
E467-G054	8004.	0.35	1.099	1.171	21.05	2.403	0.300
NGC 7385	7528.	0.51	1.292	1.682	21.95	2.414	0.324
IC 5328	2917.	0.80	1.565	1.397	20.27	2.295	0.280
NGC 7785	3453.	0.77	1.553	1.440	20.46	2.464	0.296
NGC 3606	3389.	0.58	1.348	1.055	19.83	2.314	0.286
E507-G025	3618.	0.84	1.607	1.377	20.05	2.393	0.298
NGC 7391	2716.	0.70	1.495	1.304	20.19	2.436	0.317
NGC 2904	2703.	0.63	1.418	1.151	19.92	2.365	0.311
IC 2311	2109.	0.91	1.666	1.234	19.32	2.346	0.255

Table 2.13b Elliptical galaxies in loose groups.

Name	v_{CMB} (km s^{-1})	logD^B (0.1′)	logD^V (arcsec)	logR_e (arcsec)	SB_e (mag arcs^{-2})	logσ (km s^{-1})	Mg_2 (mag)
NGC 596*	1557.	0.93	1.693	1.728	19.92	2.179	0.249
NGC 636*	1563.	0.83	1.584	1.552	19.69	2.193	0.273
NGC 1052*	1164.	1.00	1.781	1.835	20.00	2.313	0.316
NGC 1453*	3914.	0.78	1.571	1.760	20.45	2.462	0.327
NGC 1700*	4044.	0.90	1.668	1.562	19.40	2.368	0.278
NGC 2300*	2018.	0.87	1.674	1.868	20.47	2.430	0.319

Table 2.13b Cont.

Name	v_{CMB} (km s^{-1})	logD^B (0.1′)	logD^V (arcsec)	logR_e (arcsec)	SB_e (mag arcs^{-2})	logσ (km s^{-1})	Mg_2 (mag)
NGC 3193*	1596.	0.93	1.714	1.808	20.13	2.311	0.295
NGC 3377*	1141.	1.06	1.812	1.788	19.70	2.116	0.270
NGC 3379*	1144.	1.24	2.025	1.882	19.29	2.303	0.308
NGC 3605*	1469.	0.57	1.322	1.595	20.74	2.078	0.213
NGC 3608*	1469.	0.89	1.661	1.775	20.19	2.310	0.312
NGC 3610*	2006.	1.02	1.773	1.444	18.53	2.201	0.257
NGC 3640*	1900.	1.03	1.791	1.834	19.95	2.246	0.263
NGC 4125*	1883.	1.11	1.855	2.162	20.83	2.359	0.295
NGC 4278*	1058.	1.09	1.867	1.772	19.44	2.425	0.291
NGC 4283*	1058.	0.74	1.506	1.262	18.87	2.001	0.268
NGC 4374*	1495.	1.25	2.031	1.993	19.67	2.458	0.305
NGC 4589*	1699.	0.88	1.656	1.937	20.77	2.332	0.320
NGC 4660*	1489.	0.91	1.706	1.382	18.56	2.296	0.297
NGC 4915*	3494.	0.76	1.535	1.246	18.67	2.320	0.291
NGC 5018*	3061.	1.04	1.784	1.649	19.30	2.349	0.209
NGC 5322*	2075.	1.06	1.823	1.841	19.86	2.350	0.276
NGC 5557*	3689.	0.87	1.647	1.752	20.18	2.415	0.310
NGC 5576*	1883.	0.98	1.731	1.547	19.09	2.272	0.253
NGC 5831*	1885.	0.77	1.547	1.762	20.55	2.220	0.289
NGC 5982*	2833.	0.88	1.651	1.688	19.93	2.425	0.296
NGC 7619*	3115.	0.83	1.620	1.788	20.39	2.528	0.336
NGC 7626*	3115.	0.79	1.504	2.107	21.72	2.369	0.336

error in $\{\log R_e - 0.3\ SB_e\}$ in turn amounts to only 0.013 dex. Davies *et al.* (1987) estimate that the uncertainty in the listed σ and Mg_2 measurements is 0.041 dex (i.e. $\sim$10%) and 0.010 mag, respectively. Note that these values are not in the same σ and Mg_2 system previously described.

3 THE FUNDAMENTAL RELATIONSHIPS OF ELLIPTICAL GALAXIES

3.1 INTRODUCTION

Elliptical galaxies show strong correlations between the global parameters which describe their overall dynamical structure and metal abundance. Early investigations concentrated on monovariate relations, i.e. the galaxy luminosity (L) was shown to be correlated with effective radius (R_e) (Fish 1964), central velocity dispersion (σ) (Faber & Jackson 1976), effective surface brightness (SB_e) (Binggeli, Sandage & Tarenghi 1984) and colours (Sandage 1972) or Mg_2 line strength index (Terlevich *et al.* 1981). These results suggested that elliptical galaxies form a one-dimensional family with luminosity (or mass) as the main parameter defining the sequence.

Subsequent studies extended this analysis to lower luminosity objects and found that all the correlations involving effective parameters showed an abrupt change of slope at $M_B \sim -18$ mag (Wirth & Gallagher 1984, Kormendy 1985). This effect turned out to be one of the major results derived from the study of these global correlations, i.e. there are two fundamentally different kinds of elliptical galaxies, loosely called giants and dwarfs. Giants are the luminous, ordinary ellipticals, characterized by relatively high luminosity density and relatively low mass-to-light ratios. Despite the similarity in morphological appearance, dwarfs show opposite characteristics. Dwarf ellipticals may represent galaxies swept by galactic winds during their initial starburst phase, leading to

the metal-poor, low-density remnants we see today (Dekel & Silk 1986, Yoshii & Arimoto 1987). Whereas galactic winds could drive out baryons by pressure, they would not affect any non-baryonic dark matter, thus perhaps accounting for the large mass-to-light ratios characteristic of these objects (Dekel & Silk 1986). Alternatively, giants are thought to be descendant of protogalaxies massive enough to retain their processed material, explaining thus the high metallicities observed. Dissipative collapse, be it smooth or by gradual merging, leads naturally to higher luminosity densities. However, despite the evidence for different formation processes for both galaxy families, Caldwell (1983) has shown that the colour-magnitude relation for giants extends smoothly down to the dwarf ellipticals. Also, the correlations between the velocity dispersion and luminosity or Mg_2 line strength index are apparently universal for both galaxy families (Tonry 1981, Bender 1991a). This regularity in the stellar population properties of all ellipticals, independent from their large variety in structure and kinematics, remains both a challenge and an important clue for the development of a consistent picture of galaxy formation.

Recently, a substantial step forward in the understanding of galaxy properties has been made by studying correlations of higher dimensionality. All of the above correlations show a residual scatter which is not accounted for by measurement errors. The observed trends of the residuals in the $L - \sigma$ relation with other physical variables such as axial ratio, M/L, surface brightness or colour, hinted at hidden-parameter effects (Terlevich *et al.* 1981, Tonry & Davis 1981, de Vaucouleurs & Olson 1982, Efstathiou & Fall 1984, Lauer 1985). For giant ellipticals, a new, bivariate correlation between L, σ and SB_e was found by Dressler *et al.* (1987) and Djorgovski & Davies (1987), i.e. the 'fundamental plane'. Surface brightness may also be incorporated into the colour (or Mg_2)–L relation to derive a similar plane relative to the properties of the stellar population, rather than the overall structure, of elliptical galaxies (de Carvalho & Djorgovski 1989). Both bivariate correlations show a significantly smaller scatter compared to the $L - \sigma$ and $L - Mg_2$

relations. The basic result from these studies is that giant elliptical galaxies appear to form a biparametric, nearly planar family (in logarithmic units). The different monovariate correlations have been interpreted as its oblique projections while the tilt relative to the coordinate planes determines the intrinsic scatter (Faber *et al.* 1987, Djorgovski 1991). The two-dimensionality of this galaxy family suggests that the M/L must be a function of only two structural variables and the virial theorem is the only strong constraint on the structure of giant ellipticals (Faber *et al.* 1987). For dwarf ellipticals, however, no similar bivariate correlations seems to exist although the samples studied so far are relatively sparse and may not be representative (Bender, Burstein & Faber 1992, de Carvalho & Djorgovski 1992).

In this Chapter we investigate the fundamental relations of elliptical galaxies, i.e. the basic laws common to all ellipticals from which the wide variety of observed correlations are derived. The coefficients of these relations imply direct constraints on the structure and stellar populations of present day ellipticals. In addition, they provide direct information on the physical variables that controlled the early formative processes. Here we address the problem of determining the coefficients of these fundamental relations. Our analysis is largely based on R_e, SB_e, σ and Mg_2 measurements for our sample of 66 giant ellipticals in the Coma cluster. This study is subsequently extended to include other samples of cluster/field ellipticals and spheroidal systems in general. In Section 3.2 we show that giant ellipticals do not uniformly cover the fundamental plane. Based on this result we develop in Section 3.3 a new framework in which only three fundamental relations are needed to derive all the global correlations of giant ellipticals. This framework is generalized in Section 3.4 to provide a common set of fundamental relations for all spheroidal systems. Finally, in Section 3.5 we discuss the results of our framework within a simple picture of galaxy formation based on the hierarchical clustering scenario and the galactic wind model.

3.2 THE DISTRIBUTION OF GIANT ELLIPTICALS ON THE FUNDAMENTAL PLANE

Giant elliptical galaxies populate a plane in the three dimensional space of $\log R_e$ (or $\log L$), SB_e and $\log\sigma$. This relation is often referred to as the fundamental plane (hereafter FP). The existence of monovariate correlations indicates that elliptical galaxies do not populate this plane homogeneously but must lie on a relatively narrow locus on it (see Peacock 1990). The area of the plane covered by ellipticals is, in principle, determined by selection effects of the galaxy sample. Disney (1976) pointed out that correlations such as Fish's law (i.e. $L/R_e^2 \sim$ constant) may be caused by selecting objects with a small range of surface brightness and thus be entirely spurious. If selection effects are indeed responsible for the above correlations, ellipticals should be randomly scattered over the area of the plane limited by these effects.

In Figure 3.1 we plot the face-on view of the FP for a magnitude-limited sample of 37 ellipticals brighter than $m_V = 15.5$ mag that are located in the central area of the Coma cluster (squares). This data set possesses three important characteristics: homogeneity, equidistant objects and completeness. The best fitting FP for this sample is :

$$-\log R_e - 0.785 \log I_e + 1.140 \log \sigma = -0.046 \qquad (3.1)$$

where R_e is expressed in units of kpc, I_e is the average intensity within R_e in $L_\odot pc^{-2}$ and σ is in km s^{-1} (adopting $H_o = 50$ km s^{-1} Mpc^{-1}, $cz_{\rm Coma} = 7200$ km s^{-1} and $M_{V\odot} = 4.78$, then 1″ is equivalent to 0.7 kpc and I_e is related to SB_e by $\log I_e = (26.35 - SB_e)/2.5$). For Figure 3.1 we have adopted the following coordinate system:

$$x = (1.890 \log R_e - 0.785 \log I_e + 1.140 \log\sigma)/2.342$$

$$y = (1.140 \log I_e + 0.785 \log\sigma)/1.384$$

$$z = (-\log R_e - 0.785 \log I_e + 1.140 \log\sigma)/1.707$$

where the z-axis is perpendicular to the FP and $\{x, y\}$ define an orthogonal coordinate system on the FP with the x-axis being simply proportional to $\log R_e$. We have plotted in Figure 3.1 the five lines that limit the "observing window" of the data set. This region is partly defined by the sample selection, i.e. $m_V \leq 15.5$ mag and $\sigma \geq 100$ km s^{-1}. The upper limit in absolute magnitude corresponds to the maximum of the luminosity function for ellipticals (i.e. $M_V \sim -25$ mag). Surface brightness limits characteristic of unusually compact and unusually diffuse objects are also considered. Roughly, objects with $SB_e \leq 17$ mag arcsec^{-2} are too stellar-like and those with $SB_e \geq 23$ mag arcsec^{-2} have too low surface brightness to have been included in this sample; these limits, however, do not significantly affect the results presented below.

Figure 3.1 clearly shows that elliptical galaxies do not uniformly cover the FP; rather they are confined to a relatively narrow band that is *not* a result of selection effects. Within the "observing window" of the data set there are no very luminous ellipticals with high surface brightness or galaxies with both low surface brightness and low velocity dispersion. The 29 ellipticals (brighter than $m_V \sim 14.5$ mag) that lie in the outer area of the cluster are also shown in Figure 3.1 (circles). Although these additional ellipticals do not form a magnitude limited sample, they strengthen the evidence that the distribution of points on the FP is not the result of selection effects alone.

This result can be shown quantitatively using a simple Monte Carlo simulation. We consider the null hypothesis that there is no intrinsic correlation between galaxy luminosity and surface brightness, i.e. the distribution of galaxies on the FP is only due to selection effects. To test this hypothesis we calculate the probability that the correlation coefficient (r_o) of the actual galaxy distribution on the plane may be obtained with a simulated random sample of similar characteristics. A typical galaxy in our simulations has random

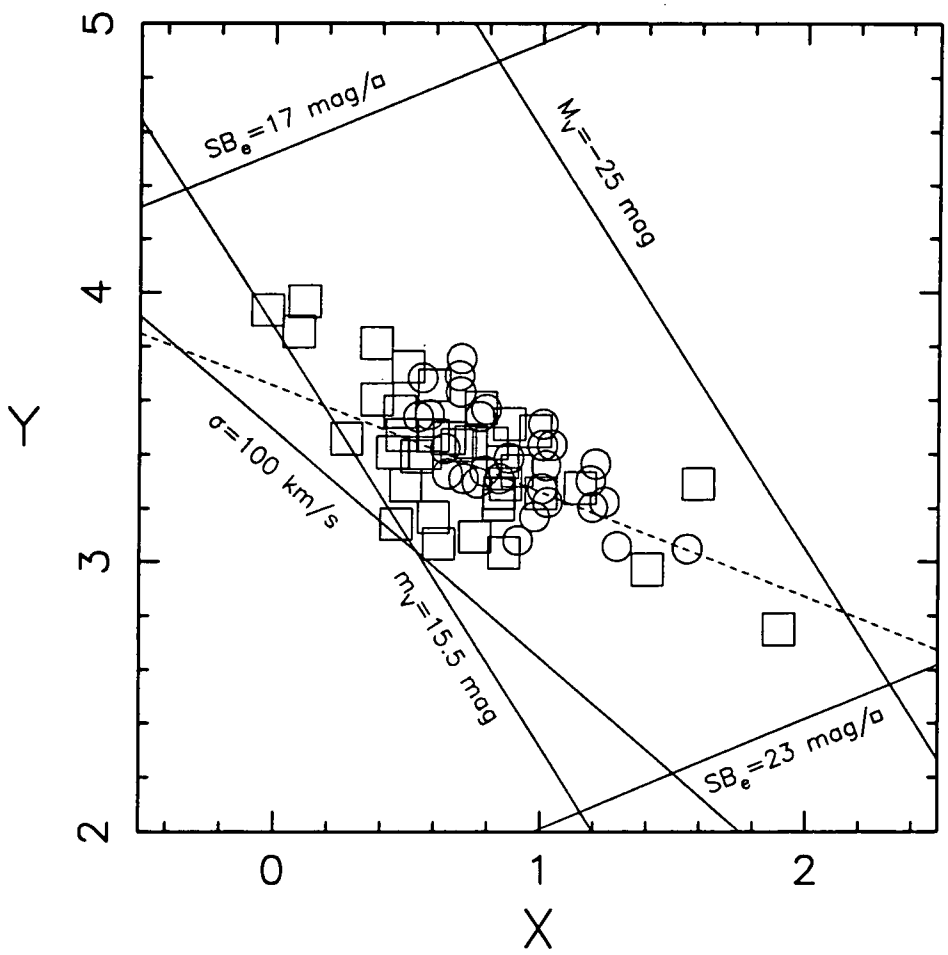

Figure 3.1. The face-on view of the FP for 66 ellipticals in Coma. Squares: magnitude limited sample in the central area of the cluster ($R < 0.7°$). Circles: halo sample ($0.7° < R < 5°$). Solid lines limit the area corresponding to our "observing window". The dashed line is our best fit to the data.

luminosity and surface brightness selected from our combined data set and a velocity dispersion derived from the equation of the FP i.e.

$$\log \sigma = 0.442 \log L + 0.250 \log I_e - 0.390 \tag{3.2}$$

(Note that throughout this chapter we adopt $L = 2\pi I_e R_e^2$). The corresponding data point on the plane must lie in the region allowed by our selection effects to be finally selected. The surface brightness limits have been reduced to the maximum and minimum values observed in our Coma sample (i.e. $SB_e = 18$ and $SB_e = 22.5$ mag arcsec^{-2}, respectively) to provide a more robust test. Each simulated sample with these characteristics produces a different distribution of data points on the plane for which we compute the correlation coefficient r_s. After 10^5 simulations we obtained no value of r_s such as $|r_s| \geq |r_o|$. The probability that the observed distribution on the FP is due to selection effects alone is thus less than 10^{-5}. Therefore we conclude that this null hypothesis is completely ruled out.

The position of ellipticals on the FP is adequately described by:

$$\mathrm{y} = -0.39\ \mathrm{x} + \mathrm{constant} \tag{3.3}$$

(dashed line in Figure 3.1). When this relation is combined with the FP equation given above and R_e, I_e and σ are eliminated in turn, the following expressions result:

$L \propto R_e^{1.2}$	(cf. Fish 1964)
$L \propto \sigma^{3.7}$	(cf. Faber & Jackson 1976)
$I_e \propto R_e^{-0.8}$	(cf. Kormendy 1977)
$L \propto I_e^{-1.5}$	(cf. Binggeli, Sandage & Tarenghi 1984)

The slopes of the derived correlations are similar to the values previously reported in the literature. Therefore each of these four monovariate relations are a direct result of *both* the projection of the FP *and* the intrinsic distribution of galaxies on the plane.

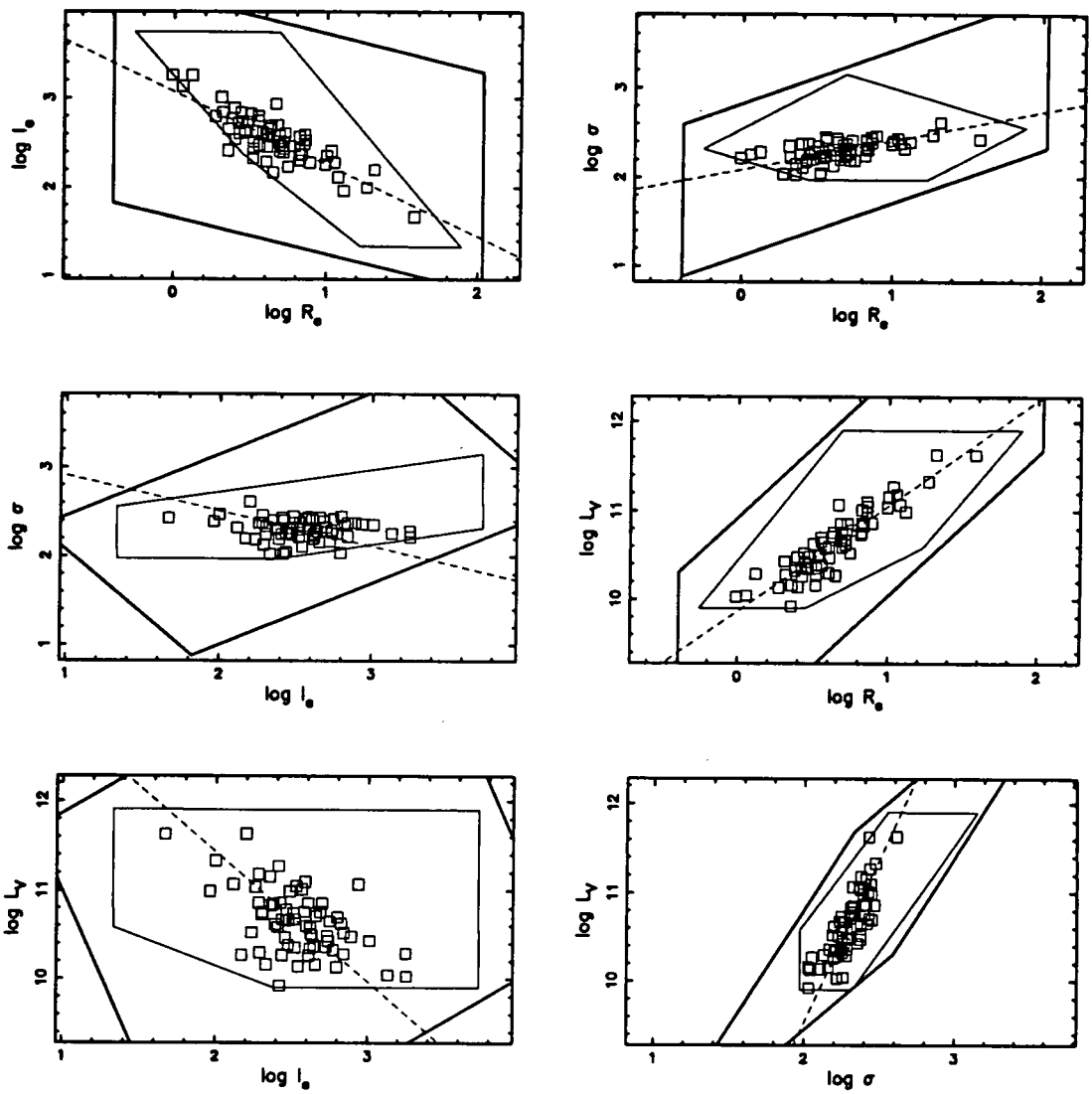

Figure 3.2. Projections of the FP area shown in Figure 1 onto different planes of observables (thick solid lines). Thin solid lines represent the projected "observing window". The dashed line is our best fit to the distribution of galaxies on the FP.

In Figure 3.2 we show the projections of the FP and the selection boundaries onto different planes of observables. The important feature of these plots is that the axes are equally scaled so that the range of values for each coordinate is always the same (e.g. three logarithmic units, as in Figure 3.1). Our observing window is represented by thin solid lines. The thick solid lines outline the boundaries of Figure 3.1 and thus allow the tilt of the FP with respect to each plane of observables to be seen. Since the angle between the $\{I_e, L\}$ and FP planes is only $\sim 27°$, this projection provides a good representation of the face-on view of the FP in terms of physically meaningful variables. An almost edge-on view of the FP is shown in the $\{\sigma, L\}$ projection. Yet, because of the projection angle, the observed scatter around the Faber-Jackson correlation will be significantly smaller than the actual scatter across the plane.

Figure 3.2 allows the correct interpretation of the $\{I_e, \sigma\}$ and $\{R_e, I_e\}$ projections to be made. In previous work (Faber *et al.* 1987), the $\{I_e, \sigma\}$ plane was considered to show the FP almost face-on. Since the plot of I_e vs σ, scaled according to the range of data points, shows a scatter diagram, elliptical galaxies were thought to cover the plane uniformly and hence, to form a biparametric family. The $\{R_e, I_e\}$ plane in turn was interpreted as an almost edge-on view of the FP such that the correlation between R_e and I_e (Kormendy 1977) would simply reflect the tilt of the FP. As Figure 3.2 shows, both the $\{I_e, \sigma\}$ and $\{R_e, I_e\}$ projections form a similar angle of $\sim 50°$ with respect to the FP. Thus Kormendy's relation is not only the result of the tilt of the FP but reflects the actual distribution of galaxies on the FP. The relation that describes this distribution (given above) is shown projected onto each plane of observables (dashed lines). This relation provides an accurate description of the observed trends in each projection. The apparently poor correlation between I_e and σ is simply an artifact of projection effects due to the particular orientation of the galaxy distribution on the FP relative to the $\{I_e, \sigma\}$ plane.

The existence of the FP has been physically interpreted as the expression of the virial theorem in terms of "luminosity" variables. This explanation assumes that the luminous part of giant ellipticals is self-gravitating and suggests a weak dependence of the M/L ratio on galaxy mass, i.e. $M/L \propto M^{0.2}$ (Faber *et al.* 1987). The distribution of ellipticals on the FP implies that there is a second constraint on the galaxy structure in addition to the virial theorem. Using the above scaling law for M/L, the observed distribution translates into the relationship between scale length and galaxy mass, $M \propto R_e^{1.5}$, or in terms of the binding energy, $M \propto E_b^{3/4}$ (cf. Fish 1964, Saito 1979). We note that this additional constraint is not as well-defined as the virial theorem. The rms of the distribution of data points across the FP is ~ 4 times the rms observed perpendicular to the FP (in $\log L$ units), i.e. elliptical galaxies are distributed neither on a plane nor along a line but on a band.

3.3 THE FUNDAMENTAL RELATIONS OF GIANT ELLIPTICALS

In this section we present a simple framework that describes the global correlations observed for elliptical galaxies. Previous work on this subject treated these separately and the coefficients (i.e. slopes and zero-points) were fitted to each correlation independently. However, as stated in Section 3.2, not all the correlations between global parameters are independent. In particular, we have shown that the structural parameters of giant ellipticals are strongly constrained by the two equations that define the "fundamental band" in the $\{R_e, I_e, \sigma\}$ space. The correlations between metallicity and galaxy dynamical quantities pose a different constraint on the stellar content of these galaxies. Our approach aims to identify the minimum number of basic relationships from which all the observed

correlations for ellipticals can be derived. The choice of the actual set of relations is not, however, unique. In our framework, the galaxy structure and metal abundance are described by only three fundamental relations:

$$M \propto R \langle v^2 \rangle \qquad \text{(I)}$$

$$M \propto R^{\zeta} \qquad \text{(II)}$$

$$Z \propto \langle v^2 \rangle^{\xi} \qquad \text{(III)}$$

where M is the galaxy mass, R is the half-mass radius, $\langle v^2 \rangle$ is the mean square speed of the system's stars and Z is the average metallicity of the stellar population. ζ and ξ are constants which can be determined from the observations.

The first relation is the virial theorem (we assume that all ellipticals have similar dynamical structure, i.e. the constant of proportionality does not vary significantly with galaxy mass). The second relation represents the additional constraint on the scale length and galaxy mass discussed in Section 3.2. Note that this relation is now formulated in terms of the half-mass radius instead of the half-light radius. The third relation links the chemical composition to the dynamical structure of the galaxy. This relation is inferred from observations which suggest that the metallicity of ellipticals is primarily related to the mean depth of the potential well rather than the mass of the galaxy (Tonry & Davis 1981, Franx & Illingworth 1990, Bender 1991).

In order to express the fundamental relations in terms of the observed parameters we have made the following simple assumptions:

(a) the luminosity depends in some general way on galaxy mass, i.e. $M/L \propto M^{\eta}$, as suggested by Faber *et al.* (1987);

(b) the ratio between the scale lengths of the mass and light distributions depend also on galaxy mass. By analogy with the M/L parameterization we adopt $R/R_e \propto$

M^{λ}. Such dependence is suggested in some dissipative models of galaxy formation (Navarro 1992). Hereafter we will refer to R/R_e as the effective collapse factor, since this ratio can be interpreted as the amount by which the luminous matter has collapsed relative to the overall mass distribution;

(c) elliptical galaxies all have very similar luminous profile. Thus we adopt $L \propto I_e\ R_e^2$. By definition of I_e, this constant is simply 2π;

(d) the galaxy potential depth can be adequately represented by the projected central velocity dispersion, i.e. $\langle v^2 \rangle \propto \sigma^2$;

(e) the central Mg_2 line strength index is mainly sensitive to metallicity, i.e. $\log Z \propto Mg_2$; note that hereafter we simply use Z to represent the metallicity scale defined by Mg_2.

Assumptions (a) and (b) can be regarded more as hypotheses since the processes of gas loss and dissipation are not well understood yet. Although it may seem unappealing to introduce these extra degrees of freedom, in fact it is possible to constrain simultaneously the values of both constants η and λ via observation as we will show later. The remaining assumptions are to some extent approximations and will introduce a certain scatter in the observed correlations. In particular, central velocity dispersion measurements may be affected by rotation/projections effects since less luminous ellipticals are flattened by rotation while bright ellipticals are supported by velocity anisotropy (Davies *et al.* 1983). Also, although the adoption of Mg_2 as a metallicity scale is justified by Mould's (1978) theoretical analysis, we note that this index is also affected by differences in age of the stellar population (cf. Burstein *et al.* 1988, Schweizer *et al.* 1990). In our framework we will assume that differences in galaxy kinematics and age of the stellar content are second-order effects that are likely to offset the zero-points rather than to alter significantly the slopes of the global correlations.

With the above assumptions we can express the fundamental relations in terms of the "observable" parameters and derive the global correlations as linear combinations of these relations. In Figure 3.3 we summarize the assumed relations in our framework and their transformation into the different correlations as a function of ζ, ξ, η and λ. The fundamental plane [eq. (i)] is the expression of the virial theorem (I) in terms of "luminosity" variables using the assumed transformations for M, M/R^2 and $\langle v^2 \rangle$ (cf. Faber *et al.* 1987). Applying the same transformation to the second fundamental property (II) we obtain not only the correlation between L and I_e [eq. (ii)] but also the L-R_e and I_e-R_e correlations [eq. (iv) and (v), respectively]. These correlations represent the same constraint on scale length and galaxy mass but they are expressed in different "luminosity" variables. Finally, the third fundamental relation (III) translates directly into the observed correlation between Mg_2 and σ [eq. (iii)]. Equations (i), (ii) and (iii) are thus equivalent forms of our fundamental relations (I), (II) and (III). The remaining correlations are linear combinations of these three relations. Thus, combining (i) and (ii) we obtain not only Faber-Jackson's relation [eq. (vi)] but also the correlation between R_e and σ [eq. (vii)]. From (i) and (iii) we derive the equivalent expression of the plane defined in de Carvalho & Djorgovski (1989) [eq. (viii)]. Finally, the combination of (i), (ii) and (iii) gives the Mg_2 line index (or colour) – magnitude relation [eq. (ix)].

We have explored which values of ζ, ξ, η and λ are simultaneously consistent with all nine correlations for the same sample of 66 Coma ellipticals we used in Section 3.2. We first calculate for each correlation the two least squares slopes resulting from minimizing in the abscissa and ordinate axes (a similar procedure is used for the bivariate correlations [eq. (i) and (viii)]). These two values define the allowed range of variation for each slope. The zero-points are not considered in our analysis at this stage. From the nine global correlations listed in Figure 3.3 we obtain a system of eleven inequalities and four unknowns, i.e. ζ, ξ, η and λ. For example, the two regression lines of the $L - R_e$

THE FRAMEWORK

FUNDAMENTAL PROPERTIES

$$\begin{array}{rcll} M & \propto & R\,\langle v^2\rangle & \text{(I)} \\ M & \propto & R^{\zeta} & \text{(II)} \\ Z & \propto & \langle v^2\rangle^{\xi} & \text{(III)} \end{array}$$

ASSUMPTIONS

$$\begin{array}{rcl@{\quad}rcl} M/L & \propto & M^{\eta} & \Rightarrow & M & \propto & L^{\frac{1}{1-\eta}} \\ R/R_e & \propto & M^{\lambda} & \Rightarrow & R & \propto & R_e\, L^{\frac{\lambda}{1-\eta}} \\ L & \propto & I_e\, R_e^2 & \Rightarrow & M/R^2 & \propto & I_e\, L^{\frac{\eta-2\lambda}{1-\eta}} \\ \multicolumn{3}{c}{\text{Isotropy}} & \Rightarrow & \langle v^2\rangle & \propto & \sigma^2 \\ \multicolumn{3}{c}{\text{Metallicity index}} & \Rightarrow & \log Z & \propto & Mg_2 \end{array}$$

GLOBAL CORRELATIONS

$$\begin{aligned}
-\log R_e - \tfrac{1-\lambda}{1+\eta-2\lambda}\log I_e + \tfrac{2(1-\eta)}{1+\eta-2\lambda}\log\sigma &= k_1 && \text{(i)}\\
\log L + \tfrac{\zeta(1-\eta)}{2(1-\lambda\zeta)-\zeta(1-\eta)}\log I_e &= k_2 + \log(2\pi 10^6) && \text{(ii)}\\
Mg_2 - 2\xi\log\sigma &= k_3 && \text{(iii)}\\
\log L - \tfrac{\zeta(1-\eta)}{1-\lambda\zeta}\log R_e &= \left(1-\tfrac{\zeta(1-\eta)}{2(1-\lambda\zeta)}\right)k_2 + \log(2\pi 10^6) && \text{(iv)}\\
\log I_e + \tfrac{(1-2\lambda+\eta)(1-\lambda\zeta)-(\zeta-1)(1-\eta)}{(1-\lambda\zeta)(1-\lambda)}\log R_e &= \left(1-\tfrac{\zeta(1-\eta)}{2(1-\lambda\zeta)}\right)k_2 && \text{(v)}\\
\log L - \tfrac{2\zeta(1-\eta)}{\zeta-1}\log\sigma &= -\tfrac{(1+\eta-2\lambda)\zeta}{\zeta-1}k_1 - \tfrac{2(1-\lambda\zeta)-\zeta(1-\eta)}{2(\zeta-1)}k_2 + \log(2\pi 10^6) && \text{(vi)}\\
\log\sigma - \tfrac{\zeta-1}{2(1-\lambda\zeta)}\log R_e &= \tfrac{(1+\eta-2\lambda)\zeta}{2(1-\eta)}k_1 + \tfrac{[2(1-\lambda\zeta)-\zeta(1-\eta)](1-\lambda)}{4(1-\lambda\zeta)(1-\eta)}k_2 && \text{(vii)}\\
-\log R_e - \tfrac{1-\lambda}{1+\eta-2\lambda}\log I_e + \tfrac{(1-\eta)}{\xi(1+\eta-2\lambda)}Mg_2 &= k_1 + \tfrac{(1-\eta)}{\xi(1+\eta-2\lambda)}k_3 && \text{(viii)}\\
\log L - \tfrac{\zeta(1-\eta)}{\xi(\zeta-1)}Mg_2 &= -\tfrac{(1+\eta-2\lambda)\zeta}{\zeta-1}k_1 - \tfrac{2(1-\lambda\zeta)-\zeta(1-\eta)}{2(\zeta-1)}k_2 - \tfrac{\zeta(1-\eta)}{\xi(\zeta-1)}k_3 + \log(2\pi 10^6) && \text{(ix)}
\end{aligned}$$

Figure 3.3. Outline of our framework.

correlation for our Coma data set have slopes of 1.1 and 1.5. Equation (iv) then implies the following inequality:

$$1.1 \leq \frac{\zeta(1-\eta)}{1-\lambda\zeta} \leq 1.5 \tag{3.4}$$

We have solved the system of eleven inequalities using simple Monte Carlo simulations. A set of random ζ, ξ, η and λ values is generated in each simulation and the resulting combination is considered to be valid if it satisfies all the inequalities.

In Figure 3.4 we show the locus occupied by the different $\{\zeta, \eta, \xi, \lambda\}$ combinations obtained in our simulations in the $\{\eta, \zeta\}$, $\{\eta, \lambda\}$ and $\{\eta, \xi\}$ projections. For simplicity, we have restricted these combinations to those solutions with $\zeta \leq 4$. The projections clearly suggest that the space of valid $\{\zeta, \eta, \xi, \lambda\}$ combinations is strongly degenerate. In particular, we note that the locus of possible solutions in the $\{\eta, \zeta\}$ projection is mainly determined by the slope of the $L-\sigma$ relation. Since the value of this slope lies approximately between 3 and 4, then the condition:

$$\frac{4}{2\eta+2} \leq \zeta \leq \frac{3}{2\eta+1} \tag{3.5}$$

roughly defines the area of the parameter space allowed by the observations. Alternatively, the linear relation between η and λ is primarily determined from the coefficients of the fundamental plane, e.g.:

$$1.5\ \eta - 0.5 \leq \lambda \leq 1.3\ \eta - 0.3 \tag{3.6}$$

Hence, once we adopt a value for one of these parameters the range of variation for the remaining two is strongly constrained. Obviously, the parameter space in the $\{\eta, \xi\}$ projection is uniquely determined by the range of variation of the $Mg_2 - \sigma$ slope. In all cases, there is no solution for $\eta \leq -1$ and $\eta > 1$. In conclusion, as it is clear from Figure 3.4, there is a large variety of possible combinations of $\{\zeta, \eta, \xi, \lambda\}$ values consistent with the observed global correlations. This apparent indetermination in our framework simply reflects the lack of knowledge about the dark matter distribution in elliptical galaxies.

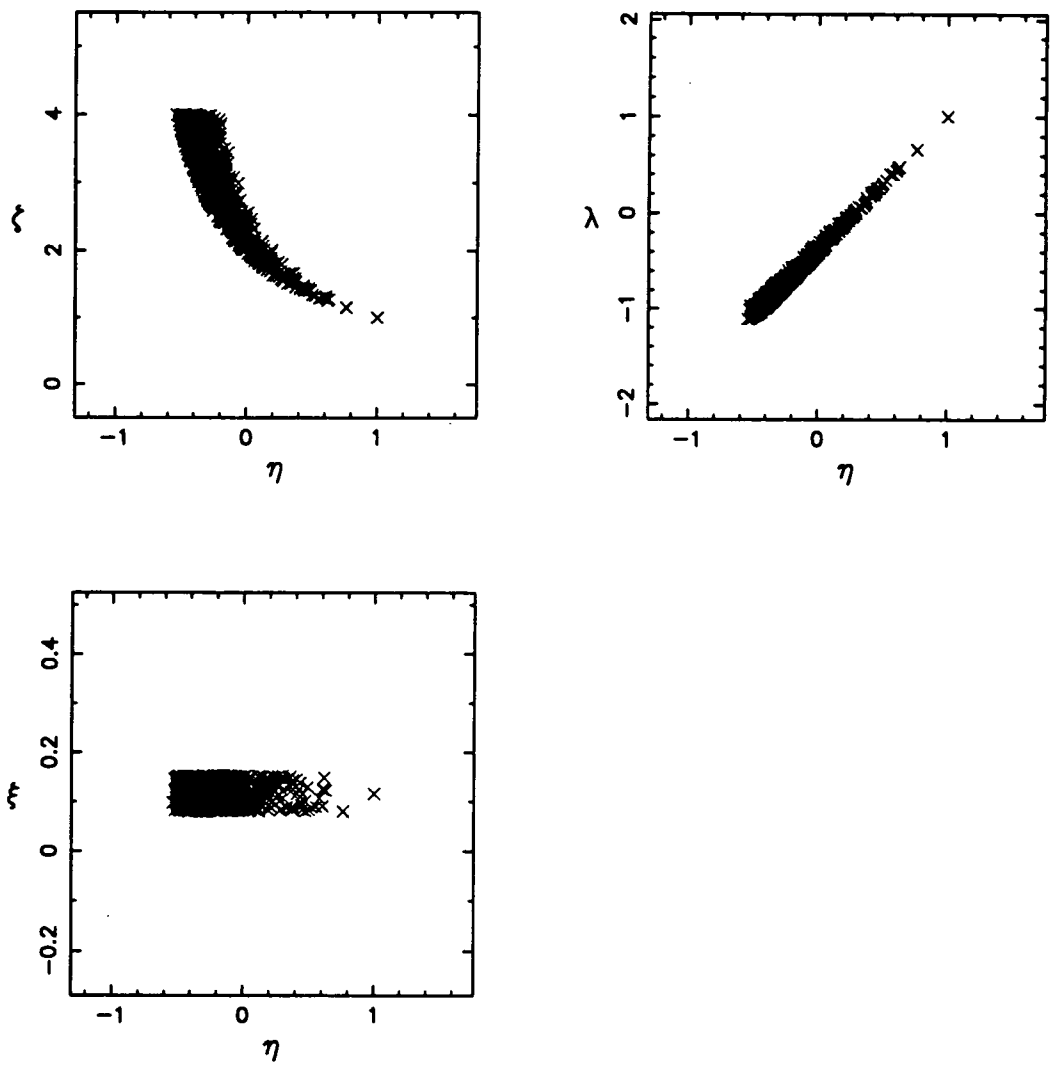

Figure 3.4. Projections of the 4D hyper-volume defined by one thousand $\{\zeta, \eta, \xi, \lambda\}$ combinations consistent with the observed correlations for giant ellipticals onto the $\{\eta, \zeta\}$, $\{\eta, \lambda\}$ and $\{\eta, \xi\}$ coordinate planes.

Particularly interesting is the solution corresponding to $\lambda = 0$, i.e. $R \propto R_e$. Hereafter we refer to this solution as the constant collapse factor case. This is equivalent to assuming that, for giant elliptical galaxies, the mass and light distributions are similar and includes the case $R = R_e$ (i.e. elliptical galaxies are baryon-dominated). For our Coma sample:

$$\zeta = 1.635, \quad \xi = 0.116, \quad \text{and} \quad \eta = 0.274.$$

These values are the mean of the distribution of possible solutions with $\lambda = 0$. The standard deviations of each distribution are 0.068, 0.021 and 0.013 respectively. Substituting the values of ζ, ξ, η and λ into equations (i)–(ix) the slopes for each of the nine correlations are directly obtained (see Table 3.1). These slopes are very similar to values previously reported in the literature for the individual correlations. Finally, the resulting slopes of our fundamental relations (i), (ii) and (iii) are used to derive the mean values of the zero-points k_1, k_2 and k_3 from our data set. The zero-points of the remaining six correlations are then calculated using the linear combinations given in Figure 3.3. We show in Figure 3.5 the linear fits to the different observed correlations for the Coma sample as listed in Table 3.1. The first two top panels show the edge-on and almost face-on views of the FP. The third top panel shows the $Mg_2 - \sigma$ relation. As noted previously, these three correlations represent our three fundamental relations. The remaining panels simply show different combinations of these relations. Clearly, our framework provides an excellent description of the observed correlations for giant elliptical galaxies in Coma.

In Figures 3.6 and 3.7 we show the correlations listed in Table 3.1 superimposed to the A2199 and A2634 clusters sample. The zero-points of these correlations are calculated from the mean k_1, k_2 and k_3 values derived for these data sets. As it can be readily seen, our fits are also in excellent agreement with the observed trends in each plot. The Coma, A2199 and A2634 samples constitute a homogeneous population of cluster ellipticals. Field ellipticals, however, appear to be a more heterogeneous galaxy population (Burstein 1978;

Table 3.1. Derived fits for our sample of giant ellipticals in the Coma cluster.

Eq.	Global Correlation		$\langle ZP \rangle$	rms
(i)	$-\log R_e - 0.785\ \log I_e + 1.140\ \log \sigma$	=	−0.046	0.073
(ii)	$\log L + 1.460\ \log I_e$	=	14.41	0.377
(iii)	$Mg_2 - 0.232\ \log \sigma$	=	−0.249	0.018
(iv)	$\log L - 1.187\ \log R_e$	=	9.891	0.151
(v)	$\log I_e + 0.813\ \log R_e$	=	3.093	0.151
(vi)	$\log L - 3.739\ \log \sigma$	=	2.079	0.253
(vii)	$\log \sigma - 0.317\ \log R_e$	=	2.090	0.095
(viii)	$-\log R_e - 0.785\ \log I_e + 4.913\ Mg_2$	=	−1.270	0.124
(ix)	$\log L - 16.115\ Mg_2$	=	6.094	0.354

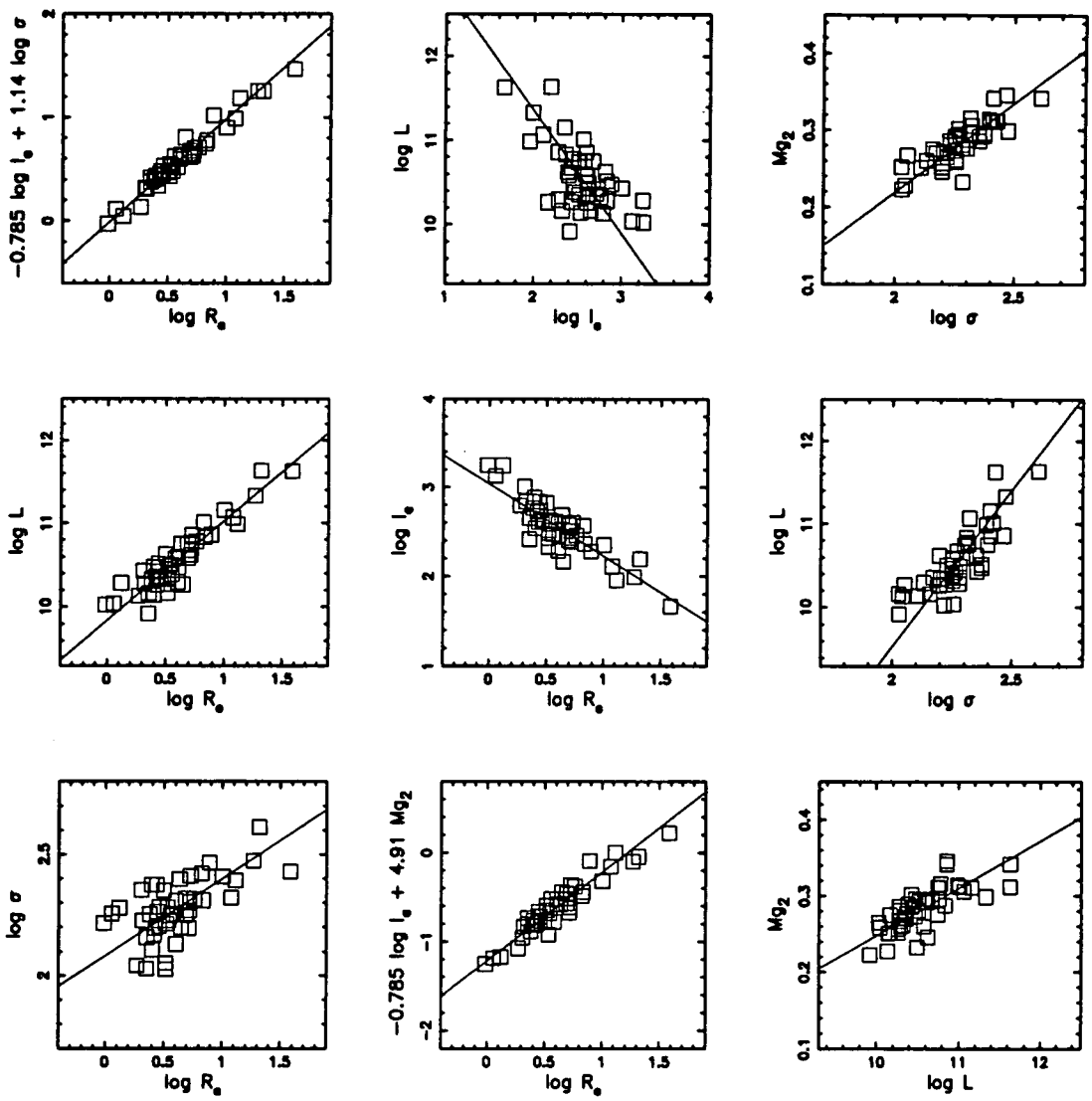

Figure 3.5. The well-known global correlations of giant elliptical galaxies for our Coma sample. Solid lines are the fits to the data derived from our framework as listed in Table 3.1.

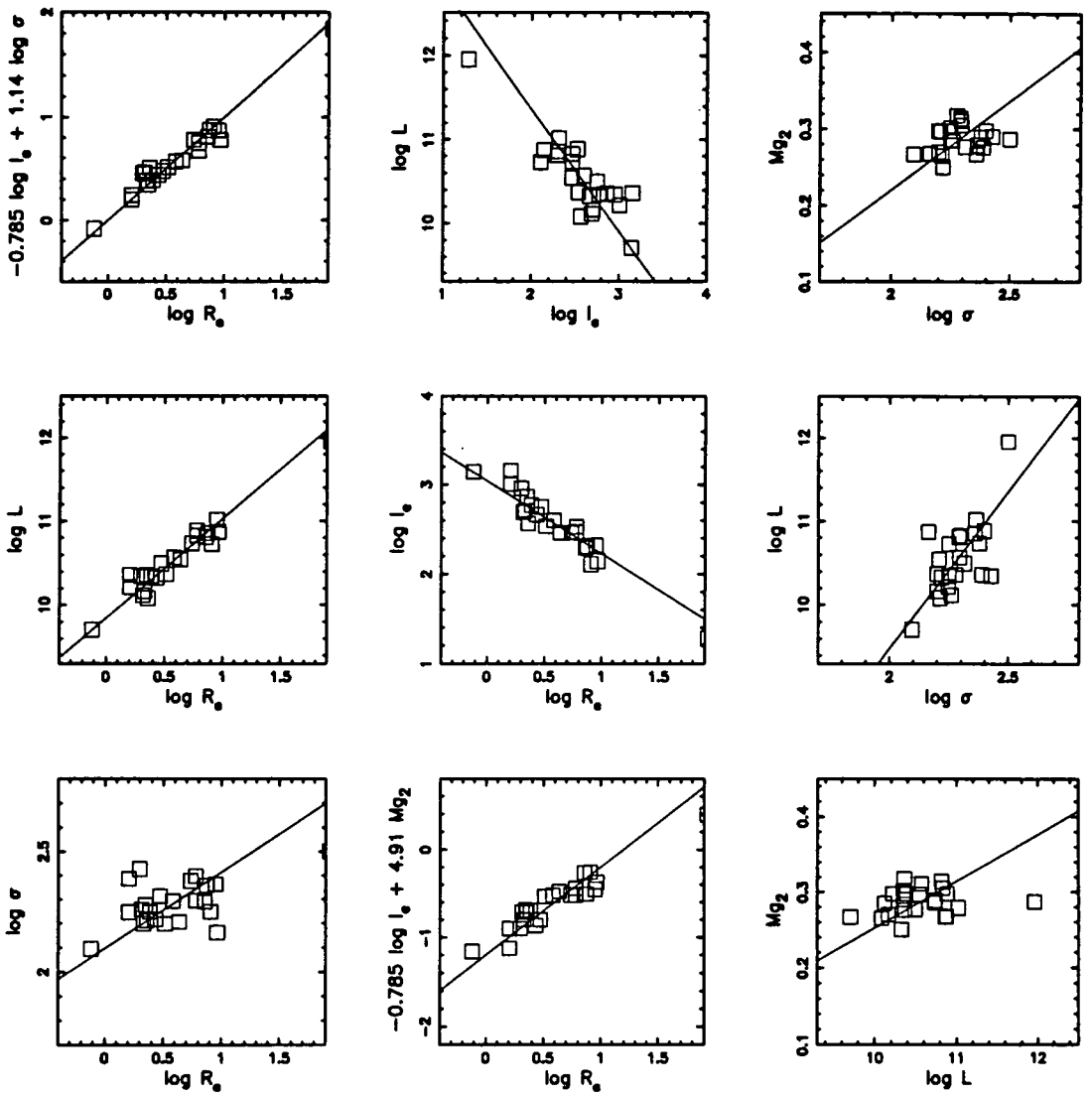

Figure 3.6. As in Figure 3.5 for our sample of A2199 cluster ellipticals. Solid lines represent the correlations listed in Table 3.1.

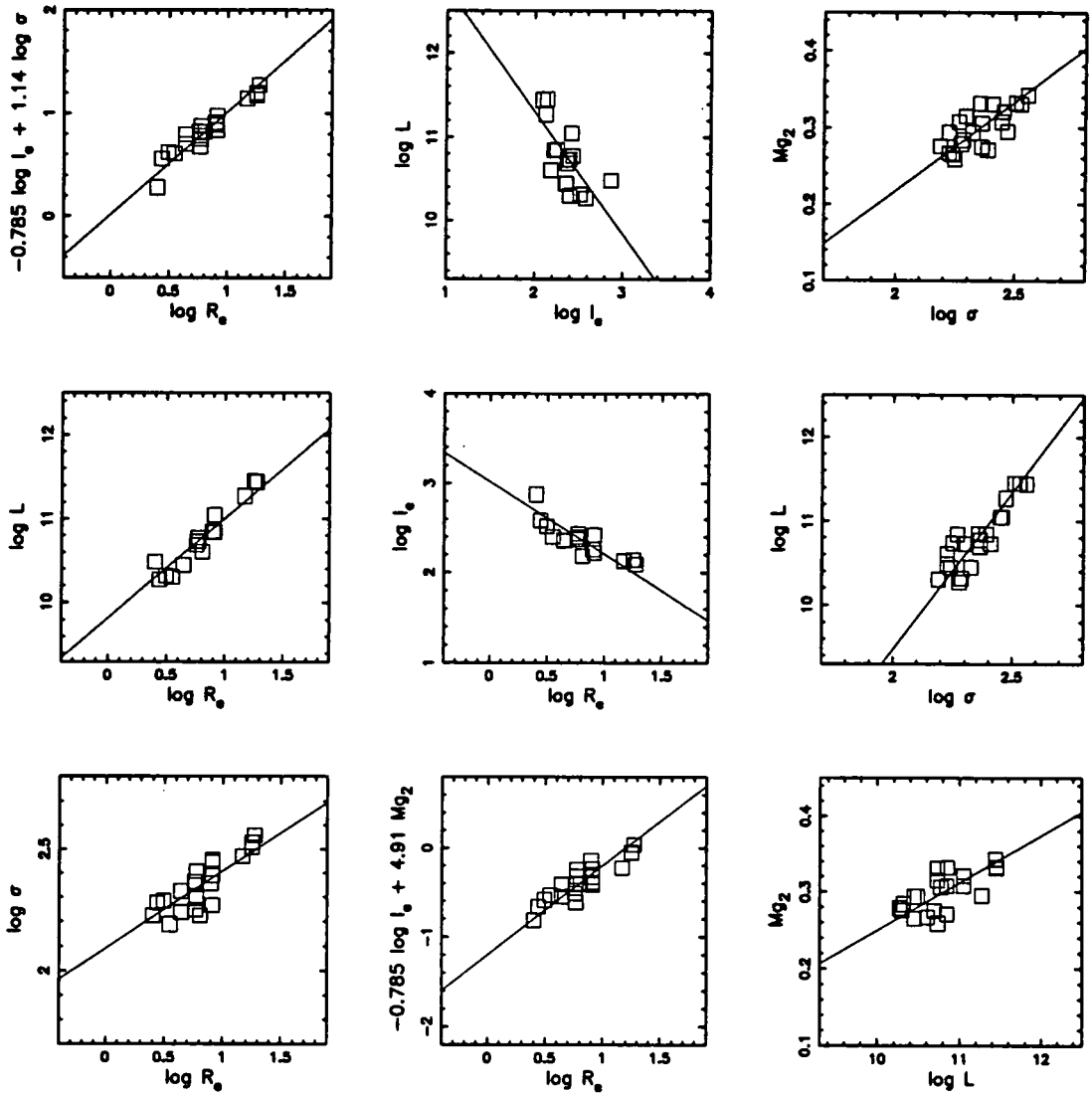

Figure 3.7. As in Figure 3.5 for our sample of A2634 cluster ellipticals. Solid lines represent the correlations listed in Table 3.1.

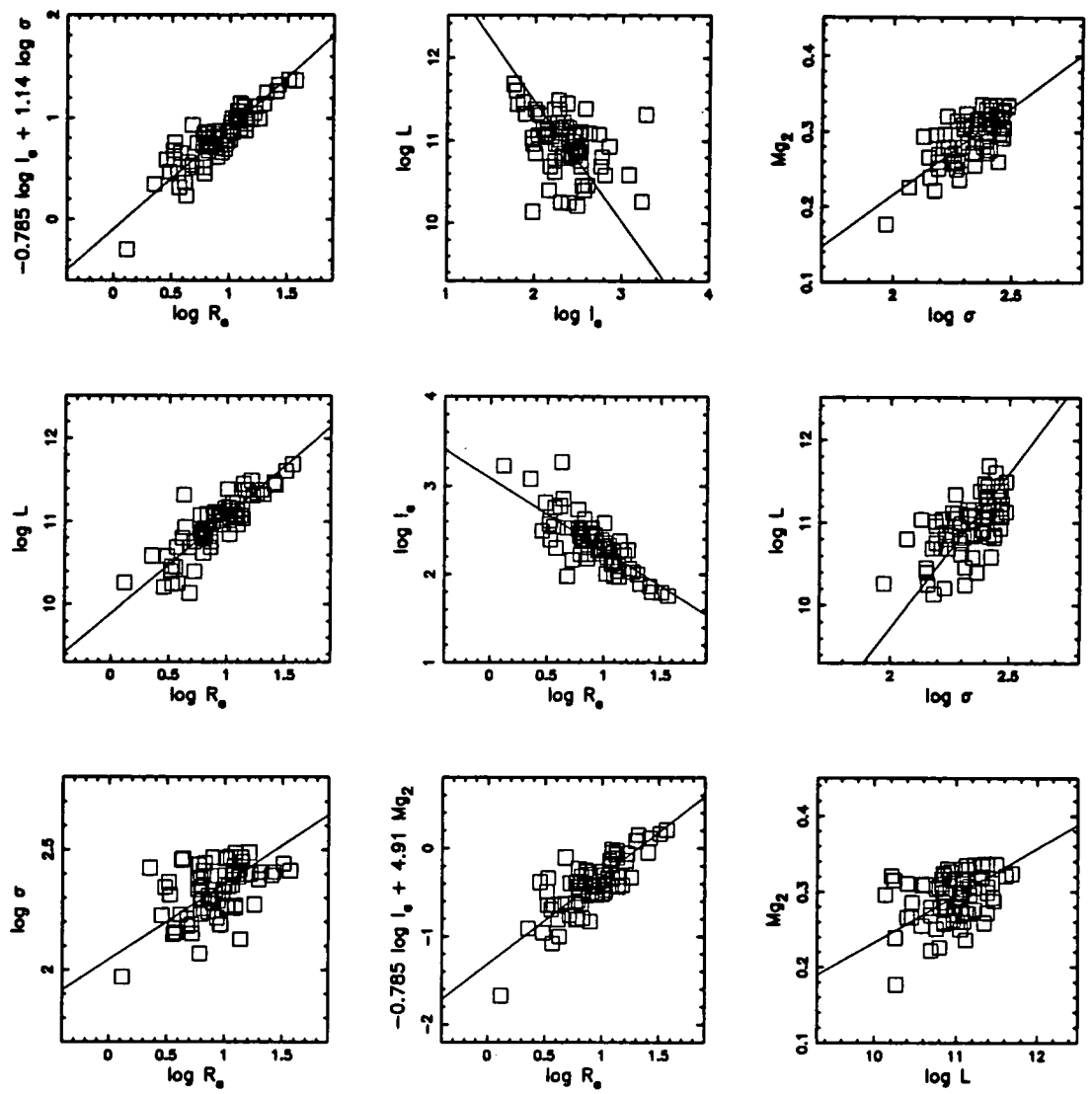

Figure 3.8. As in Figure 3.5 for our sample of field giant ellipticals. Solid lines represent the correlations listed in Table 3.1, zero-pointed to the mean values of this data set.

Larson, Tinsley & Caldwell 1980). The different global correlations for our field sample are shown in Figure 3.8. Superimposed on the new data set we have plotted the same fits derived for our Coma sample zero-pointed to the mean k_1, k_2 and k_3 values for this data set. Again, despite the significantly larger scatter, our fits provide an accurate description of the observed trends in all plots. Although this data set may be affected by larger measurement errors and uncertainties in the distance estimates to field ellipticals, at least part of this extra scatter is associated to intrinsic differences between the stellar populations of ellipticals located in high- and low-density environments (see de Carvalho & Djorgovski 1992b). A detailed discussion on this environmental effect is presented in Chapter 4.

Although the fits shown in Table 3.1 correspond to the particular case discussed above, there are, in fact, a whole host of other valid $\{\zeta, \xi, \eta, \lambda\}$ combinations. If the assumption that $\lambda = 0$ is relaxed we can choose, for example, the following combination from the solutions shown in Figure 3.4:

$$\zeta \sim 3, \quad \xi \sim 1/10, \quad \eta \sim -1/5 \quad \text{and} \quad \lambda \sim -2/3.$$

This value of ζ defines a different mass-radius relation for giant ellipticals. However, when this solution is substituted into equations (i)–(ix) almost identical coefficients to those shown in Table 3.1 are immediately obtained. This case will be discussed further in Section 3.5.

Therefore we have demonstrated that the slopes and zero-points of all global correlations observed for giant ellipticals can be fitted simultaneously in a consistent manner, assuming these correlations are simply linear combinations of only three fundamental relations. This set of basic laws is not, however, unique. The precise functional form, i.e. the $\{\zeta, \eta, \lambda\}$ values, will depend on the intrinsic mass distribution in elliptical galaxies.

3.4 GENERALISATION: THE FUNDAMENTAL RELATIONS OF SPHEROIDAL SYSTEMS

The conventional morphological classification divides the spheroidal systems into giant ellipticals, compact ellipticals, dwarf ellipticals, dwarf spheroidals and bulges. However, according to their structural properties, these objects can be grouped in two different galaxy families. Giants, bulges and compacts define a major single sequence in which the effective surface brightness decreases with both luminosity and effective radius, while dwarf ellipticals and dwarf spheroidals show the opposite behaviour (cf. Kormendy 1977, Wirth & Gallagher 1984, Binggeli, Sandage & Tarenghi 1984, Kormendy 1985). Hereafter we refer to these two families simply as "giants" and "dwarfs". The structural and stellar population properties of a relatively homogeneous sample in which all types of spheroidal systems are well represented, have been recently studied by Bender, Burstein & Faber (1992, 1993) (hereafter BBF). Their analysis is based on the distribution adopted by each galaxy type in a new, physically motivated, coordinate system which they term the κ-space. They conclude that the giants sequence is, in fact, characterized by a declining role for gas versus stars with increasing mass. However, although mass loss may be a major factor, the cause driving the dwarfs sequence remains yet unknown. BBF's results are further discussed at the end of this section.

In Figure 3.9 we show the different global correlations for BBF's sample. Dwarfs (filled symbols) show an abrupt change of slope with respect to the characteristic trend for giants (open symbols) in all the correlations involving the effective parameters. However, despite these differences, it is important to stress that all types of spheroidal systems follow the same $L - \sigma$ relation (cf. Tonry 1981). In addition, Bender (1991a) has recently shown that the $Mg_2 - \sigma$ correlation is universal for all spheroidal systems. In order to understand the intrinsic differences and similarities between the two galaxy families we

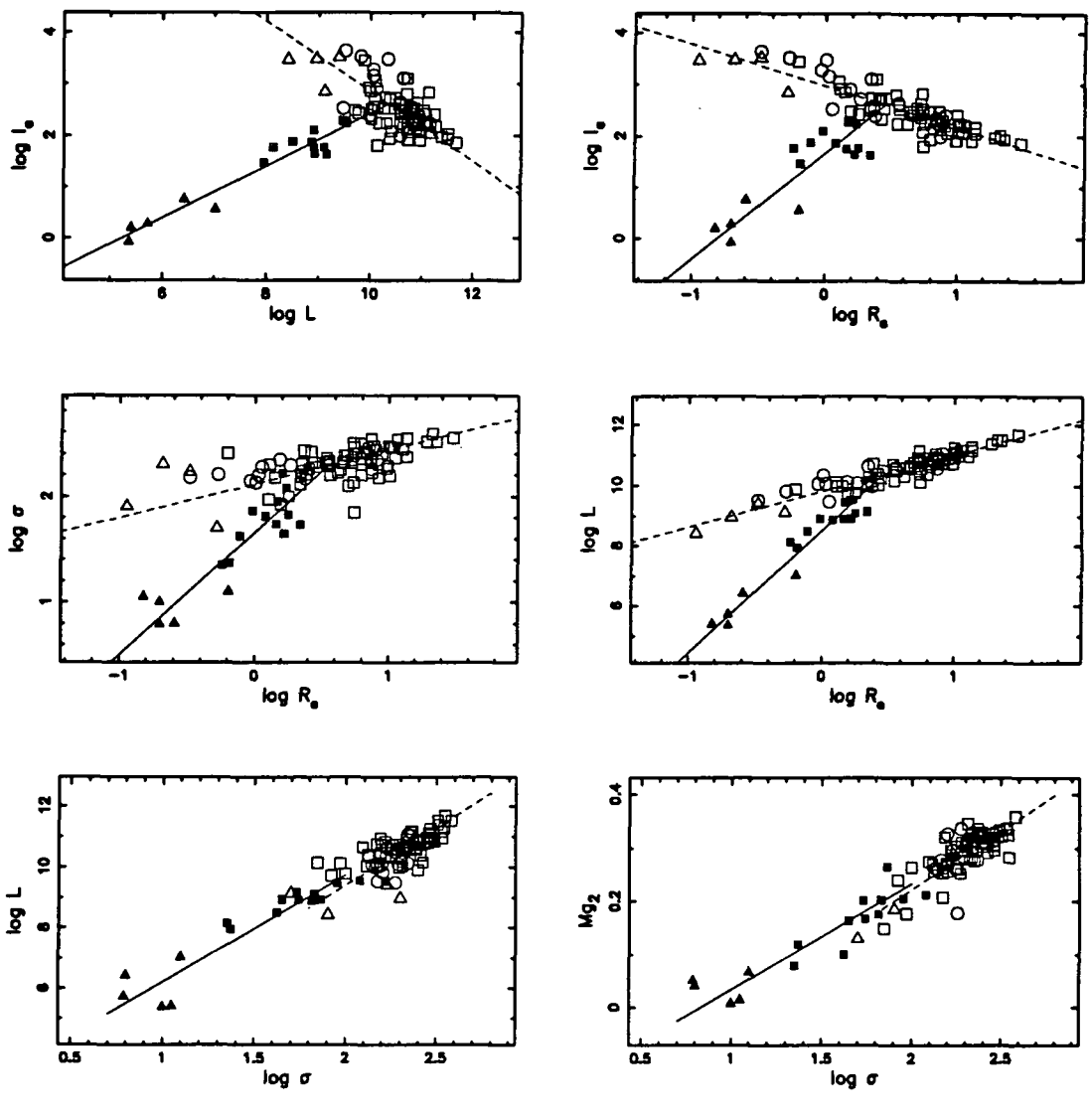

Figure 3.9. The monovariate global correlations for BBF's sample of spheroidal systems: giant ellipticals (open squares), compact ellipticals (open triangles), bulges of disk galaxies (open circles), dwarf ellipticals (filled squares) and dwarf spheroidals (filled triangles). Dashed lines and solid lines are the fits to the data points derived in our framework for "giants" and "dwarfs", respectively.

have analysed BBF's sample using the same framework adopted for Coma ellipticals, i.e. under the assumptions specified in Figure 3.3 we express the global correlations in terms of four constants (ζ, ξ, η and λ) which are determined from BBF's data set.

For luminous ellipticals, bulges and compacts, the observed similarity in the global correlations suggests that the same relations we presented in the previous section may also be representative of both compacts and bulges. The dashed lines superimposed on this sample of giants in Figure 3.9 are, in fact, the same correlations listed in Table 3.1 zero-pointed to the mean values derived for this data set. Clearly, our framework provides an excellent fit to the data for each correlation. Hence, we conclude that the same fundamental relations that describe the correlations observed for giant ellipticals are equally valid to characterize the structure and metal abundance of both compact ellipticals and bulges of disk galaxies.

Dwarf ellipticals and dwarf spheroidals, however, show significant differences compared to giants in most global correlations. We have thus studied which fundamental relations are required in our framework to derive these different correlations for BBF's dwarfs sample. This data set consists of L, R_e, I_e, σ and Mg_2 measurements for 17 objects. Following the same procedure to that used for giants we have obtained the set of ζ, ξ, η and λ values consistent with all the global correlations for this sample (Figure 3.10). The projections in the $\{\eta, \zeta\}$ and $\{\eta, \xi\}$ planes are consistent with those shown in Figure 3.4 (dashed lines) since the allowed area is mainly determined by the slopes of the $L - \sigma$ and $Mg_2 - \sigma$ correlations (see Section 3.3), which are universal for both giants and dwarfs. The smaller variation in ξ observed for dwarfs simply reflects a better determination of the $Mg_2 - \sigma$ slope for this sample. The projections of the parameter space involving λ *do* show, however, significant changes between both galaxy families.

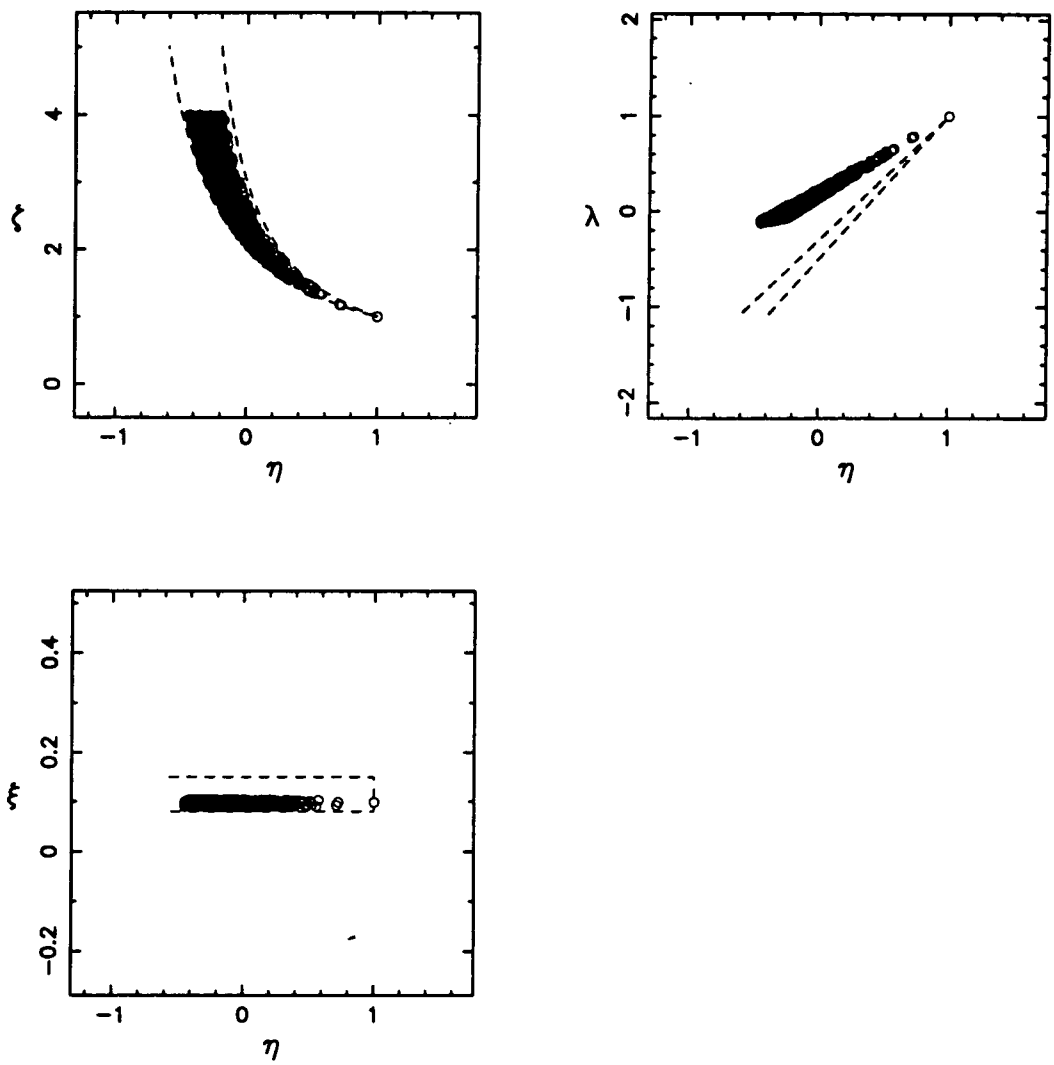

Figure 3.10. Projections of the 4D hyper-volume defined by one thousand $\{\zeta, \eta, \xi, \lambda\}$ combinations consistent with the observed correlations for dwarf ellipticals onto the $\{\eta, \zeta\}$, $\{\eta, \lambda\}$ and $\{\eta, \xi\}$ coordinate planes. Dashed lines represent the approximate areas defined by giant ellipticals (see Figure 3.4).

As in Section 3.3, we discuss first the solution corresponding to the assumption of constant collapse factor. If $\lambda = 0$ then:

$$\zeta = 3.298 \quad \xi = 0.097 \quad \text{and} \quad \eta = -0.231,$$

where, as before, these values are the mean of the distribution of valid solutions. The standard deviations of each distribution are 0.164, 0.006 and 0.047 respectively. Substituting these values into equations (i)–(ix) shown in Figure 3.3 we obtain our fits to BBF's dwarfs data set. These fits are shown in Figure 3.9 (solid lines) superimposed on BBF's sample of dwarfs. As before, the adopted zero-points are simply the mean zero-points derived from the data for each correlation. In all cases the fits provide an excellent representation of the observed distribution of data points.

Thus, for the constant collapse factor case (i.e. $\lambda = 0$), the fundamental relations of giants and dwarfs ellipticals can be summarized as follows:

Dwarfs	Giants
$M \propto R_e \langle v^2 \rangle$	$M \propto R_e \langle v^2 \rangle$
$M \propto R_e^{3.3}$	$M \propto R_e^{1.6}$
$Z \propto \langle v^2 \rangle^{0.1}$	$Z \propto \langle v^2 \rangle^{0.1}$

Hence, *if* mass and light are similarly distributed in all spheroidal systems then dwarf and giant galaxies have intrinsically different relations between mass and scale length. Also, since consistency with observations yields $M/L \propto M^{-0.23}$ for dwarfs and $M/L \propto M^{0.27}$ for giants, they would show completely opposite variations of the mass-to-light ratio with galaxy mass. However, the universality of the $L - \sigma$ relation implies a strange conspiracy between the coefficients of both relations (i.e. ζ and η) to keep this slope, defined in our framework as $\frac{2\zeta(1-\eta)}{\zeta-1}$, constant. The constant collapse factor case requires thus a non-trivial relation between the structure and the stellar population of elliptical galaxies that seems difficult to understand.

The observed universality of the $Mg_2-\sigma$ correlation suggests, however, a different, more simple interpretation. The existence of this relation implies a less complete conversion of the protogalactic gas into stars in less massive systems. Hence, the same physical process driving this relation will also cause a variation in M/L with galaxy mass. The observed constancy in the $Mg_2-\sigma$ slope, i.e. $\xi_{dwarfs} \sim \xi_{giants}$, then suggests $\eta_{dwarfs} \sim \eta_{giants}$. In this case, the universality of the $L-\sigma$ relation would simply reflect a common mass-radius relation for dwarf and giant ellipticals, i.e. $\zeta_{dwarfs} \sim \zeta_{giants}$. As pointed out in Section 3.3, our fitting procedure ensures that any set of $\{\zeta, \eta, \xi, \lambda\}$ values represented in Figure 3.10 can equally describe the observed distribution of points in Figure 3.9. In particular, we note that it is possible to find solutions with *precisely the same* $\{\zeta, \eta, \xi\}$ values for all spheroidal systems *if* λ takes different values for dwarfs and giants. The universality of both the $L-\sigma$ and $Mg_2-\sigma$ correlations can be thus interpreted in our framework to imply that the only difference between the two galaxy families is simply the dependence of the effective collapse factor on galaxy mass. This new interpretation is fully discussed in the following section.

Obviously, our framework should be able to describe any other representation of the structure and stellar content properties of spheroidal systems. In particular, BBF have proposed a new coordinate system to study the structural characteristics of spheroidal systems, i.e. the κ-space. Figure 3.11 shows BBF's parameterization of the edge-on and face-on views of the FP (i.e. the κ_1–κ_3 and κ_1–κ_2 planes) equivalent to Figures 2a and 2b of their paper. These three variables are defined in terms of the observed parameters as follows:

$$\kappa_1 = \log(R_e\ \sigma^2)/\sqrt{2}$$

$$\kappa_2 = \log(R_e^{-1}\ I_e^2\ \sigma^2)/\sqrt{6}$$

$$\kappa_3 = \log(R_e^{-1}\ I_e^{-1}\ \sigma^2)/\sqrt{3}$$

Our fundamental relations (I) and (II) then imply that these variables will be related by:

$$\kappa_3 = \sqrt{\frac{2}{3}}\,\frac{\eta-\lambda}{1-\lambda}\kappa_1$$
$$\kappa_2 = \sqrt{\frac{2}{6}}\,\frac{3(\zeta-2)-\zeta(2\eta-5\lambda)}{\zeta(1-\lambda)}\kappa_1$$

Substituting the values of ζ, η and λ as specified above we obtain the fits to the observed distributions of giant and dwarf galaxies in Figure 3.11. As expected, the resulting fits can successfully describe the position of data points in both the κ_1–κ_3 and κ_1–κ_2 planes.

Therefore we have shown that only three fundamental relations are required to describe *all* the global correlations of *all* spheroidal systems. The value of ζ that characterises the mass-radius relation depends on the assumed transformation between R and R_e for dwarf and giant ellipticals. Thus our framework cannot provide an unique expression of these fundamental relations purely from the observations. However, it naturally suggests a simple solution in which the only difference between dwarf and giant ellipticals is the scaling law for the effective collapse factor.

Despite the good description that our framework provides of the correlations observed for this sample, our conclusions on the properties of dwarfs are not, however, as robust as the results we derived for giants. As BBF point out, this dwarfs sample may be affected by selection effects. Although the derived correlations between photometric parameters show a reasonable good agreement with those found in the literature for larger samples (cf. Binggeli and Cameron 1991), no definite results can be drawn until larger data sets (especially velocity dispersion and Mg_2 measurements) of magnitude-limited samples of dwarf galaxies are obtained.

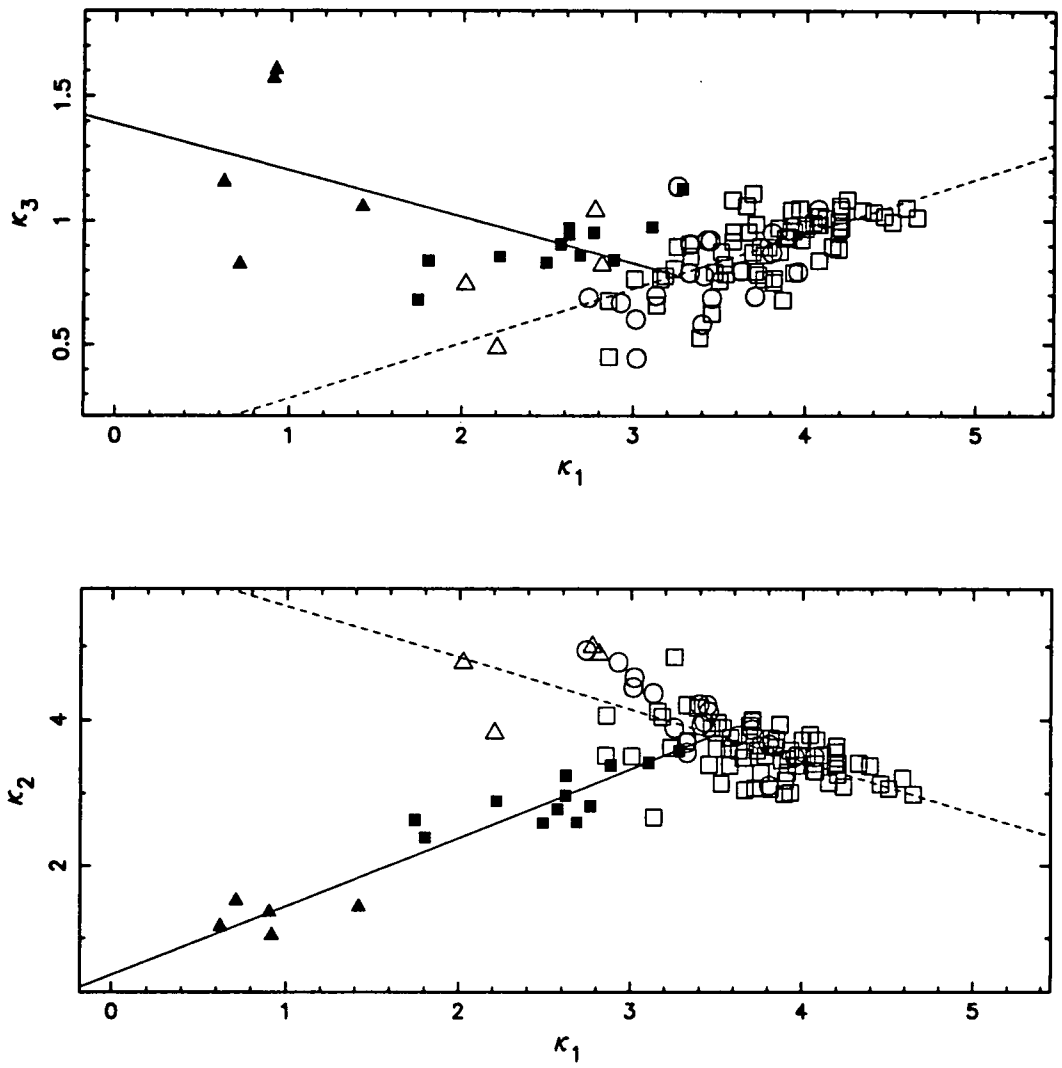

Figure 3.11. The $\kappa_1 - \kappa_3$ and $\kappa_1 - \kappa_2$ planes for BBF's data set. Symbols have the same meaning as in Figure 3.9. The dashed lines and solid lines represent the trends implied by our framework for giants and dwarfs, respectively.

3.5 IMPLICATIONS FOR GALAXY FORMATION

The observational framework presented in the previous sections is based on three fundamental relations for ellipticals. Two determine the galaxy structure, i.e. the virial theorem and the mass-radius relation. The third links the metal abundance of the stellar population to the galaxy potential well. A coherent theory of galaxy formation must be able to explain these three relations in a consistent manner. The theoretical picture we discuss here combines the hierarchical clustering scenario with the galactic wind model, following Dekel & Silk (1986) analysis on the origin of dwarf galaxies. This picture of galaxy formation may provide a simple, consistent explanation to the fundamental relations we have presented in our framework.

3.5.1 On the formation of giant elliptical galaxies.

Previous studies on the scaling laws for galaxies have used the observed correlations to probe their formation within the hierarchical clustering scenario (Faber 1982; Djorgovski 1992). This is based on dissipationless gravitational clustering of dark halos, coupled with dissipational settling of gaseous matter within the halo cores (White & Rees 1978). These halos form in a hierarchical fashion. At each epoch, there is a certain scale of density fluctuations where the rms fluctuation amplitude is just entering the non-linear regime of growth. This scale therefore provides a characteristic mass (M_H) that is just beginning to collapse at each epoch. If the spectrum of the density fluctuations is assumed to be a simple power law with spectral index n then this scale is related to the redshift at formation (Peebles, 1980):

$$M_H \propto (1+z)^{\frac{-6}{n+3}} \tag{3.7}$$

Each epoch has an associated characteristic density:

$$\rho \propto (1+z)^3 \tag{3.8}$$

Since the final virialised density of the halos forming at this epoch is some constant multiple of the background density,

$$\frac{M_H}{R_H^3} \propto \rho \tag{3.9}$$

then there is a characteristic relation between the masses of the objects formed and their radii:

$$M_H \propto R_H^{\frac{6}{n+3}} \tag{3.10}$$

For the standard CDM model, the effective value of the spectral index in the relevant mass range of giant ellipticals is $n = -2$ (Blumenthal *et al.* 1984). Thus the characteristic relation predicted between mass and radius is:

$$M_H \propto R_H^2 \tag{3.11}$$

This relation, together with the virial theorem,

$$\frac{M_H}{R_H} \propto \langle v^2 \rangle_H \tag{3.12}$$

constitute the two basic laws that determine the structure of massive dark halos independently of galaxy type.

In this scenario, the structural properties of visible galaxies are simply presumed to relate directly to the dark halos in which they are embedded. This is, however, a non-trivial assertion. The main assumptions required to contrast the theoretical predictions with the observed relations are briefly summarized below (see Faber 1982 for a detailed description). Initially, all protogalaxies are considered to have the same baryonic-to-dark matter ratio. The baryonic component will be, however, more densely concentrated than the dark matter halo due to dissipative processes. In spheroidal systems, dissipation ends when the baryonic matter turns from gas into stars thus preventing further collapse. After the onset of star formation, the galaxy luminosity will be simply proportional to the mass in stars (M_S). Strictly, this is only valid if the typical age and stellar initial mass function

are roughly the same for all galaxies; this is generally accepted to be the case for ellipticals. Under these assumptions, the structure of elliptical galaxies can be directly linked to the predicted properties of their dark halos in terms of two quantities: the collapse factor (R_H/R_e) and the dark matter-to-light ratio (M_H/L). These free parameters in the model simply reflect the lack of any *a priori* ideas on the amount of dissipation and gas loss that took place during the early formative processes of the galaxy.

The conventional approach is to assume that the collapse factor is constant, i.e. $R_e \propto R_H$. This is based on the idea that the mean gas density at the onset of star formation is a constant fraction of the halo density (Mathews 1972): an assertion which can be justified by consideration of the instability and fragmentation of the gas cloud during its collapse. Since star formation is presumed to halt the collapse of baryonic matter, the half-light radius is then directly proportional to the characteristic radius of the surrounding halo. Within this radius, the luminous matter in giant ellipticals is presumed to be self-gravitating. Under these assumptions, Faber (1982) showed that the halo variables can be directly related to the global parameters of visible galaxies (i.e. the half-light radius R_e, the mean square stellar velocity $\langle v^2 \rangle$ and the virial mass M within R_e). Thus the two structural scaling laws for giant ellipticals arise in a natural way in this scenario. Indeed, the results of this approach are entirely equivalent to the constant collapse factor case discussed in Section 3.3. In our framework, the structural relations for this case are:

$$M \propto R_e \langle v^2 \rangle \tag{3.13}$$

$$M \propto R_e^{1.6} \tag{3.14}$$

While these relations are in rough agreement with the theoretical predictions a more detailed analysis reveals that the conventional approach does not provide an adequate description. In particular, there are two relevant problems.

First, it is important to note that, since the luminous matter is assumed to be self-gravitating, the dark halo properties do not enter into the virial relation; their effect is only to *indirectly* define the parameter R_e in the mass-radius relation (through Mathew's gas-cloud instability criterion). However, whereas CDM predicts a slope $\zeta = 2$ for this relation we find in our framework $\zeta = 1.6$. These two values are inconsistent at the level of over 5 standard deviations (see Section 3.3). There are a number of effects that might account for small changes in this slope. In particular, the assumption that the luminous part of the galaxies is self-gravitating may not be entirely correct. We will return to this point later.

Secondly, Faber *et al.* (1987) showed that consistency with the observed fundamental plane of elliptical galaxies would imply a small but significant increase of M/L with galaxy mass within the effective radius. For the constant collapse factor case our framework yields $M/L \propto M^{0.27}$. A possible explanation is that the stellar content varies with galaxy mass (i.e. M_S/L is not constant). This variation is not likely to be explained in terms of age differences since it requires the stellar populations of less massive ellipticals to be younger, while according to the hierarchical clustering scenario these systems formed earlier. The required change in M_S/L thus suggests a variation of the IMF with galaxy mass. This explanation would lead us to a highly speculative area which is beyond the scope of this paper. A second possibility is to consider that more massive halos are less efficient in forming stars. But if this is the case, why is the metal abundance higher in these systems? So far in this analysis we have not made use of the third fundamental relation established in our framework. Specifically, the high metallicity characteristic of more massive ellipticals (strictly deeper potential depth) implies that a greater fraction of the initial gas content has been converted into stars. The only *a priori* assumption we have made about the initial baryon-to-dark matter ratio is that it is similar in all systems. Therefore, if M_S/L is constant, we conclude that M/L must be a *decreasing* function of

galaxy mass. This is, however, the contrary to the observed scaling law derived above. Note that the effect of metallicity on the integrated light of the galaxy also cannot totally explain the observed trend in M/L. As noted by Dressler *et al.* (1987) the increasing bolometric correction with galaxy mass would account for a slope of only ~ 0.07 in the above scaling law for M/L in the B-band. Furthermore, Djorgovski & Santiago (1992) have shown that although this slope varies slightly with the effective bandpass wavelength, it is always significantly different from zero.

In conclusion, we find that the conventional approach (i.e. $R_H/R_e \sim$ constant) cannot provide a simple explanation of the structural relations of giant ellipticals. Also, the required variation in M/L directly contradicts the observed metallicity-velocity dispersion relation.

3.5.2 Towards a global picture of galaxy formation?

The standard model discussed above requires two free parameters (i.e. R_H/R_e and M_H/L) to describe the structure of visible galaxies. Since there are only two observational structural constraints (i.e. correlations (i) and (ii) of Figure 3.3), this theoretical picture lacks, as it stands, any real predictive power. The good correlation between metal abundance and velocity dispersion (correlation (iii) of Figure 3.3) adds a new, important constraint.

The most widely accepted explanation of this correlation is based on the galactic wind model (Larson 1974). After the onset of star formation, both the frequency of supernovae explosions and gas metal enrichment in spheroidal systems increase very rapidly. When the thermal energy of the gas heated up by SN explosions exceeds the galaxy binding energy, the gas will be driven out of the system and the formation of new stars is halted thereafter. Because of the decreasing binding energy of the gas, a wind occurs much earlier

in less massive systems, i.e. the time at which this galactic wind blows is an increasing function of the initial mass of gas M_G. As a consequence, *both* the average metallicity *and* the M_S/M_G fraction also increase with M_G. Under the assumptions that both the initial baryon-to-dark matter ratio and the stellar mass-to-light ratio are constant (i.e. $M_G \propto M_H$ and $M_S \propto L$), the variation of M_H/L can be thus determined consistently with the metallicity-velocity dispersion relation by incorporating the galactic wind model to the hierarchical clustering scenario discussed above. Hence there is no need of any *a priori* ideas on the collapse factor and the assumption $R_H/R_e \sim$ constant of the conventional approach can be relaxed. The scaling law for the collapse factor remains thus as the only unknown to be determined from the observations.

In order to estimate the dependence of the mass-to-light ratio on galaxy mass we have used Arimoto & Yoshii's (1987) galactic wind model. Assuming a star formation rate per unit mass proportional to the fractional gas mass and a universal IMF, this model has successfully reproduced the chemical and photometric properties of spheroidal systems, i.e. the colour–magnitude diagram. Due to the uncertainties associated to the transformation between the $[Fe/H]$ metallicity indicator that Arimoto & Yoshii modelled and the Mg_2 index used in this paper (see Worthey, Faber & González 1993), our analysis is not based on a direct comparison with the metallicity-velocity dispersion relation of our framework. Note, however, that the mass-metallicity relationship derived in their model is in rough agreement with the empirical relation given by Mould (1984) and the different colour-magnitude diagrams observed by Persson *et al.* (1979). From Table 2 of Arimoto & Yoshii's paper we derive the following average relation:

$$M_G/M_S \propto M_G^{-\frac{1}{3}} \tag{3.15}$$

Arimoto & Yoshii's model is only concerned with gas protoclouds. In the picture of galaxy formation we are discussing here the star-forming gas cloud is considered to be embedded

in a dark halo. Since $M_G \propto M_H$ and $M_S \propto L$, we obtain:

$$M_H/L \propto M_H^{-\frac{1}{5}} \tag{3.16}$$

This scaling-law provides thus the predicted variation of M_H/L when galactic winds are considered to be the physical process driving the observed metallicity-velocity dispersion relation. It is important to stress at this point that the metallicity-velocity dispersion relation is *universal*. This suggests that the process of gas loss should be equally efficient in the whole range of galaxy masses from dwarfs to giants. The above scaling law thus applies to *all* elliptical galaxies.

The formation of dwarf galaxies as a result of galactic winds has been discussed by Dekel & Silk (1986). They find that the observed $L-R_e$, $L-\sigma$ and $L-Z$ relations for dwarfs can be produced inside dominant halos with a mass-radius relation that resembles the predictions of the CDM standard model. The observational evidence for dark matter in dwarfs is compelling (see Ashman 1992 and references therein). Therefore, we have used a similar theoretical picture to study the properties of dwarf ellipticals in contrast with our observational framework. If we assume that the dark halo dominates the gravitational potential then the halo properties are directly related to the global parameters of visible galaxies, i.e. $M_H \sim M$, $R_H \sim R$ and $\langle v^2 \rangle_H \sim \langle v^2 \rangle$. In this case, the above condition on the galaxy mass-to-light ratio is, in fact, equivalent to considering $\eta \sim -1/5$ in our framework. Figure 3.10 shows that this value constrains ζ and λ to be $2.5 \leq \zeta \leq 4.0$ and $-0.1 \leq \lambda \leq 0.1$, respectively. We recall here the results obtained in our discussion of the constant collapse factor case for dwarf ellipticals. For $\lambda = 0$ we found that $\zeta = 3.298$ $(1\sigma = 0.164)$ and $\eta = -0.231$ $(1\sigma = 0.047)$. This value of η is remarkably similar to the theoretical prediction. Thus our framework suggests that a plausible solution consistent with the galactic wind model is simply $\zeta \sim 3$, $\eta \sim -1/5$ and $\lambda \sim 0$. For this case, the two structural relations for dwarf ellipticals are:

$$M \propto R_e \, \langle v^2 \rangle \tag{3.17}$$

$$M \propto R_e^3 \tag{3.18}$$

This mass-radius relation is in good agreement with the theoretical relation predicted by CDM in the relevant mass range of dwarf ellipticals (Dekel & Silk 1986). Hence, the observations naturally allow a solution for the ζ and η values consistent with both the CDM hierarchical clustering and the galactic wind models. More interestingly, the implied constancy in the collapse factor (i.e. $R_e \sim R_H$) agrees very well with Mathews' (1972) original idea that passage over a critical threshold induces star formation in spheroidal systems and thus halts the collapse of the baryonic matter. Therefore, our framework clearly suggests that dwarf ellipticals may have simply formed as a direct result of the initial density fluctuations in a CDM universe, in agreement with Dekel & Silk's result.

In Section 3.4 we noted that the universality of the $Mg_2 - \sigma$ and $L - \sigma$ correlations naturally suggests a solution within our framework in which both, dwarfs and giants, differ only in the scaling law for the collapse factor. This solution indirectly assumed that the luminous matter in all spheroidal systems is not self-gravitating. Contrary to the widely accepted evidence for dwarfs, the presence of dark matter in giant ellipticals is still controversial (see reviews by Faber 1982 and Ashman 1992). However, in Section 3.5.1 we showed that the assumption of self-gravitation (i.e. $R = R_e$) in giant ellipticals failed to provide a consistent agreement between the theoretical predictions and the observed fundamental relations in our framework. A possible way to solve this disagreement is to assume that giant ellipticals are also embedded in a dark halo that determines the galaxy gravitational potential. In this case, if λ is not *a priori* assumed to be equal for all ellipticals, then we can adopt the same scaling laws predicted by the hierarchical clustering and galactic wind models for dwarfs to describe the structure and stellar content of giant ellipticals (i.e. $\zeta \sim 3$ and $\eta \sim -1/5$). This value of ζ corresponds to a spectral index of the density fluctuations $n = -3$. This is not in complete agreement with the canonical value derived in the CDM standard model on this galaxy scale (i.e. $n = -2$). However,

such a flat spectrum remains a plausible alternative, specially if CDM is to be reconciled with the recent COBE observations showing that the CDM standard model does not have enough power on large scales (Efstathiou, Bond & White 1992). This discrepancy might be solved by simply shifting the CDM spectrum to slightly larger scales which would result in a more negative power spectrum on galaxy scales.

The values of ζ and η for both dwarfs and giants are thus determined according to the theoretical predictions. From Figure 3.10 we then deduce that, unlike the result found for dwarfs, $\lambda \sim -2/3$ for giant ellipticals, i.e. the collapse factor must decrease with galaxy mass. Hence *in more massive systems the luminous matter is apparently less concentrated relative to the dark matter than in less massive systems.* This is the same effect shown by Navarro (1992) in his simulations of dissipative galaxy formation in a CDM universe. As he suggests, a possible interpretation for the origin of this effect is that more massive systems have, on average, undergone more numerous mergers *after* the bulk of their stars were formed. These mergers would tend to mix stars and dark matter more thoroughly in larger systems, resulting in the stars being less concentrated respect to the dark matter in more luminous ellipticals. This may prove a plausible interpretation given the growing evidence of merger signatures in giant ellipticals, e.g. shells and distorted isophotes (Schweizer *et al.* 1990) and kinematically decoupled cores (Bender 1991b). The idea that the final mergers leading to larger galaxies in this family were more stellar (and less gaseous) is also consistent with the observed trends of other properties with galaxy mass, including bulge-to-disk ratio, radio properties, rotation, degree of velocity anisotropy and peculiar kinematics (BBF). Indeed, from the analysis of the structural properties alone, BBF reach a conclusion similar to the result we find here, i.e. CDM predictions can be made to fit the data for giants only if dissipation decreases significantly with galaxy mass. In our study, however, the required variation in the collapse factor is

derived in the context of a global, common picture of galaxy formation consistent with both the structure and stellar population properties of all spheroidal systems.

In conclusion, *if* both dwarfs and giants are dark matter-dominated the following relations:

$$M \propto R \langle v^2 \rangle \tag{3.19}$$

$$M \propto R^3 \tag{3.20}$$

$$Z \propto \langle v^2 \rangle^{\frac{1}{10}} \tag{3.21}$$

$$M/L \propto M^{-\frac{1}{3}} \tag{3.22}$$

constitute a set of scaling laws common to *all* spheroidal systems. These relations are in good agreement with a theoretical picture of galaxy formation based on hierarchical clustering in a CDM universe and the galactic wind model. Our framework then implies that *the only difference between dwarfs and giants is the scaling law for the collapse factor.* For dwarfs: $R/R_e \sim$ constant, whereas for giants: $R/R_e \propto M^{-\frac{2}{3}}$. These relations suggest different formative processes for each galaxy family. The derived constancy of the collapse factor for dwarfs is in excellent agreement with Mathews' gas cloud instability criterion. This result suggests that dwarf ellipticals originated directly from the initial density fluctuations. Thus, part of the scatter observed around the global correlations may be caused by a spread in the formation epoch of these galaxies. However, a different process is needed to explain the required variation between the mass and light distributions within giants. Mergers appear as a plausible alternative. Although the simplicity of our framework makes this picture rather appealing we note that our results are far from conclusive. In particular, the question of how the mass-radius and metallicity-velocity dispersion relations can be preserved in the merging scenario may probably have no simple answer. Theoretical models that specifically address the influence of mergers on the observed properties of giants and larger, homogeneous data sets for dwarfs are needed

before we can be certain that these results provide real clues to a better understanding of the process of galaxy formation.

3.6 CONCLUSIONS

The main results presented in this Chapter can be summarized as follows:

(i) We have shown that the fundamental plane of giant elliptical galaxies is not uniformly populated. Giant ellipticals are located in a relatively narrow band which is not the result of selection effects. This implies a second constraint between scale length and galaxy mass in addition to the virial theorem. The observed $L - R_e$, $L - I_e$, $L - \sigma$ and $I_e - R_e$ correlations are simply the projections of this band onto the different coordinate planes.

(ii) We have developed a simple framework to describe the structure and stellar content properties of giant ellipticals based on the analysis of our Coma sample. In our framework there are only three fundamental relations: $M \propto R \langle v^2 \rangle$, $M \propto R^{\zeta}$ and $Z \propto \langle v^2 \rangle^{\xi}$. The coefficient ξ is uniquely determined from the observations. If Mg_2 is adopted as metallicity indicator then $\xi = 0.11$. The coefficient ζ depends, however, on the assumed variations of the mass-to-light ratio and the effective collapse factor with galaxy mass. We have assumed $M/L \propto M^{\eta}$ and $R/R_e \propto M^{\lambda}$. The conventional approach is to assume that the effective collapse factor is constant, i.e. $\lambda = 0$ (or, equivalently, giant ellipticals are baryon dominated). In this case we find that $\zeta = 1.6$ and $\eta = 0.27$. However, there is a whole host of other valid solutions for the $\{\zeta, \eta, \lambda\}$ values. All the observed correlations for giants are consistently derived as linear combinations of these fundamental relations.

(iii) We have demonstrated that this framework can also successfully describe the global correlations of dwarf elliptical galaxies. Our framework provides new insights into the differences and similarities between the two galaxy types. In particular, the observed universality of the luminosity- and metallicity-velocity dispersion correlations strongly suggests a simple solution within our framework in which ζ, ξ and η adopt the same values for both dwarf and giant ellipticals. In this case, the dependence of R/R_e on galaxy mass is the only difference between the two galaxy families.

(iv) We have discussed the results of our observational framework within a simple picture of galaxy formation based on the hierarchical clustering scenario and the galactic wind model. For giant ellipticals, we have shown that this theoretical picture is not consistent with the fundamental relations derived under the assumption of self-gravitation (i.e. $R = R_e$). Theory and observations can be reconciled in a simple way if both dwarf and giant ellipticals are assumed to be dark matter dominated. For dwarf ellipticals, this theoretical picture provides a consistent explanation of the observed fundamental properties provided that R/R_e is constant. This result suggests that these systems may have simply formed as a direct result of the initial density fluctuations in a CDM universe. However, for giant ellipticals we find that R/R_e must decrease with galaxy mass, i.e. the luminous matter in giant ellipticals is apparently less concentrated inside their dark halos with increasing mass. This effect suggests a different origin for giant ellipticals in which mergers may have played a determinant role.

4 ENVIRONMENTAL EFFECTS ON THE DISTANCE INDICATORS $D-\sigma$ AND $D-Mg_2$

4.1 INTRODUCTION

Elliptical galaxies reside in environments ranging from the dense cores of rich clusters to the general field. As shown in Chapter 3, the analysis of the global relations demonstrate that ellipticals in a wide range of present-day environments formed, to first order, in an uniform way according to rather simple scaling laws. However, since mergers –an environment-dependent process– are likely to be an important formative mechanism, it is also possible that the environment may induce slight differences in the galaxy properties. In rich clusters, merging today is inefficient due to the high velocity dispersions, but might be endemic during an early epoch of galaxy and cluster formation. In the merging scenario cluster ellipticals formed early, through dissipative infall and merging of many gas-rich fragments, while the field ellipticals can form at any time, possibly through a single merger of two progenitor galaxies. Cluster ellipticals would then be a coeval, relatively homogeneous population of objects, while the field ellipticals may be more heterogeneous in the mean ages of their stellar populations. This picture is in agreement with observations of relatively recent mergers which rejuvenated the stellar populations of some ellipticals located in low-density environments (Schweizer *et al.* 1990).

Indeed, the detailed analysis of the global correlations suggests that field ellipticals form a more heterogeneous family of objects, i.e. they show more intrinsic scatter in their

correlations than do the cluster ellipticals (Burstein 1977; Larson, Tinsley & Caldwell 1980; Burstein *et al.* 1988; de Carvalho & Djorgovski 1992b). These studies show that, at a fixed effective radius or luminosity, field ellipticals tend to be too blue, have too low a Mg_2 index or too high a surface brightness, compared to cluster ellipticals. Although distance errors might contribute to the larger scatter observed in the correlations for field galaxies, these results agree qualitatively with the general concept that star formation terminated at a more recent epoch in some field ellipticals.

The idea that the environment may induce slight variations in age of the stellar populations is also supported by spectral synthesis studies. While early work modelled elliptical galaxies as old, single-age, metal-rich stellar systems, recent studies have shown that a single population of unique age and metallicity is unable to reproduce adequately the observed spectral energy distributions and line strengths of all ellipticals (cf. O'Connell 1980; Pickles 1985; Rose 1985 and Bica 1988). These studies conclude that an intermediate age stellar population (IASP), whose age is $\sim$5 Gyr, must be present in some elliptical galaxies. Recently, Bower *et al.* (1990) have shown that the presence of an IASP in elliptical galaxies depends on environment in the sense that those galaxies located in the field possess, on average, a stronger IASP component.

The presence of this IASP component modifies the galaxy mass-to-light ratio (M/L) since the contribution of younger stars increases the galaxy luminosity. As noted by Faber *et al.* (1987), the major source of scatter around fundamental plane based distance indicators, such as the $D-\sigma$ and $D-Mg_2$ relations, is related to intrinsic differences in the M/L ratio. Although the effect of this IASP component on the integrated light appears to be small, the implied systematic variation in M/L due to the environment may result in a zero-point offset of these distance indicators and hence lead to spurious peculiar velocities (Kaiser 1988; Silk 1989; Djorgovski, de Carvalho & Han 1988).

One powerful and simple test of the environmental dependence of the $D - \sigma$ and $D - Mg_2$ relations is to compare the elliptical galaxies that reside in the core with those in the halo of an individual cluster. If an environmental effect exists there will be a systematic difference between the cluster distances derived from the core and halo samples. To perform this test we use the Coma sample presented in Section 2.2. This sample includes elliptical galaxies that reside in very different environments but are at roughly the same distance. In Section 4.2 we discuss the $D - \sigma$ and $D - Mg_2$ correlations for this sample and present evidence for a small environmental effect. For completeness we also discuss the environmental variation of the $\sigma - Mg_2$ correlation. In Section 4.3 we show that the observed offsets are all consistent with the hypothesis that the halo ellipticals have, on average, younger stellar populations. Using our framework of galaxy properties together with evolutionary spectral synthesis models, we then design in Section 4.4 a new relation for elliptical galaxies that is independent of small variations in age of the stellar population. Finally, in Section 4.5 we present a detailed discussion of the $D - \sigma$ versus $D - Mg_2$ residuals plot, i.e. the $\delta - \delta$ diagram.

4.2 THE $D - \sigma$, $D - Mg_2$ AND $\sigma - Mg_2$ RELATIONS FOR THE COMA SAMPLE

In Chapter 2 we showed that the photometric diameter D is related to the effective radius and surface brightness by:

$$\log D[\text{arcsec}] = \log R_e[\text{arcsec}] - 0.286\ SB_e[\text{mag arcsec}^{-2}] + \text{constant}. \qquad (4.1)$$

Hence, the standard form of the $D - \sigma$ relation:

$$-\log D[\text{arcsec}] + 1.2\ \log \sigma[\text{km s}^{-1}] = \text{constant}, \qquad (4.2)$$

is then an approximate expression of the equation of the fundamental plane:

$$-\log R_e[\text{arcsec}] + 0.314\ SB_e[\text{mag arcsec}^{-2}] + 1.14\ \log\sigma[\text{km s}^{-1}] = \text{constant}. \quad (4.3)$$

According to our framework, the $D - Mg_2$ relation is simply an alternative form of the $D - \sigma$ relation where σ has been replaced by Mg_2 using the $\sigma - Mg_2$ relation. Since:

$$Mg_2[\text{mag}] - 0.232\ \log\sigma[\text{km s}^{-1}] = \text{constant}, \quad (4.4)$$

the form of the $D - Mg_2$ relation we adopt here is derived as:

$$\{-\log D + 1.2\ \log\sigma\} + \frac{1.2}{0.232}\ \{Mg_2 - 0.232\ \log\sigma\} = \text{constant}. \quad (4.5)$$

i.e.:

$$-\log D[\text{arcsec}] + 5.2\ Mg_2[\text{mag}] = \text{constant}. \quad (4.6)$$

In practice, this is equivalent to considering that the velocity dispersion and metallicity are not independently related to luminosity (cf. Tonry & Davies 1981).

4.2.1 Dependence on the environment.

The $D - \sigma$, $D - Mg_2$ and $\sigma - Mg_2$ relations for our sample of 66 Coma ellipticals are shown in Figure 4.1. We use different symbols to denote core (filled squares) and halo (open squares) ellipticals. Following the discussion in Section 2.2.1, we have chosen a 1° cluster radius as the division between these two samples. A difference between the two samples is apparent in the sense that: a) halo ellipticals tend to have lower Mg_2 at a given value of D or σ while their D diameters are, in turn, slightly larger at a given σ; and b) core ellipticals present slightly tighter correlations. These effects are qualitatively similar to the variations that have been reported by previous studies when comparing ellipticals that reside in high and low-density environments (e.g. Larson, Tinsley & Caldwell 1980).

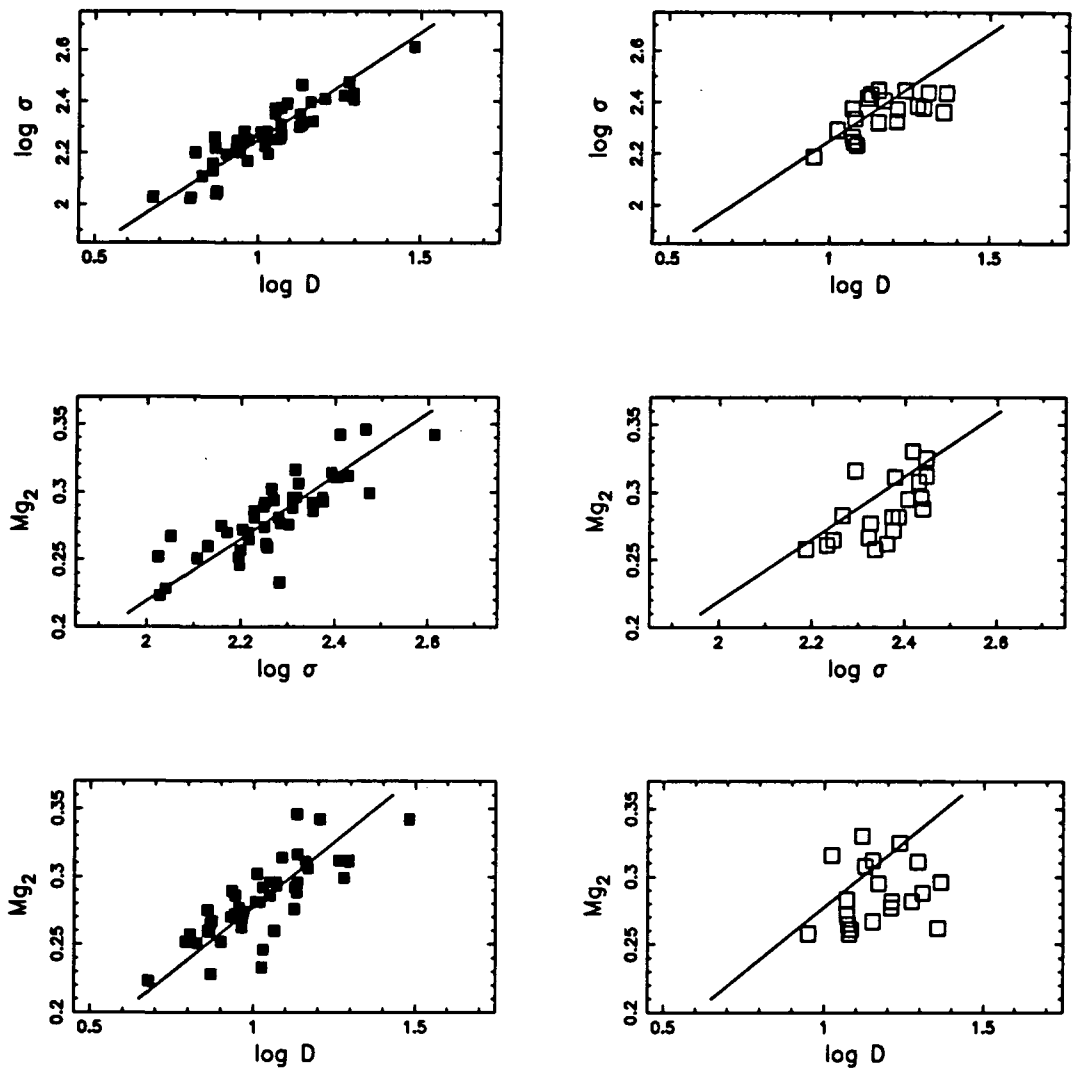

Figure 4.1. The $D-\sigma$, $\sigma-Mg_2$ and $D-Mg_2$ relations for our sample of 66 Coma ellipticals. Core galaxies ($R < 1°$) are represented by filled squares. Halo galaxies ($R > 1°$) are plotted as open squares. The linear fits to the core sample are also shown superimposed on both the core and halo ellipticals.

To quantify the observed environmental differences in our sample, we assume our adopted slopes are universal and determine the zero-points for the different samples. We have used Wilcoxon's Rank Sum Test to determine the relative offsets (see Dressler 1984). With this technique the derived offset is the median of all pair differences between the core and halo samples. The error estimate is derived directly from the distribution of the pair differences.

In Table 4.1 we list the derived $D-\sigma$, $D-Mg_2$ and $\sigma-Mg_2$ zero-points for the core and halo samples along with their median offsets. We find that, on average, the halo ellipticals have larger D diameters by 0.042 ± 0.023 dex at a fixed σ and 0.122 ± 0.035 dex at a fixed Mg_2 than those in the core. For the same sample division, the $\sigma-Mg_2$ relation is offset by 0.016 ± 0.005 mag in the sense that the halo ellipticals have, on average, lower Mg_2 for a given σ. The observed offsets for the Mg_2 correlations are both significant at the level of 3 standard deviations. Different slopes allowable within the errors of the fitting procedure all give qualitatively similar results.

Another approach to illustrate these results is shown in Figure 4.2 where we plot the $D-\sigma$, $D-Mg_2$ and $\sigma-Mg_2$ zero-points derived from each galaxy against the logarithm of the distance from the cluster centre. After removing the contribution of our measurement errors, we estimate that the intrinsic scatter around the $D-\sigma$ relation for our core and halo samples is 0.061 dex and 0.082 dex, respectively. For the $D-Mg_2$ relation the intrinsic scatter is 0.082 dex and 0.139 dex, respectively. The estimated uncertainty of these values amounts to $\sim$0.005 dex. Therefore, there is evidence of a significantly larger scatter in the $D-\sigma$ and $D-Mg_2$ relations for those ellipticals located in the cluster halo. For the $\sigma-Mg_2$ relation the intrinsic scatter is 0.012 mag and 0.014 mag, respectively. We note that the joint contribution of both the $D-\sigma$ and $\sigma-Mg_2$ intrinsic scatters to that observed around $D-Mg_2$ amounts to 0.087 dex and 0.110 dex for the core and halo samples, respectively. The propagation of the scatter in the $\sigma-Mg_2$ relation onto the

Table 4.1. Derived $D - \sigma$, $D - Mg_2$ and $\sigma - Mg_2$ zero-points and median offsets.

Range	n	$\langle 1.2 \log\sigma - \log D \rangle$	$\langle 5.2\, Mg_2 - \log D \rangle$	$\langle Mg_2 - 0.232 \log\sigma \rangle$
$0° < R < 1°$	46	1.701 (rms=0.068)	0.442 (rms=0.098)	−0.245 (rms=0.016)
$1° < R < 5°$	20	1.660 (rms=0.088)	0.328 (rms=0.149)	−0.259 (rms=0.018)
Median diff.		0.042 ± 0.023 dex	0.122 ± 0.035 dex	0.016 ± 0.005 mag

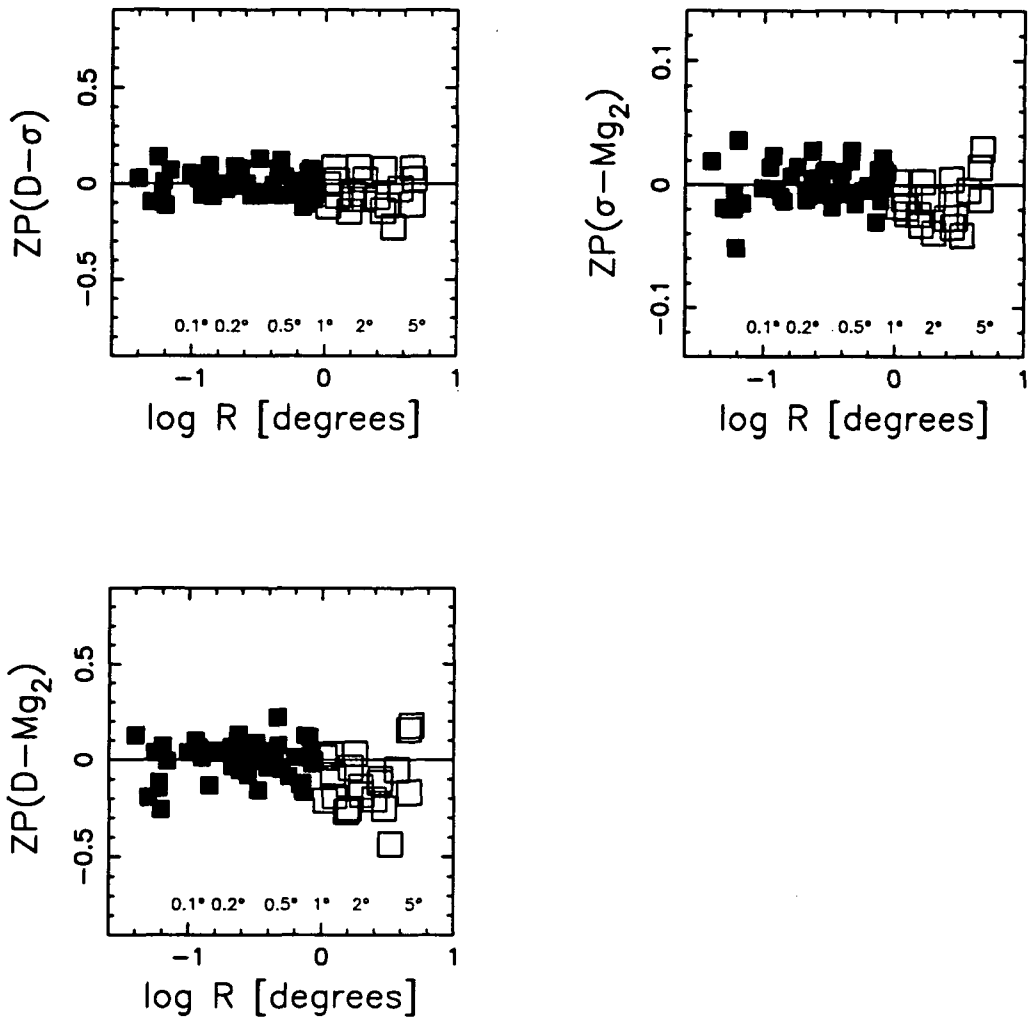

Figure 4.2. The variation of $D-\sigma$, $\sigma-Mg_2$ and $D-Mg_2$ zero-points for each elliptical, relative to the corresponding mean value for the core sample, as a function of projected distance from the cluster centre. The lowest data point in the $D-Mg_2$ plot is NGC 4673.

$D - Mg_2$ relation may account for the larger scatter in $D - Mg_2$ compared to $D - \sigma$ for core ellipticals. However, halo ellipticals show an extra scatter which is intrinsic to the $D - Mg_2$ relation for this sample, i.e., the environmental effect is significantly enhanced in the $D - Mg_2$ relation.

4.2.2 Implications for peculiar velocities.

We have shown that the $D - \sigma$ zero-point for ellipticals in Coma does not significantly depend on distance from the cluster centre. We measured a zero-point offset between the core and halo samples of 10 ± 5 per cent. The environmental effect, however, is clear in the observed $D - Mg_2$ zero-point offset, i.e. 30 ± 10 per cent. While for $D - \sigma$ distances the offset is not significant in our data, we cannot exclude the possibility that an environmental effect at this level does exist. Indeed, this possibility is strongly supported by the consistent explanation to both the $D - \sigma$ and $D - Mg_2$ offsets presented in the following section. For $D - Mg_2$, the statistical significance and the size of this effect *do* provide strong arguments against the use of this relation as a distance indicator.

The statistical uncertainty of our conclusions is, moreover, uncomfortably large in terms of peculiar velocities. For both relations the measured zero-point offsets are in the sense that halo ellipticals possess, on average, larger D diameters at a fixed σ or Mg_2. Distances to the Coma cluster derived for the halo sample will then be $\sim$10% or $\sim$30% smaller than those derived for the core sample, respectively. Considered in terms of peculiar velocities, this implies that the halo Coma ellipticals have values that are, on average, 720 km s^{-1} and 2160 km s^{-1} greater than those measured for the core ellipticals using the $D - \sigma$ and $D - Mg_2$ relations, respectively. The environment-dependent effect translates thus into a *spurious positive peculiar velocity.* The consequences of such an

effect for some unusually large peculiar motions observed in the nearby universe will be discussed in detail in Chapter 5.

4.3 AGE HYPOTHESIS

In this section we address the possibility that the environmental differences observed in the $D-\sigma$, $D-Mg_2$ and $\sigma-Mg_2$ relations are caused by the presence of an IASP component in some halo ellipticals. Hereafter we will refer to this possibility as the *age hypothesis* and to the variation that it causes in the galaxy parameters as the *age effect.*

4.3.1 Overview.

The general idea is very simple. Any recent star formation makes a galaxy brighter in the V-band and, therefore, increases the photometric diameter D. Also, the significant contribution of upper main-sequence stars to the galaxy spectrum dilutes the Mg_2 line strength index. The average age of the stellar population is assumed to have no effect on the velocity dispersions. Hence recent star formation will offset the $D-\sigma$ relation towards larger D diameters at a given σ. This offset will be obviously larger for the $D-Mg_2$ relation since recent star formation also decreases the Mg_2 index. The environmental effect will be then more noticeable in the $D-Mg_2$ relation.

4.3.1.1 The age effect on the D diameter.

According to Buzzoni's (1989) models of evolutionary population synthesis, the relative contributions of dwarf and giant stars to the integrated light of an old stellar population in

the V-band amount to $\sim 50\%$ for both stellar types. The significant contribution of main-sequence stars in this part of the spectrum implies that the addition of an IASP component will decrease the galaxy V-magnitude by a certain amount Δm_V. Since ellipticals all have similar luminosity profiles, the galaxy magnitude is related to the effective radius and surface brightness by:

$$m_V = SB_e - 5 \log R_e - 2.5 \log(2\pi) \tag{4.7}$$

We assume that R_e is not greatly affected by residual star formation: an assertion that can be justified by recent observations showing that this rejuvenation process occurs globally in the stellar populations of elliptical galaxies (Schweizer & Seitzer 1992). Thus SB_e will vary in the same way as m_V, i.e.:

$$\Delta SB_e = \Delta m_V. \tag{4.8}$$

Using equation [4.1] we then estimate that the age effect produces a variation in the D diameter such as:

$$\Delta \log D = -0.286\ \Delta SB_e \tag{4.9}$$

Therefore, since ΔSB_e is negative, the addition of an IASP component will increase the D diameter.

4.3.1.2 The age effect on the Mg_2 line-strength index.

The adoption of Mg_2 as a metallicity scale for composite stellar populations is partly justified by Mould's (1978) theoretical analysis. This showed that Mg_2 in an old ($\sim$ 13 Gyr) population is sensitive to metallicity and insensitive to the shape of the stellar initial mass function. However Mg_2 not only reflects the average metallicity of the population but also depends on the temperatures and surface gravities of the stars (Burstein *et al.* 1984, Faber *et al.* 1985). The variation of Mg_2 with stellar surface gravity and V–K

colour (used as a temperature index) has been recently analysed by Gorgas *et al.* (1991). In this study they show the well-known strong dependence of Mg_2 on temperature, in the sense that the Mg_2 strength increases with redder $V-K$ colours, once the metallicity dependence has been removed. Gravity effects are also shown to be important in late spectral type stars, i.e. for a given temperature, K giants possess lower Mg_2 than K dwarfs. If giant stars dominate the integrated light of an old population, then metallicity will be the dominant parameter because the temperature of the giant branch depends mainly on the metal abundance and gravity effects are small (Faber *et al.* 1985). However, a significant contribution from main sequence stars would make Mg_2 sensitive not only to variations in the metal abundance but also to any possible difference in the temperature and gravity of the composite stellar population. In this case Mg_2 will not depend uniquely on metallicity. Indeed, the significant contribution of dwarf stars at $\sim$ 5200 Å, as shown in Buzzoni's models, causes Mg_2 to be also dependent on the temperature of the main-sequence turnoff point. This in turn implies that Mg_2 *must* be sensitive to differences in the average age of the stellar population.

According to evolutionary population synthesis models, the strength of Mg_2 increases as the population gets older (Aragón, Gorgas & Rego 1987). Observational evidence for the effect of a young population on Mg_2 has been reported by Burstein *et al.* (1988) who found that some elliptical galaxies with the weakest values of Mg_2 for a given σ are actively forming stars. Schweizer *et al.* (1990) found that, for a given absolute magnitude, the strength of Mg_2 decreases systematically with the amount of fine structure in giant ellipticals, while the strength of the nuclear $H\beta$ absorption line increases. They interpreted this effect as a result of systematic variations in mean age, rather than mean metallicity, of the stellar populations. Thus there is a consensus that the addition of a young population decreases the strength of Mg_2.

4.3.2 Model predictions.

To test the age hypothesis we have used Bruzual's (1983) evolutionary spectral synthesis models to simulate the effect of a recent burst of star formation superimposed on the old stellar population characteristic of an elliptical galaxy. Since spectral synthesis studies suggest the existence of a 5 Gyr old stellar component we consider that this second burst occurred 5 Gyr ago. Bruzual's code does not include stars in late stages of evolution. However these models are suitable to analyse *differences* between populations due to a young stellar component. The model we have adopted assumes a Miller-Scalo IMF and a constant star formation rate for the burst period and uses the stellar libraries of Gunn & Stryker (1982) and Jacoby, Hunter & Christian (1984). Although these libraries are deficient in K dwarfs, this is not likely to cause a sizable change in the integrated Mg_2. Following a similar procedure to that used by Aragón, Gorgas & Rego (1987), we have calculated luminosities, colours and line indices from the resulting composite spectrum at different epochs after the initial burst of star formation.

In Figure 4.3 we show the time evolution of Mg_2 and the V-band absolute magnitude for the single-burst and the two-bursts models. The effect of an IASP is clear: a significant contribution of upper main-sequence stars to the galaxy spectrum dilutes Mg_2 and increases the luminosity of the galaxy in the V-band.

To quantify the changes caused by the presence of an IASP we consider the strength of the burst as a free parameter. The effect of a star formation burst on the different observable features depends on both the mass fraction involved, i.e. the strength of the burst, and the time since this last star formation event occurred, i.e. the age of the burst. Clearly, several possible pairs of burst strength and age can yield the same variation in Mg_2 and m_V. Unfortunately all of the studied quantities vary similarly and it is not possible to discriminate between these different pairs. In practice, this ambiguity implies

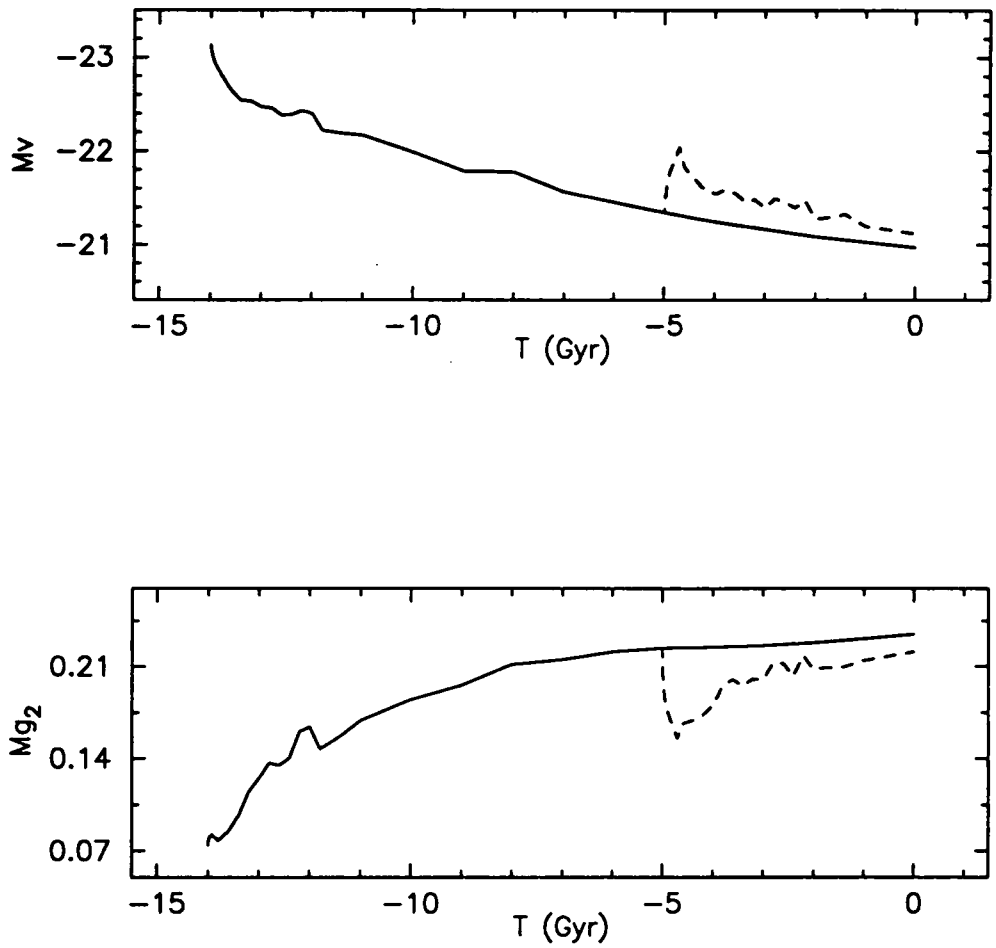

Figure 4.3. The time evolution of the V-band absolute magnitude, M_V, and Mg_2 after a first burst of star formation ~15 Gyr ago. The computed models assume a solar metallicity, a Miller-Scalo IMF and a constant stellar formation rate. Solid lines represent the single-burst model. The dotted lines correspond to a second burst of star formation, 10% strength in mass, 5 Gyr ago.

that the effects of a secondary burst in our model are indistinguishable from star formation continuing over an extended period. Hereafter, we adopt the term *last burst* to denote the last period of significant star formation although it does not need to be a burst in the sense of a sharp increase in the stellar formation rate. If we fix the age of this event to be ~5 Gyr, a last burst of 10% in mass decreases Mg_2 by 0.015 mag. The resulting m_V will be 0.15 mag brighter. Since SB_e varies in the same way as m_V then, according to equation [4.9], D increases by 0.043 dex.

With these results it is then straightforward to predict the consequences of the age effect on the $D-\sigma$, $D-Mg_2$ and $\sigma-Mg_2$ relations. The D diameters are increased by 0.043 dex and thus the $D-\sigma$ relation is offset by this amount. Mg_2 is lowered by 0.015 mag and hence the $\sigma-Mg_2$ relation is similarly offset. For the $D-Mg_2$ relation we must consider the effect of the IASP on both Mg_2 and D. From the adopted $D-Mg_2$ slope the 0.015 mag decrease in Mg_2 is equivalent to increasing D by 0.078 dex. Therefore the net effect of an IASP on the $D-Mg_2$ relation increases D by 0.121 dex at a fixed Mg_2.

In Figure 4.4 we show the median difference between the zero-points of the core and halo samples for the three relationships as a function of the sample division along with the model predictions. As can be readily seen *all* the observed offsets are consistent with the hypothesis that star formation continued to a more recent epoch in some halo ellipticals.

Finally, we emphasize that the average effect of a 10% strength burst is enough to account for the observed offset of most halo ellipticals. Nevertheless, those galaxies with the more negative $D-Mg_2$ residuals: NGC 4673, NGC 4789, NGC 4952, NGC 4876 and NGC 5004, would require, according to our model, a larger last burst of star formation. In particular, NGC 4673, the most extreme case, would have experienced an abnormally strong burst in which at least $\sim$ 40% of the total mass was converted into stars. This

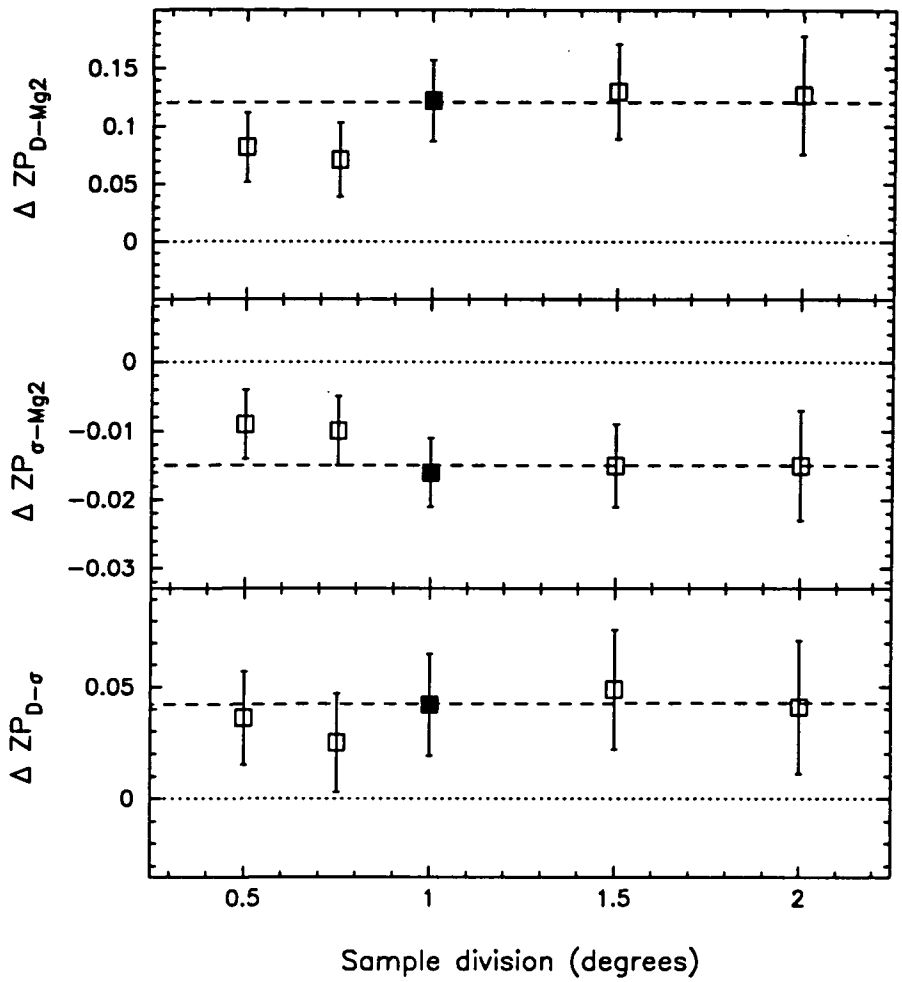

Figure 4.4. Median zero-point offsets between the core and halo samples for the $D-\sigma$, $\sigma-Mg_2$ and $D-Mg_2$ relations as a function of the sample division. Estimated error bars are shown for each case. The dotted lines represent no zero-point difference between the two samples. The dashed lines correspond to the predicted offsets from our model of a second star formation burst, 10% strength in mass, 5 Gyr ago.

result suggests that, if age is the only factor driving the observed environmental differences, the last burst of star formation in these galaxies would have occurred at a later epoch, probably only $\sim$ 2–3 Gyr ago.

4.4 A NEW, AGE-INDEPENDENT RELATION FOR ELLIPTICAL GALAXIES

We have shown that the age effect can consistently account for the observed $D - \sigma$, $D - Mg_2$ and $\sigma - Mg_2$ offsets between ellipticals that lie in the halo and the core of the Coma cluster. This systematic variation in age of ellipticals located in low-density environments induces spurious peculiar velocities as derived from both the $D - \sigma$ and $D - Mg_2$ distance indicators. Clearly, it would be very desirable for current studies on peculiar motions to develop techniques to correct for this environmental/age effect. Here we address precisely this problem: to design an age-independent distance indicator for ellipticals.

In Chapter 3 we demonstrated that all observed global correlations for elliptical galaxies are derived as linear combinations of only three: the fundamental plane, $L - I_e$ and $\sigma - Mg_2$ relations (equations [i], [ii] and [iii] in Table 3.1, respectively). In our framework, any new correlation between galaxy global parameters *will also be* a certain combination of these basic relations. To be used as a distance indicator, the new correlation must: a) combine distance-dependent with distance-independent quantities; b) possess small intrinsic scatter so that measurements of peculiar motions are meaningful; and c) be independent from environmental/age differences to avoid the derivation of spurious peculiar motions. Both the fundamental plane and the $L - I_e$ relations correlate distance-dependent with distance-independent parameters and, in principle, can be used to estimate

distances. In practice, the large intrinsic scatter around $L-I_e$ ($\sim$0.18 dex in log$L$) prevents this relation to be used as distance indicator. Hence we do not consider it further in our analysis. The remaining two basic relations, i.e. the fundamental plane and $\sigma - Mg_2$, are, indeed, the best-defined correlations for ellipticals. However, both are sensitive to the age effect. The idea is then very simple: we combine both relations so that the age effect cancels out.

As discussed in Section 4.3, the presence of a younger stellar component decreases SB_e and Mg_2. Hence, for a 'younger' elliptical galaxy the fundamental plane and $\sigma - Mg_2$ relations are modified as follows:

$$-\log R_e + 0.314\ (SB_e - \Delta SB_e) + 1.140\ \log\sigma = \text{constant},$$

$$(Mg_2 - \Delta Mg_2) - 0.232\ \log\sigma = \text{constant},$$

where Δ denotes the age effect on each quantity. The new correlation is then derived as the linear combination:

$$\{-\log R_e + 0.314\ SB_e + 1.140\ \log\sigma\} + \beta\ \{Mg_2 - 0.232\ \log\sigma\} = \text{constant}, \qquad (4.10)$$

such as β satisfies the condition:

$$0.314\ \Delta SB_e + \beta\ \Delta Mg_2 = 0; \qquad (4.11)$$

i.e.:

$$\beta = -0.314\ (\Delta SB_e/\Delta Mg_2). \qquad (4.12)$$

To calculate the value of β we need to know the relation between the age effects on SB_e and Mg_2, i.e. $\Delta SB_e/\Delta Mg_2$. This ratio is provided by Bruzual's galaxy evolution models.

Following the discussion in Section 4.3.2, the younger component responsible for the age effect is assumed to form in a second burst of star formation that occurred 5 Gyr

ago and involved 10% of the galaxy mass. In Figure 4.5 we plot the time evolution of the ratio between this age effect on the total magnitude and the Mg_2 index, i.e. $\Delta m/\Delta Mg_2$, for different bands. According to Bruzual's models, this second burst decreases both m and Mg_2 in such a way that the ratio $\Delta m/\Delta Mg_2$ remains approximately constant after the initial 1-2 Gyr. The decreasing value of this ratio from the ultraviolet to the infrared simply reflects the smaller contribution of main sequence stars to the integrated galaxy light at longer wavelengths. For the V-band we adopt:

$$\Delta m_V/\Delta Mg_2 = 10. \tag{4.13}$$

Burst strengths a factor two lower or higher give ratios that differ in less than 10 per cent from this value. A similar value is derived using the new version of these models (Bruzual & Charlot 1993). Using equation [4.8], we then derive:

$$\Delta SB_e/\Delta Mg_2 = 10. \tag{4.14}$$

Hence, according to equation [4.12] we conclude that the adequate value of β required to cancel the age effect is:

$$\beta = -3.14. \tag{4.15}$$

Substituting this value onto equation [4.10], we obtain the new age-independent distance indicator for ellipticals, i.e.:

$$-\log R_e + 0.314\ SB_e + 1.868\ \log\sigma - 3.14\ Mg_2 = \text{constant}. \tag{4.16}$$

This relation is shown in Figure 4.6 for our Coma sample. Here, the effective radius R_e, rather than the photometric diameter D, is the distance-dependent parameter. To derive this relation we have implicitly assumed that the rejuvenation process of the stellar population is not limited to the galaxy nucleus but occurs globally (Schweizer & Seitzer 1992). This suggests that R_e should not be greatly affected by the presence of the

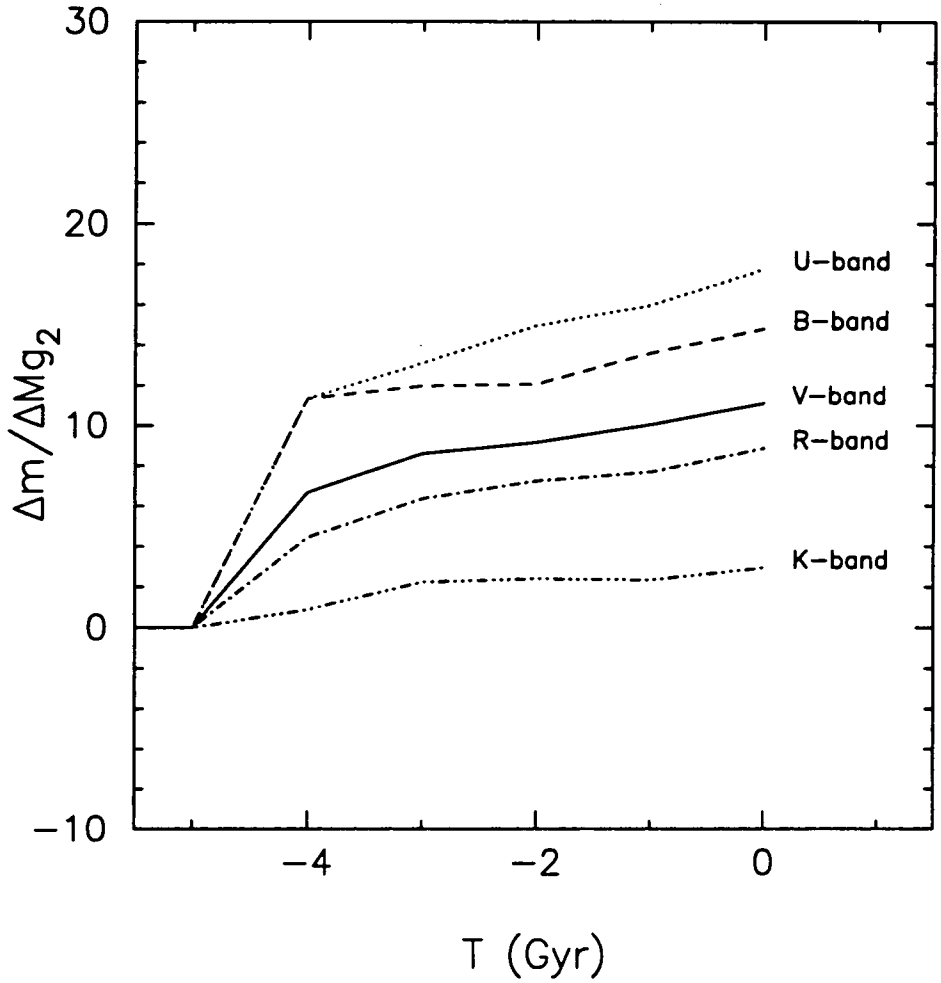

Figure 4.5. The time evolution of the ratio between the effect of residual star formation on the total magnitude (Δm) and Mg_2 (ΔMg_2), as predicted by Bruzual's models for different bands. Each line represents the effect of a 5 Gyr old burst of star formation superimposed to a 15 Gyr old stellar population.

younger stellar component. However, if star formation occurs exclusively in the galaxy nucleus, only the central luminosity would be increased and, therefore, the measured R_e would be *underestimated.* While a centrally located IASP component decreases R_e, the effect on the distance estimates derived using the above relation is, however, negligible. This apparent contradiction has a very simple explanation. It is well-known that all elliptical galaxies, whether having an IASP component or an old, single-age population, follow approximately the same surface brightness profile. For a de Vaucouleours' law, the decrease in the effective radius due to a younger central component ($\Delta \log R_e$) in turn implies a decrease in the effective surface brightness (ΔSB_e) such as (equation [2.1]):

$$\Delta SB_e \sim 3\ \Delta \log R_e.$$

In this case, it is straightforward to show that the zero-point of the new relation will vary by:

$$-(1 - 3 \times 0.314)\ \Delta \log R_e.$$

Hence, the zero-point turns out to be practically independent of $\Delta \log R_e$, i.e. the galaxy is moved "along" rather than "off" the new relation. The only effect due to a central younger component would thus arise from the overall net increase in luminosity, which is accounted for by the Mg_2 term.

The scatter around this relation for the Coma sample is only 0.085 dex, which is significantly smaller than the observed scatter in $D - Mg_2$, i.e. 0.126 dex, but slightly larger than $D - \sigma$, i.e. 0.077 dex. This results from the addition of the Mg_2 term and the larger coefficient of the $\log\sigma$ term. In fact, despite the contribution of the spread in metallicity at a given σ, the intrinsic scatter of the age-independent relation is *smaller*, i.e. 0.062 dex compared to 0.070 dex for $D - \sigma$ or 0.112 dex for $D - Mg_2$. Thus, in principle, higher precision observations would yield a smaller scatter distance indicator.

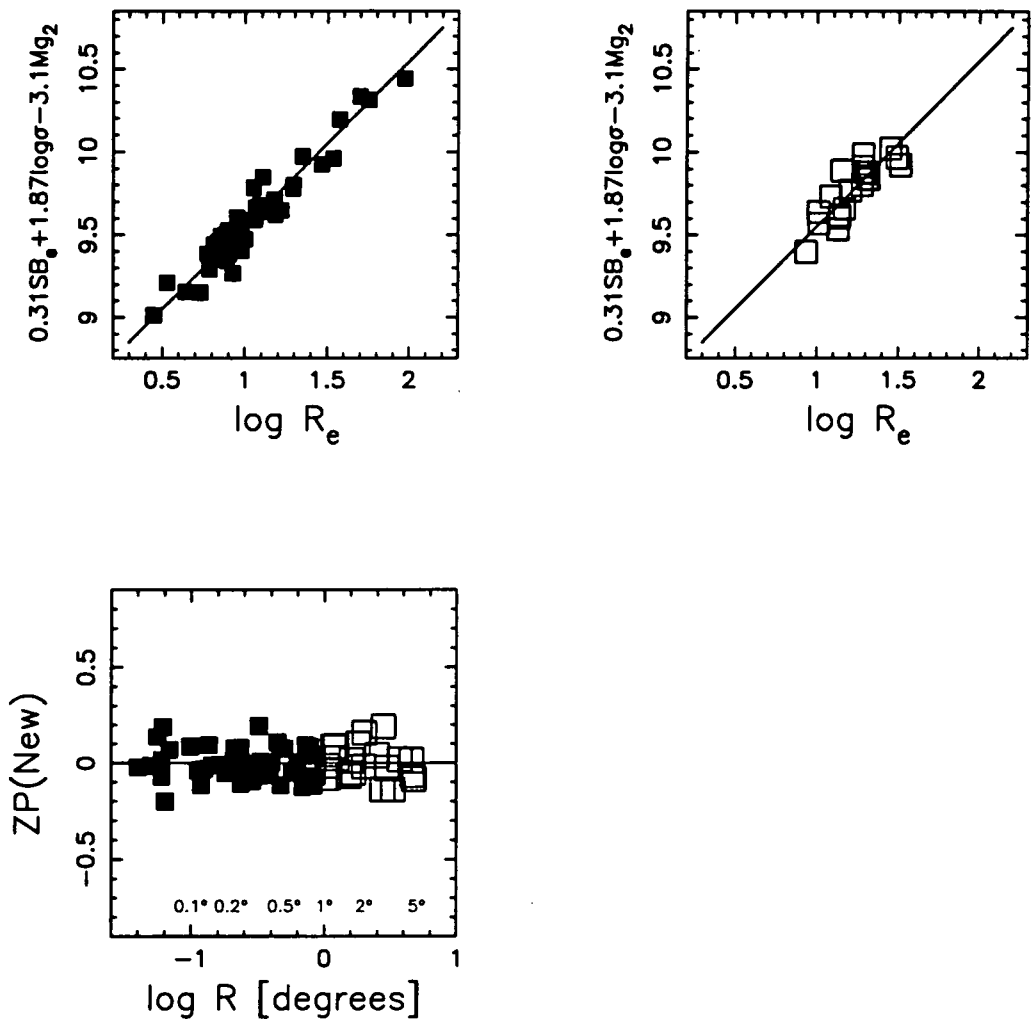

Figure 4.6. Top panels: The new relation for the core (filled squares) and halo (open squares) Coma samples. Bottom panel: The zero-point of the new relation for each elliptical as a function of projected distance from the cluster centre.

Table 4.2. Comparison between the observed and predicted offsets.

	$\langle D-\sigma \rangle$	$\langle D-Mg_2 \rangle$	$\langle \sigma-Mg_2 \rangle$	$\langle$ New $\rangle$
Median diff.	0.042 ± 0.023	0.122 ± 0.035	0.016 ± 0.005	-0.002 ± 0.023
Model pred.	0.043 dex	0.121 dex	0.015 mag	0.000 dex

Finally, as discussed previously, the distance to the Coma cluster derived for halo ellipticals, using both $D - \sigma$ and $D - Mg_2$, is systematically underestimated compared to the distance obtained for the core sample. Our relation is designed to overcome this environmental effect on the distance estimates and, thus, remove the spurious peculiar motions introduced by residual star formation. In Table 4.2 we list the observed offsets between the core and halo Coma ellipticals for $D - \sigma$, $D - Mg_2$ and the new relation. For this relation the observed offset in zero-point between core and halo ellipticals is, as expected, negligible.

The new, age-independent relation thus satisfies all three conditions which characterize an optimum distance indicator. Its application to estimate distances to elliptical galaxies located in different environments and the implications for current measurements of the local peculiar velocity field is fully discussed in Chapter 5.

4.5 THE $\delta - \delta$ DIAGRAMS REVISITED.

Terlevich *et al.* (1981) found a striking correlation of the residuals for their two distance indicators, the $L - \sigma$ and $L - Mg_2$ relations, for a sample of mostly field ellipticals. This is in the sense that galaxies with velocity dispersions that are higher than the mean at a given luminosity also have Mg_2 indices that are too large; that is, they are more metal rich. This correlation of residuals was termed the $\delta - \delta$ diagram. In a follow-up to this study, Dressler (1984) found that the $\delta - \delta$ diagram for a sample of cluster ellipticals showed only a weak trend. Since the distance error vector roughly aligns with the distribution of points in this diagram, a straightforward interpretation of these results is that the distances to the field ellipticals were incorrectly predicted by their recession velocities. However, the enormous size of the required distance errors, i.e. a factor of 2, ruled out this explanation.

The $\delta - \delta$ diagram was then interpreted to imply that, in addition to luminosity, at least a second parameter was needed to describe the properties of elliptical galaxies. In order to explain the differences between the field and cluster samples, this hidden parameter would have to vary significantly in field ellipticals but little for cluster galaxies. Although several candidates for the second parameter were initially considered, e.g. the intrinsic flattening of the galaxy (Terlevich *et al.* 1981), surface brightness (de Vaucouleurs and Olson 1982) or mass-to-light ratio (Efstathiou and Fall 1984), the lack of large, representative samples of elliptical galaxies prevented to reach any definite conclusion.

The understanding of the $\delta - \delta$ diagram motivated the large surveys of ellipticals which resulted in the discovery of the fundamental plane (Dressler *et al.* 1987; Djorgovski and Davis 1987). The existence of this plane was interpreted to demonstrate the biparametric nature of the elliptical galaxy family. Surface brightness, acting as a second parameter in both the $L - \sigma$ and $L - Mg_2$ relations, was then considered as the main factor responsible for the observed trends in the $\delta - \delta$ diagram, while distance errors in the field sample would contribute to the stronger correlation of residuals as compared to the cluster sample. Once the effects of the second parameter and distance errors are removed, no trend should remain in the $\delta - \delta$ diagram. Dressler *et al.* (1987) showed that the surface brightness dependence can be removed by using the photometric diameter D as the independent variable instead of luminosity. However, a new $\delta - \delta$ diagram, this time with residuals calculated from the $D - \sigma$ and $D - Mg_2$ relations, for a large sample of cluster ellipticals showed the same puzzling trend observed in the original Terlevich *et al.*'s (1981) diagram, although to a lesser degree (Dressler *et al.* 1987). This result implies that, contrary to the common belief, neither surface brightness acting as a second parameter nor distance errors are actually the main responsibles for the observed trends in the $\delta - \delta$ diagrams. Despite the better understanding of the properties of elliptical galaxies achieved in these new surveys we are left with the same ambiguity raised by Terlevich *et*

al.'s (1981) results. There must be another cause of correlated scatter which has not yet been associated with any observed parameters for elliptical galaxies.

In this Section we offer a simple explanation to the observed trends in the $\delta - \delta$ diagrams based in the framework we developed in Chapter 3. We also show that the differences in these diagrams for ellipticals located in high- and low-density environments can be interpreted as a result of the age effect.

4.5.1 The origin of the correlated scatter in the $\delta - \delta$ diagrams.

Before starting the discussion on the $\delta - \delta$ diagrams, it is important to note that the $D - \sigma$ and $L - \sigma$ are intrinsically different relations, i.e. $D - \sigma$ is not an improved version of $L - \sigma$ where a surface brightness dependence has been removed. While the former is an approximate representation of the edge-on view of the fundamental plane, the latter provides a description of the distribution on the fundamental plane face-on. The physical processes which determine both relations are, indeed, very different (see discussion in Section 3.3).

In the framework presented in Chapter 3, the $D - Mg_2$ and $L - Mg_2$ relations are simply an alternative form of $D - \sigma$ and $L - \sigma$ where σ has been replaced by Mg_2 using the $\sigma - Mg_2$ relation. Thus:

$$-\log D + 5.2\ Mg_2 = \{-\log D + 1.2\ \log\sigma\} + 5.2\ \{Mg_2 - 0.232\ \log\sigma\}$$

$$\log L - 16.11\ Mg_2 = \{\log L - 3.74\ \log\sigma\} - 16.11\ \{Mg_2 - 0.232\ \log\sigma\}$$

With this result it is then straightforward to predict the trends in the different $\delta - \delta$ diagrams (hereafter this term is used to refer to any plot showing the residuals of two correlations). Since these trends are likely to depend on the environment, we first discuss the results for the Coma core sample. According to our framework, $D - \sigma$ and $\sigma - Mg_2$

are two independent relations. Hence, the $\delta - \delta$ diagram of both residuals will simply show a scatter diagram. However, since $D - Mg_2$ is a linear combination of both previous relations, the $D - Mg_2$ residuals will be correlated such as:

$$\delta(D - Mg_2) = \delta(D - \sigma)$$

$$\delta(D - Mg_2) = 5.2\ \delta(\sigma - Mg_2).$$

Similarly, for the $L - Mg_2$ residuals we derive:

$$\delta(L - Mg_2) = \delta(L - \sigma)$$

$$\delta(L - Mg_2) = -16.11\ \delta(\sigma - Mg_2).$$

In Figures 4.7 and 4.8 we show the different $\delta - \delta$ diagrams for our Coma core sample. As expected, there is no correlation between the residuals of the $D - \sigma$ and $\sigma - Mg_2$ relations. The trends observed in all remaining $\delta - \delta$ diagrams are accurately described by the predicted correlations given above. Therefore, we conclude that the main cause of the correlated scatter in these diagrams is simply the fact that σ and Mg_2 *are not independently related* to D or L.

4.5.2 The effect of the environment on the $\delta - \delta$ diagrams.

Following the discussion in Section 4.3, we consider that any environmental difference in the $\delta - \delta$ diagrams is due to the presence of an IASP component in some ellipticals located in low-density environments. We first analyse the environmental effect on the $D - \sigma$ versus $\sigma - Mg_2$ residual plot. This $\delta - \delta$ diagram is shown in Figure 4.9 for the whole Coma sample. Superimposed to the data we have drawn a box which defines approximately the area in which 'old' ellipticals are most likely to scatter. To calculate this area we consider

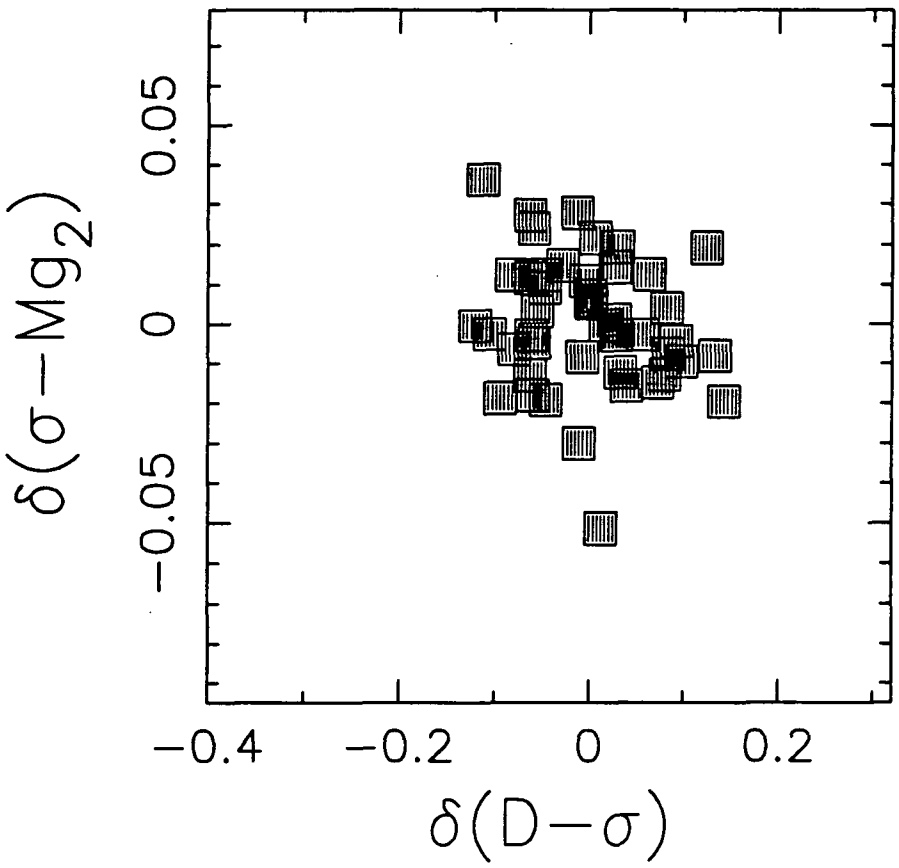

Figure 4.7. The $D-\sigma$ versus $\sigma - Mg_2$ $\delta - \delta$ diagram for the Coma core galaxy sample.

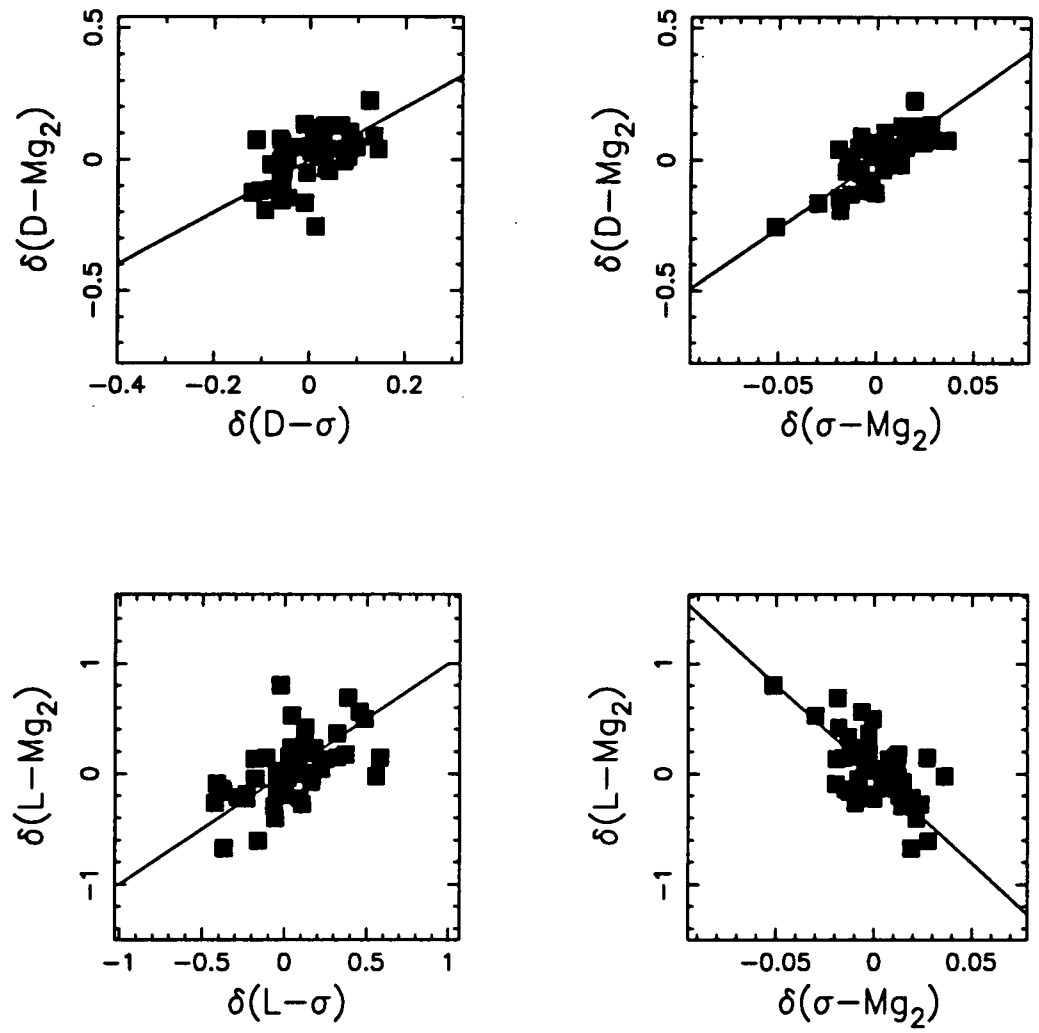

Figure 4.8. Different $\delta - \delta$ diagrams for the Coma core galaxy core sample. Solid lines represent the predicted trends in each case.

that the residuals of the $D-\sigma$ and $\sigma - Mg_2$ relations may be caused by four different sources of scatter:

a) measurement errors (ϵ_M),

b) intrinsic scatter in σ at a given D (ϵ_σ),

c) intrinsic scatter in metallicity at a given σ (ϵ_{Mg2}), and

d) variations in age of the stellar populations (ϵ_A).

The contribution of the measurement errors is already known, i.e. 0.032 dex for $D-\sigma$ and 0.012 mag for $\sigma - Mg_2$. Since the relation derived in Section 4.4 is not affected by the age effect, it is then possible to estimate roughly the importance of ϵ_σ, ϵ_{Mg2} and ϵ_A from the observed scatter around $D-\sigma$, $\sigma - Mg_2$ and this new relation. We find:

$\epsilon_\sigma \sim$0.058 dex, $\epsilon_{Mg2} \sim$ 0.010 mag and $\epsilon_A \sim$ 0.037 dex $\sim$ 0.010 mag.

Based in the above estimates, the expected scatter around $D-\sigma$ and $\sigma - Mg_2$ for 'old' ellipticals would be due to a combination of measurement errors and intrinsic variations in velocity dispersion and metallicity alone, i.e. $\sim$0.066 dex and $\sim$0.016 mag, respectively. The box shown in Figure 4.9 defines roughly these 3-sigma errors.

Under the age hypothesis, those ellipticals located outside the box are candidates to have an IASP component. As expected, the vast majority of these objects belong to the halo sample. These galaxies would have been moved in this diagram towards lower values of both residuals due to recent star formation. The arrow shows the effect of this young stellar component as predicted by Bruzual's models. Its size corresponds to a 10% second burst of star formation occurred 5 Gyr ago. Although, as discussed previously, the most deviant galaxies would require a larger burst of star formation, the age hypothesis provides a plausible interpretation of the observed distribution in this $\delta - \delta$ diagram.

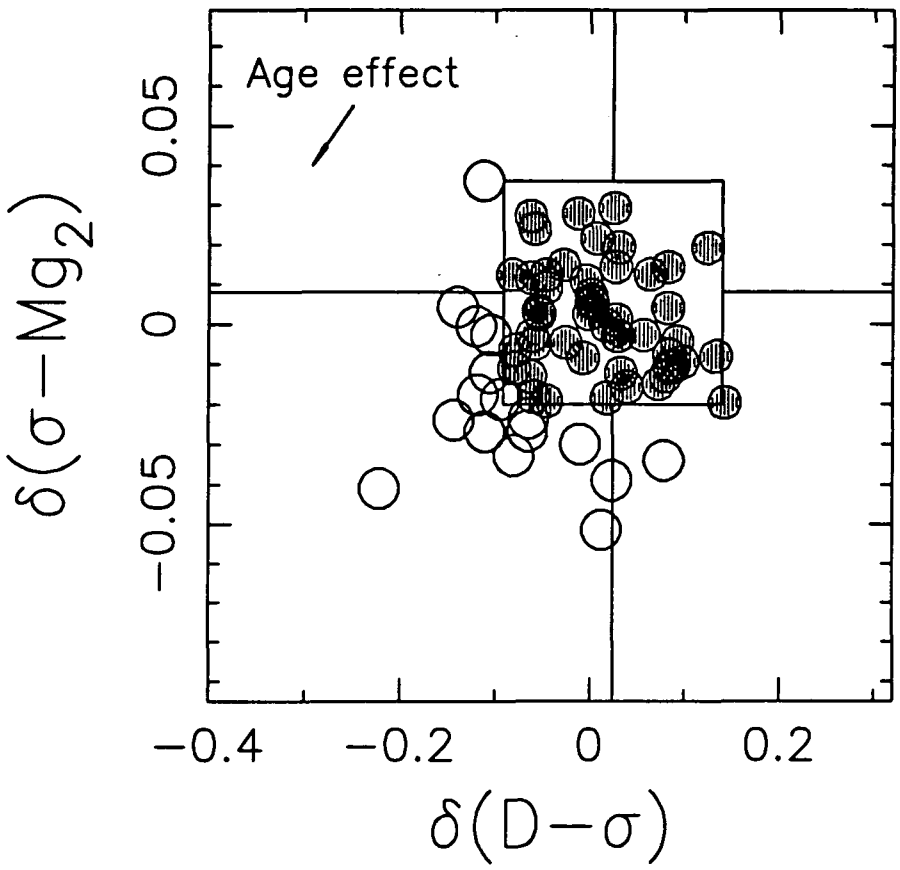

Figure 4.9. The $D-\sigma$ versus $\sigma - Mg_2$ $\delta - \delta$ plot for the whole Coma sample. Filled circles: objects which are most likely to have an old, single age stellar population. The central box defines the area occupied by these 'old' ellipticals (see text). Open circles: objects which are most likely to have an IASP component. The arrow represents the effect of a 10% second burst of star formation occurred 5 Gyr ago, as predicted by Bruzual's models. The most deviant point is NGC 4673.

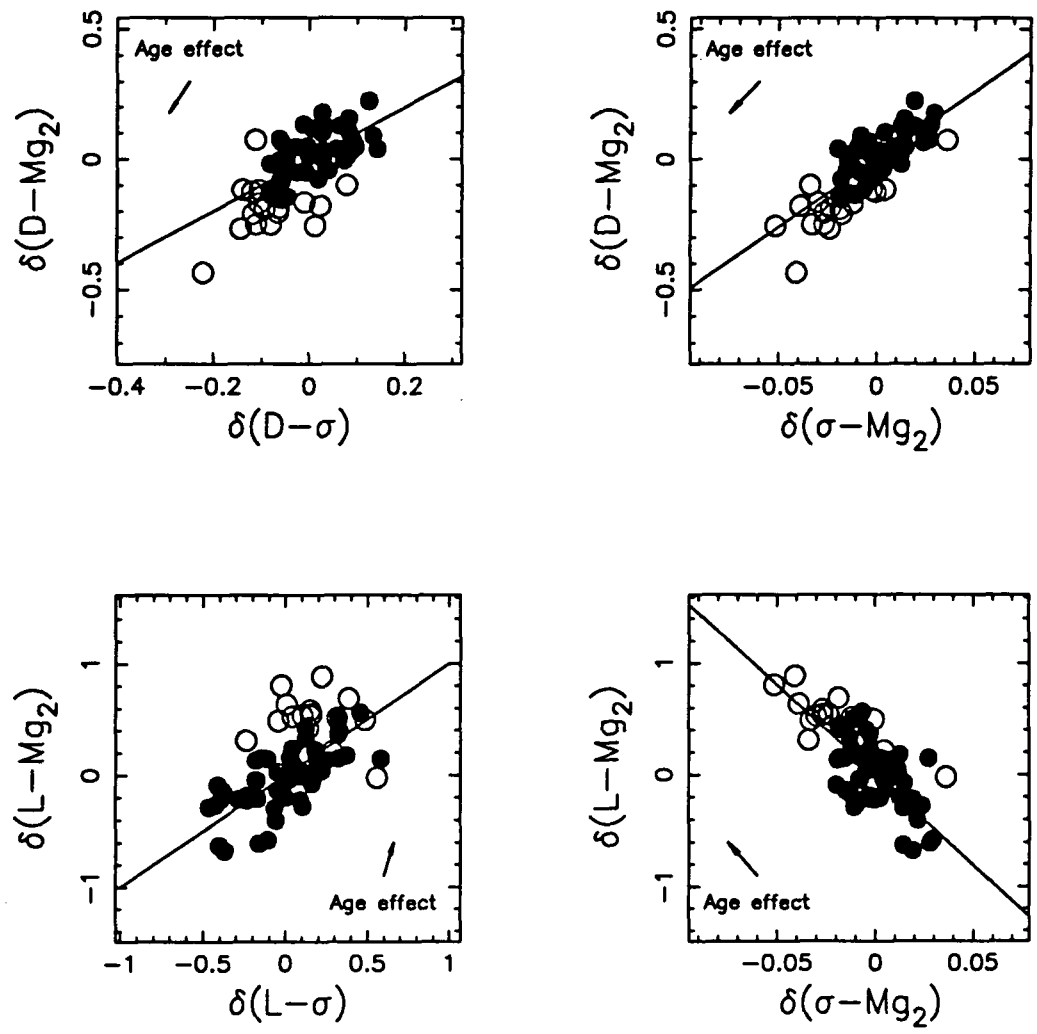

Figure 4.10. Different $\delta - \delta$ diagrams for the whole Coma sample. Solid lines represent the predicted trends in each case. Symbols have the same meaning as specified in Figure 4.9.

In Figure 4.10 we show the remaining $\delta - \delta$ diagrams for the Coma sample. In all cases, the predicted correlations fit accurately the trends followed by the 'old' ellipticals, while the age effect provides a *consistent* explanation to the deviations from these mean lines observed for the 'younger' ellipticals. More interestingly, the age effect roughly aligns with the intrinsic correlated scatter in most diagrams. Since field ellipticals are likely to be more heterogeneous in the mean ages of their stellar populations, the trends observed in the $\delta - \delta$ diagrams will be then enhanced compared to cluster ellipticals. *The age of the stellar population* appears thus as a good candidate for the 'hidden' parameter whose larger variation in field galaxies would explain the differences between the cluster and field samples.

Therefore we conclude that correlated errors is the main cause of the observed trends in the $\delta - \delta$ diagrams. The age effect in turn may provide a plausible explanation to the stronger correlations observed for ellipticals located in low-density environments.

4.6 CONCLUSIONS

The main results presented in this Chapter can be summarized as follows:

(i) To assess the level of any environmental dependence in the distance indicators for elliptical galaxies, we have compared the $D - \sigma$ and $D - Mg_2$ relations for ellipticals located in the core and the halo of the Coma cluster. By studying the variations within one cluster, we avoid the difficulty of decoupling effects induced by distance errors from those due to real environmental differences. We have shown that these relations possess a small environmental effect. At a fixed σ or Mg_2, ellipticals located in the cluster halo have, on average, larger D diameters

by 0.042 ± 0.023 dex or 0.122 ± 0.035 dex, respectively. The halo ellipticals also have a significantly larger scatter about both relations. For completeness, the environmental effect on the $\sigma - Mg_2$ relation has also been analysed. We have shown that halo ellipticals have, on average for a given σ, lower Mg_2 by 0.016 ± 0.005 mag compared to core ellipticals. All the above results are qualitatively in agreement with the differences found in previous studies between field and cluster ellipticals. Hence, while the environmental dependence of the $D - \sigma$ zero-point is not significant in our data, the observed offset in the $D - Mg_2$ zero-point provides a strong argument against the use of this relation as a distance indicator. In both cases, the environment-dependent effect translates into a spurious positive component of the peculiar velocity field.

(ii) We have investigated the possibility that the observed offsets in the $D-\sigma$, $D-Mg_2$ and $\sigma - Mg_2$ relations are caused by star formation continuing to a more recent epoch in some halo ellipticals. Bruzual's evolutionary population synthesis models have been used to predict the effect of an intermediate-age stellar population on the photometric diameter D and the Mg_2 index. We have demonstrated that all the observed offsets are consistent with this hypothesis.

(iii) Using Bruzual's models to correct for the effect of an intermediate-age stellar population, we have designed a new distance indicator for elliptical galaxies which is independent of mean stellar age. The new relation is derived as a linear combination of the fundamental plane and the $\sigma - Mg_2$ relation such as the predicted age effect cancels out. The zero-point of this age-independent distance indicator varies by only 0.002 ± 0.023 dex between the core and halo samples. This new relation allows distances to be determined with an uncertainty of $\sim$20 per cent, comparable to the most accurate methods used for elliptical galaxies.

(iv) We have demonstrated that correlated errors is the main cause of the observed trend in the $D - \sigma$ versus $D - Mg_2$ residuals plot (the $\delta - \delta$ diagram). This diagram is simply a consequence of σ and Mg_2 not being independently related to D (or luminosity). We have also shown that the effect of an intermediate-age stellar population provides a plausible explanation to the observed differences in the $\delta - \delta$ diagrams for ellipticals located in high- and low-density environments.

5 DISTANCE ESTIMATES AND PECULIAR MOTIONS

5.1 INTRODUCTION

In the last few years considerable observational work has been undertaken to measure the motions of galaxies relative to the Hubble flow. These 'peculiar velocities' provide direct information of the large-scale distribution of matter in the nearby universe. In practice, the peculiar velocities of galaxies are determined by subtracting the estimated distances from their measured redshifts. The accuracy of such determinations is mainly limited by the uncertainty in the distance estimates. For elliptical galaxies, the most widely used distance indicator is the $D - \sigma$ relation (Dressler *et al.* 1987). The $D - Mg_2$ relation has often been used to corroborate the results derived from $D - \sigma$ (Dressler *et al.* 1987; Dressler, Faber & Burstein 1991). These two empirical relations allow distances to be estimated with an uncertainty of ~20% and ~30%, respectively. By averaging over individual galaxies in groups and clusters, it is then possible to measure peculiar velocities to an accuracy of ~5-10% of the Hubble flow.

One of the major results derived from these studies has been the discovery of large, positive peculiar velocities in the Hydra-Centaurus region, which led to the concept of a Great Attractor, i.e. a very large and extended mass, dominating the nearby peculiar velocity field (Lynden-Bell *et al.* 1988). Although originally attributed to high-amplitude

density fluctuations on scales [1] of ~4000 km s^{-1}, evidence is accumulating which suggests that the coherent streaming flow may be generated over much larger scales (cf. Mathewson, Ford & Buchhorn 1992; Courteau *et al.* 1993; Lauer & Postman 1993). Whatever the origin, bulk motions on these scales are a challenge to models for the formation of structure based on hot or cold dark matter, both of which appear unable to generate such large fluctuations in the mass distribution (Bertschinger & Juszkiewicz 1988).

Because of the serious implications of the large-scale streaming motions for cosmology, several authors have stressed the importance of understanding the nature of the distance indicators used and any systematic effects or sources of errors (Kaiser 1988; Silk 1989). As discussed in Chapters 3 and 4, the $D-\sigma$ distance indicator, as well as $D-Mg_2$, relies on the fundamental assumption that the galaxy mass-to-light ratio is a universal function of the observed structural variables for ellipticals. Lynden-Bell *et al.*'s original study used the rich clusters galaxy sample to define the $D-\sigma$ relation and then apply it to all ellipticals in the Faber *et al.*'s (1989) sample, including galaxies located in poor groups and in the field. This approach, however, does not allow for any systematic variations in M/L that would be manifest as an offset in the zero-point calibration. If these variations are linked to the environment, then the zero-point of the distance indicator will change from one region to another and the observed streaming motions could be entirely spurious.

Recently, Burstein, Faber & Dressler (1990) have presented strong arguments supporting the reliability of the $D-\sigma$ distance indicator. These authors conclude that there is no significant dependence of the $D-\sigma$ zero-point on cluster richness or stellar population differences (as measured by the $B-V$ and Mg_2 versus logσ residuals). They have also emphasised that the distance determinations from the infrared Tully-Fisher relation

[1] Following Lynden-Bell *et al.*, all distances in this Chapter are expressed in units of km s^{-1}, which bypasses the Hubble constant.

to spiral galaxies and from $D-\sigma$ to early-type galaxies in several clusters, are in good agreement.

However, while the agreement of the distance estimates for most clusters is encouraging, some clusters *do* show large discrepancies either between their $D-\sigma$ and Tully-Fisher distances, or between their $D-\sigma$ distances as derived from different authors. Abell 2634 and Abell 2199 are, respectively, the best examples of such discrepancies. Whereas the $D-\sigma$ distance to Abell 2634 is 12243 ± 606 km s^{-1}, the Tully-Fisher relation implies a distance of 8690 ± 480 km s^{-1} (Lucey *et al.* 1991). The mean redshift of Abell 2634 is $\sim$9000 km s^{-1}. Hence the $D-\sigma$ relation implies that this cluster possesses a large negative peculiar velocity of -3200 km s^{-1}, compared to the value $+300$ km s^{-1} as derived from Tully-Fisher. For Abell 2199, Faber *et al.*'s $D-\sigma$ work derived a peculiar velocity of -2919 ± 723 km s^{-1}. Lucey *et al.*, however, measured a peculiar velocity of -1800 ± 800 km s^{-1} for this cluster. Both Abell 2199 and Abell 2634 are among the most distant clusters studied so far using the $D-\sigma$ relation. The observed discrepancies may then reflect an intrinsic lower precision of the D and σ measurements at larger distances due to seeing effects or inadequate signal-to-noise ratio spectra.

In addition, de Carvalho & Djorgovski (1992) have recently shown that, using the global correlations of cluster ellipticals as fiducial, field ellipticals tend to be too blue, have too low an Mg_2 index and too high a surface brightness at a fixed effective radius or luminosity. These results are qualitatively in agreement with the growing evidence that elliptical galaxies located in low-density environments have, on average, slightly younger stellar populations (Larson, Tinsley & Caldwel 1980; Bower *et al.* 1990). As discussed in Chapter 4, both the $D-\sigma$ and $D-Mg_2$ distances to ellipticals with younger stellar populations are systematically underestimated and, as a result, their derived peculiar motions will tend to be systematically positive. Indeed, Gregg (1992) has shown that ellipticals with recent star formation have large positive and, probably, spurious positive

peculiar velocities as derived from $D - \sigma$. Limits of the accuracy of distance indicator relations, such as $D - \sigma$ or $D - Mg_2$, due to environment dependent stellar population differences, should be better understood before secure measurements of large-scale peculiar velocities can be made.

In this Chapter we undertake a comparative analysis of the peculiar velocities derived from $D - \sigma$, $D - Mg_2$ and our new, age-independent relation for ellipticals located in the cluster and field environments. Our aim is to assess the reality of previous measurements of large peculiar motions in the nearby universe. To test the reliability of the new distance indicator, we first readdress in Section 5.2 the measurements of peculiar velocities for the sample of ellipticals with recent star formation studied by Gregg. In Section 5.3 we present new measurements of peculiar motions for Abell 2199 and Abell 2634 derived from the analysis of our sample of ellipticals in both clusters. The reality of previous measurements of peculiar velocities for field ellipticals is discussed in Section 5.4. Finally, in Section 5.5 we present preliminary results on a similar study in the Great Attractor area.

5.2 STELLAR POPULATION-INDUCED PECULIAR MOTIONS

For a sample of ellipticals located mostly in the field and in groups, Schweizer *et al.* (1990) and Schweizer & Seitzer (1992) found that, at a given absolute magnitude, the UBV colours and the Mg_2, $H\beta$ and CN strengths are correlated with the amount of fine structure (i.e. ripples, jets of luminous matter, x-structure and boxy isophotes). They showed that these correlations were very probably due to systematic differences in mean age, in the sense that ellipticals with a large fine structure index (Σ) show the most evidence of residual star formation. Gregg (1992) showed that these 'distorted' ellipticals

tend to have large positive peculiar velocities, as derived from $D-\sigma$, which could be possibly due to recent star formation increasing their D diameters. He concluded that the derived peculiar velocities were thus almost certainly spurious.

As an independent test of our new distance indicator, we have made a comparative analysis between $D-\sigma$, $D-Mg_2$ and the new relation using the same sample of ellipticals studied by Gregg. Rather than adopting the previously published B-band photometric parameters we use here the V-band D, R_e and SB_e values listed in Table 2.13 to match precisely the scheme described in Section 4.4. Velocity dispersions and Mg_2 indices are taken from Faber *et al.* (1989).

For all three indicators, the galaxy distance (d_e) has been estimated relative to the Coma cluster following the standard procedure described in Lynden-Bell *et al.* (1988):

$$\log d_e = \text{Distance Indicator} + \log\left(\frac{1+7/4z}{1+7/4z_{\text{Coma}}}\right) - \text{Zero point}_{\text{Coma}} + \log cz_{\text{Coma}} \quad (5.1)$$

The distance indicators used here are the empirical relations: $\{1.2\ \log\sigma - \log D\}$, $\{5.2\ Mg_2 - \log D\}$ and $\{-\log R_e + 0.314\ SB_e + 1.868\ \log\sigma - 3.14\ Mg_2\}$. The second term in equation [5.1] corrects for cosmological effects on the distances estimated from apparent diameters, assuming a $q_o = \frac{1}{2}$ cosmology. The Coma cluster zero-points of all V-band relations analysed in this Chapter are summarized in Table 5.1. Because of the environmental effect discussed in Chapter 4, the zero-points have been calculated using only elliptical galaxies that reside in the core of the Coma cluster. For those correlations involving our own measurements of σ or Mg_2, we apply the zero-points derived for our core sample of 46 ellipticals (INT system). For Faber *et al.*'s measurements, we used Dressler *et al.* (1987) sample of 28 ellipticals as listed in Faber *et al.* (1989). Finally, we adopt $cz_{Coma} = 7200$ km s^{-1} as the redshift for the Coma cluster in the CMB rest frame. The difference between a galaxy estimated distance and its redshift in the CMB frame then gives the galaxy peculiar velocity.

Table 5.1. The mean zero-points of the different correlations for the Coma cluster.

INT system: N = 46

Correlation	Zero-point	RMS
$\langle Mg_2 - 0.232 \log\sigma\rangle$	-0.245 ± 0.002	0.017
$\langle 1.2 \log\sigma - \log D\rangle$	1.701 ± 0.010	0.068
$\langle 5.2\, Mg_2 - \log D\rangle$	0.442 ± 0.015	0.098
$\langle -\log R_e + 0.314\, SB_e + 1.868 \log\sigma - 3.14\, Mg_2\rangle$	8.844 ± 0.013	0.085

Faber *et al.* system: N = 28

Correlation	Zero-point	RMS
$\langle Mg_2 - 0.232 \log\sigma\rangle$	-0.228 ± 0.004	0.019
$\langle 1.2 \log\sigma - \log D\rangle$	1.674 ± 0.012	0.064
$\langle 5.2\, Mg_2 - \log D\rangle$	0.502 ± 0.021	0.108
$\langle -\log R_e + 0.314\, SB_e + 1.868 \log\sigma - 3.14\, Mg_2\rangle$	8.760 ± 0.016	0.084

In Figure 5.1 we plot the ratio between the galaxy velocity relative to the CMB (as listed in Faber *et al.*) and the estimated distance versus Σ for Gregg's sample. This representation ensures that distance errors have equal weights for all the data points. Following Gregg's analysis, Malmquist-like bias and diameter bias corrections, as applied by Lynden-Bell *et al.*, have been left out in order to test the sensitivity of the 'raw' distance estimates. In the first panel we show Gregg's result: galaxies with larger Σ tend to have larger positive peculiar velocities as derived using $D - \sigma$. The probability that there is no correlation in the distribution of data points with $\Sigma > 0$ is $p = 0.003$. As discussed in Chapter 4, the observed trend is probably caused by an enhancement of surface brightness due to residual star formation, resulting in an increase in D and the consequent underestimation of the distance. The second panel shows the trend of peculiar velocities derived using $D - Mg_2$ with Σ. As expected, the resulting positive peculiar velocities are larger and the correlation with Σ is more noticeable (i.e. $p = 0.001$) since residual star formation affects now to both D and Mg_2, reducing further the corresponding distance estimates. Finally, we show in the third panel the results for the new age-independent relation. For this case $p = 0.269$, i.e. the trend of positive peculiar velocities towards larger values of Σ has been removed after correcting from residual star formation effects in the distance estimates.

The level at which star formation biases the distances derived from the usual indicators can be thus estimated by comparison with our new relation. In Table 5.2 we show the differences between the distances estimated using each indicator. It is important to stress that all three relations yield the same results for $\Sigma = 0$ galaxies. This agreement implies that: a) the age-independent relation is a reliable distance indicator for $\Sigma = 0$ ellipticals, and b) these objects have very similar stellar populations to the calibrating sample of Coma cluster ellipticals. However, for ellipticals exhibiting fine structure we conclude that $D - \sigma$ distances are, on average, underestimated by $20\% \pm 4\%$. The effect

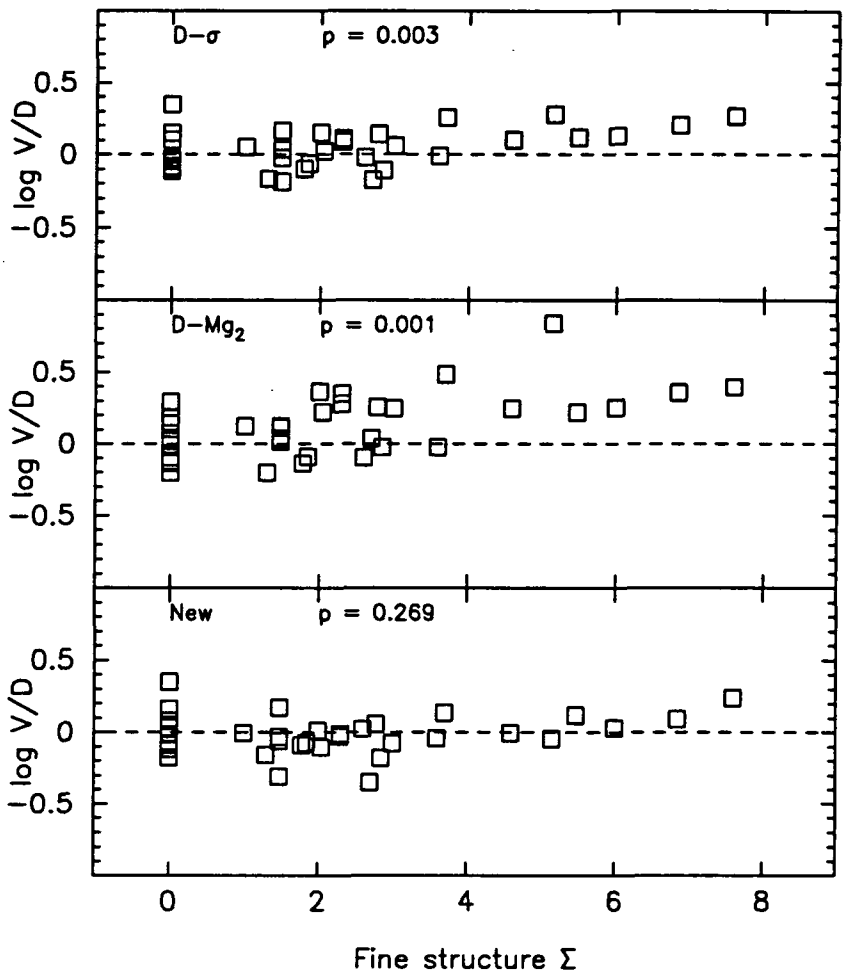

Figure 5.1. The ratio of the CMB velocity and the estimated distance plotted against the fine-structure index of Schweizer *et al.* for Gregg's sample. The upper panel is for distances derived from $D - \sigma$. The middle panel is for distances derived from $D - Mg_2$. The lower panel is for distances derived using the age-independent relation. Also shown in each panel is the probability associated with the Spearman rank correlation coefficient.

Table 5.2. Differences between the distance estimates (in log units) for Gregg's sample.

		V-band		
	N	log $(\langle d_e \rangle_{(D-\sigma)} / \langle d_e \rangle_{(D-Mg_2)})$	log $(\langle d_e \rangle_{(New)} / \langle d_e \rangle_{(D-\sigma)})$	log $(\langle d_e \rangle_{(New)} / \langle d_e \rangle_{(D-Mg_2)})$
$\Sigma = 0$	9	$+0.002 \pm 0.030$ dex	-0.005 ± 0.021 dex	-0.007 ± 0.050 dex
$\Sigma > 0$	25	$+0.123 \pm 0.027$ dex	$+0.080 \pm 0.016$ dex	$+0.203 \pm 0.042$ dex

amounts to 59% ± 14% for the distances derived from the $D - Mg_2$ relation. These variations are even larger for the B-band $D - \sigma$ and $D - Mg_2$ distance estimates, i.e. 28% ± 7% and 70% ± 20%, as expected according to the increasing effect of residual star formation towards shorter wavelengths shown in Section 4.4.

A potential problem that may arise when this relation is applied to heterogeneous data sets is that of systematic errors. Since these errors are, typically, ∼0.015 dex and ∼0.003 mag in the σ and Mg_2 measurements, respectively, their contribution to the uncertainty in the distances derived with the new indicator may amount to ∼9%. However, we stress that this age-independent relation corrects for an intrinsic systematic environmental bias that, in extreme cases, amounts to a ∼20% and ∼60% effect in the $D - \sigma$ and $D - Mg_2$ distance estimates, respectively.

5.3 THE PECULIAR MOTIONS OF ABELL 2199 AND ABELL 2634

Previous $D-\sigma$ work found surprisingly large negative peculiar velocities for Abell 2199 and Abell 2634 (Faber *et al.* 1989; Lucey *et al.* 1991). Faber *et al.*'s study of Abell 2199 was based on observations of 12 ellipticals. The σ measurements were made with the double spectrograph on the 200 inch. The quoted accuracy is 10%. D diameters were derived from g-band CCD images and no seeing corrections were applied. Their $D - \sigma$ relation for this cluster showed a large scatter, i.e. 0.14 dex as compared to the usually observed 0.09. From this data set, Faber *et al.* derived a peculiar velocity of -2919 ± 723 km s^{-1}.

Lucey *et al.* reported observations of 12 early-type galaxies in Abell 2199, 18 in Abell 2634 and 9 in Abell 194. Velocity dispersions were measured with the FLEX system (a plug-in fibre aperture-plate system) on the 4.2m William Herschel telescope. The fibre

diameter size was 1.8″. Overlap with previously published σ's (Faber *et al.* 1989; Lucey & Carter 1988) implied that the systematic error was less than 5%. D diameters were derived from V-band CCD images taken with both the INT and the JKT; seeing corrections were applied. For Abell 2199, this new $D-\sigma$ data yielded a peculiar velocity of -1800 ± 800 km s^{-1}. However, as compared to the Faber *et al.*'s measurements, their velocity dispersions were 10% smaller and the D diameters were 7.4% larger. This latter difference can be attributed to the inclusion of a seeing correction in Lucey *et al.*'s study. Both these offsets are in the sense that the Faber *et al.*'s data yield a larger negative peculiar velocity.

For Abell 2634, Lucey *et al.*'s $D-\sigma$ data gave a cluster distance that implied a highly significant peculiar velocity of -3400 ± 600 km s^{-1}. This result must be compared with the infrared Tully-Fisher work which gives a peculiar velocity of $+300 \pm 500$ km s^{-1} (Aaranson *et al.* 1986). These authors speculated that tidal stripping in the core of this cD dominated cluster may have caused a zero-point difference in the $D-\sigma$ relation, i.e. the large observed peculiar motion for Abell 2634 may be spurious.

The $D-\sigma$ results for Abell 2199 and Abell 2634 contrast with the measured peculiar velocities for most rich clusters, which are found to be not significantly different from zero. Although peculiar motions of a few hundred km s^{-1} can easily be masked within the measurement errors (typically $\sim$500 km s^{-1}), larger values appear to have been ruled out (Lucey & Carter 1988). To clarify these discrepancies we have made new observations of ellipticals and S0 galaxies in Abell 2199 and Abell 2634 that doubles the previously published sample sizes. The results discussed here are based on the analysis of the data set for elliptical galaxies listed in Table 2.12. The inclusion of the S0 galaxy sample does not significantly alter the conclusions reached in this Section.

5.3.1 New results for Abell 2199 and Abell 2634.

The $D-\sigma$, $D-Mg_2$ and new distance indicators for Abell 2199 and Abell 2634 are shown in Figure 5.2. The mean zero-points derived for each cluster are summarized in Table 5.3. The rms dispersions are similar to those found for other clusters.

To convert these zero-points into distance estimates we applied the equation [5.1]. The new σ and Mg_2 data for Abell 2199 and Abell 2634 are accurately zero-pointed onto the Coma measurements (see Section 2.3.3). Although these values have not been corrected from the aperture effect (Davies *et al.* 1987) such correction is very small (i.e. 1.5% in logσ and 1.8% in Mg_2) and does not significantly affect our conclusions. Also, we estimate that the diameter bias correction, as formulated by Lynden-Bell *et al.* is very similar in all three clusters and thus does not alter the following results. Comparison with the INT-system zero-points listed in Table 5.1 then yields distances of ~9450 km s^{-1}, ~9670 km s^{-1} ahd ~9060 km s^{-1} for Abell 2199, as derived from $D-\sigma$, $D-Mg_2$ and the new distance indicator, respectively (see Table 5.3). For Abell 2634 we measure ~9180 km s^{-1}, ~9000 km s^{-1} and ~9480 km s^{-1}, respectively. Hence, all three distance indicators yield very similar distances to both clusters (see Table 5.4). This agreement implies that the galaxies studied in Abell 2199 and Abell 2634 have very similar populations to the Coma cluster ellipticals used to zero-point our distance scale. This is as expected from our previous discussion on environmental effects since, for all three clusters, the galaxy samples include mostly ellipticals located in the cluster core.

The radial velocities of Abell 2199 and Abell 2634 in the local CMB rest frame are 8929 $\pm$ 183 km s^{-1} and 9025 $\pm$ 160 km s^{-1}. Therefore, our new $D-\sigma$ data imply peculiar velocities of -520 ± 490 km s^{-1} and -160 ± 500 km s^{-1} for Abell 2199 and Abell 2634, respectively. Both these values are considerably less than previous estimates and are

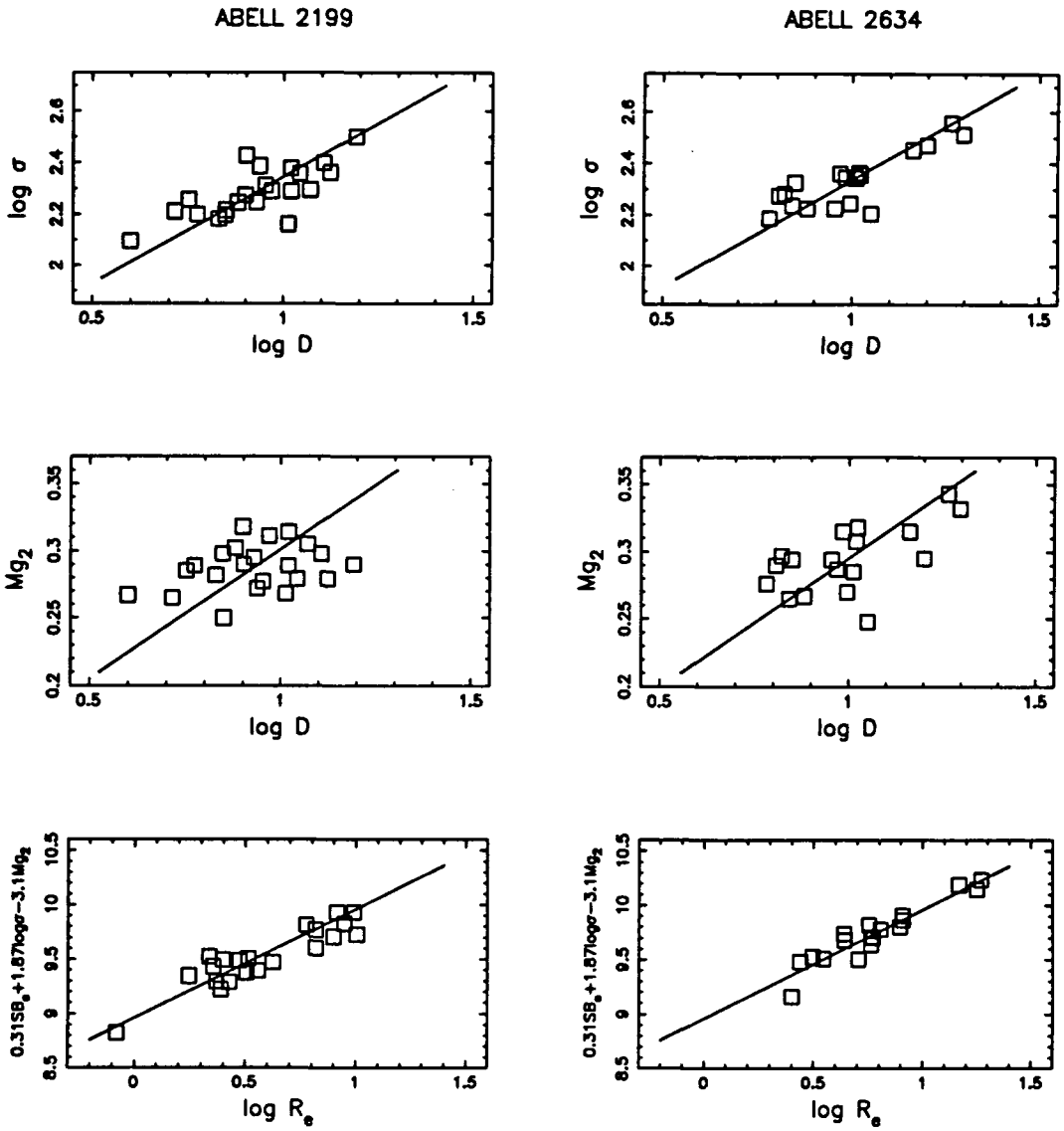

Figure 5.2. The $D-\sigma$, $D-Mg_2$ and new relations for Abell 2199 (left) and Abell 2634 (right).

Table 5.3. Zero-points and distance estimates for Abell 2199 and Abell 2634.

Abell 2199: N = 22

Distance Indicator	Zero-point	RMS	d_e (km s^{-1})
$\langle 1.2\ \log\sigma - \log D\rangle$	1.815 ± 0.021	0.097	9450 ± 490
$\langle 5.2\ Mg_2 - \log D\rangle$	0.566 ± 0.031	0.143	9670 ± 740
$\langle -\log R_e + 0.314\ SB_e + 1.868\ \log\sigma - 3.14\ Mg_2\rangle$	8.940 ± 0.026	0.117	9060 ± 540

Abell 2634: N = 18

Distance Indicator	Zero-point	RMS	d_e (km s^{-1})
$\langle 1.2\ \log\sigma - \log D\rangle$	1.803 ± 0.021	0.086	9180 ± 500
$\langle 5.2\ Mg_2 - \log D\rangle$	0.535 ± 0.032	0.130	9000 ± 770
$\langle -\log R_e + 0.314\ SB_e + 1.868\ \log\sigma - 3.14\ Mg_2\rangle$	8.960 ± 0.022	0.089	9480 ± 550

Table 5.4. Differences between the distance estimates (in log units) for the Abell 2199 and Abell 2634 samples.

Abell 2199

	log	log	log
N	$(\langle d_e \rangle_{(D-\sigma)} / \langle d_e \rangle_{(D-Mg_2)})$	$(\langle d_e \rangle_{(New)} / \langle d_e \rangle_{(D-\sigma)})$	$(\langle d_e \rangle_{(New)} / \langle d_e \rangle_{(D-Mg_2)})$
22	-0.010 ± 0.028 dex	-0.018 ± 0.015 dex	-0.028 ± 0.042 dex

Abell 2634

	log	log	log
N	$(\langle d_e \rangle_{(D-\sigma)} / \langle d_e \rangle_{(D-Mg_2)})$	$(\langle d_e \rangle_{(New)} / \langle d_e \rangle_{(D-\sigma)})$	$(\langle d_e \rangle_{(New)} / \langle d_e \rangle_{(D-Mg_2)})$
18	$+0.009 \pm 0.018$ dex	$+0.014 \pm 0.012$ dex	$+0.023 \pm 0.030$ dex

not significantly different from zero. These results are also supported from the distance determinations derived from the $D - Mg_2$ relation and our new distance indicator.

5.3.2 The causes of the discrepancy in the measured peculiar motions.

Our original sample includes 14 ellipticals and 15 S0 galaxies in common with Lucey *et al.*'s study. Although the above peculiar velocities were derived using only the sample of elliptical galaxies, the analysis of our S0 sample strongly supports these values. It seems therefore surprising that, despite the large overlap, the results derived in both studies differ so greatly. This suggests an intrinsic uncertainty in the accuracy of measurement of D and σ. In this Section we address a more detailed comparison of the individual D and σ measurements between this study and Lucey *et al.*'s work.

As shown in Section 2.3.2, our photometry is in excellent agreement with Lucey *et al.*'s values. The average difference between their D diameters and our new values is only -0.005 dex. The rms scatter is 0.008 dex. However, comparison of the INT σ data and the FLEX-based data shows that while the Abell 2199 galaxies are in very good agreement, i.e. an offset of 0.000 ± 0.015 dex (N = 11), the Abell 2634 galaxies show a sizable systematic offset, i.e. -0.048 ± 0.018 dex (N = 18) (Figure 5.3). This is in the sense that the FLEX data implies a significantly larger peculiar velocity for Abell 2634.

We have undertaken a detailed examination of both datasets to investigate the cause of this offset. Comparison of the line profiles of the galaxies with those of the night sky lines at various stages of the data reduction demonstrates that errors in the data reduction are not the cause of this offset. In addition, John Lucey has performed a new, independent reduction of the FLEX data and this is in good agreement with the previously published values. The CCD detector used with FLEX did suffer from poor charge transfer at the lowest count rates. While tests show that this is unlikely to account for the offset,

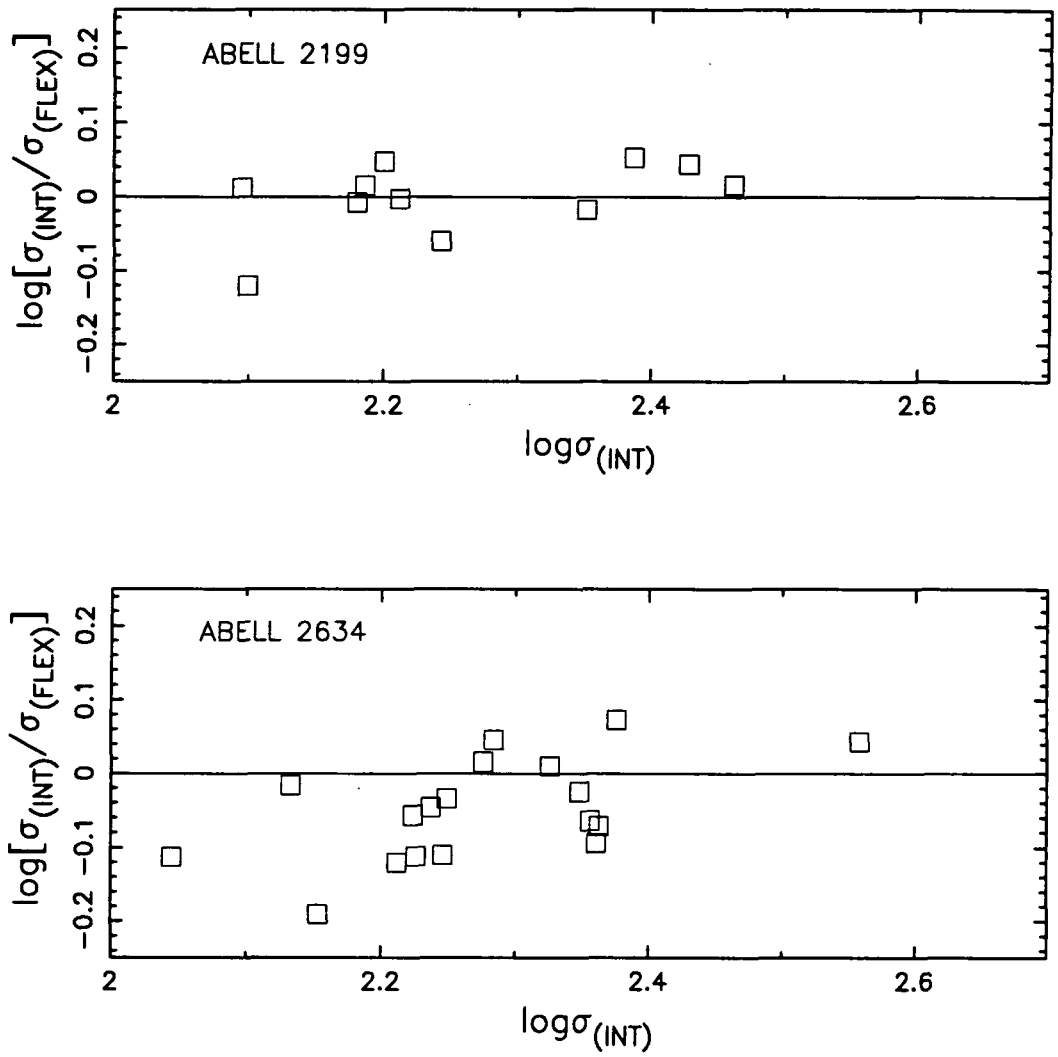

Figure 5.3. Comparison of the velocity dispersions measured in this study (INT) with those derived in Lucey *et al.* (1991) (FLEX) for elliptical galaxies in Abell 2199 (top panel) and Abell 2634 (bottom panel).

further investigations are in progress. Another possibility is that aperture size differences between the INT and the FLEX data are the cause of the observed offset. However once again this seems unlikely. Furthermore, for both the INT and FLEX runs the Abell 2199 and Abell 2634 galaxies were observed on the same nights and thus it is quite bizarre that an offset is present for one cluster and not for the other. So far we have been unable to find a satisfactory explanation for the offset.

A second factor that contributes to the observed differences with Lucey *et al.*'s measurements of peculiar velocities for both clusters is the zero-point calibration. Lucey *et al.* assumed that their FLEX σ data were in the same system as Dressler's σ measurements in Coma (listed in Davies *et al.* 1987). Using 26 Coma ellipticals they derived a median zero-point of 1.661 ± 0.013 dex. This value should be compared with our adopted Coma zero-point, i.e. 1.701 ± 0.010 dex. As discussed in Section 2.3.3, our new $D - \sigma$ data for Abell 2199 and Abell 2634 are accurately zero-pointed onto our INT system. Comparison between the INT and FLEX σ data for Abell 2199 then suggests that the $D - \sigma$ zero-point adopted by Lucey *et al.* may have been underestimated by $\sim$0.040 dex. Again, this is in the sense that their derived distance estimates imply larger negative peculiar motions for both clusters.

Therefore we conclude that the difference between the peculiar velocity of Abell 2199 derived in this study and that measured by Lucey *et al.* is mainly due to a different zero-point calibration. The larger difference observed for Abell 2634 simply reflects the systematic offset in the velocity dispersions measured in both studies. Since the cause of this offset is still unknown, the upper limit to the peculiar velocity of Abell 2634 remains relatively high.

5.3.3 The surface brightness bias question.

Lucey, Bower & Ellis (1991) first showed that, for a sample of Coma ellipticals, the residuals from the $D-\sigma$ relation depend on the galaxy effective surface brightness. The observed correlation is such that the brighter SB_e ellipticals ($SB_e \sim 18$ mag arcsec^{-2}) would indicate a distance that is ~25% greater than that derived from the fainter SB_e ellipticals ($SB_e \sim$ 21 mag arcsec^{-2}). Although Lynden-Bell *et al.* (1988) had previously noted that high surface brightness galaxies tend to yield systematically too large $D-\sigma$ distances, the correlation discussed here refers to ellipticals of normal surface brightness. A similar trend is also present in Lucey *et al.*'s (1991) sample of ellipticals in Abell 2199 and Abell 2634 although not at a significant level. These authors argued that this correlation arises because, at least for the Coma ellipticals, D does not give a precise edge-on view of the fundamental plane. They concluded that the derived distances to both clusters were not affected significantly by this surface brightness bias. Jorgensen *et al.* (1992) claimed, however, that this effect would introduce systematic errors of ~5% in the $D-\sigma$ distances. In this Section we discuss briefly the importance of such bias on our distance estimates to Abell 2199 and Abell 2634.

As discussed in Section 2.2.2, assuming all elliptical galaxies follow a $r^{\frac{1}{4}}$- density profile, then $\log D$ is not simply a linear combination of $\log R_e$ and SB_e (Phillips 1988). Hence, the $D-\sigma$ relation is expected to give a bent and slightly tilted edge-on view of the fundamental plane (FP). If the FP is linear and universally valid, then the use of the $D-\sigma$ relation will introduce systematic errors dependent on SB_e (Jorgensen *et al.*). In Figure 5.4 we show the residuals of the $D-\sigma$ and FP relations plotted versus SB_e for our sample of Coma ellipticals. The correlation found by Lucey, Bower & Ellis is shown in the top left panel. The trend with SB_e is, however, removed when the FP is used instead of $D-\sigma$ (bottom left panel). If the FP is indeed linear, then it is straightforward to predict

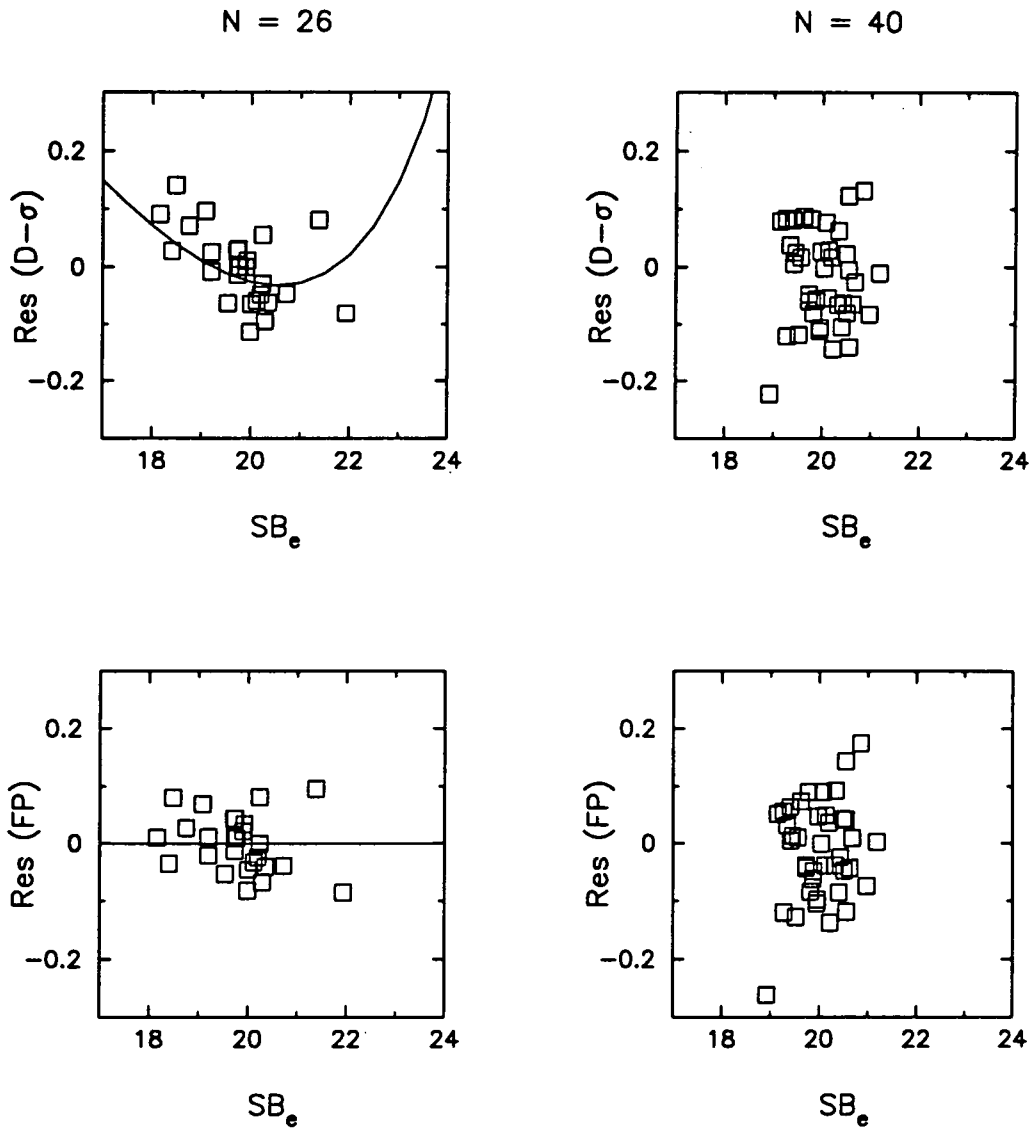

Figure 5.4. The residuals from the $D-\sigma$ and FP relations versus the effective surface brightness for our Coma sample. Left panels: ellipticals studied by Lucey, Bower & Ellis (N = 26). The solid lines represent the equation of the fundamental plane. Right panels: the remaining ellipticals in our sample (N = 40).

the surface brightness bias in the $D-\sigma$ relation. Following the same procedure used in Figure 2.5, we have superimposed onto the $D-\sigma$ residuals the equivalent line to the mean horizontal line drawn in the FP residuals plot. This line describes adequately the surface brightness bias present in the $D-\sigma$ data. Hence, galaxies with $19 > SB_e > 21$ mag arcsec^{-2} will tend to have systematically higher residuals in $D-\sigma$ as compared to the FP. As a result, the $D-\sigma$ distances to galaxy samples which *only* include ellipticals with such surface brightnesses will be systematically overestimated relative to a calibrating sample, such as our Coma sample, in which ellipticals of a wide range in SB_e are well represented. This analysis thus supports Jorgensen *et al.*'s conclusions in the sense that the FP is a slightly better distance indicator over a larger range in galaxy surface brightnesses. Both relations, however, would show no significant differences for galaxies with $19 < SB_e < 21$ mag arcsec^{-2}, as it can be seen for our sample of remaining Coma ellipticals (right panels). We note that the scatter in these plots is mainly dominated by differences in age of the stellar populations (see Section 4.3).

In Figure 5.5 we show the $D-\sigma$ and FP residual plots for our sample of ellipticals in Abell 2199 and Abell 2634. The observed lack of correlation for Abell 2634 ellipticals is consistent with the restricted range in SB_e characteristic of this sample. More interestingly, Abell 2199 shows a significant correlation of both the FP and $D-\sigma$ residuals with SB_e. A similar trend is also found in the S0 sample for this cluster. This implies that the surface brightness term of the FP for Abell 2199 is significantly larger than that for Coma. Using a least squares linear fit we obtain:

$$-\log R_e + 0.314\ SB_e + 1.14\ \log\sigma = -0.048(\pm 0.015)\ SB_e + 9.128. \qquad (5.2)$$

The scatter around the new FP for Abell 2199 is only $\sim$0.068 dex (i.e. $\sim$50% smaller than the observed scatter around $D-\sigma$ for the same sample). This new equation of the FP for Abell 2199 is shown in Figure 5.5 (solid lines). Again, the predicted effect on the $D-\sigma$

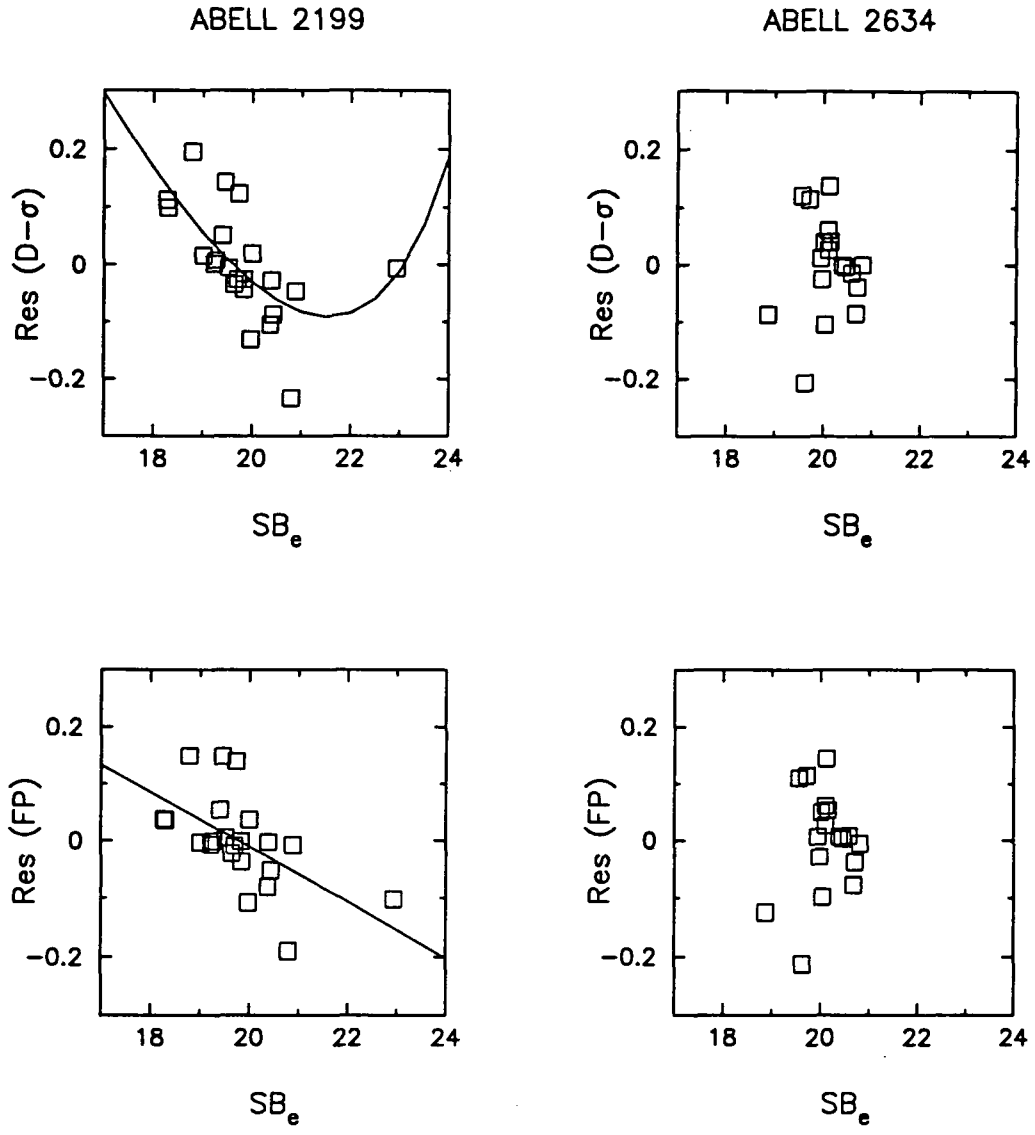

Figure 5.5. The residuals from the $D-\sigma$ and FP relations versus the effective surface brightness for our cluster sample. Left panels: ellipticals in Abell 2199 (N = 22). The solid lines represent the fundamental plane defined in equation [5.2]. Right panels: ellipticals in Abell 2634 (N = 18).

relation describes adequately the observed surface brightness bias. Clearly, it would be of great interest to investigate the reality of such surface brightness dependence in the FP of cluster ellipticals. New observations of large samples of ellipticals within a wide range of SB_e in several clusters would be thus very valuable. If confirmed, these results would question the assumed universality of the fundamental plane of elliptical galaxies.

Despite the observed differences between the FP and $D-\sigma$, the distances to Abell 2199 and Abell 2634 derived using both relations do not differ significantly. This is as expected giving the range of galaxy SB_e covered in both clusters. For Abell 2199, ellipticals cover a very similar range in SB_e to the calibrating Coma ellipticals and hence the surface brightness bias should be similar in both samples. For Abell 2634, most ellipticals have $19 < SB_e < 21$ mag arcsec^{-2}, for which no surface brightness bias is observed. The FP estimated distances to Abell 2199 and Abell 2634 are, respectively, 9160 ± 420 km s^{-1} and 9330 ± 490 km s^{-1}. Both values are in good agreement with the distances derived using the $D-\sigma$ relation.

5.4 THE PECULIAR MOTIONS OF FIELD ELLIPTICALS

Field elliptical galaxies show systematic differences in their global correlations compared to those located in rich clusters. In particular, de Carvalho & Djorgovski (1992b) have recently demonstrated that, using the relations for the cluster ellipticals as fiducial, field ellipticals tend to be too blue, have too low an Mg_2 index and too high a surface brightness at a fixed effective radius or luminosity. These systematic deviations are in the sense expected if the field ellipticals contain an admixture of younger stellar populations. Indeed, spectral synthesis studies have demonstrated the existence of an intermediate age stellar component in ellipticals located mostly in low-density environments (Bower *et al.* 1990).

As shown in Section 5.2, the presence of a younger stellar population affects the distances derived using both $D-\sigma$ and $D-Mg_2$, which tend to be systematically underestimated. This in turn translates into positive peculiar velocity measurements that are entirely spurious. In fact, Burstein, Faber & Dressler (1990), in their study on the reliability of the $D-\sigma$ distance indicator, note that the peculiar motions of field ellipticals with negative $\sigma - Mg_2$ residuals tend to be also positive. This is in the sense of the effect that residual star formation would have on both D and Mg_2. These authors argue, however, that, in order to underestimate the distances derived using $D-\sigma$ by $\sim$0.2 dex (see Figure 9 of their paper), the required amount of star formation would have to change the apparent B-magnitude by $\sim$0.65 mag, which in turn would change Mg_2 by $\sim$0.15 mag. Since such a large variation in Mg_2 is not observed they conclude that this age effect is weak and simply contributes to noise in the measured velocity field. However, as shown in Chapter 4, Bruzual's models predict that the change produced in Mg_2 is only $\sim$0.05 mag (see Figure 4.5), which is indeed consistent with the observed trend in the peculiar motions of field ellipticals with the $\sigma - Mg_2$ residuals. This strongly suggests that some of the positive peculiar velocities derived for Faber *et al.*'s (1989) field sample may be an artifact of stellar population effects.

In this Section we readdress the measurements of peculiar velocities for Faber *et al.*'s sample of field ellipticals (listed in Table 2.13). Following the approach adopted previously, this new analysis is based on the comparative study of the distance estimates derived using equation [5.1] for the $D-\sigma$, $D-Mg_2$ and our new, age-independent distance indicator. As shown in Sections 5.2 and 5.3, all three relations yield, on average, very similar distances to those elliptical galaxies which are most likely to have old, single-age stellar populations, i.e. those with $\Sigma = 0$ or located in the core of rich clusters. For ellipticals with recent star formation, the different sensitivity of each relation to the age effect induces a significant variation in the distance estimates. In Table 5.5 we show the

difference between the raw distance estimates derived using $D-\sigma$, $D-Mg_2$ and the new relation for our sample of field ellipticals. Clearly, there is no agreement between the three distance indicators. The observed differences are, however, remarkably similar to those observed for the sample of ellipticals with recent star formation (see Table 5.2).

So far in our analysis we have not applied any correction for the Malmquist-like bias. This selection bias potentially afflicts any diameter- or magnitude-limited sample of galaxies which are not located in rich clusters. As there are more galaxies at greater distances in any sample limited by diameter or apparent brightness, there will be more large/bright galaxies erroneously included in the sample from larger distances than there are galaxies omitted from the sample at smaller distances. Thus, these samples are contaminated by galaxies that are measured to have large D diameters for their σ or Mg_2. This generates the illusion that galaxies are nearer than their true distance and would generate spurious positive peculiar velocities. The effect is similar to the age effect here discussed. Hence, before reaching any conclusions on stellar population-induced peculiar motions for field ellipticals, we test whether the observed differences in the raw distance estimates shown in Table 5.5 can be explained as a result of this bias.

Lynden-Bell *et al.* (1988) show that the correction for this bias depends on the size of the dispersion in the distance indicator and on the true spatial distribution of galaxies. If the latter is parameterized as a power law in number density such that the number of field galaxies in an shell between r and $r+dr$ is $n(r)\ dr/r$, so that

$$n(r)\frac{dr}{r} \propto r^{\alpha-1}dr \tag{5.3}$$

then the correction for the bias is given by equation [2.11] of Lynden-Bell *et al.*:

$$d = d_e\ \exp\left[\left(\alpha+\frac{1}{2}\right)\right]\ \Delta^2 \tag{5.4}$$

Table 5.5. Differences between the distance estimates (in log units) for Faber *et al.*'s field sample.

	V-band		
	log	log	log
N	$(\langle d_e \rangle_{(D-\sigma)}/\langle d_e \rangle_{(D-Mg_2)})$	$(\langle d_e \rangle_{(New)}/\langle d_e \rangle_{(D-\sigma)})$	$(\langle d_e \rangle_{(New)}/\langle d_e \rangle_{(D-Mg_2)})$
77	$+0.102 \pm 0.013$ dex	$+0.076 \pm 0.008$ dex	$+0.178 \pm 0.021$ dex
Malmquist bias	+0.054	+0.010	+0.045

where Δ is the dispersion of the distance indicator (in natural logarithmic units), d_e is the raw estimate of the distance derived from equation [5.1] and d is the corrected value. The typical uncertainties in the $D-\sigma$, $D-Mg_2$ and new distance indicators are ~20%, ~30% and ~22%, respectively. Hence, for a uniform distribution ($\alpha = 3$) the effect can amount to a +12%, +27% and +15% correction in the distance estimates, respectively[2].

In Table 5.5 we also show the predicted differences in the distance estimates due to the correction for the Malmquist-like bias in the uniform distribution case. These differences simply reflect the variation in the correction applied to the raw distance estimates derived from different indicators. For instance, since the corrections for the $D-\sigma$ and $D-Mg_2$ relations amount to +0.049 dex and +0.103 dex, respectively, the expected difference between the two distance estimates due to Malmquist-like bias is ~0.054 dex. Clearly, this effect cannot provide an adequate explanation of the disagreement between the different distance indicators for field ellipticals. Thus the observed variations are not an artifact of the Malmquist-like bias. Rather they reflect an intrinsic variation in the galaxy properties of the field sample compared to the calibrating sample of Coma cluster ellipticals, as we show below (hereafter we focus our analysis on the 'raw' distance estimates).

According to our framework, the $D-Mg_2$ relation is an alternative form of the $D-\sigma$ relation where σ has been replaced by Mg_2 using the $\sigma - Mg_2$ relation, i.e.:

$$\{5.2\ Mg_2 - \log D\} = \{1.2\ \log\sigma - \log D\} + \frac{1.2}{0.232}\{Mg_2 - 0.232\ \log\sigma\} + \text{constant.}$$

Applying equation [5.1] we then obtain:

$$\log d_{e\ (D-\sigma)} - \log d_{e\ (D-Mg2)} = 5.2\,[\{Mg_2 - 0.232\log\sigma\} - \langle Mg_2 - 0.232\log\sigma\rangle_{\rm Coma}] \quad (5.5)$$

[2] The corrections are smaller for aggregates of galaxies, falling as $1/N$ when there are N galaxies with independently estimated distances d_e.

Hence, any difference between the raw distances estimated using $D-\sigma$ and $D-Mg_2$ for a given galaxy sample simply reflects an intrinsic variation in the zero-point of the $\sigma-Mg_2$ correlation for these galaxies, relative to the calibrating Coma sample. This correlation involves two distance-independent quantities and, therefore, should be free of any geometrical biases such as the Malmquist-like bias. It is possible however that, since this sample may be biased towards brighter galaxies, the probability of including ellipticals with younger stellar populations increases. Indeed, field ellipticals have, on average at a given σ, Mg_2 indices that are 0.020 ± 0.005 mag lower than those for Coma ellipticals. This is in the sense of the effect that residual star formation would have on Mg_2 (diluting the observed strength of the line index while probably leaving σ unaffected). This zero-point offset is the real cause of the observed differences between the $D-\sigma$ and $D-Mg_2$ distance estimates to field ellipticals. Using equation [5.5] we derive a difference:

$$\langle \log d_e \rangle_{(D-\sigma)} - \langle \log d_e \rangle_{(D-Mg_2)} = +0.102 \text{ dex.}$$

which is exactly the same value quoted in Table 5.5. Similarly, for elliptical galaxies with recent star formation ($\Sigma > 0$), the larger difference in the $D-\sigma$ and $D-Mg_2$ distance estimates simply reflects a larger mean offset in their $\sigma-Mg_2$ relation compared to Coma, i.e. -0.024 ± 0.006 mag. Cluster ellipticals and ellipticals with $\Sigma = 0$, however, show no significant systematic offset. For Abell 2199 and Abell 2634 galaxies, the difference in the $\sigma-Mg_2$ zero-point relative to Coma amounts to only $+0.002\pm0.006$ mag and -0.002 ± 0.005 mag, respectively. For ellipticals with $\Sigma = 0$ this offset is 0.000 ± 0.006. A similar argument can be also applied to the differences involving our new distance indicator since it is the result of a linear combination of the FP (which is equivalent to $D-\sigma$) and the $\sigma-Mg_2$ relation. We note that the above offsets cannot be explained in terms of systematic errors in the σ and Mg_2 measurements. These errors typically amount to $\sim$0.015 dex and $\sim$0.003

mag, respectively. Thus the largest possible contribution to the $\sigma - Mg_2$ offsets is only $\sim$0.006 mag.

If age is indeed the main effect responsible for the observed $\sigma - Mg_2$ zero-point variation, then our new, age-independent relation suggests that the distances to field ellipticals are, on average, underestimated by $\sim$19% and $\sim$50% as derived from $D - \sigma$ and $D - Mg_2$, respectively. This in turn implies that the inferred peculiar motions of field ellipticals will be systematically positive. In Figure 5.6 we plot the ratio between the galaxy velocity relative to the CMB and the estimated distance as a function of the radial velocity for each distance indicator. As expected, the peculiar velocities of field ellipticals derived using the $D - \sigma$ relation are, on average, systematically positive by $+17\% \pm 4\%$ of the galaxy velocity. The effect is significantly larger for the peculiar velocities derived using $D - Mg_2$, i.e. $+47\% \pm 7\%$. These results are similar to those obtained in Section 5.2 for the sample of ellipticals with residual star formation. However, when the new, age-independent relation is applied, the average peculiar velocities of field ellipticals amount to only $-2\% \pm 4\%$, i.e. the Hubble flow dominates the average motion of field galaxies. The environmental/age effect translates thus into a spurious positive component of the local peculiar velocity field [3].

5.5 IS THE COSMIC DRIFT A COSMIC MYTH?

Unusually large positive peculiar motions have been observed in the Hydra-Centaurus region (Lynden-Bell *et al.* 1988). These motions have been interpreted as a gravitationally generated bulk flow towards a very large and extended concentration of mass, i.e. the

[3] Note that this environmental effect is reduced to $\sim$10% for $D - \sigma$ distances after Malmquist-like bias correction is applied.

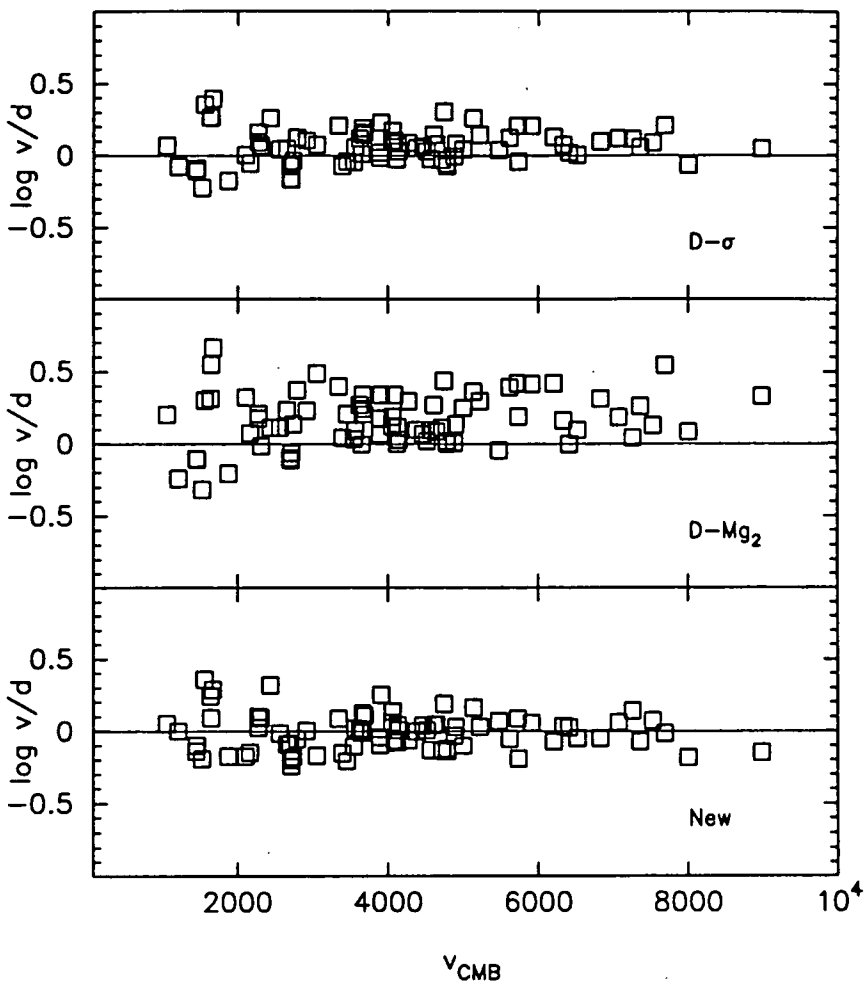

Figure 5.6. The ratio of the CMB velocity and the estimated distance versus the CMB velocity for each galaxy of our field sample of 77 E's. The upper panel is for distances derived from $D - \sigma$. The middle panel is for distances derived from $D - Mg_2$. The lower panel is for distances derived using the age-independent relation.

'Great Attractor'. Although the evidence for the positive velocities measured in this region seems compelling, an important question is the magnitude of this coherent large-scale flow. Since residual star formation mimics the effects of peculiar motions, the use of an un-biased, age-independent relation is required to fully understand the nature of the streaming motions.

In this Section we readdress the measurements of peculiar velocities towards the Great Attractor using Dressler, Faber & Burstein's (1991) sample of 136 early-type ellipticals in the Hydra-Centaurus region (hereafter HC sample). As in previous Sections, our analysis is based on the comparison of the distances estimated using $D-\sigma$, $D-Mg_2$ and our new distance indicator. To convert these distances into motions we then assume the simplest model for the local velocity field, i.e. a pure Hubble flow in the CMB rest frame.

The photometric data for Dressler, Faber & Burstein's sample were measured in the B-band. Hence, we first design an equivalent relation to our age-independent distance indicator in the B-band. To test the reliability of this new relation we extend our comparative analysis to other samples of cluster and field ellipticals listed in Faber *et al.* (1989). Dressler, Faber & Burstein have shown that their photometric and spectroscopic measurements for the HC sample are on the same system than Faber *et al.*'s measurements and have a similar accuracy. The cluster sample includes 80 ellipticals with good quality photometric data (i.e. class 1 or 2) located in Pisces, Abell 194, Perseus, Fornax, Virgo, C2345-28 and Abell 2199. The field sample includes all 78 elliptical galaxies listed in Table 2.13. Both the cluster and field samples can be simply regarded as control samples to test the internal consistency among the various distance indicators.

5.5.1 The new, age-independent distance indicator in the B-band.

Following the discussion in Chapter 4 we design here a new relation in the B-band for

ellipticals which is independent of mean stellar age. There are no published effective radii (R_e) and surface brightnesses (SB_e) for the HC sample. Hence we adopt here the $D-\sigma$ formalism rather than the 'fundamental plane'. Since:

$$\log D = \log R_e - 0.32\ SB_e + \text{constant}$$

(equation [2.2]), the effect of a younger stellar component on the B-band D diameter is such that:

$$\Delta \log D = -0.32\ \Delta SB_e = -0.32 \times (14\ \Delta Mg_2).$$

(see Section 4.4). The new, age-independent distance indicator combines the $D-\sigma$ and $\sigma - Mg_2$ relations so that the age effect cancels out, i.e.:

$$\{-\log D + 1.2\ \log\sigma\} - 0.32 \times 14\{Mg_2 - 0.232\ \log\sigma\} = \text{constant},$$

or, equivalently:

$$-\log D + 2.2\ \log\sigma - 4.5\ Mg_2 = \text{constant}. \qquad (5.6)$$

This relation allows distances to be estimated with an uncertainty of ~25%. The larger scatter, as compared to the equivalent V-band distance indicator, arises from the greater contribution of measurement errors due to the new coefficients of the $\log\sigma$ and Mg_2 terms. The zero-points of all three distance indicators in the B-band were derived from the same sample of 28 Coma ellipticals used in the V-band case and are summarized in Table 5.6. The adopted zero-point for $D-\sigma$ is the same value used by Lynden-Bell *et al.* (1988).

5.5.2 New peculiar velocity measurements in Hydra-Centaurus.

In Table 5.7 we show the difference between the raw distance estimates derived using $D-\sigma$, $D-Mg_2$ and our new relation for the cluster, field and HC galaxy samples. All distances have been calculated applying equation [5.1] (using the B-band Coma zero-points listed

Table 5.6. The mean zero-points of the different correlations for the Coma cluster.

Faber *et al.* system (B-band): N = 28

Correlation	Zero-point	RMS
$\langle Mg_2 - 0.232\ \log\sigma\rangle$	-0.228 ± 0.004	0.019
$\langle 1.2\ \log\sigma - \log D\rangle$	2.462 ± 0.012	0.064
$\langle 5.2\ Mg_2 - \log D\rangle$	1.291 ± 0.020	0.105
$\langle -\log D + 2.2\ \log\sigma - 4.5\ Mg_2\rangle$	3.388 ± 0.023	0.118

Table 5.7. Differences between the distance estimates (in log units) for the cluster, field and HC samples.

		B-band		
	N	log $(\langle d_e \rangle_{(D-\sigma)} / \langle d_e \rangle_{(D-Mg_2)})$	log $(\langle d_e \rangle_{(New)} / \langle d_e \rangle_{(D-\sigma)})$	log $(\langle d_e \rangle_{(New)} / \langle d_e \rangle_{(D-Mg_2)})$
Cluster	80	-0.011 ± 0.016 dex	-0.011 ± 0.013 dex	-0.022 ± 0.029 dex
Field	78	$+0.102 \pm 0.013$ dex	$+0.087 \pm 0.011$ dex	$+0.189 \pm 0.025$ dex
HC	136	$+0.117 \pm 0.013$ dex	$+0.100 \pm 0.008$ dex	$+0.217 \pm 0.021$ dex

in Table 5.6). The results for the cluster and field samples are in excellent agreement with those previously reported in Sections 5.3 and 5.4. This implies that the new B-band age-independent relation is as reliable as its equivalent in the V-band. Note that the observed variations for the field sample are slightly larger than those derived in the V-band, as expected according to the increasing effect of residual star formation towards shorter wavelengths discussed in Section 4.4. More interestingly, all three distance indicators show a remarkable lack of agreement for the HC sample. The observed differences in the distance estimates are analogous to those observed for ellipticals with residual star formation and for the field sample. In Section 5.4 we showed that the Malmquist-like bias cannot account for the whole effect in single galaxies. The correction for this bias should be even less noticeable for the HC sample since most of these galaxies are located in groups.

The real cause of the observed differences is an intrinsic variation in the galaxy stellar properties of this sample as compared to the Coma sample (see Section 5.4). Indeed, elliptical galaxies in the Hydra-Centaurus region have, on average at a given σ, Mg_2 indices that are 0.022 ± 0.004 mag lower than their counterparts in the Coma cluster. These offsets for all four galaxy samples are shown in Figure 5.7. If the age effect is the main responsible for the observed $\sigma - Mg_2$ zero-point offset, then our new, age-independent relation suggests that the distances to HC ellipticals are, on average, underestimated by as much as $\sim$26% and $\sim$65%, as derived from $D - \sigma$ and $D - Mg_2$ respectively. This in turn implies that the inferred positive peculiar motions may be entirely spurious.

To illustrate this result we plot in Figure 5.8 the ratio between the galaxy velocity relative to the CMB and the estimated distances as a function of the galaxy recession velocity for the HC sample. The average peculiar velocities derived using $D - \sigma$ and $D - Mg_2$ are, respectively, $+24\% \pm 4\%$ and $+62\% \pm 6\%$ of the galaxy recession velocity. These results are in very good agreement with Dressler & Faber's (1990) study. However, when

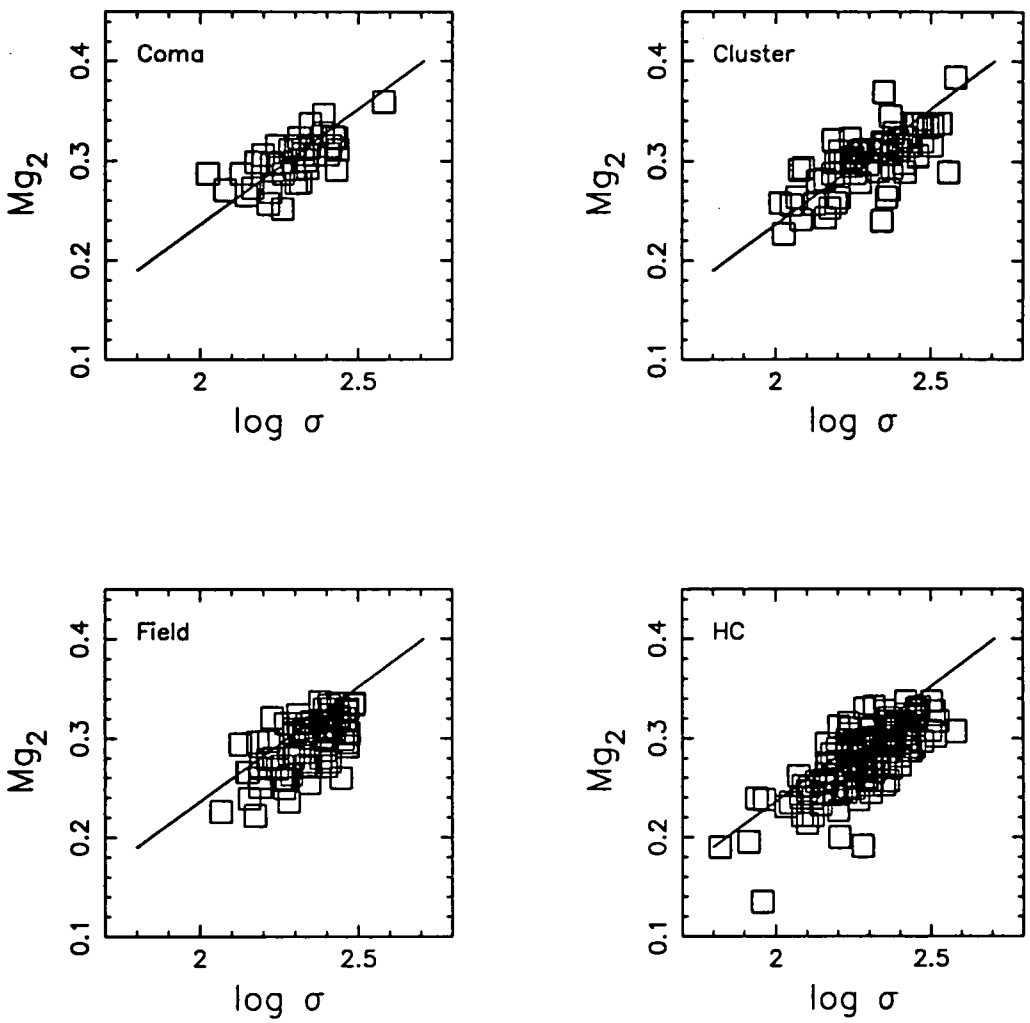

Figure 5.7. The $\sigma - Mg_2$ relation for all samples of ellipticals analysed in this section (data from Faber *et al.* 1989 and Dressler, Faber & Burstein 1991). The solid line represents the linear fit zero-pointed to the Coma cluster.

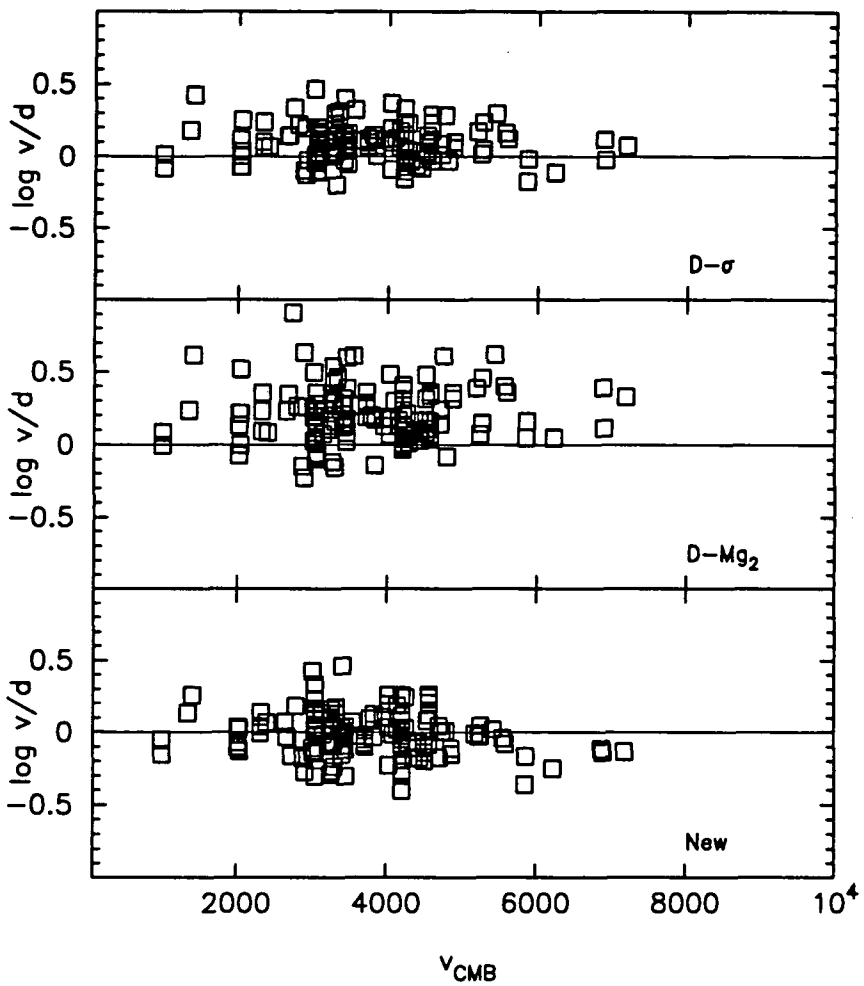

Figure 5.8. The ratio of the galaxy CMB velocity and the estimated distance versus the CMB velocity for early-type galaxies in Hydra-Centaurus. The upper panel is for distances derived from $D - \sigma$. The middle panel is for distances derived from $D - Mg_2$. The lower panel is for distances derived using the age-independent relation.

Table 5.8. Average ratios between galaxy CMB velocities and estimated distances for the cluster, field and HC samples.

		B-band		
	N	$\langle \log(v/d_e) \rangle_{D-\sigma}$	$\langle \log(v/d_e) \rangle_{D-Mg2}$	$\langle \log(v/d_e) \rangle_{New}$
Cluster	80	$+0.009 \pm 0.016$ dex	$+0.021 \pm 0.021$ dex	-0.001 ± 0.021 dex
Field	78	$+0.080 \pm 0.014$ dex	$+0.182 \pm 0.022$ dex	-0.007 ± 0.016 dex
HC	136	$+0.093 \pm 0.014$ dex	$+0.209 \pm 0.017$ dex	-0.007 ± 0.016 dex

the new, age-independent relation is applied, the average peculiar velocities of galaxies in Hydra-Centaurus are found to be not significantly different from zero, i.e. $-2\% \pm 4\%$. These measurements are summarized in Table 5.8.

Therefore, from the study of early-type galaxies alone, we find no evidence for the reality of large-scale positive streaming motions towards a 'Great Attractor'. Previous measurements of positive peculiar velocities in the Hydra-Centaurus region are found to be the result of a bias in the usual distance indicators induced by an intrinsic variation in the stellar population properties of these galaxies. This difference is apparent as a zero-point offset in the $\sigma - Mg_2$ relation relative to the calibrating sample of Coma cluster ellipticals. If such offset is caused by residual star formation, then the use of our age-independent distance indicator demonstrates that there is no difference in the peculiar velocities of elliptical galaxies in the Hydra-Centaurus region, as compared to those located in rich clusters or in the general field. We note, however, that these results alone do not prove conclusively the spurious nature of the 'Great Attractor'. Evidence for a large-scale, large-amplitude flow in Hydra-Centaurus is also supported by the peculiar motions of spiral galaxies in this region (Mathewson, Ford & Buchhorn 1992; Courteau *et al.* 1993). Clearly, a similar, detailed study of the environmental effects on the distance indicators for spiral galaxies is needed before we can be certain that these results provide a better understanding of the peculiar velocity field in the nearby universe.

5.6 CONCLUSIONS

The results presented in this Chapter can be summarized as follows:

(i) To test our new, age-independent distance indicator, we have reanalysed the peculiar velocities of Schweizer *et al.*'s (1990) sample of ellipticals with residual star formation. We have shown that the large, positive peculiar motions previously derived using $D-\sigma$ and $D-Mg_2$ for these galaxies are eliminated. These spurious measurements are caused by the underestimation of galaxy distances due to the effect of residual star formation on the D and Mg_2 parameters. By comparison with our new relation we have estimated that $D-\sigma$ distances are, on average, underestimated by 18%. This effect amounts to 54% for the distances derived from the $D-Mg_2$ relation.

(ii) Using a new sample of 40 ellipticals in Abell 2199 and Abell 2634 we have readdressed the large, negative peculiar velocities previously measured for both clusters. Our analysis included the $D-\sigma$, $D-Mg_2$ and the new relations. All three distance indicators were found to yield very similar distances to both clusters. This agreement implies that these galaxies have very similar stellar populations to the Coma cluster ellipticals used to zero-point our distance scale. The peculiar velocities derived using our new $D-\sigma$ data for Abell 2199 and Abell 2634 are -520 ± 490 km s^{-1} and -160 ± 500 km s^{-1}, respectively. Both these values are considerably less than previous estimates and are not significantly different from zero.

(iii) We have analysed the peculiar velocities of field ellipticals. Unlike the results for cluster ellipticals, we found a remarkable lack of agreement between the different distance indicators. This is in the sense that the raw $D-\sigma$ and $D-Mg_2$ distances are, on average, systematically underestimated by $\sim$19% and $\sim$50%, respectively, as compared to the values derived using our new relation. This result cannot be caused by the Malmquist-like bias but is qualitatively in agreement with the growing evidence that field ellipticals have, on average, slightly younger stellar populations than their cluster counterparts. Using the raw $D-\sigma$ and $D-Mg_2$

distances we have shown that field galaxies appear to have, on average, peculiar velocities of $+17\% \pm 4\%$ and $+47\% \pm 7\%$ of the galaxy velocity, respectively. However, when the new, age-independent distance indicator is applied, the derived average peculiar velocity is only $-2\% \pm 4\%$. The environmental-dependent effect translates thus into a spurious positive component of the local peculiar velocity field.

(iv) Following the discussion on the derivation of the new distance indicator, we have designed a similar relation in the B-band that combines the D, σ and Mg_2 parameters. We have used this new relation to readdress the peculiar velocities of Dressler, Faber & Burstein's (1991) sample of early-type galaxies in Hydra-Centaurus. These galaxies appear to have average peculiar velocities of $+24\% \pm 4\%$ and $+62\% \pm 6\%$ of the galaxy velocity, as derived from the raw $D-\sigma$ and $D-Mg_2$ distance estimates, respectively. However, when our new relation is applied, the derived average peculiar velocity is only $-2\% \pm 4\%$. If confirmed, this result will severely challenge the reality of the 'Great Attractor'.

6 CONCLUSIONS AND FUTURE WORK

6.1 CONCLUSIONS

In this thesis, we set out to study the effect of the environment on the distance indicators for elliptical galaxies. In particular, we wished to investigate if the $D - \sigma$ and $D - Mg_2$ relations were affected by any systematic differences in the stellar populations of ellipticals located in high- and low-density environments. The final goal of this study was to test the reality of the large peculiar velocities measured in the local universe as derived using these relations. The research leading to the conclusions presented here was carried out in three stages.

We started this study with a general analysis of the observed correlations between the global parameters of elliptical galaxies. Our analysis was based on a new phenomenological framework of galaxy properties. We showed that, despite the wide variety of observed correlations, only three provide independent information on the overall structure and stellar population of elliptical galaxies, i.e. the virial theorem, the mass-radius relation and the metallicity-velocity dispersion relation. The implications of these three fundamental relations for current theories of galaxy formation and evolution were briefly discussed. The results derived from this work are summarized in Section 6.1.1.

The analysis of the global correlations provided the necessary background for the next stage of our study: to assess the level of any environmental dependence in the most widely used distance indicators for elliptical galaxies, i.e. the $D-\sigma$ and $D-Mg_2$ relations. To test this dependence we compared the ellipticals that reside in the core with those in the halo of the Coma cluster. By studying the variations within one cluster, we avoided the difficulty of decoupling effects induced by distance errors from those due to real environmental differences. Both distance indicators were found to show an environmental dependence, consistent with the hypothesis that star formation continued to a more recent epoch in some halo ellipticals. This pointed out towards systematic effects in the measurements of peculiar motions as derived using $D-\sigma$ or $D-Mg_2$ for ellipticals located in different environments. Using our framework of galaxy properties, we designed a new, age-independent distance indicator to correct for this environmental effect on the measurements of peculiar motions. A summary of these results is presented in Section 6.1.2.

Finally, we used the new distance indicator to readdress previous measurements of large peculiar velocities in both the cluster and field environments. We found no evidence for the reality of such large peculiar motions derived using the $D-\sigma$ and $D-Mg_2$ relations. In particular, we showed that, for both distance indicators, the environment-dependent effect translates into a spurious positive component of the local peculiar velocity field. This effect may provide a simple explanation of the large positive peculiar motions observed towards the Great Attractor. These results are summarized in Section 6.1.3.

6.1.1 Fundamental Relations.

We have shown that the fundamental plane of giant elliptical galaxies is not uniformly populated. Giant ellipticals are located in a relatively narrow band which is not the result

of selection effects. This implies a second constraint between scale length and galaxy mass in addition to the virial theorem. The observed $L - R_e$, $L - I_e$, $L - \sigma$ and $I_e - R_e$ correlations are simply the projections of this band onto the different coordinate planes.

We have developed a simple framework to describe the structure and stellar content properties of giant ellipticals. In our framework there are only three fundamental relations: $M \propto R \langle v^2 \rangle$, $M \propto R^\zeta$ and $Z \propto \langle v^2 \rangle^\xi$. The coefficient ξ is uniquely determined from the observations. If Mg_2 is adopted as metallicity indicator then $\xi = 0.11$. The coefficient ζ depends, however, on the assumed variations of the mass-to-light ratio and the effective collapse factor with galaxy mass. We have assumed $M/L \propto M^\eta$ and $R/R_e \propto M^\lambda$. The conventional approach is to assume that the effective collapse factor is constant, i.e. $\lambda = 0$ (or, equivalently, giant ellipticals are baryon dominated). In this case we find that $\zeta = 1.6$ and $\eta = 0.27$. However, there is a whole host of other valid solutions for the $\{\zeta, \eta, \lambda\}$ values. All the observed correlations for giants are consistently derived as linear combinations of these fundamental relations.

We have demonstrated that this framework can also successfully describe the global correlations of dwarf elliptical galaxies. Our framework provides new insights into the differences and similarities between the two galaxy types. In particular, the observed universality of the luminosity- and metallicity-velocity dispersion correlations strongly suggests a simple solution within our framework in which ζ, ξ and η adopt the same values for both dwarf and giant ellipticals. In this case, the dependence of R/R_e on galaxy mass is the only difference between the two galaxy families.

We have discussed the results of our observational framework within a simple picture of galaxy formation based on the hierarchical clustering scenario and the galactic wind model. For giant ellipticals, we have shown that this theoretical picture is not consistent with the fundamental relations derived under the assumption of self-gravitation

(i.e. $R = R_e$). Theory and observations can be reconciled in a simple way if both dwarf and giant ellipticals are assumed to be dark matter dominated. For dwarf ellipticals, this theoretical picture provides a consistent explanation of the observed fundamental properties provided that R/R_e is constant. This result suggests that these systems may have simply formed as a direct result of the initial density fluctuations in a CDM universe. However, for giant ellipticals we find that R/R_e must decrease with galaxy mass, i.e. the luminous matter in giant ellipticals is apparently less concentrated inside their dark halos with increasing mass. This effect suggests a different origin for giant ellipticals in which mergers may have played a determinant role.

6.1.2 Environmental Effects.

To assess the level of any environmental dependence in the distance indicators for elliptical galaxies, we have compared the $D - \sigma$ and $D - Mg_2$ relations for ellipticals located in the core and the halo of the Coma cluster. We have shown that these relations possess a small environmental effect. At a fixed σ or Mg_2, ellipticals located in the cluster halo have, on average, larger D diameters by 0.042 ± 0.023 dex or 0.122 ± 0.035 dex, respectively. The halo ellipticals also have a significantly larger scatter about both relations. For completeness, the environmental effect on the $\sigma - Mg_2$ relation has also been analysed. We have shown that halo ellipticals have, on average for a given σ, lower Mg_2 by 0.016 ± 0.005 mag compared to core ellipticals. All the above results are qualitatively in agreement with the differences found in previous studies between field and cluster ellipticals. Hence, while the environmental dependence of the $D - \sigma$ zero-point is not significant in our data, the observed offset in the $D - Mg_2$ zero-point provides a strong argument against the use of this relation as a distance indicator. In both relations, the environmental-dependent effect translates into spurious 'peculiar motions' of $\sim$700 km s^{-1} and $\sim$2100 km s^{-1}, respectively, for the Coma cluster.

We have investigated the possibility that the observed offsets in the $D-\sigma$, $D-Mg_2$ and $\sigma - Mg_2$ relations are caused by star formation continuing to a more recent epoch in some halo ellipticals. Bruzual's evolutionary population synthesis models have been used to predict the effect of an intermediate-age stellar population on the photometric diameter D and the Mg_2 index. We have demonstrated that all the observed offsets are consistent with this hypothesis.

Using our framework of galaxy properties in combination with Bruzual's models, we have designed a new distance indicator for ellipticals which is independent of mean stellar age. The new relation is derived as a linear combination of the fundamental plane and the $\sigma - Mg_2$ relation such as the predicted age effect cancels out. The zero-point of this age-independent distance indicator varies by only 0.004 ± 0.023 dex between the core and halo samples. This new relation allows distances to be determined with an uncertainty of $\sim$20 per cent, comparable to the most accurate methods used for elliptical galaxies.

We have demonstrated that correlated errors is the main cause of the observed trend in the $D - \sigma$ versus $D - Mg_2$ residuals plot (the $\delta - \delta$ diagram). This diagram is simply a consequence of σ and Mg_2 not being independently related to D (or luminosity). We have also shown that the effect of an intermediate-age stellar population provides a plausible explanation to the observed differences in the $\delta-\delta$ diagrams for ellipticals located in high- and low-density environments.

6.1.3 Peculiar Motions.

To test our new, age-independent distance indicator, we have reanalysed the peculiar velocities of Schweizer *et al.*'s (1990) sample of ellipticals with residual star formation. We have shown that the large, positive peculiar motions previously derived using $D - \sigma$ and $D - Mg_2$ for these galaxies are eliminated. These spurious measurements are caused by

the underestimation of galaxy distances due to the effect of residual star formation on the D and Mg_2 parameters. By comparison with our new relation we have estimated that $D-\sigma$ distances are, on average, underestimated by 18%. This effect amounts to 54% for the distances derived from the $D-Mg_2$ relation.

Using a new sample of 40 ellipticals in Abell 2199 and Abell 2634 we have readdressed the large, negative peculiar velocities previously measured for both clusters. Our analysis included the $D-\sigma$, $D-Mg_2$ and the new relations. All three distance indicators were found to yield very similar distances to both clusters. This agreement implies that these galaxies have very similar stellar populations to the Coma cluster ellipticals used to zero-point our distance scale. The peculiar velocities derived using our new $D-\sigma$ data for Abell 2199 and Abell 2634 are -520 ± 490 km s^{-1} and -160 ± 500 km s^{-1}, respectively. Both these values are considerably less than previous estimates and are not significantly different from zero.

We have analysed the peculiar velocities of field ellipticals. Unlike the results for cluster ellipticals, we found a remarkable lack of agreement between the different distance indicators. This is in the sense that the raw $D-\sigma$ and $D-Mg_2$ distances are, on average, systematically underestimated by $\sim$19% and $\sim$50%, respectively, as compared to the values derived using our new relation. This result cannot be caused by the Malmquist-like bias but is qualitatively in agreement with the growing evidence that field ellipticals have, on average, slightly younger stellar populations than their cluster counterparts. Using the raw $D-\sigma$ and $D-Mg_2$ distances we have shown that field galaxies appear to have, on average, peculiar velocities of $+17\% \pm 4\%$ and $+47\% \pm 7\%$ of the galaxy velocity, respectively. However, when the new, age-independent distance indicator is applied, the derived average peculiar velocity is only $-2\% \pm 4\%$. The environmental-dependent effect translates thus into a spurious positive component of the local peculiar velocity field.

Following the discussion on the derivation of the new distance indicator, we have designed a similar relation in the B-band that combines the D, σ and Mg_2 parameters. We have used this new relation to readdress the peculiar velocities of Dressler, Faber & Burstein's (1991) sample of early-type galaxies in Hydra-Centaurus. These galaxies appear to have average peculiar velocities of $+24\% \pm 4\%$ and $+62\% \pm 6\%$ of the galaxy velocity, as derived from the raw $D - \sigma$ and $D - Mg_2$ distance estimates, respectively. However, when our new relation is applied, the derived average peculiar velocity is only $-2\% \pm 4\%$. If confirmed, this result will severely challenge the reality of the 'Great Attractor'.

6.2 DIRECTIONS FOR FUTURE WORK

In the discussion below we outline a future research programme to further investigate the results presented in this thesis. In particular, these new studies will allow us to test our conclusions on the origin of the 'fundamental plane' (FP) and the nature of the observed peculiar motions towards the Great Attractor.

6.2.1 The origin of the FP.

The FP provides a very suitable description of the overall structure of spheroidal systems (see also BBF), and can be regarded as an equivalent tool to the H-R diagram for stars. Several groups have already started to study the evolution of galaxies on this plane from $z \sim 0.5$ to the present epoch. However, our understanding of the physical mechanisms involved is still in its very early stages. The tests here described focus on three different aspects of the FP: the tilt, the scatter and the locus occupied by different types of spheroidal systems.

6.2.1.1 The tilt of the FP.

The tilt of the FP implies a systematic variation either in the IMF or the dark and luminous matter distribution with galaxy mass (Faber *et al.*, 1987; Djorgovski 1991; BBF; Renzini & Ciotti 1993). We have argued that, in the first case, the required bottom-heavy IMF for massive, metal-rich ellipticals goes the wrong way with respect to the need of producing the metallicity-velocity dispersion relation, and thus favoured a dark matter origin of the FP tilt. This second possibility requires that the ratio between the effective radii of the mass and light distributions (R_H/R_e) decreases by a factor $\sim$10 between the faint and bright ellipticals, i.e. dissipation decreases along the plane.

Unlike the IMF origin, the dark matter origin of the tilt is potentially testable by observations. Renzini & Ciotti (1993) have shown that if the dissipation picture is correct the galaxy σ-gradients should be significantly steeper at the bright end of the FP than at the faint end. Radial σ-gradients for bright ellipticals ($-23 < M_V < -20.5$) have already been measured (e.g. Franx 1988). We have recently been granted telescope time at La Palma to obtain new long-slit spectroscopic observations of faint ellipticals ($-20.5 < M_V < -18$). This combined data set will allow us to test if the interpretation of the FP tilt put forward in this thesis is correct.

6.2.1.2 The distribution of different galaxy types on the FP.

We have shown that the distribution of galaxies on the FP implies an intrinsic relation between galaxy mass and radius. This is of special interest because of the information it provides on galaxy formation. The slope of this relation was found to be adequately reproduced by the CDM hierarchical clustering model (see also Faber 1982; Blumenthal *et al.* 1984). However, this model predicts a significantly larger scatter to that observed (Cole & Kaiser 1989). It would be possible to reconcile both theory and observations if,

as envisaged by Faber (1982), the different morphological types are stratified along lines of constant ν (here ν denotes the initial amplitude of the density fluctuations from which galaxies were originated). This would be the case if, for instance, the transition from the spheroid-forming to disk-forming regimes occurs at a critical pressure or surface density (Evrard 1989).

A first step to test these ideas is to study the distribution of a large, homogeneous sample of cluster S0 galaxies on the FP. These objects occupy a transitional position in the Hubble sequence of galaxy types. If S0 galaxies are indeed the result of smaller amplitudes of the initial density fluctuations, then S0's should be significantly offset from the main relation defined by the ellipticals on the FP. This test is part of an on-going project to study the global properties of S0 galaxies.

6.2.1.3 Sources of scatter around the FP.

The scatter around the FP is mainly caused by intrinsic differences in galaxy M/L at a given mass (Faber *et al.* 1987). The understanding of this scatter is of fundamental importance to reduce the uncertainty and systematic effects on the distance estimates derived using the FP (or FP-related distance indicators such as $D - \sigma$ and $D - Mg_2$). There are two main factors that contribute to variations in M/L. The first one, discussed in detail in this thesis, is the presence of a younger component in the stellar populations of ellipticals located predominantly in low-density environments (see also de Carvalho and Djorgovski 1992). The second factor is related to the effect of rotational support on the mass estimates. It is now accepted that bright ellipticals tend to be more supported by velocity anisotropy and show 'boxy' isophotes, while faint ellipticals are oblate 'disky' systems flattened by rotation. Neglect of rotation leads to a significant underestimate of M/L for these rotating spheroidal systems (BBF).

An indirect measurement of a system's rotation is provided by the c_4 parameter (Bender 1992). Although there seems to be a trend between the residuals from the FP and c_4, samples so far studied are relatively sparse to provide a conclusive answer (Jorgensen *et al.* 1993). We intend to measure the c_4 parameter for our sample of 66 ellipticals in the Coma cluster. This study is complemented by the analysis of the Coma S0 galaxy sample described in Section 6.2.3.

6.2.2 The positive peculiar motions in the Hydra-Centaurus region.

Although recent Tully-Fisher studies support the picture of positive flow velocities towards the Great Attractor (Courteau *et al.* 1993), there is new evidence that *both* the $D-\sigma$ *and* Tully-Fisher distance indicators are affected by intrinsic differences in the stellar populations of galaxies in the Hydra-Centaurus region (Campos *et al.* 1994). In this thesis we have shown that, in order to correct for the age effect, the distance indicator relations need to incorporate line strength (or colour) terms or simply use infrared photometry. The small correction required in the K band naturally suggests the use of the FP in the near infrared as a plausible alternative to the new distance indicators we have designed in the V and B bands. This K band distance indicator would also benefit from a lower sensitivity to both systematic errors and extinction corrections.

We intend to readdress the peculiar motions measured towards the Great Attractor using K band photometric observations of early-type galaxies in the Hydra-Centaurus region. In order to provide an accurate zero-point in the new infrared distance scale, K band photometry for our Coma sample would be also required. The new data will provide a clean test of the preliminary results discussed in this thesis questioning the reality of such large peculiar velocities.

6.2.3 Directions for future work.

The research guidelines summarized above are focused on nearby, giant spheroidal systems. The results will provide, however, secure grounds for two more ambitious projects: the study of the global correlations for dwarf galaxies and the evolution of galaxy properties from $z \sim 0.5$ to the present time. Both projects are of the greatest importance for modern Cosmology. Dwarf galaxies constitute the predominant galaxy population in the universe, may be un-biased tracers of the large-scale mass distribution and their properties are likely to be a direct consequence of the initial conditions rather than the result of merging processes. While dwarf galaxies may tell us on the initial process of galaxy formation, the variation of the three fundamental relations stated in our framework with look-back time will provide an accurate picture of how galaxies evolve. Both projects will soon be possible due to the recent advances in astronomical instrumentation for multiobject spectroscopy and the new observational frontiers opened up by the Hubble and Keck telescopes.

BIBLIOGRAPHY

Aaranson, M., Huchra, J., Mould, J., Schechter, P.L. & Tully, R.B. , 1982. *Astrophys. J.*, **258**, 64.

Aaranson, M., Bothum, G.D., Mould, J., Huchra, J., Schommer, R.A. & Cornell, M.E., 1986. *Astrophys. J.*, **302**, 536.

Aaranson, M., Bothum, G.D., Mould, J., Huchra, J., Schommer, R.A. & Cornell, M.E., 1989. *Astrophys. J.*, **338**, 654.

Aragón, A., Gorgas, J. & Rego, M., 1987. *Astron. Astrophys.*, **185**, 97.

Arimoto, N. & Yoshii, Y., 1987. *Astron. Astrophys.*, **173**, 23.

Ashman, K.M., 1992. *Publ. Astron. Soc. Pacific*, **104**, 1109.

Bender, R., 1991a. in *The Stellar Population of Galaxies (IAU Symposium 149)*, Ed. Barbury, B., Kluwer Academic Publishers, Dordrecht.

Bender, R., 1991b. in *The Stellar Population of Galaxies (IAU Symposium 149)*, Ed. Barbury, B., Kluwer Academic Publishers, Dordrecht.

Bender, R., 1992. in *Structure, Dynamics and Chemical Evolution of Early-Type Galaxies*, Ed. Danzinger, J., Zeilinger,W.W. & Kjar, K., p3.

Bender, R., Burstein, D. & Faber, S.M., 1992. *Astrophys. J.*, **399**, 462.

Bender, R., Burstein, D. & Faber, S.M., 1993. *Astrophys. J.* , preprint.

Bertschinger, E. & Juskiewicz, R., 1988. *Astrophys. J.*, **334**, L59.

Bica, E. & Alloin, D., 1988. *Astron. Astrophys.*, **181**, 270.

Bica, E., 1988. *Astron. Astrophys.*, **195**, 76.

Binggeli, B., Sandage, A. & Tarenghi, M., 1984. *Astron. J.*, **89**, 64.

Binggeli, B. & Cameron, L.M., 1991. *Astron. Astrophys.*, **252**, 27.

Blumenthal, G.R., Faber, S.M., Primack, J.R. & Rees, M.J., 1984. *Nature*, **311**, 527.

Bower, R.G., Ellis, R.S., Rose, J.A. & Sharples, R.M., 1990. *Astron. J.*, **99** , 530.

Bower, R.G., Lucey, J.R. & Ellis, R.S., 1991a. *Mon. Not. R. astr. Soc.* , **254**, 589.

Bower, R.G., Lucey, J.R. & Ellis, R.S., 1991b. *Mon. Not. R. astr. Soc.* , **254**, 601.

Bruzual, A.G., 1983.. *Astrophys. J.*, **273**, 105.

Bruzual, A.G. & Charlot, G., 1993. *Astrophys. J.*, **405**, 538.

Burstein, D., 1977. in *Evolution of Galaxies and Stellar Populations*, Ed. Tinsley, B.M. & Larson, R.B., p.191., Yale University Observatory, New Haven.

Burstein, D. & Heiles, C., 1984. *Astrophys. J. Suppl.*, **54**, 33.

Burstein, D., Faber, S.M., Gaskell, C.M. & Krumm, N. , 1984. *Astrophys. J.*, **287**, 586.

Burstein, D., Davies, R.L., Dressler, A., Faber, S.M., Stone, R.P.S., Lynden-Bell, D., Terlevich, R.J. & Wegner, G. , 1987. *Astrophys. J. Suppl.*, **64**, 601.

Burstein, D., Davies, R.L., Dressler, A., Faber, S.M., Lynden-Bell, D., Terlevich, R.J. & Wegner, G., 1988. in *Towards Understanding Galaxies at Large Redshift*, Ed. Kron, R.G. & Renzini, A., p.17, Kluwer Academic Publishers, Dordrecht.

Burstein, D., Faber, S.M. & Dressler, A., 1990. *Astrophys. J.*, **354**, 18.

Butcher, H.R. & Oemler, A., 1985. *Astrophys. J. Suppl.*, **65**, 665.

Buzzoni, A., 1989. *Astrophys. J. Suppl.*, **71**, 817.

Caldwell, N., 1983. *Astron. J.*, **88**, 804.

Campos, A., Guzmán, R., Prieto, M. & Young, P., 1994. *in prep*, .

Courteau, S., Faber, S.M., Dressler, A. & Willick, J.A. , 1993. *Astrophys. J.*, **412**, L51.

Davies, R.L., 1981. *Mon. Not. R. astr. Soc.*, **194**, 879.

Davies, R.L., Efstathiou, G., Illingworth, G.D. & Schechter, P. , 1983. *Astrophys. J.*, **266**, 41.

Davies, R.L., Burstein, D., Dressler, A., Faber, S.M., Lynden-Bell, D., Terlevich, R.J. & Wegner, G., 1987. *Astrophys. J. Suppl.*, **64**, 581.

de Carvalho, R.R. & Djorgovski, S., 1989. *Astrophys. J.*, **341**, L37.

de Carvalho, R.R. & Djorgovski, S., 1992a. in *Cosmology and Large-Scale Structure in the Universe*, Ed. de Carvalho, R.R., A.S.P. Conf. Ser..

de Carvalho, R.R. & Djorgovski, S., 1992b. *Astrophys. J.*, **387**, L49.

Cole, S. & Kaiser, N., 1989. *Mon. Not. R. astr. Soc.*, **237**, 1127.

de Vaucouleours G. & Olson D., 1982. *Astrophys. J.*, **256**, 346.

Dekel, A. & Silk, L., 1986. *Astrophys. J.*, **303**, 39.

Disney, M.J., 1976. *Nature*, **263**, 573.

Dixon, K.L., Godwin, J.G. & Peach, J.V., 1989. *Mon. Not. R. astr. Soc.*, **239**, 459.

Djorgovski, S. & Davies, M., 1987. *Astrophys. J.*, **313**, 59.

Djorgovski, S., de Carvalho R. & Han, M.S., 1988. in *Extragalactic Distance Scale*, Ed. van den Bergh, S. & Pritchet, C.J., p329, A.S.P. Conference Series.

Djorgovski, S., 1991. in *Morphological and Physical Classification of Galaxies*, Ed. Bussarello, G., Longo, G. & Capaccioli, M., Springer Verlag.

Djorgovski, S., 1992. in *Cosmology and Large-Scale Structure in the Universe* , Ed. de Carvalho, R.R., A.S.P. Conference Series.

Djorgovski, S. & Santiago, B.X., 1992. in *Structure, Dynamics and Chemical Evolution of Early-Type Galaxies*, Ed. Danzinger, J., Zeilinger,W.W. & Kjar, K., p59.

Dressler, A., 1980. *Astrophys. J. Suppl.*, **42**, 565.

Dressler, A., 1984. *Astrophys. J.*, **281**, 512.

Dressler, A., 1987. *Astrophys. J.*, **317**, 1.

Dressler, A., Lynden-Bell, D., Burstein, D., Davies, R.L., Faber, S.M., Terlevich, R.J. & Wegner, G., 1987. *Astrophys. J.*, **313**, 42.

Dressler, A. & Faber S.M., 1990. *Astrophys. J.*, **354**, 13.

Dressler, A., Faber S.M. & Burstein, D., 1991. *Astrophys. J.*, **368**, 54.

Efstathiou, G. & Fall, S.M., 1984. *Mon. Not. R. astr. Soc.*, **206**, 453.

Efstathiou, G., Bond, J.R. & White, S.D.M., 1992. *Mon. Not. R. astr. Soc.*, **258**, 1.

Evrard, A., 1989. *Astrophys. J.*, **341**, 26.

Faber, S.M., & Jackson, R.E., 1976. *Astrophys. J.*, **204**, 668.

Faber, S.M., 1982. in *Astrophysical Cosmology*, Ed. Bruck, H.A., Coyne, G.V. & Longair M.S., p.191, Vatican City: Ponti. Acad. Sci.

Faber, S.M., Burstein, D., Friel, E. & Gaskell, C. M., 1985. *Astrophys. J. Suppl.*, **57**, 711.

Faber, S.M., Dressler, A., Davies, R.L., Burstein, D., Lynden-Bell, D., Terlevich, R.J. & Wegner, G., 1987. in *Nearly Normal Galaxies, From the Planck Time to the Present*, Ed. Faber, S.M., p.175, Springer Verlag, New York.

Faber, S.M., Wegner, G., Burstein, D., Davies, R.L., Dressler, A., Lynden-Bell, D. & Terlevich, R.J., 1989. *Astrophys. J. Suppl.*, **69**, 763.

Fish, R.A., 1964. *Astrophys. J.*, **139**, 284.

Frenk, C.S., White, S.D., Efstathiou, G. & Davis M., 1985. *Nature*, **317**, 595.

Franx, M., 1988. *Ph.D. Thesis*, University of Leiden.

Franx, M. & Illingworth, G., 1990. *Astrophys. J.*, **359**, L41.

Godwin, J.G. & Peach, J.V., 1977. *Mon. Not. R. astr. Soc.*, **181**, 323.

Godwin, J.G., Metcalfe, N. & Peach, J.V., 1983. *Mon. Not. R. astr. Soc.*, **202**, 113.

Gorgas, J., Faber, S.M., Burstein, D., Gonzalez, J.J., Courteau, S. & Prosser, C., 1991. *Astrophys. J.*, preprint.

Gorgas, J., Efstathiou, G. & Aragón Salamanca, A., 1990. *Mon. Not. R. astr. Soc.*, **245**, 217.

Gregg, M.D., 1992. *Astrophys. J.*, **384**, 43.

Gunn, J.E. & Gott J.R. III., 1972. *Astrophys. J.*, **176**, 1.

Gunn, J.E. & Stryker, L.L., 1982. *Astrophys. J. Suppl.*, **52**, 121.

Guth, A.H., 1981. *Phys. Rev.*, **D23**, 347.

Hamabe, M & Kormendy, J., 1987. in *Structure and Dynamics of Elliptical Galaxies*, eds de Zeeuw, T., p.378, Reidel Publishing Company.

Huchra, J.P., Davis, M., Latham, D. & Tonry, J. , 1983. *Astrophys. J. Suppl.*, **52**, 89.

Inglis, I., 1985. *PhD thesis*, University of Durham.

Jacoby, G.H., Hunter, D.A. & Christian, C.A. , 1984. *Astrophys. J. Suppl.*, **56**, 257.

Jacoby, G.H. *et al.*, 1992. *Publs. astr. Soc. Pacif.*, **104**, 599.

Jorgensen, I., Franx, M. & Kjaergaard, P., 1993. *Astrophys. J.*, preprint.

Kaiser, N., 1988. in *Large-Scale Structure and Motions in the Universe*, ICTP.

Kent, S.M. & Gunn, J.E., 1982. *Astron. J.*, **87**, 945.

Kormendy, J., 1977. *Astrophys. J.*, **218**, 333.

Kormendy, J., 1985. *Astrophys. J.*, **295**, 73.

Larson, R.B., 1974. *Mon. Not. R. astr. Soc.*, **169**, 229.

Larson R.B, Tinsley, B.M. & Caldwell, C.N. , 1980. *Astrophys. J.*, **237**, 692.

Landolt, A.U., 1983. *Astron. J.*, **88**, 439.

Lauer, T.R., 1985. *Astrophys. J.*, **292**, 104.

Lauer, T.R. & Postman, M., 1993. *Astrophys. J.*, preprint.

Longo, G. & de Vaucouleurs, A., 1983. in *U, B, V Galaxy Catalog* , Astronomy Monographs no. 3, University of Texas.

Longo, G. & de Vaucouleurs, A., 1985. in *Supplement to the U, B, V Galaxy Catalog*, Astronomy Monographs no. 3A, University of Texas.

Lucey, J.R. & Carter, D., 1988. *Mon. Not. R. astr. Soc.*, **235**, 1177.

Lucey, J.R., Bower, R.G. & Ellis, R.S. , 1991. *Mon. Not. R. astr. Soc.*, **249**, 755.

Lucey, J.R., Gray, P.M., Carter, D. & Terlevich R.J. , 1991. *Mon. Not. R. astr. Soc.*, **248**, 804.

Lynden-Bell, D., Faber, S.M., Burstein, D., Davies, R.L., Dressler, A., Terlevich, R.J. & Wegner, G., 1988. *Astrophys. J.*, **326**, 19.

Mathews, W.G., 1972. *Astrophys. J.*, **174**, 101.

Mathewson, D.S., Ford, V.L. & Buchhorn, D. , 1992. *Astrophys. J.*, **389**, L5.

Merritt, D., 1987. *Astrophys. J.*, **313**, 12.

Mould, J.R., 1978. *Astrophys. J.*, **220**, 434.

Mould, J.R., 1984. *Publ. Astron. Soc. Pacific*, **96**, 773.

Navarro, J.F., 1992. in *Structure, Dynamics and Chemical Evolution of Early-Type Galaxies*, Ed. Danzinger, J., Zeilinger,W.W. & Kjar, K., p385.

O'Connell, R.W., 1980. *Astrophys. J.*, **236**, 430.

Oke, J.B. & Sandage, A., 1968. *Astrophys. J.*, **154**, 21.

Peacock, J.A., 1990. *Mon. Not. R. astr. Soc.*, **243**, 133.

Peebles, P.J.E., 1980. in *The Large-Scale Structure of the Universe*, Princeton, Princeton Univ. Press.

Persson, S.E., Frogel, J.A. & Aaronson, M. , 1979. *Astrophys. J.Suppl.*, **39**, 61.

Phillips, S., 1988. *Mon. Not. R. astr. Soc.*, **233**, 561.

Pickles, A.J., 1985. *Astrophys. J.*, **296**, 340.

Renzini, A. & Ciotti, L., 1993. *Astrophys. J.*, **416**, L49.

Roddier, F., 1981. *Progress in Optics*, **19**, 280.

Rose, J.A., 1985. *Astron. J.*, **90**, 1927.

Rood, H.J., & Sastry, G.N., 1972. *Astrophys. J.*, **77**, 451.

Rowan-Robinson, M. *et al.*, 1990. *Mon. Not. R. astr. Soc.*, **247**, 1.

Saito, M., 1979. *Pub. Astr. Soc. Japan*, **31**, 181.

Sandage, A., 1972. *Astrophys. J.*, **176**, 21.

Sargent, W.L.W., Schechter, P.L., Boksenberg, A., & Shortridge, K., 1977. *Astrophys. J.*, **212**, 326.

Schweizer, F., Seitzer, P., Faber, S.M., Burstein, D., Dalle Ore, C., & Gonzalez, J.J., 1990. *Astrophys. J.*, **364**, L33.

Schweizer F. & Seitzer, P., 1992. *Astron. J.*, **104**, 1039.

Silk, J., 1989. *Astrophys. J.*, **345**, L1.

Strom K.M. & Strom S.E., 1978. *Astron. J.*, **83**, 1293.

Terlevich, R.J., Davies, R.L, Faber, S.M. & Burstein, D. , 1981. *Mon. Not. R. astr. Soc.*, **196**, 381.

The, L.S. & White, S.D.M., 1986. *Astron. J.*, **92**, 1248.

Tonry, J.L. & Davis, M., 1981. *Astrophys. J.*, **246**, 680.

Tonry, J.L., 1981. *Astrophys. J.*, **251**, L1.

Tully, R.B. & Fisher, R., 1977. *Astr. Astrophys.*, **54**, 661.

Wall, J.V., Laing, R.A., Argyle, R.W. & Wallis, R.E., 1989. in *A User Guide to the INT Prime Focus CCD*, RGO user manual no. 12.

White, S.M. & Rees, M.J., 1978. *Mon. Not. R. astr. Soc.*, **183**, 341.

Wirth, A. & Gallagher, J.S., 1984. *Astrophys. J.*, **282**, 85.

Worthey, G., Faber, S.M. & González, J.J. , 1992. *Astrophys. J.*, **398**, 69.

Yoshii, Y. & Arimoto, N., 1987. *Astron. Astrophys.*, **188**, 13.

ACKNOWLEDGMENTS

This thesis is very much the result of long, solitary hours in front of a computer terminal. However, I doubt it would have ever been written without the support of good friends and colleagues who encouraged me to develop my own ideas in the early stages of this project, when I felt lost so often. To all of them, my warmest thanks for having believed in those ideas even before I did.

I would like to thank my supervisor John Lucey for having offered me a clear, well-defined project. His good advice and 'healthy skepticism' greatly impulsed the work done in this thesis. I especially thank Alfonso Aragón, Richard Bower, Ian Smail and Steve Zepf for excellent discussions about elliptical galaxies. These 'old style' conversations, often in front of a blackboard or around a good cup of coffee, are among the best moments I spent in the Department. I am indebted to Richard Ellis, Carlos Frenk, John Major, Alan Lotts and David Carter for their continuous support in the many times I asked for their help. I would also like to extend my thanks to the different generations of graduate students and postdocs as well as the staff of the Department of Physics. During the four years I spent in Durham I shared their enthusiasm for all the new ideas that were being developed in the Department. They created an excellent atmosphere of open participation and a certain feeling of identity that I now realise are quite unique. Despite the hectic working schedules, I will always remember these years with a bit of nostalgia. I gratefully acknowledge the Scientific and Engineering Research Council, St. Hilde and Bede College and Graduate Society for the financial support I received during this work.

Many thanks to all the people that filled so many good moments with their friendship during these years, in particular to Elaine, Anne, Renee and several generations of

'Shincliffers', Pat, Peggy, Ian, Ishbel, Michael, Nick, Paco, Jenny, Pablo, Alberto, Francisco, Lourdes y el pequeño Diego... and many others. I especially thank Mike, Nicole and Alfonso for their generosity, good-spirited company and the many things they taught me about myself. I thank the members of my GSBC crew for those excellent early mornings rowing on the river Wear and the memorable experience of the marathon on the river Tyne. Thanks also to my friends in Madrid and Sevilla for their close presence despite time and distance. I would like to give very especial thanks to my family for the continuous, unconditional support they have always given me in all aspects of my life. Finally, I thank Esperanza for all the good moments we shared together.